Advanced Materials '95

Edited by
Y. Bando
M. Kamo
H. Haneda
T. Aizawa

National Institute for Research in Inorganic Materials

Advanced Materials '95

— New Directions in Ultimate Analysis —

Proceedings
of
The 2nd NIRIM International Symposium on Advanced Materials (ISAM '95)
Tsukuba, Japan, March 6 – 10, 1995

Edited by

Y. Bando, M. Kamo, H. Haneda and T. Aizawa

National Institute for Research in Inorganic Materials

EXECUTIVE COMMITTEE

Chairman	Y. Bando	National Institute for Research in Inorganic Materials (NIRIM)
Members	K. Furuya	National Research Institute for Metals (NRIM)
	S. Ichimura	Electrotechnical Laboratory (ETL)
	H. Ichinose	University of Tokyo
	N. Yamamoto	Tokyo Institute of Technology
	T. Aizawa	NIRIM
	H. Haneda	NIRIM
	M. Kamo	NIRIM
	H. Kanda	NIRIM
	Y. Koike	NIRIM
	K. Kojima	NIRIM
	Y. Matsui	NIRIM
	R. Souda	NIRIM

Published by:

National Institute for Research in Inorganic Materials
Namiki 1-1, Tsukuba, Ibaraki 305
Japan

Printed by:

International Communications Specialists, Inc.
Kasho Bldg., 2-14-9 Nihombashi
Chuo-ku, Tokyo 103
Japan

Printed in Japan

PREFACE

This international symposium is the second in a series to promote realization of the National Institute for Research in Inorganic Materials (NIRIM) to become the Center of Excellence (COE) since last year. The COE project was introduced in the fiscal year of 1994 for fostering the establishment of Centers of Excellence in National Institutes. NIRIM had the honor of being selected as one of the first laboratories for hosting the COE project. The theme of the project at NIRIM may be termed "Research on advanced materials using extreme conditions." Faithful to this, we aim at settlement of the real COE by conducting the research programs in three areas: extremely high pressure, high temperature, and advanced structural analytical techniques.

In the promotion of the Center of Excellence (COE), engaging and training capable personnel, improving and upgrading research foundations, giving mobility and greater latitude to researchers, accurate assessment of the results of research plus their freer dissemination... the importance of all of which has been recognized and the effort is being made to maximum extent. In last year, an international symposium, the NIRIM International Symposium on Advanced Materials, was held in relation to all the three fields of research mentioned. Now facing the end of the second year in the 5 year project, we focus on the advanced structural analytical techniques and hold an opportunity to discuss to some depth on the present status and future prospect in this fields. Some of our recent results in NIRIM will also be presented.

The symposium will be attended by many leading researchers from Japan and abroad, in addition to NIRIM members, and will act as a forum for exchange from global view points on the high resolution electron microscopy (HREM), the analytical transmission electron microscopy (ATEM), the ion scattering spectroscopy (ISS), the high resolution energy loss spectroscopy (HREELS), the secondary ion mass spectroscopy (SIMS) and the scanning tunneling microscopy (STM) among others.

Although NIRIM has been actively engaged in research among the three disciplines for many years, we stand determined to exert every effort so as to progress even more, with the help by and collaboration with the experts throughout the world.

We sincerely hope that the symposium is a remarkable contribution to the advancement of research activities of all the attendants and the readers.

Yoshizo Inomata
Director-General
The National Institute for Research in Inorganic Materials

CONTENTS

Some Aspects of Present and Future High Resolution Electron Microscopy of Materials

Hatsujiro Hashimoto
Faculty of Engineering, Okayama University of Science, Ridai-cho, Okayama 700, Japan

Abstract

Some early developments of electron microscopy and current topics which are closely related to the present author and seemed to affect the future development of electron microscopy of materials are discussed in the following topics.

1. Early works using specimen treating devices and image recording systems in electron diffraction cameras and electron microscopes.
2. Observations of single atom images andmoving atom images in crystals accompanied by the movement of lattice defects.
3. Observation of atomic images of three crystals on both sides of two interfaces by pseudo-AFF image condition.
4. Observation of monoatomic layer of Cu-O chain molecules on copper.
5. Atomic images formed by the inner L-shell loss electrons in Si and their contrast mechanism.

1. Introduction

Theoretical prediction on the image contrast of single atoms and atomic images of crystals by Boersch (1946-47) and Scherzer (1949)became more realistic problem when Menter observed crystal lattice fringes in 1956. Improvements of magnification, resolution and contrast of the images and also the recording systems made possible to observe the images of atoms in molrcules (1971) and record the moving atom images in molecules (1978) and crystals(1979). The subsequent developments of atomic resolution electron microscopy were widely utilized in many fields of science and technology and are producing many useful results. This tendency is accelerated by the increase of the function of the microscopes, i.e. producing imaging lens with very small aberration, increasing the coherency of illuminating electron beams, increasing the function of element analysis by detecting their characteristic X-ray and energy loss electrons, making specimen chambers with various types of specimen treating devices such as heating, cooling, high vacuum and reactive and non reactive gas atomosphere.

This of cource is a subject to which many microscopists in different countries have made contributions. However, instead of presenting yet another overall review of the field to add to the large member now existing, it seemed to me that it might be more interesting to use this special occasion to describe from an individual point of view, especially looking back over my own experience since 50 years ago, when I suffered from atomic bomb explosion.

2. My first experiments in combined microscopy and diffraction and early observations by dynamic processes

My first research using electron diffraction camera was carried out in 1944 in Hiroshima to study the materials formed inside the water cooling pipes of the engines of warship. Our university lay at about one mile from the epicenter of the atomic bombing and almost all the rooms and equipments were destroyed and

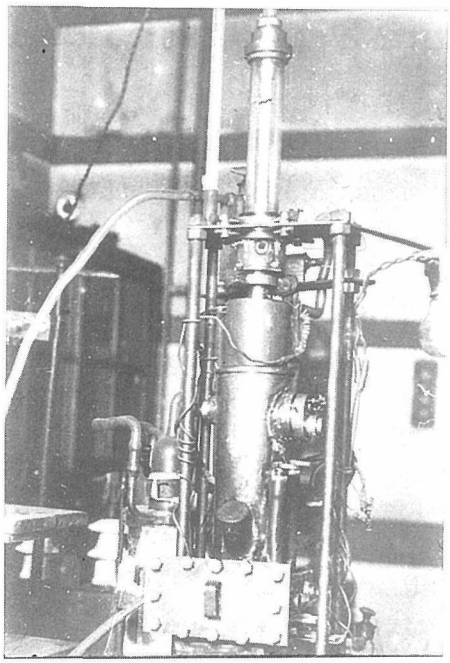

Fig.1(a). Electron diffractron camera(1951) of my own making. Anti-aircraft shell cases are used.

Fig.1(b). Universal Electron Diffraction Microscope(1953) (Prof.Tanaka and Hashimoto).

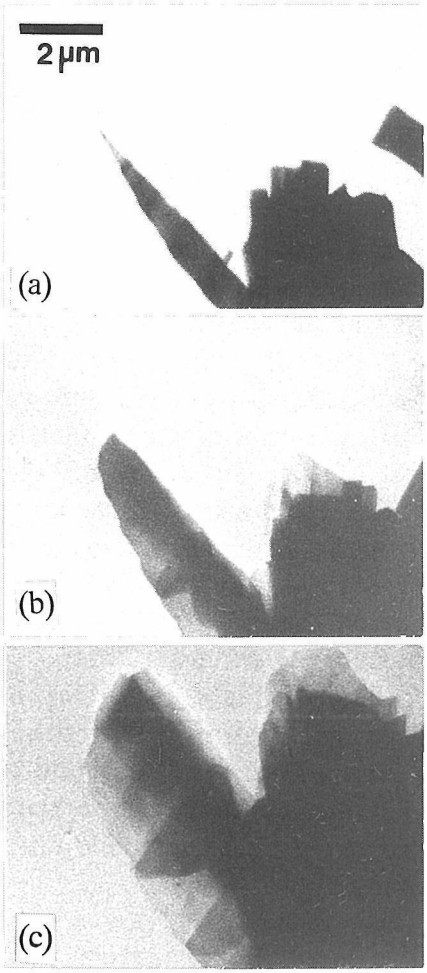

Fig.2. Groth of $WO_{2.72}$. (a) (b) (c) are from movie film of 16 frames/ sec. Intervals are 1sec. (1958 - 59)

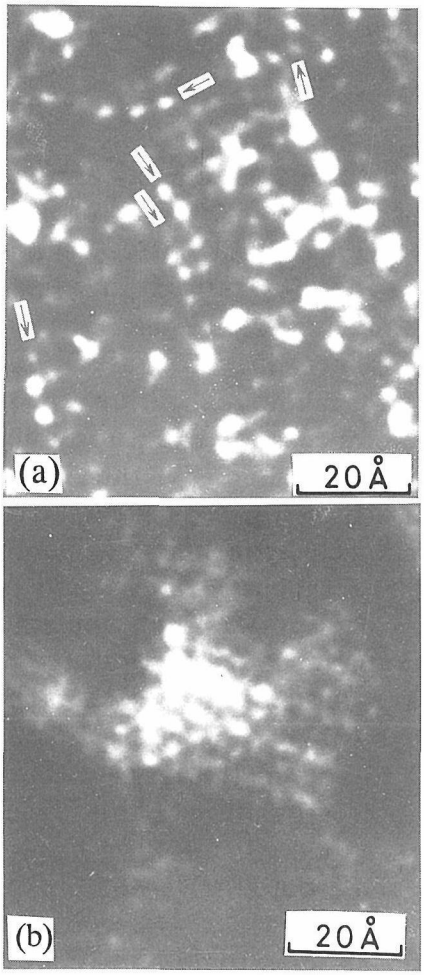

Fig.3. Dark field images. (a) Th-pyromeritate molecules (arrows). (b) Small ThO_2 crystal (1971 - 78).

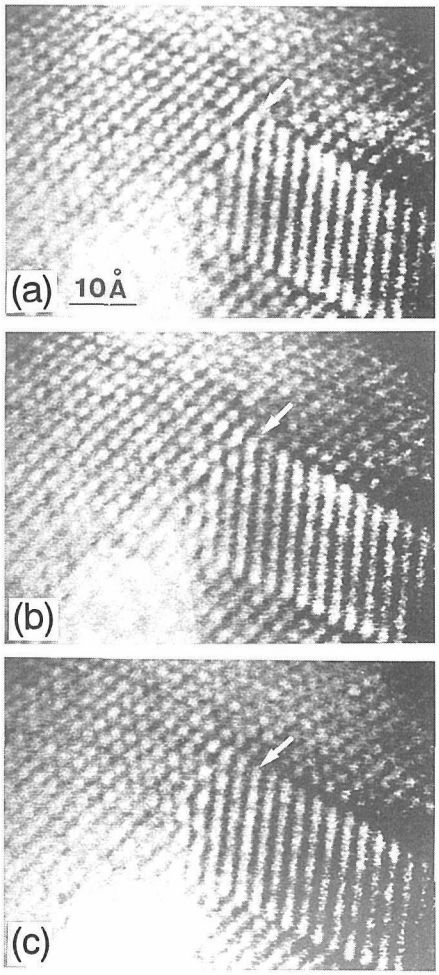

Fig.4. Movement of atoms at the tip of twin in Au crystal. Intervals are 0.07 sec. (1979)

burnt down, but thanks to two water tanks which I placed in our room and to my timely fire figting, our equipment survived and was successfully used afterwards by S.Kuwabara.

In 1946, I moved to kyoto and worked in kyoto Technical University and Kyoto University where condition, though difficult (with gas available only by day and electricity only at night) , were incomparably better than there in Hiorshima. Fig.1(a) shows the electron diffraction camera which I built and machined myself from anti-aircraft shell cases and brass cylinders which were going to be used in the war. The resolution was improved by the use of electron lens. I noted some fine structue in the electron diffraction patterns was chosely related to the morphology of the crystals which grew. I was stimulated by the idea of Boersch(1936)[1] and Hillier and Baker(1946)[2], and after some optical set up observations, we mad three-lens electoron microscope which could also functon as a high resolution electron diffeacton camera and called the Universal Electron Diffraction Microscope (UEDM) in 1953 (Fig.1(b))[3]. The three-lens electron microscope constructed by Le Poole(1947) was not yet known in Japan when we started to construct our one.

Using this UDEM, I was able to observe a variety of diffraction contrast(1954)[4] including dislocation image (at that time I did not realize), subsidiary maxima of electron diffraction, shadow election micrographs and convergent beam electron diffraction patterns. The dislocation images appeaing in moire patterns from two overlapping crystals were also obserbed(1957).

An energy analizer of the net-filter type developed by Boersch was incorporated in the UEDM and we were able to show the Kikuchi lines from zinc blend crystals contained both an elastic and inelastic component.(1956)

After fitting UEDM with specimen heating and gas reaction cartridge, we studied the processes of growth and evaporation of tungsten oxide and molybden oxide crystals (1958~61). I then constructed a new microscope with improved specimen gas reaction chamber and heating cartridge with the aid of Shimadzu Co. and made a number of in-situ observations of dynamic processes by recording with cine film directly from fluorescent screen(1959~60)Fig.2(a)

Later I used TEOL 7A microscope for these experiments(1968) and employed a TV orthicon camera(1970). In those observations it was noted that molten oxide drops behave the important role of crystal growth, which was named as drop growth by us(1960), Sulphurization process of copper in H_2S gas and reduction of cupric iodide to copper in hydrogen at 700°C were also carried out.

3.Images of single atoms and in-situ observation of moving atoms

Difficulty of observation of single atoms is not only in their small size($\sim 10^{-8}$cm) but also in their empty structure, which do not absorb the incoming electrons. They simply scatter them through small angles and indeed act like phase object. In order to increase the image contrast and eliminate the effect of supporting film, long chain pyromeritate molecules containing Th atoms were supported on a thin crystalline graphite substrate and their dark field images were photographed by using objective aperture to exclude the Bragg reflected beams from the substrate and to accept the electrons scattered at small angles by Th atoms as shown in Fig.3(a). The image of a small ThO_2 crystal formed by the decomposition of Th-pyromeritate molecules is shown in Fig.3(b)(1971,1973[6]). Since it seemed interesting to see the movement of atoms under strong beam irradiation, the transition process from Th-pyromeritate molecules to small ThO_2 crystals was recorded in TV film by modifying the TV camera and electron

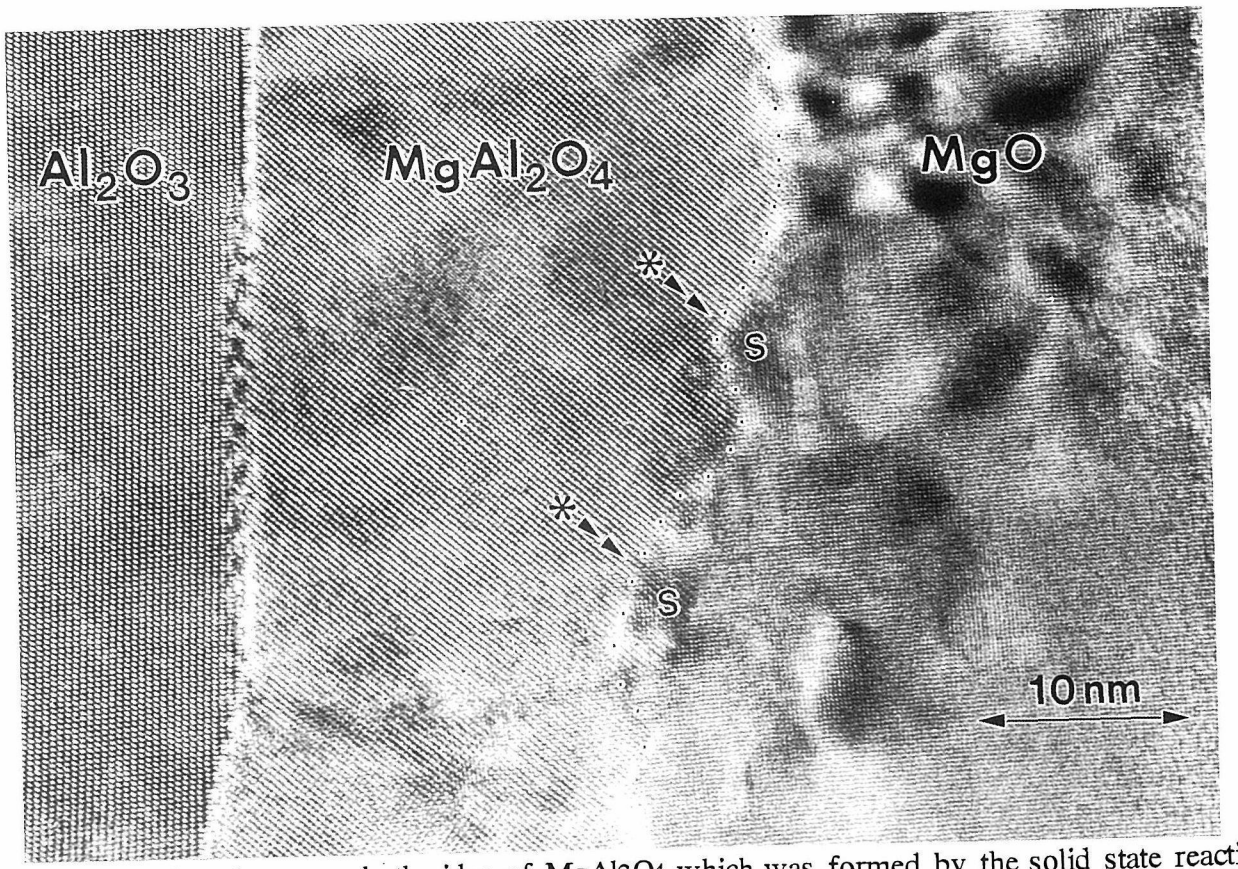

Fig.5.Two interfaces on both sides of $MgAl_2O_4$ which was formed by the solid state reaction between MgO and Al_2O_3crystals (Courtesy by D.Hesse R.Scholz,St.Seng and J.Heydenreich; Int.Nat.Symp.HV and HREM Stuttgart Feb.21-24(1994).

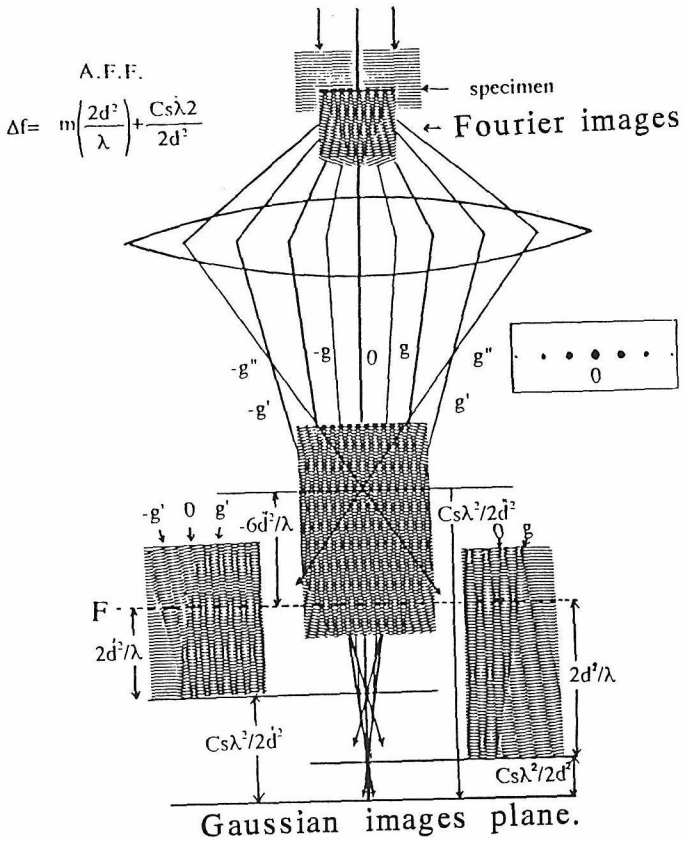

Fig.6.Relation of AFF condition and Fourier images.

microscope to get final magnification of 24 million at TV screen and to get beam current density of 100 amp/cm^2 (1978)[7],[8]. This TV system and electron microscope (JEOL 120C) were used to record the movement of atoms in crystals , which are accompanied by the movements of crystal lattice imperfections such as dislocations, stacking faults, and growth of twins and dislocation loops. Many further examples have been obtained(1979)[8] some of which can be seen on film and in Fig.4. TV system which can record the atomic level images was commercialized in 1985.

4.atomic level imaging of crystals on either sides of interfaces using pseudo AFF condition

The atomic structure images of crystals on both sides of the interface are not so easy to be recorded at the same time, because of the misorientation and/or big difference of lattice spacings of the crystals and no use of Scherzer focus applicable to the weak phase objects. Fig.5 shows the images of two interfaces in three crystal lattice images of Al_2O_3, $MgAl_2O_4$ and MgO. The images of three crystals are seen clearly with high contrast even though the lattice spacings have large difference. Even though these lattice spacings are within the resolution limit (0.18 nm) the thickness of the specimen and focussing of the lens play important roles to obtaining the images with high contrast and image peaks at atom positions. Scherzer forcus is available only for weak phase object. In the convectional transmission electron microscope, shift of the phase angle of electron waves by the spherical aberration is compensated by the defocusing Δf . At the appropriate defocus Δf, the relative phase may be simply related in the same way as for a zero aberration lens. This Aberration Free Focus (AFF) [9] condition is given, by setting phase shift to be $2m\pi$, as

$$\Delta f = m\frac{2d^2}{\lambda} + \frac{Cs\lambda^2}{2d^2}$$

where λ : wave length, Cs : spherical aberration coefficient, m=0, ±1, ..., AFF image are formed on either side of the focussing point which locates from the Gaussian image plane with the distance of $Cs\lambda^2/2d^2$. and with the period of $2d^2/\lambda$, which is the Fourier images. As shown in Fig.6, if many Bragg reflect waves are exited in the specimen, the interference of the waves with g,0,-g ; g',0,-g'; g'', 0, -g''.... produce corresponding Fourier images of the period of $2d^2/\lambda$.... at the distance of $Cs\lambda^2/2d^2$ from Gaussian images plane. In the AFF conditions, intensity maxima of those Fourier images with certain order superimpose exactly. In Fig.6, the intensity maxima of Fourier images at $2d^2/\lambda$, $2d'^2/\lambda$.... and $6d''^2/\lambda$, which are formed by the interference of g, 0, -g; g', 0, -g': g'', 0, -g'' are superimposed exactly at the focus plane F. In order to interfere the wave with enough high contrast ,degree of coherence of the waves has to be high. For the partially coherent waves, which are currently used, only the few waves from the low order reflections can contribute to the images.

For the lattice fringe spacing are 0.2106nm (MgO), 0.2552nm (Al_2O_3), 0.2859nm ($MgAl_2O_4$), 0.3481nm (Al_2O_3), $Cs\lambda^2/2d^2$ are 30.46nm, 20.74nm, 16.52nm, 11.16nm and half periods of Fourier images d^2/λ become 26.98nm, 39.62nm, 49.72 nm and 73.72nm for Cs=1mm and λ=0.00164385nm (400kV).

Thus, the maximum intensities of respective Fourier images of 7th, 5th, 4th, 3rd locate nearly on the plane at 219.3nm separated from the Gaussian image plane. By adjusting the focus of imaging lens to this plane, the crystal lattice fringes appearing at the bottom surfaces of MgO, $MgAl_2O_4$, and Al_2O_3 will be

well projected to the image plane if the coherence of the waves is high, (for example beam divergence q=0.1mrad. chromatic defocus value Δ=1nm). The image contrast calculated by using the currently available coherence (q=1mrad, Δ =10nm) suggests that the focus of 30.4nm~16.5nm gives the bright spots images with high contrast, some of which correpond to the positions of atoms and their groups. These focus conditions may be called as pseudo-AFF condition. However, since all Bragg reflected waves are not included in the imaging and the wave intensity at the bottom surface is dependent of crystal thickness, for identifying the atomic position from the images, the calculation of image contrast considering crystal thickness and imaging parameters is still necessary.

5. Observation of monoatomic layer of CuO chain molecules formed on copper surface.

During the 200kV EM observations of pure Cu-thin films in 110 orientation in the vacuum 10^{-4}Pa, the specimen thickness became decreased by the sputtering and faint fringe contrasts became visible when the thickness of Cu specimen becomes smaller than several nanometers. Such fringes were also observed in 100 and 210 orientations and their atomic structures are seen together with the ones from substrate Cu crystals. By analysing the formation condition, the orientation relation to the substrate copper and probable relationship to the oxidation, we assumed that such fringe contrast might stem from an oxygen-induced surface reconstruction. This assumption was confirmed by a multi-slice image simulation on the basis of the well-known electron diffraction and imaging theory using an added-row reconstruction model [10]. Our calculated results indicate that an added-Cu-O-chain surface reconstruction can generate a regular fringe arrangement with sufficient contrast in a thin copper film with a thickness of several nanometers. Good agreement between the calculated and the observed images suggests that our assumption is appropriate. The present study [11] demonstrates the potential of HREM to investigate surface structure and surface reaction at the atomic level.

6. Images of atoms formed by the inner L shell loss electrons in Si and their contrast mechanism

The characteristic energy loss electrons which have excited the inner shell electrons in atoms can be used for characterization of atoms. Using JEOL400kV electron microscope with the sector type electron image filter made by Gatan R&D, an electro-polished thin film of Al-1.2wt%Si alloy containing plate shaped Si precipitates shown in Fig.7(a) was investigated. Figure 7(b) is a magnified image formed by zero loss electrons with an energy window 5eV, in which crystal lattice structures of Al matrix and Si precipitates are seen. Energy loss spectra from the circled regions A and B are shown in (c). The spectrum from region A shows the existence of Al L_1 and $L_{2,3}$ edges and the one from region B shows only the Si $L_{2,3}$ edge with no detectable edges of Al. The images obtained by using inner shell loss electrons of 119eV (Si $L_{2,3}$) is shown in (d). From the image shown in (d) we subtracted the image of the same area formed by using 88± 2.5eV electrons (background of EELS in (c)). The result is shown in (e), in which many bright dots are seen in both Si crystal and surrounding Al regions. The Al region appears dark due to the higher intensity at 88eV than at 119eV. Since the thickness of the specimen crystal was estimated to be less than 10nm from the image contrast of low magnifrcation in (a), the bright spots in (e) are the images of individual Si atom columns formed by inner shell loss electrons, and not the

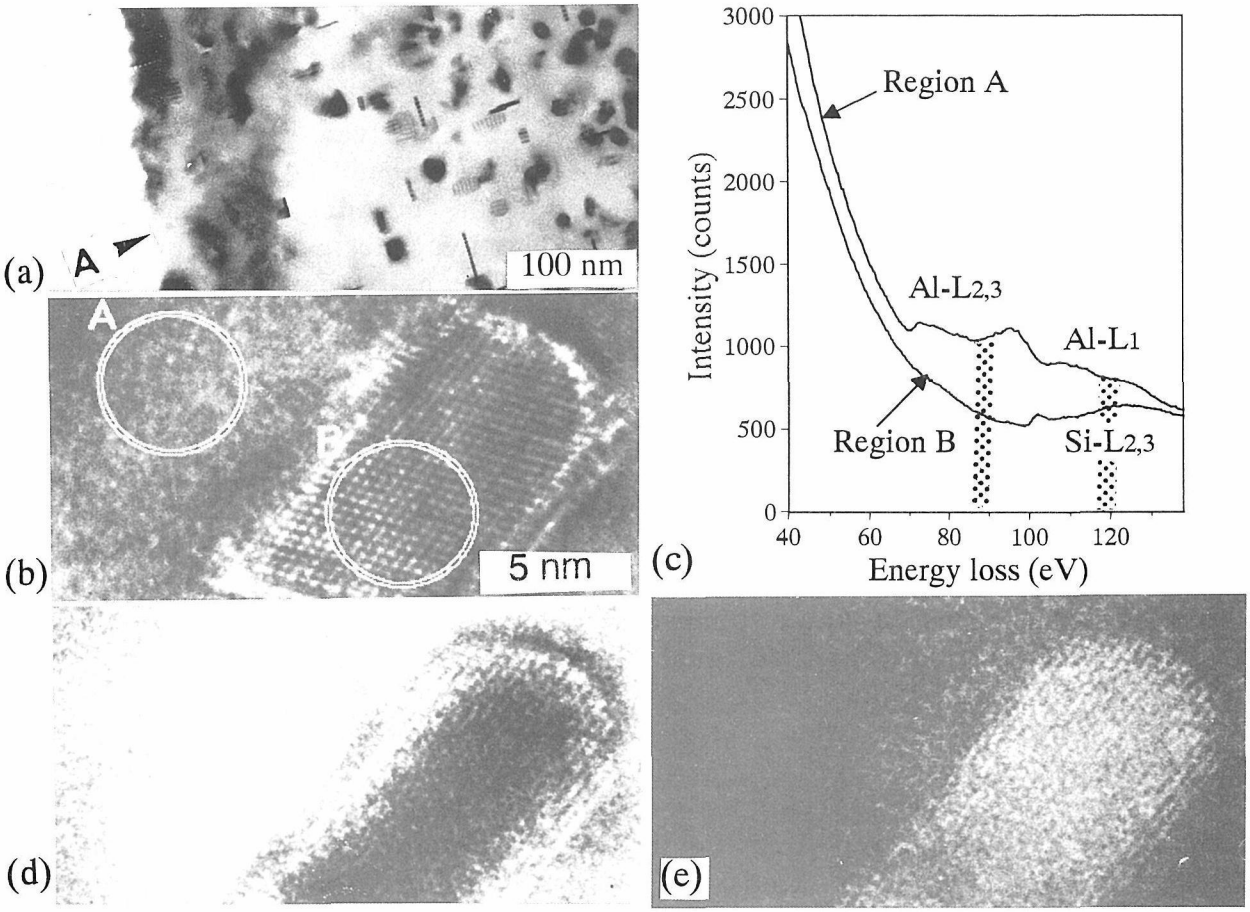

Fig.7.(a).Images of electropolished Al-1.2wt% Si film with Si platelet precipitalions. (b).Large magnifraction image of thin region A in (a) formed by zero loss electrons. (c).EELS from areas A and B in (b). (d).Image formed by 119 eV (SiL_{23})loss electrons. (e).Same image with (d) after subtracting the image at 88 eV (back ground of spectrum) from image (d).

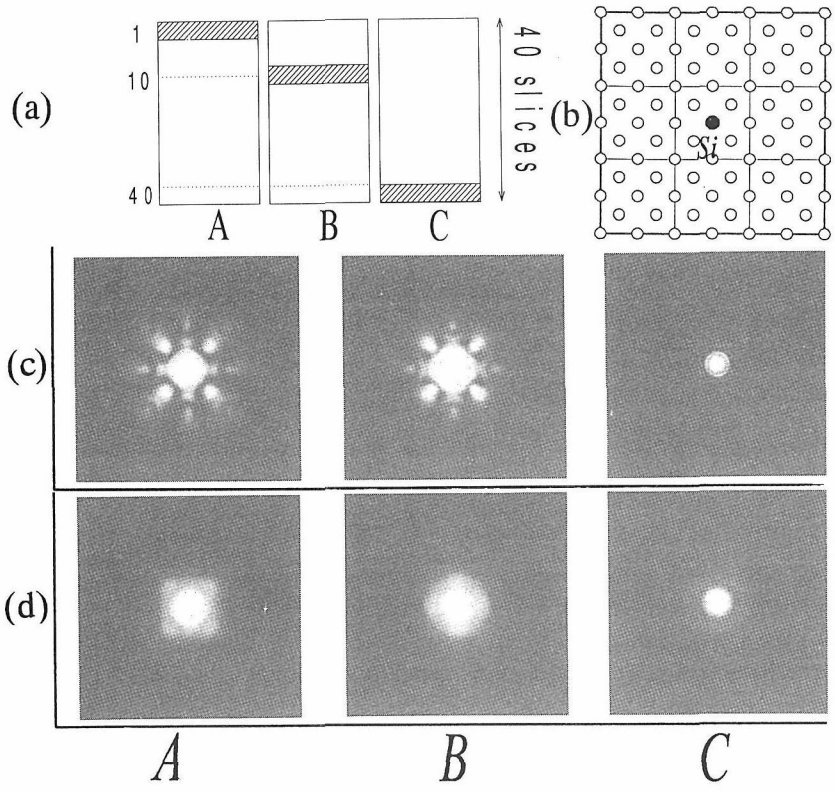

Fig.8.(a) and (b) are depth position and location of Si atom undergone inner shell excitation. A: in first unit cell (top), B: in 10th unit cell, C: in 40th unit cell (bottom). (c) Intensity distribution of core loss electrons from a Si atom at the bottom of A,B,C in (a). (d) EM images corresponding to (c). 200kV, C_s=0.75mm , C_{ch}=1.5 mm, Δ =30nm, $\Delta\alpha$ =0.5 mrad. Δf=43.3 nm.

structure images formed by the interference of Bragg reflected electrons.

In order to simulate the image contrast of Si atoms formed by electrons that have undergone losses at their inner shells, the corresponding inelastic scattering factors for Si L_3 ionization have been derived by the program of modified hydrogenic L-shell cross section[12]. By embedding the inelastic event of Si atom at the depth of 1st. 10th and 40th (bottoms) unit cells of the Si(Fig.8(a)) in a multi-slice computation for elastic scattering in Si crystals with 40 unit cells thickness were carried out and the intensity distribution of electron waves at the bottom surfaces of the crystals are derived, which are shown in Fig.8(c). Fig.8(d) represents the electron microscope images corresponding to the intensity in (c). The atom images formed by the core loss electrons near the bottom surface appear shaper than those near the top surface. The above results agree with the scheme proposed by Krivanek [13]. But for very thin crystals (less than 10nm in Si), even though elastic scattering has taken place after the electrons underwent energy losses, electrons flow along a specific atomic column and appear as bright spot images at the bottom surface of the crystal. Thus for a very thin crystal, the bright spots observed in the energy filtered image are the summation of the images of individual atoms in atomic columns that have suffered from inner shell ionization.

7. Some future prospects

The atoms whose hypothesis appeared in 17th centry are now visible in some atoms and can be recorded together with their movements by the TEM since 1970 - 1979. Though the kinds of visible atoms are limited at present, by understanding that all kinds of materials, including newly producing complicated ones in future, consist of about one hundred kinds of atoms, the much energy will be focussed to the observations of atomic structure of complicated materials, atomic clusters and behaviours of foreign atoms in the materials together with their characterization. The function of transmission electron microscopies will be developed more by including and producing new functions such as SEM, field emission tips, holography, STM and related techniques, use of high voltage and low voltage electrons, clean vacuum, research method of surface atomic reconstruction etc. The electronic structure of the materials especially very thin films and surface layer will be studied by combining atomic level imaging with EELS.

Reference

[1] H.Boresch:Ann.d.Phys.27(1936)75

[2] J.Hillier and R.F.Baker:J.Appl.Phys.17(1946)12

[3] K.Tanaka and H.Hashimoto:Rev.Sci Inst.24(1953)669

[4] H.Hashimoto:J.Phys.Soc.Japan 9(1954)150

[5] H.Hashimoto:J.Elect.Microscopy 9(1960)130

[6] H.Hashimoto,A.Kumao,K.Hino,H.Endoh,H.Yotsumoto,and A.Ono:Japan J.Appl.Phys.10(1971)1115,J.Elect. Micrs.22(1973)123

[7] H.Hashimoto,A.Kumao and H.Endoh:Proc.9th Int.Nat.Congr.Toronto 3(1978) 244

[8] H.Hashimoto,Y.Yokota,Y.Takai,H.Endoh and A.Kumao:Chemica Scripta, Proc.Nobel Symp.14(1979)125 and Japan,J.Appl.Phys.19(1980)L1-4.

[9] H.Hashimoto,E.Endoh,Y.Takai,H.Tomioka and Y.Yokota:Chemica Scripta, Proc.Nobel Symp.14(1979)23

[10] D.J.Coulman et al:Phys.Rev.Latter 64(1980)176, F.Jensen et al:Phys.Rev.B41(1990)10233, Y.Kuk et al: ibid B41(1990)12393.

[11] R.Guan,R.S.Li,S.H.Xu,S.Y.Li and H.Hashimoto,Read at,C.E.M.S. meeting(1994)

[12] H.Endoh and H.Hashimoto:Ultramicroscopy 54(1994)351, H.Endoh,H.Hashimoto and Y.Makita:ibid 56(1994)108.

[13] O.L.Krivanek,A,J.Gnbbenz,N.Delby,C.E.Mayer:Micros.Microanal.Microstruct 3(1992)187

Atomic Resolution Electron Microscopy and Applications to Interface Science

F. Phillipp and M. Rühle
Max-Planck-Institut für Metallforschung, Seestr. 92, D-70174 Stuttgart, Germany

Abstract
The basic characteristics of the new high-voltage atomic resolution electron microscope (JEOL JEM-ARM1250) in Stuttgart are described. The instrument reaches its theoretical point resolution of 0.105 nm at an accelerating voltage of 1250 kV. The defocus spread due to chromatic aberrations was determined quantitatively by extensive diffractogram tests. An information transfer limit between 0.08 and 0.09 nm can be deduced from the results of these tests. Applications to interface science are presented.

1. Introduction

A small *point resolution,* d_S, is most desirable in high-resolution electron microscopy since structure images taken at Scherzer defocus offer the advantage of direct interpretability: all spatial frequencies between zero and the value corresponding to the point resolution are transferred without gaps or phase inversion. In a first approximation the image reflects a projection of the atomic structure of a sufficiently thin specimen in the direction of the electron beam [1,2]. A point resolution of $d_S \sim 0.1$ nm requires a high voltage of 1.25 MeV if the objective lens possesses a constant of sperical aberration of $C_S \approx 1$ mm.

Thus, a decrease in wavelength by an increase of the accelerating voltage of the electron microscope has been the route towards higher resolution followed in the past. Early projects for megavolt microscopes designed for Ångström resolution date back to the mid-sixties [3]. However, it took until the beginning of the 1980s for the first megavolt microscopes to surpass the 0.2 nm resolution limit [4,5]. The major problems encountered are instabilities of various kinds: fluctuations of high-voltage and objective-lens current as well as AC stray magnetic fields, which attenuate the contrast transfer owing to chromatic aberration. Mechanical vibrations of the specimen are a further source of instabilities. As a consequence, the information transfer of the megavolt microscopes was cut off at spatial frequencies smaller than the first zero of the transfer function at Scherzer defocus, i.e., the theoretical point resolution could often not be reached.

Since the beginning of the 1990s a new generation of high-voltage *atomic resolution* microscopes has been installed in Tsukuba (Hitachi H-1500, 1990 [6]), Sendai (JEM-ARM1250, 1991), Tokyo (JEM-ARM1250, 1992), and Stuttgart (JEM-ARM1250, 1992/1993) which promised to reach their point resolution of ca. 0.1 nm. The characteristics of the instrument and the testing procedures are described in the following and first results are presented (see Phillipp et al [7]).

2. The JEM-ARM1250 in Stuttgart

2.1 Basic design and characteristic parameters

The high-voltage system of the JEM-ARM1250 (for short "ARM") is installed in a twin-tank system (similar to its precursor, the JEM-ARM1000 in Kyoto [8]) which effectively separates the AC-components (Cockroft-Walton generator) from the DC-components (electron source, accelerator, sampling and monitor resistors). A highly stable, low-ripple accelerating voltage is achieved. During the testing of the high-voltage stability paticular attention was paid to

measurements continuously over the entire frequency range from DC up to 10 kHz. A special feedback system was developed and incorporated after the installation of the instrument in Stuttgart. The feedback system improved the high-voltage stability to $< 10^{-6}$/min peak-to-peak. The brightness of the electron gun (single-crystal LaB_6 filament) is $6 \cdot 10^7$ e/cm^2/str allowing us to take high-resolution micrographs at a beam convergence of 0.3 mrad with an exposure time of ~ 2 sec on photographic plates at a magnification of 500.000 x.

The accelerating voltage can be varied between 200 kV and 1250 kV in minimum steps of 20 V. For ease of operation the appropriate currents of the lenses and alignment coils are adjusted automatically at 400 kV, 500 kV, 600 kV, 800 kV, 1000 kV, and 1250 kV by computer control.

The high-resolution objective lens (Tab. 1) has a C_S-value of 1.6 mm at 1250 kV, resulting in a theoretical point resolution of 0.105 nm. The fluctuations of the objective-lens current are $< 6 \cdot 10^{-7}$/min peak-to-peak. The top-entry goniometer is equipped with a z-shift mechanism (Δz = 4 mm) which allows us to locate the specimen in the optimum height position (optimum C_S or pre-field strength) depending on the operating condition (high-resolution imaging or convergent-beam diffraction) or on the accelerating voltage employed. Thus, the point resolution of 0.16 nm reached at 400 kV corresponds to the resolution of a dedicated 400 kV high-resolution microscope (Tab.1). Maximum tilting angles of the double-tilt goniometer are $\pm 40^o$ in the high-resolution specimen position at 1250 kV. The specimen-drift rate has been determined to be $\leq$ 0.004 nm/s, sufficiently small to acquire micrographs with the full electron-optical resolution. Two intermediate and two projector lenses allow the magnification to be varied between 200 and 2.000.000.

The high-resolution objective lens can be replaced by a lens with a side-entry goniometer for in-situ work. Two pole pieces with different gap widths are provided with this lens in order to find the best compromise between resolution and available space in the specimen area (Tab.2). The side-entry lens with the small-gap pole piece has been tested during October 1994 resulting in a C_S-value of 2.8 mm (Tab. 2). The point-to-point resolution of 0.12 nm has been demonstrated, the information limit is at ~ 0.1 nm. Presently, a heating stage (maximum temperature 1150 K) and a cooling stage (liquid Nitrogen) are available. Recently, the stability of these double-tilt stages has been demonstrated.

For image acquisition the ARM is equipped with a standard camera for photographic films. A TV-rate CCD-camera with an image intensifier at the microscope column is coupled to a computer for fast Fourier transform of the micrographs and is used for focusing and beam alignment (a tilt wobbler for coma-free alignment is part of the alignment system). The software package DIGITAL MICROGRAPH is used for on-line image processing.

An imaging electron energy filter [9] with an energy resolution better than 1 eV is mounted below the microscope camera. This energy-filter system (GATAN GIF) has two further CCD cameras: a TV-rate camera which is mainly used during the adjustment procedure of the correcting elements of the filter, and a cooled slow-scan camera (1024x1024 pixels) for digital recording of electron-energy loss spectra as well as energy-filtered images and diffraction patterns.

The energy filter has been used to measure the total width ΔE of the energy distribution of the electrons without specimen. Depending on operation condition and acquisition time ΔE = 0.6 eV to 1.6 eV (FWHM) was determined, demonstrating both good energy resolution of the filter as well as excellent stability of the accelerating voltage of the microscope.

2.2 Resolution Tests

Extensive resolution tests have been carried out by diffractometry of micrographs taken from thin amorphous germanium films [1] employing standard laser diffraction as well as numerical Fourier transformation of digitized micrographs.

The optical diffractograms in Fig. 1 show a minimum in the intensity at spatial frequencies between 9 nm^{-1} and 10 nm^{-1} proving a point resolution of 0.10 nm to 0.11 nm which coincides with the theoretical value. Furthermore, intensity is clearly visible on the diffractogram outside the first minimum. This demonstrates that the information transfer limit is beyond the point resolution.

The ultimate information limit of an electron microscope is determined by the chromatic damping of the contrast transfer function (CTF) [1,2,10] without considering mechanical vibrations and other environmental effects. Energy spread of the cathode, fluctuations of the accelerating voltage and of the objective lens current, and AC stray magnetic fields give rise to a defocus spread Δ which determines the width of the envelope function to the CTF. Particular efforts were made to determine Δ quantitatively [11]. Astigmatic images from amorphous germanium were evaluated. A minimum defocus spread of Δ = 10 nm was determined according to the definition of [10]. Additionally, the intensity profile in laser diffractograms of stigmatic micrographs was evaluated quantitatively and fit to a theoretical CTF (Fig. 2). Fitting at different ranges of spatial frequencies resulted in values of Δ = 8 nm to Δ = 10 nm. The evaluation procedures required special attention to proper correction of the data for the scattering factor of the specimen, the modulation transfer function of the film and the digitizing camera, as well as for background and noise. During the evaluation of the laser diffractograms a correction for the diffraction efficiency of the emulsion surface grating of the film has been employed as well.

The experimentally determined Δ-values yield an information limit of 0.08 nm to 0.09 nm if one assumes that the information transfer is limited by the spatial frequency where the chromatic envelope drops to exp(-2) [2],. The information limit estimated in ref. [2] for the JEM-ARM1250 thus has to be corrected for the instrument in Stuttgart. Further experimental proof of the information transfer beyond 0.1 nm are images of (400) lattice fringes in diamond (d = 0.089 nm) taken with axial illumination and the specimen tilted such that only the (400) reflections were excited, i.e., the fringes *do not* arise from non-linear interference of lower spatial frequency reflections.

Several difficulties are encountered in verifying the 0.1 nm regime of resolution, e.g. decreasing scattering factors at high spatial frequencies, limitations in the weak-phase object approximation when using amorphous specimens, or even limitations from electron-beam induced atom motion [6,12,13].

However, the results obtained during the tests of the Stuttgart ARM demonstrate that high-voltage microscopes may well be characterized in that regime and that *1- Ångström point-resolution microscopy* is possible with a high-voltage electron microscope, provided high stability of the instrument and proper installation conditions are realized.

3. Applications

At present the main activities at the Stuttgart ARM are investigations of defects and interfaces in crystalline materials such as semiconductors, metals, ceramics and composites materials. Some results are presented in the following.

3.1 Semiconductors

For high-resolution studies of defects in semiconductors with the diamond or sphalerite structure the <110> projection is most suitable since, e.g., planar defects lying on {111} planes can be imaged edge on. For the study of the core structure of dislocations with a <110> line direction, e.g. Lomer-dislocations, it is essential to look at them end on which, again, needs the <110> specimen orientation. However, in many semiconductors, the closest separation of atom colums in this orientation is ca. 0.14 nm, i.e. beyond the point resolution of the medium-voltage microscopes, which makes image interpretation difficult [13]. With the Stuttgart ARM, however, structural imaging with atomic resolution is now possible for these materials.

Fig. 3 shows an image of a wedge shaped GaP specimen in the <110> projection, together with simulated images for various thickness values. A strong asymmetry between the contrasts at the positions of the Ga-atoms columns and the P-atom columns is recognized at certain thickness values: In the thinner part of the specimen the contrast of the Ga columns is brighter than the contrast of the P-columns (due to the stronger scattering of Ga), in the thicker parts the asymmetry is reversed. This asymmetry can be used for the determination of the nature of {111}-twin boundaries in the sphalerite structure [15]. As illustrated in Fig. 4, basically two different types of such boundaries may exist (see, e.g., [16]): in one configuration unlike atoms are facing each other (rotation twin), in the second type atoms of the same species are facing each other across the boundary (reflection twin). The experimental micrograph of a {111}-twin boundary in GaP in Fig. 8 shows that the contrasts of the closest atom colums across the boundary are different, thus indicating the configuration of a *rotation twin.*

This example demonstrates that with the Stuttgart ARM the closest atom columns can be separated and that different chemical species can be distinguished reliably. From this we expect valuable information in the study of defects in semiconductors. Of course, one has to keep in mind that even with a high point-resolution at Scherzer-defocus non-linear interferences in thicker specimens could give rise to difficulties in image interpretation. However, the limits set by such effects are much less stringent than in lower-voltage, lower-resolution microscopes .

3.2 Atomistic structure of Cu twin boundaries with 9R phase

Using the Stuttgart ARM, Hofmann and Ernst [17,18] studied the atomistic structure of $\Sigma 3$<110> tilt boundaries in Cu. At high inclination angles, when the boundary plane approaches {211}, these boundaries adopt a complex structure. A thin slab of Cu forms parallel to the boundary plane. The slab posseses a rhombohedral crystal structure. Since the repeat unit of the rhombohedral structure consists of nine close-packed atomic layers, we denote this structure as 9R. Fig. 6 presents the image of a$\Sigma 3$<110> tilt boundary recorded in the ARM. The projection direction lies parallel to the <110> tilt axis of the boundary. In one grain, the boundary plane corresponds to {322}, while in the other grain it lies parallel to {11.4.4} planes. A phase boundary bounds the 9R slab on each side [19]. The phase boundary on the right is a high angle boundary, consisting of kite-shaped structural units. On the left side, in contrast, a regular array of partial dislocations constitutes the phase boundary between the 9R phase and Cu. This phase boundary is a small angle boundary.

To determine the positions of atomic columns in the grain boundary with maximum accuracy, Hofmann and Ernst developed [18] a semi-automatic procedure to extract the projected structure from digitized HRTEM images. The algorithm regards image points in a Euclidean space. This "image space" has one dimension for every pixel in the image, and the intensities of the pixels are the coordinates of the point representing the image. A loop of iterative structure refinement

optimizes a preliminary structure model such that its point in image space has a minimum Euclidean distance from the point representing the experimental HRTEM image.

Owing to various effects that image simulations cannot account for, the simulated image of the refined model does not exactly coincide with the experimental image. Thus, a residual distance remains between the corresponding points in image space. Hofmann and Ernst identify the level of confidence in the refined structure by this distance.

The electron optical parameters of the HRTEM instrument enter the analytical expression for the error vectors as a differential structural sensitivity Γ. This expression describes to what extent the image vector responds to a small lateral shift of an atomic column. The higher Γ, the smaller the error vectors of the atomic columns for a given residual image discrepancy. Hofmann and Ernst demonstrated that under the imaging conditions they employed the differential structural sensitivity of the ARM is higher than for the JEM-4000EX. (The latter instrument operates at 400 kV and reaches a point resolution of 0.175 nm.)

Using the ARM, the positions of the atomic columns in Cu $\Sigma3<110>$ tilt boundaries with 9R structure have been determined with an accuracy of 0.03 nm. This high accuracy proved to be a critical test for model structures calculated by molecular static relaxation.

3.3 Structure images of NiAl

NiAl is an ordered alloy with th B2 (CsCl) structure. Because of its outstanding combination of high melting point, low weight, and good corrosion resistance this material possesses a high potential for engineering applications. The brittleness of polycrystalline NiAl at room temperature, however, constitutes a major problem for potential applications. Understanding the mechanical behaviour of this material requires detailed knowledge of the atomistic structures of dislocation cores and grain boundaries. At present, little is known about these defects. Moreover, the macroscopic properties depend sensitively on the exact concentration of Ni and Al atoms.

The lattice parameter of NiAl is comparatively small: a = 0.288 nm. Therefore, imaging the structure of NiAl and lattice defects therein requires a resolution better than 0.14 nm. Fig. 7 shows a structure image of NiAl recorded in the ARM in <110> projection. The point resolution of the microscope is high enough to image the {100}, {110}, {111}, and {200} spacings in this projection. In particular, the {200} planes with a spacing of 0.14 nm are clearly resolved. For this reason, Al columns and Ni columns appear with different contrast in the image.

In Fig. 7 the local thickness of the TEM foil amounts to $\approx$ 5 nm. Since the image was recorded approximately at optimum defocus ($\approx$ 40 nm), Ni columns appear darker than Al columns. The corresponding image simulation (inset) confirms this interpretation. Since Al columns appear with different contrast than Ni columns, the image carries not only structural but also chemical information. Thus, by means of the ARM it should be possible to assess the degree of ordering and the stochiometry of crystal defects, such as grain boundaries and dislocation cores. Experimental studies on grain boundaries will be reported.

3.4 Structure of special grain boundaries in α-Al_2O_3

Recently, the structure of two special grain boundaries in α-Al_2O_3 have been studies [20,21], namely a near $\Sigma11$ boundary and a $(1\bar{1}04)$ twin. Fig. 8 shows a Fourier-filtered micrograph of the $(0\bar{1}11)\|(01\bar{1}1)$ $N\Sigma11$ boundary. A simulated image is inset in Fig. 8. An atomically sharp interface can be revealed with a characteristic periodic pattern at $(0\bar{1}11)_I$ and $(01\bar{1}1)_{II}$ facets. The pattern

was analysed quantitatively by comparing the HRTEM micrographs (taken under different focus values) with simulated images of different structures that had been relaxed by static-lattice calculations. Best agreement can usually be obtained for grain boundary structures with the lowest energy. Although this structure reproduces the relative translation state of the adjacent crystals within high precision ($\lesssim 0.02$ nm) the calculated core structure of the grain boundaries are usually not in complete agreement with the calculated periodic pattern. This was demonstrated by a quantitative image processing routine [21]. The origin of the differences is probably caused either by a slight misalignment of the two crystals adjacent to the boundary [20] or by the limited knowledge of the interatomic potentials in α-Al_2O_3 [21].

4. Conclusion

The JEM-ARM1250 high-voltage high-resolution electron microscope installed at the Max-Planck-Institut für Metallforschung in Stuttgart possesses a point resolution close to 1 Ångström and an information-transfer limit well beyond. High stability of accelerating voltage achieved with a special feed-back stabilizer, highly stable objective-lens current and proper environmental conditions make it possible for the first time that a megavolt microscope with such performance is in operation. Results obtained within a short period of time demonstrate the power of this instrument in structural analysis. The high point resolution is most advantageous for *quantitative* high-resolution electron microscopy which is the main task in structural physics of defects, small particles and in materials science in the near future.

Acknowledgements

Invaluable help of numerous colleagues from the JEOL company and the Max-Planck-Institut during the manufacturing, installation and testing of the machine is gratefully acknowledged. Prof. K.-H. Herrmann, Tübingen, supported the project through valuable advice and stimulating discussions.

Generous financial support for the realization of the project was provided by the Bundesministerium für Forschung und Technologie (BMFT), the State of Baden-Württemberg, and the Max-Planck-Society.

References

[1] J.C.H. Spence, Experimental High-Resolution Electron Microscopy, Oxford University Press, New York 1988.
[2] M.A. O'Keefe, Ultramicroscopy 47 (1992) 282.
[3] V.E. Cosslett, Contemp. Phys. 22 (1981) 3.
[4] C.J.D. Hetherington, E.C. Nelson, K.H. Westmacott, R. Gronsky, and G. Thomas, Mater. Res. Soc. Proc. 139 (1989) 277.
[5] K. Yagi, K. Takayanagi, K. Kobayashi, and S. Nagakura, ref. 5, p. 11.
[6] Y. Mastui, S. Horiuchi, Y. Bando, Y. Kitami, M. Yokoyama, S. Suehara, I. Matsui, and T. Katsuta, Ultramicroscopy 39 (1991) 8.
[7] F. Phillipp, R. Höschen, M. Osaki, G. Möbus and M. Rühle, Ultramicroscopy 56 (1994) 1.
[8] S. Isoda, S. Moriguchi, H. Kurata, T. Kobayashi, and N. Uyeda, Ultramicroscopy 39 (1991) 247.
[9] O.L. Krivanek, A.J. Gubbens, N. Dellby, and C.E. Meyer, Microsc. Microanal. Microstruct. 3 (1992) 187.
[10] R.H. Wade and J. Frank, Optik 49 (1977) 81.
[11] G. Möbus and M. Rühle, Optik 93 (1993) 108.

[12] H. Lichte, P. Kessler, F. Lenz, and W.-D. Rau, Ultramicroscopy 52 (1993) 575.
[13] J.M. Gibson, Ultramicroscopy 56 (1994) 26.
[14] A. Bourret, J.L. Rouvière, and J. Spendeler, phys. stat. sol. (a) 107 (1988) 481.
[15] F. Phillipp, D. Schaible, and N.Y. Jin-Phillipp in: Electron Microscopy 1994, Vol. 2A , Eds. B. Jouffrey, C. Colliex, J.P. Chevalier, F. Glas, and P.W. Hawkes (Les Éditions de Physique, Les Ulis, France 1994) p. 593.
[16] D.B. Holt, Journal of Materials Science 19 (1984) 439.
[17] D. Hofmann and F. Ernst, Interface Science, in press.
[18] D. Hofmann and F. Ernst, Ultramicroscopy 53 (1994) 205.
[19] U. Wolf, F. Ernst, T. Muschik, M.W. Finnis, and H.F. Fischmeister, Phil. Mag. A66 (1992) 991.
[20] T. Höche, P.R. Kenway, H.-J. Kleebe and M. Rühle, J. Am. Cer. Soc. 77 (1994) 339.
[21] T. Höche, P.R. Kenway, H.-J. Kleebe, M.W. Finnis and M. Rühle, J. Phys. Chem. Solids 55 (1994) 1067.

Tables

Table 1 Experimentally determined electron optical-data of the high-resolution objective lens with top-entry goniometer, U = acceleration voltage, C_C = chromatical aberration coefficient, C_S = spherical aberration coefficient, d_S = theoretical point resolution

U (kV)	f (mm)	C_C (mm)	C_S (mm)	d_S (nm)
1250	8	4	1.6	0.105
400	3	1.9	1	0.16

Table 2 Electron-optical data of the objective lens with side-entry goniometer for 10 mm gap (experimentally determined) and 15 mm gap (specified) at 1250 kV.

gap width (mm)	f (mm)	C_C (mm)	C_S (mm)	d_S (nm)
10	6	3.5	2.8	0.12
15	6	4.3	5.8	0.14

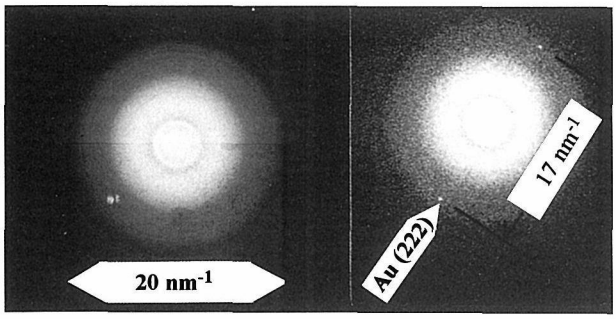

Fig. 1 Optical diffractograms from a micrograph of a thin amorphous Ge film taken near Scherzer defocus, rotationally averaged (left), non averaged (right).

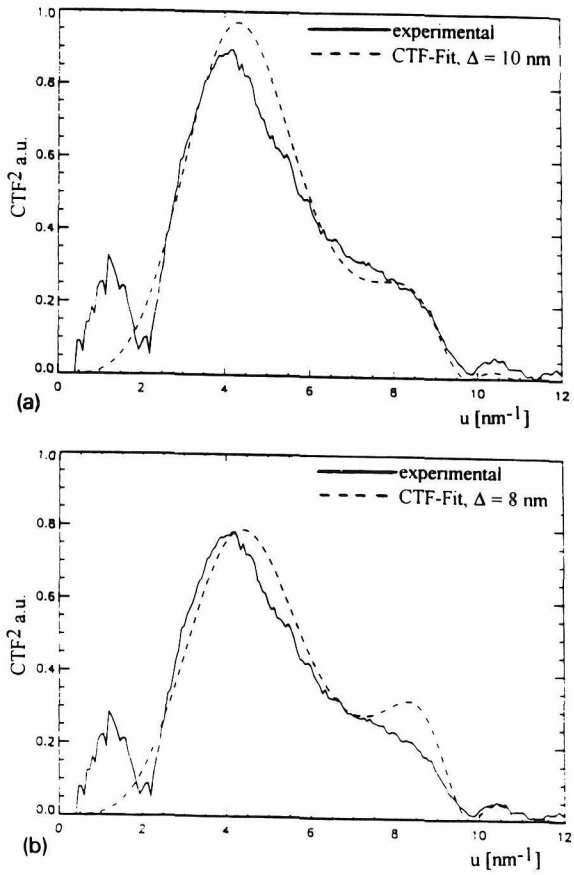

Fig. 2 Fit of a CTF to the intensity in a laser diffractogram. (a) for best fit near 8 nm^{-1} resulting in Δ=10 nm. (b) for best fit near 10 nm^{-1} resulting in Δ=8 nm

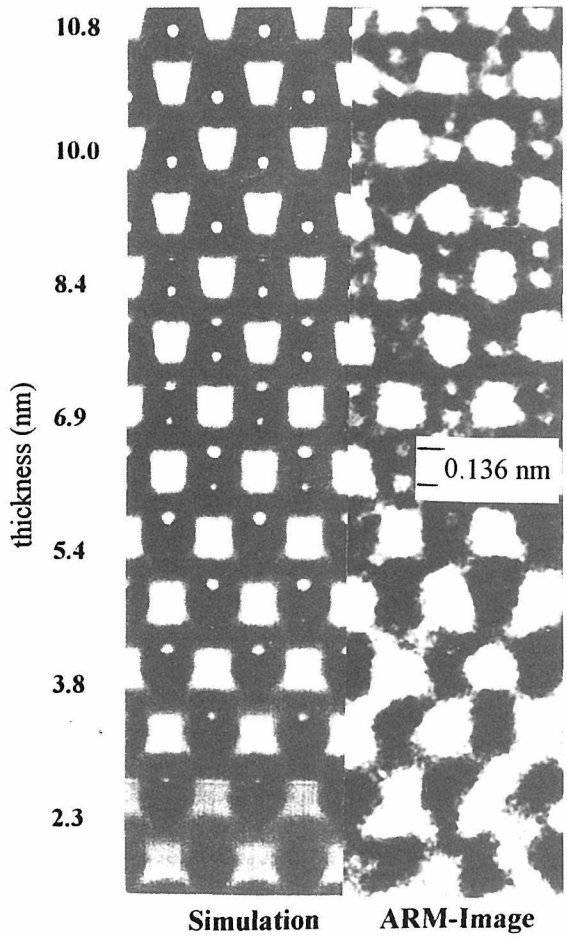

Fig. 3 Comparison between experimental image of a <110>-oriented wedge-shaped GaP specimen and simulation for 46 nm underfocus and various thickness values.

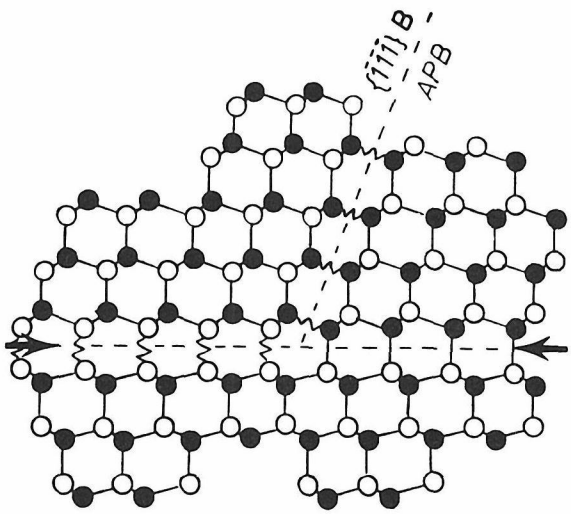

Fig. 4 Schematic configurations of {111}-twin boundaries (marked by arrows) in the <110> projection of the sphalerite structure, after [16]: rotation twin (right) and reflection twin (left), separated by an antiphase boundary (APB).

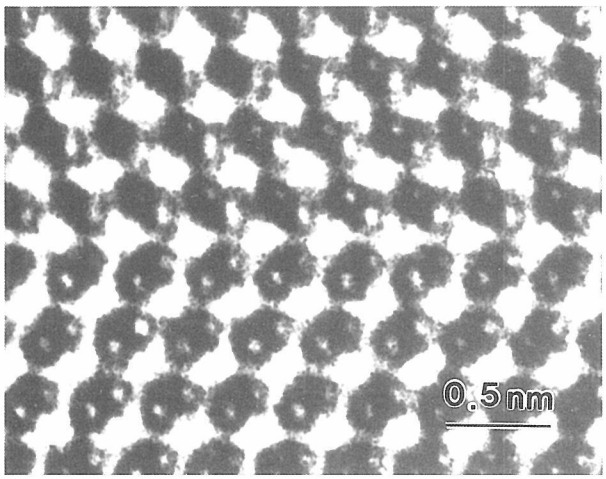

Fig. 5 ARM micrograph of a {111}-twin boundary in GaP <110> indicating the rotation-twin configuration.

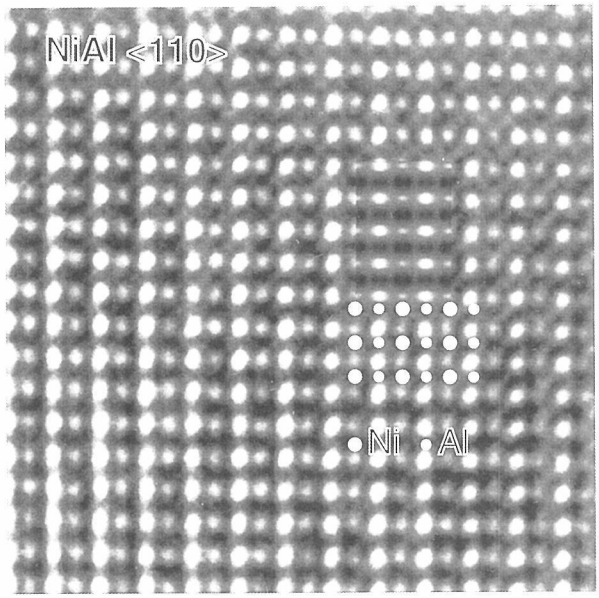

Fig. 7 Structure image of NiAl in <110> projection, recorded with the ARM. The spacings of the {110} planes (horizontal) and the {200} planes (vertical) amount to 0.2 nm and 0.14 nm, respectively. The local foil thickness was determined as ≈ 5 nm. The two insets show a model of the *B2* structure of NiAl in <110> projection and a simulated image (right above the model). *Courtesy of K. Nadarzinski and F. Ernst (unpublished work).*

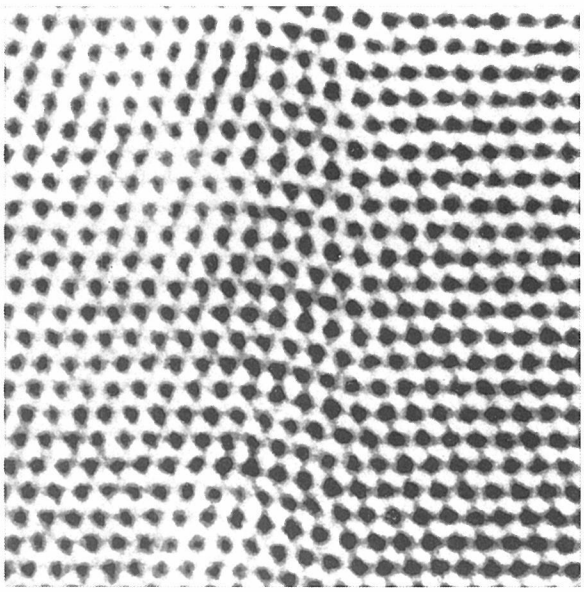

Fig. 6 Σ3<110> tilt boundary in Cu, recorded in the ARM along the <110> tilt axis. The inclination of the boundary plane amounts to 82° against the {111} orientation of the coherent twin boundary. The image reveals an extended *9R* zone, which is bound by a small angle boundary on the left side and a large angle boundary on the right side. *Courtesy of D. Hofmann and F. Ernst.*

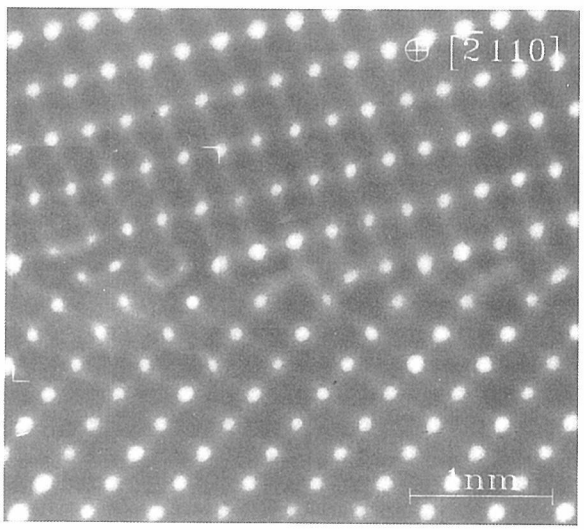

Fig. 8 Fourier-filtered micrograph of the $(0\bar{1}11)\|(01\bar{1}1)$ near Σ11 boundary in α-Al_2O_3 with a simulated image inset in the middle left.

Topics in In-Situ Experiments with the HVEM at Osaka University

H. Mori
Research Center for Ultra-High Voltage Electron Microscopy, Osaka University,
Yamadaoka, Suita, Osaka 565, Japan

ABSTRACT
Current topics in in-situ experiments with HVEM are presented, with emphasis on the work that has been carried out with a 2MV(routine)HVEM at Osaka University.

1. INTRODUCTION

High voltage electron microscopy (HVEM) possesses a number of advantages that cannot be afforded by conventional electron microscopy. Examples are (i) the large observable thickness of specimens which is well above the critical thickness to reproduce the same phenomena as those occurring in bulk materials,(ii) simultaneous excitation of many reflections which is needed to observe microstructures in differently oriented grains at the same time,(iii) the high attainable spatial resolution due to the reduced wavelengh of electrons and (iv) the large space of the specimen chamber which makes it possible to incorporate a complicated, voluminous specimen-treatment device. Another unique advantage of HVEM is the fact that continuous observation of phenomena by a variety of electron microscopy techniques is possible simultaneously with the introduction of point defects.These unique benefits of HVEM have attracted special attention in recent years[1, 2].

In this paper, current topics of in-situ experiments with HVEM will be presented, with emphasis on those that have been carried out with a 2MV(routine) electron microscope at Osaka University.

2. IN-SITU EXPERIMENTS AT HIGH TEMPERATURES (~2300K)

In-situ heating technique is one of the most important branches of in-situ HVEM experiments. The increasing demand for observations at very high temperatures in recent years has driven our research group to construct a hot stage capable of operation at temperatures of up to 2300 K[3]. The heating system consists of a tantalum(Ta) tube specimen holder, surrounded by a coaxial Ta tube supporting a hearter filament of tungsten and two coaxial Ta thermal shields. The specimen, which is mounted at the tip of the holder, is heated by electron bombardment from the filament, and the temperature is controlled by adjusting the voltage (100-600 V) applied between the filament and the specimen holder. With this stage set in the 2 MV HVEM, a variety of high temperature processes have been studied in refractory materials.Two examples of such studies will be presented here.

Figure1 is a typical sequence of electron micrographs showing the dissolution of hafnia particles into an alumina matrix at 2100 K [3]. Since this temperature is below the melting points of any alloys in the hafnia-alumina system, the dissolution takes place solely in the solid state. The micrographs were taken from a video recording, and are all bright-field images in which hafnia particles appear dark. It is shown in Fig.1 (a) through 1(f) that a somewhat elongated hafnia particle, lying on grain boundaries, completed the whole course of dissolution in 11.3 seconds. In Fig.1c is shown the entire division of the particle, which occurred in the intermediate stage of the dissolution. On the other hand, such hafnia particles, entirely embedded in the interior of alumina grains (for example, see the particles arrowed in (a)), show no detectable reduction in their size during the same period of 11.3 seconds, indicating the absence of appreciable dissolution in the grain interior. From these facts it is evident that the dissolution of hafnia particles into the alumina matrix preferentially takes place via such lattice defects as grain boundaries. A similar preferential dissolution via grain boundaries has also been observed in the alumina-zirconia binary system . These observations demonstrate the important roles played by the lattice imperfections in determining the microstructures of the refractory materials at high temperatures. To the

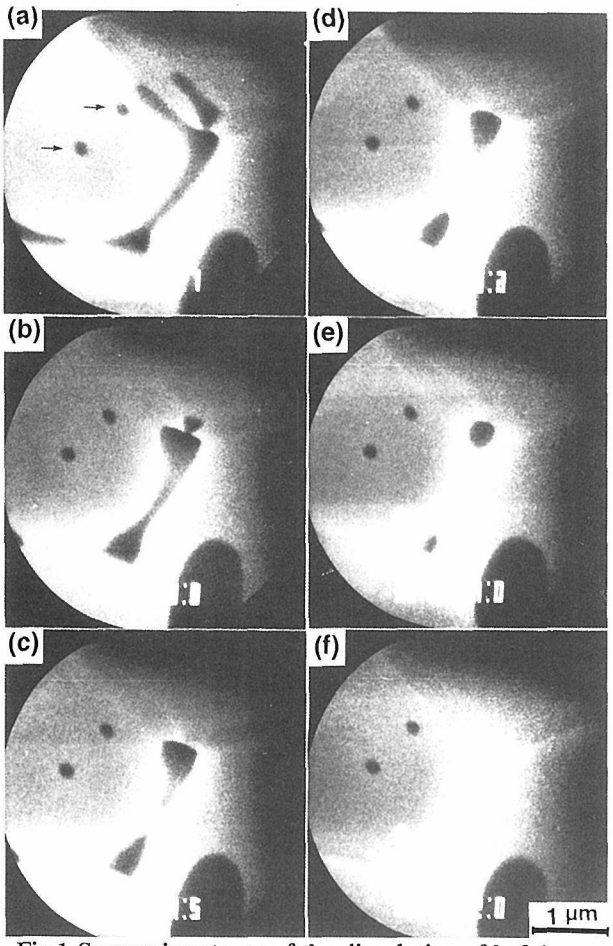

Fig.1 Successive stages of the dissolution of hafnia particles into α-alumina matrix at 2100 K.

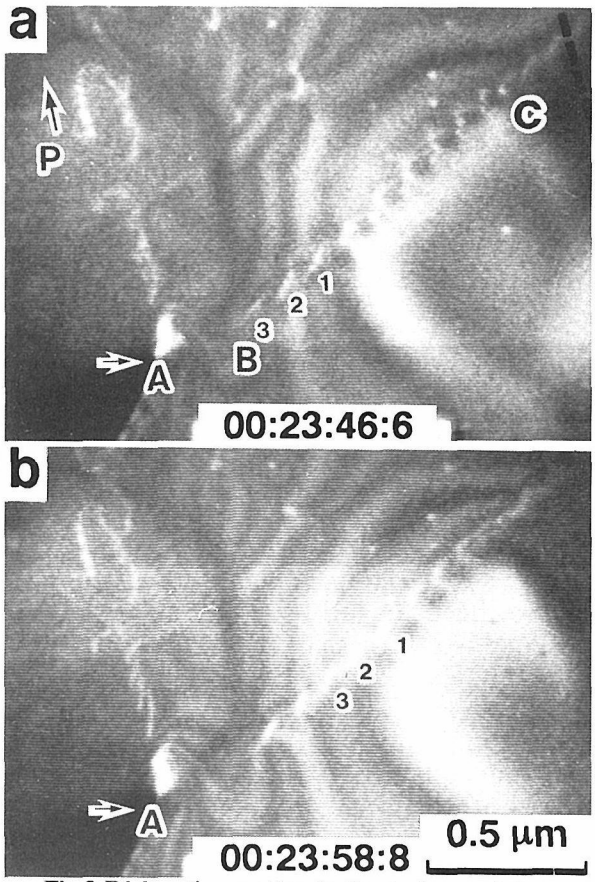

Fig.2 Dislocation motion in front of a crack in sapphire at 1720 K.

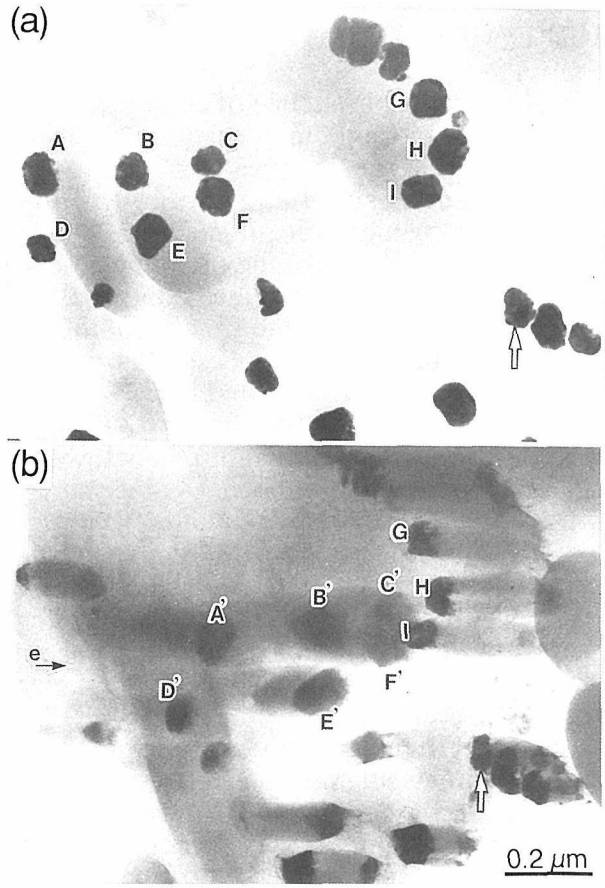

Fig.3 Gold atom implantation into silicon matrix by 2 MeV electron irradiation. (a) before irradiation, (b) the same area after irradiation.

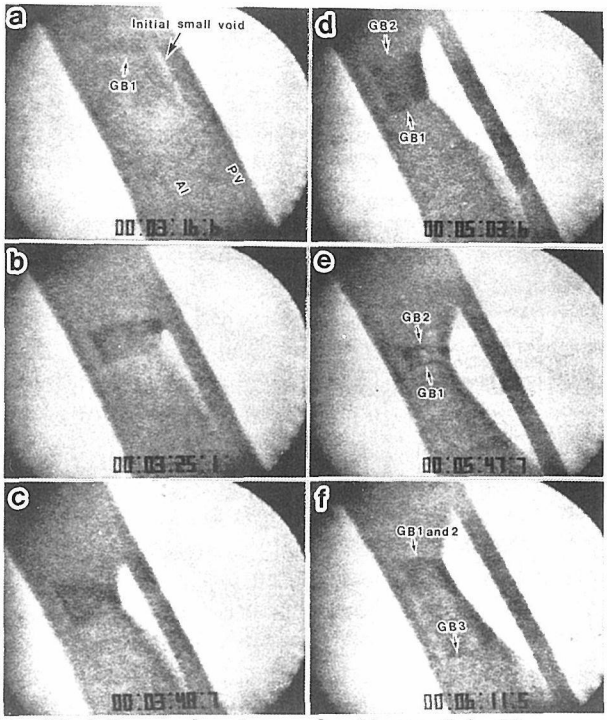

Fig.4 Successive stages of void growth in Al metallization at 723 K. Migration of grain boundaries (GB1 and GB2) accompanying shape change of the void, can be seen in (d)-(f).

author's knowledge, the temperature of 2300 K is the highest ever used in in-situ experiments with HVEM.

Figure2 is a typical sequence of electron micrographs showing dislocation motion in sapphire at 1720K[4]. The micrographs were again taken from a video recording, and are all dark-field images in which dislocation lines appear bright. The arrow on each micrograph indicates a fixed position (A), i.e. the tip of a crack. It is clearly seen from dynamic images on a video monitor that dislocations are emitted from the tip(A) of a crack and glide from position A to B in Fig.2(a) on the basal plane at a high velocity of approximately 0.6 μm/sec and at position B dislocations move in a direction not confined on the basal slip plane (i.e. toward position C), at a somewhat low velocity of approximately 0.06 μm/sec. It was, unfortunately, difficult to reproduce the former motion of dislocations over a distance from position A to B on the micrographs in Fig.2, because the dislocation velocity is somewhat high and the distance is rather short i.e. 0.37 μm. The latter motion of dislocations is, on the other hand, clearly reproduced on the sequential micrographs in Fig.2. For example, it is seen that such dislocations as labelled by numbers 1,2 and 3 move in line toward position C. The character of these dislocations has not been analysed, so it is difficult to determine, at present, whether this motion not confined on the basal plane, is cross slip of screws or climb of edges. The behavior of dislocations illustrated in Fig.2 can be explained as follows. In regions close to the tip of a crack, where the applied shear stress for the primary system is high (i.e., from position A to B), dislocations may glide on the slip plane (basal plane) at a high velocity. In regions apart from the tip of a crack, where the applied shear stress for the primary system is low (i.e., regions beyond position B) dislocation motions are not necessarily confined to the slip plane and dislocations may undergo cross-slip or climb, depending upon both the character of dislocations and stress field encountered. Motions of dislocations from position A to B and B to C were not jerky but continuous.

It should be also noted here that at 1720K there often observed activation of the prismatic slip system. An example of the prismatic slip is shown at P in Fig.2(a).

3. IN SITU EXPERIMENTS IN ENVIRONMENTAL CELLS

The use of an environmental cell in HVEM has attracted special attention in recent years. Experiments in gas atmosphere with pressures close to 0.1 MPa (the atmospheric pressure) have been carried out exclusively in window-type environmental cells. An example of such works is the direct observation of nucleation and growth of zirconium hydride in a zirconium matrix[3]. In the work, a zirconium foil was first heated to 573 K in a windowed cell evacuated to 10^{-2} Pa, and then hydrogen gas was introduced into the cell to 0.1 MPa. Upon the introduction of hydrogen, zirconium hydrides nucleate heterogeneously on the foil, and make rather rapid growth across the foil.

In the future an accelerated interest in environmental cell work will be brought about when the technique is effectively combined with noble methods of image processing.

4. IN SITU IRRADIATION EXPERIMENTS

Using HVEMs, continuous observation of phenomena is possible simultaneously with the introduction of point defects. Taking this advantage, our research group has carried out systematic studies to clarify the conditions under which non-equilibrium solid phases can successfully be produced under high-energy (MeV) electron irradiation. In the following, three of these studies will be presented.

4.1. Electron-Irradiation-Induced Amorphization

In 1982, it was discovered through HVEM studies that MeV electron irradiation can induce a crystalline-to-amorphous (C-A) transition in some intermetallic compounds such as NiTi and Fe3B. The discovery of such an electron-irradiation-induced C-A transition is of considerable significance in view of the following points. The electron-irradiation-induced amorphization contains no quenching processes since the energy transferred to the primary knock-on atoms is sufficient to produce only single or at most double atom displacements. Thus through the discovery it becomes evident that production of cascade regions and

quenching processes operating in the regions are not necessarily prerequisite for the C-A transition in crystals by particle irradiation, and that the amorphization by electron irradiation must be caused by a process in which the simplest types of crystal lattice defects play an essential role. It has been revealed that the C-A transition is a rather general phenomenon occurring not only in metallic compounds but also in non-metallic compounds and that (2) the tendency toward the C-A transition is best correlated with the position of the compounds in the temperature-composition phase diagram. Namely, those compounds whose position in the phase diagram is close to the bottom of a deep valley of liquidus have a strong tendency toward the C-A transition, while those away from such a valley show little tendency toward the C-A transition [5]. It has been suggested that the manifold in coordination, or in other words, the extent to which a variation is admissible in the atomic coordination in the material, is the most important parameter responsible for the amorphization tendency .

4.2. Electron-Irradiation-Induced Phase Decomposition in Intermetallic Compounds

It is generally accepted that an ordered alloy (or an intermetallic compound) either remains crystalline with a reduced degree of chemical order or undergoes a C-A transition when irradiated with MeV electrons at low temperatures where vacancies are thermally-immobile. Recently, however, it was found that besides these two modes of response there exists another mode of response where intermetallic compounds undergo a phase decomposition under low temperature irradiation [6]. For example it has been confirmed that Al3Ni decomposes into two phases under MeV electron irradiation; one is an aluminum-rich amorphous phases and the other crystallites of Al3Ni2.

A similar phase decomposition has been observed in such compounds as Al2Cu and Al4Pd. The finding of phase decomposition of this type is interesting in view of the following point; it is confirmed that the equilibrium to non-equilibrium phase transition which is induced by point-defect (and anti-site defect) introduction is not necessarily confined to single-phase to single-phase transitions such as an order-disorder transition and a C-A transition.

4.3. Electron-Irradiation-Induced Foreign-Atom Implantation

Hitherto foreign atom implantation into a solid has been carried out mainly by ion implantation. This ion implantation has now matured into an indispensable part of semiconductor technology. However in this method, the introduction of foreign atoms is limited to regions or positions right beneath the surface of the solid. Furthermore, severe irradiation damages are inevitably caused in the implantation regions.

A unique foreign-atom implantation technique in which irradiation effects of high energy (MeV) electrons are utilized has been put forward by Fujita[7]. The outline of the technique is as follows. First, a dopant phase comprising a target element is deposited either on the surface or the inside of the substrate. Here it is favorable that the target, dopant atom has a larger scattering cross-section for atom displacement than that of the solvent atom making up the substrate. For example, such a combination of an element with a high atomic number and a low melting point as a dopant and another element with a low atomic number and a high melting point as a substrate will be preferred. The composite specimen is then irradiated with electrons having an energy greater than the corresponding threshold energy for atom displacement. Under irradiation the target atom in the dopant phase preferentially suffers elastic collisions with electrons and recoils with sufficient energy to intrude into the substrate. The repetition of the intrusion will result in the implantation of the target atom into the substrate.

Through a systematic study by the author's group, which has been carried out with the use of the 2 MV electron microscope, it has been revealed that this technique is applicable not only to systems with metallic substrates but also to those with nonmetallic substrates [8-11].

4.3.1 Implantation into metals

Implantation of such solute atoms as Si, Ge, Sn, Pb, In, Cd, Sb, Au, Cu, W, and Ni into aluminum substrates has been studied by HVEM. The ease with which implantation takes place has been compared among the solute atoms. It has been revealed that (a) the energy of incident electrons,(b) the irradiation temperature, and (c) the atomic size ratio

between the solvent and solute atoms are the three main factors controlling the implantation into metals. Factor (a) is related to the probability of electron-atom collisions in which an energy greater than a few Td (displacement energy) is transferred from electrons to atoms, while factors (b) and (c) are concerning with the rate of back diffusion of implanted foreign atoms in the substrate towards the dopant-phase/ substrate interface.

4.3.2 Implantation into semiconductors

Applicability of the present technique to semiconductor substrates has been investigated in the Au (target) / Si (substrate) system. An example of gold-atom implantation into silicon is shown in Fig.3. Figure3(a) is a BFI showing an area before irradiation. In this micrograph, gold particles which are embedded in the silicon matrix, appear dark. The same area after irradiation with 2 MeV electrons for 7.2 ks (flux:$2.4\times10^{24}/m^2s$) is shown in (b). The white arrows in Fig.3(a) and (b) indicate a fixed position. The arrow labeled by letter e in Fig.3(b) indicates the direction of 2 MeV electron beam used in the irradiation. It is clear from a comparison of Fig.3(a) with (b) that particles A to F in Fig.3(a) have migrated by this irradiation to positions A' to F' in Fig.3(b), respectively. The distance over which particles C and F have moved, is as long as 400 nm.

Gold implantation into silicon by 2 MeV electron irradiation is considered to take place in the following manner. Target gold atoms in the gold particle suffer elastic collisions with 2 MeV electrons and recoil with energies sufficient to intrude into the substrate. The gold content in the gold-enriched region will increase with increasing total dose of electrons and eventually an amorphous Si-Au alloy will be formed there beneath the original Au/Si interface. In the amorphous Si-Au alloy, the sp^3 hybrid of silicon decays and a new bonding state is formed between silicon and gold, i.e., a type of silicide is formed. With continued irradiation, gold atoms in the amorphous Si-Au alloy will repeatedly be knocked-off and injected, across the newly-formed amorphous alloy/Si interface, into the silicon substrate at somewhat deeper positions. The repetition of displacement of gold atoms by the knock-on mechanism and subsequent alloy-formation results in the continued implantation of gold into the silicon substrate.

4.3.3 Implantation into ceramics

Applicability of the present technique to ceramic substrates has been investigated in the Au (target) / SiC (substrate), Pt/SiC , Hf/SiC , and Au/Si3N4 systems.

In the Au(target)/SiC(substrate) system, a new bonding state is formed between implanted-gold and silicon in the amorphous SiC substrate. Namely, injected gold atoms are chemically accepted in amorphous SiC. The formation of bonding between gold and silicon in amorphous SiC seems reasonable in view of the fact that the heat of formation for SiC and gold silicides are ca. 34 and 40 KJ/mole, respectively. The repetition of the knocking-off and subsequent bonding result in the implantation of gold into the SiC substrate. Platinum atoms implanted into amorphous SiC bond with silicon. Hafnium atoms implanted into amorphous SiC bond with both silicon and carbon. On the other hand, gold cannot be implanted into Si3N4. The heat of formation for Si3N4 is ca. 100KJ/mole. This value is high compared to that for gold silicides(i.e., ca 40 KJ/mole). Therefore, new stable bonding may be difficult to be formed between gold and silicon in Si3N4. It seems that such chemical constraint plays an essential role in determining the ease with which implantation into ceramics takes place[11].

5. APPLICATION TO ISSUES IN ADVANCED LSIs

Stress-induced voiding in Al lines is a serious reliability issue in advanced LSIs. The voiding process at temperatures above 673K in passivated Al metallizations, 0.5μm thick, 1.0μm wide, has been investigated by the 2 MV HVEM[12]. Figure 4 shows an example of successive stages of void growth at 723K. An initial small void appeared at the PSG/Al interface and the void grew preferentially along the interface, as shown in Fig.4 (a). In general, the initial voids were not necessarily associated with grain boundaries(GBs).

However, voids that grew extensively toward the line-width direction were always associated with GBs, as illustrated in Figs.4(b)to(f).

A wide range of applications of the HVEM will involve material issues in advanced LSIs.

6. APPLICATION TO ISSUES IN NM-SIZED MATERIALS

The study of ultrafine particles in the size range of several nm has attracted increasing interest in recent years (hereafter the ultrafine particles are designated as atom clusters or simply clusters). This is because the atom clusters often exhibit anomalous properties that are totally absent in the corresponding bulk materials. With the view of gaining insight into the diffusional properties in atom clusters, studies on the alloying behaviour of solute atoms into atom clusters has been started in this laboratory with the use of HVEM[13]. It has been confirmed that alloying takes place quite rapidly in atom clusters. For example, copper atoms can dissolve into gold clusters almost instantaneously even at room temperature and rather homogeneously mixed alloy clusters are formed. Such spontaneous alloying has been observed to occur in such systems as Au-Zn, Au-Sb, and InSb[14,15]. Studies to reveal the mechanism behind such rapid alloying in atom clusters are in progress in our laboratory.

7. CONCLUSION

In this paper, several topics in in-situ experiments with HVEM have been presented, with emphasis on the work at Osaka University. It is evident that a variety of advantages of HVEM that cannot be afforded by conventional (100-200kV) and intermediate (300-400kV) voltage electron microscopy are effectively utilized in these studies. In the furure, by taking full advantage of HVEM, in-depth studies will be made on individual subjects in materials science, especially in the development of advanced materials.

REFERENCES

1. Ultramicroscopy 56, Nos. 1-3, (1994) eds. M.Rühle, F.Phillipp, A.Seeger and J.Heydenreich
2 Ultramicroscopy 39,Nos. 1-4, (1991) eds. H.Fujita, K.Ura and H.Mori
3. H.Mori, M.Komatsu and H.Fujita, Ultramicroscopy 51 (1993) 31, see also M.Komatsu and H.Mori, Applied Physics 62 (1993) 824
4. M.Komatsu, H.Mori and K.Iwasaki, J. American Ceramic Soc. 76(1993) 839
5. H.Mori, Current Topics in Amorphous Materials, eds. Y.Sakurai et al. Elsevier (1993) 120
6. H.Mori and H.Fujita, Ultramicroscopy 39 (1991) 355
7. H.Fujita, In Situ Experiments with HVEM, ed. H.Fujita (ISBN 4-9900065-1-8), Osaka University (1985).p.1, and N.Sumida and H.Fujita, ibid, p.477
8. H.Mori, H.Yasuda, N.Sumida and H.Fujita, New Functionality Materials, eds.T.Tsuruta et al. Elsevier (1993) 221
9. H.Mori, T. Sakata, M.Maeda and H.Yasuda, Defects and Diffusion Forum 95-98 (1993)973
10. H.Mori, T.Sakata, M.Komatsu and H.Yasuda, Microscopy, Microanalysis, Microstructures 4 (1993) 137
11. H.Mori, J. Electron Microscopy, 42(1993) 361
12. H.Okabayashi, A.Tanikawa, H.Mori and H.Fujita, American Inst. Phys. Conf. Proc. No.263 (1992) p.174
13. H.Mori, M.Komatsu, K.Takeda and H.Fujita, Phil. Mag. Lett. 63 (1991) 173
14. H.Yasuda and H.Mori, Phys. Rev. Lett.69 (1992) 3747
15. H.Mori and H.Yasuda, Intermetallics 1 (1993) 30

Development of Ion Beam Interface with High Voltage Electron Microscope for "In-Situ" Observation of Irradiation and Lithography Processes

Kazuo Furuya
National Research Institute for Metals, 1-2-1 Sengen, Tsukuba, Ibaraki 305, Japan

Abstract

"In-situ" ion irradiation during the observation in the transmission electron microscope (TEM) is one of the fascinating ways to investigate the structural evolution of materials induced by particle bombardment and implantation. Two different ion beam interfaces have been developed using 200 keV TEM with dual ion beam implanters (DIBI) and with focused ion beam (FIB) for the purpose of the irradiation and lithography studies of metals and semiconductors. Ar^+ irradiation with DIBI/TEM and Ga^+ ion beam micro fabrication with FIB/TEM on Si thin samples clearly indicated the formation of secondary defects and precipitates, and amorphization and/or polycrystallization of specimens. For "in-situ high resolution TEM (HRTEM)", another DIBI interface is now being developed with 1000 keV atomic resolution ultra high voltage TEM (ARUHV-TEM) and preliminary results demonstrated the possibility of the dynamic HRTEM observation under irradiation.

1.Introduction

Ion irradiation, implantation and etching have been utilized for controlling the electric and mechanical properties of metals and semiconductors. One of the problems for this method is to eliminate and/or to evaluate the radiation damages due to the particle bombardment of the materials. Heavy ion implantation of Si, for instance, generally initiated the amorphous layer in the irradiation depth at room temperature [1] and the critical dose for the amorphization significantly increased with decreasing the mass number of ions [2]. Since the structural changes due to the knock-on damage depend upon the materials and irradiation conditions, it is very important to investigate the fundamental mechanism of ion irradiation with changing ion species and energies.

"In-situ" irradiation and lithography of materials during the observation in the transmission and scanning electron microscopes (TEM and SEM) is of course one of the ways to clarify the structural evolution due to the particles bombardment and several experimental setups using TEM or SEM incorporated with ion sources have been developed for the irradiation studies of metals and for the lithography of semiconductors [3-6]. However, the technical problems generally arise related to the limitation of resolution and continuous image drifts during irradiation [7]. The investigation of the fundamental process of radiation structural changes is, therefore, still difficult even by using "in-situ" experiments.

This paper describes the effort at National Research Institute for Metals (NRIM) to develop new experimental setups in which we are trying to break through several problems associated with interfacing ion beams with TEM. Two major categories of interface were considered for the development; namely, "in-situ" observation of ion irradiation damage of metals and alloys in atomic scale and "in-situ" experiments of ion beam lithography of semiconductors. The former project [8-10] required to develop the prototype system of dual ion beam implanter (DIBI) interface with a 200 keV TEM before designing an atomic resolution ultra high voltage TEM (ARUHV-TEM) in which the ion irradiation will be done

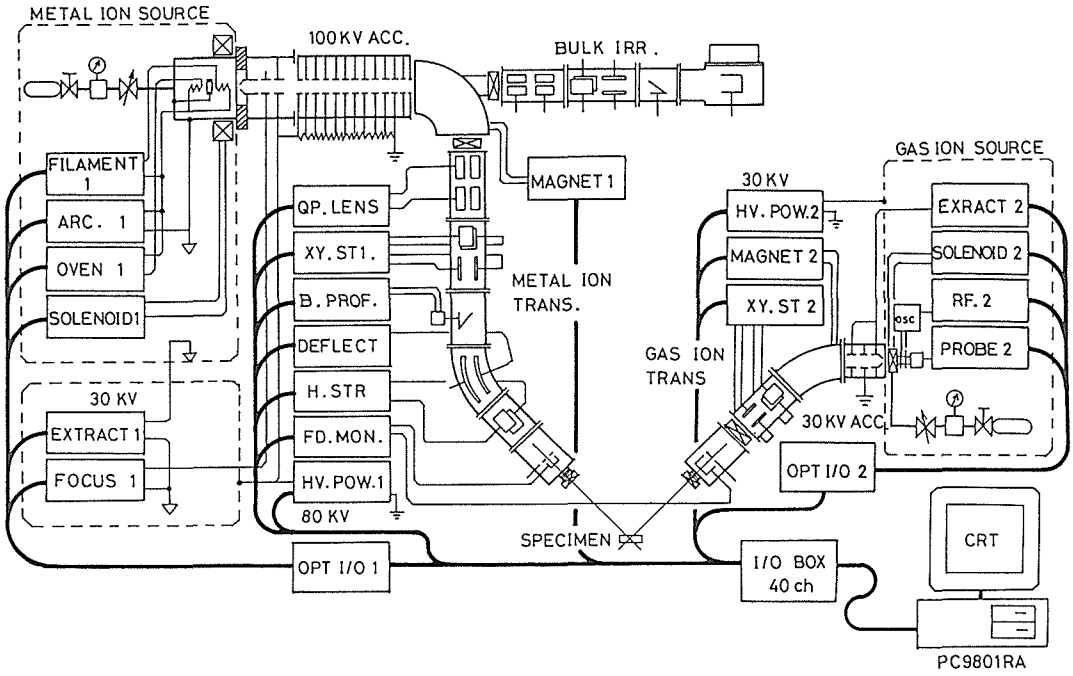

Figure 1. Schematic drawing of the dual ion beam inplanter (DIBI) for "in-situ" ion irradiation with a 200 keV TEM

with the high resolution observation as well as with micro analyses such as the energy dispersive X-ray spectroscopy (EDS) and the electron energy loss microscopy (EELM). The focused ion beam (FIB) interface was adapted for the latter project [11-12] using another 200 keV TEM.

2. Dual Ion Beam Interface with Transmission Electron Microscope (DIBI/TEM)

2.1. Prototype DIBI using 200 keV TEM

The prototype DIBI was designed using JEM-2000FX with dual ion accelerators [8-10]. The schematic drawing of accelerator systems are shown in figure 1. Hollow cathode ion source was employed for 100 keV heavy ion beam and RF discharge ion source for 30 keV gas ion beam. The high energy beam was selected through a 1.5 T analyzing magnet at an angle of 90 degrees, and then deflected vertically by an angle of 52.3 degrees for introducing into the TEM. The low energy beam was vertically analyzed before entering the port of the TEM.

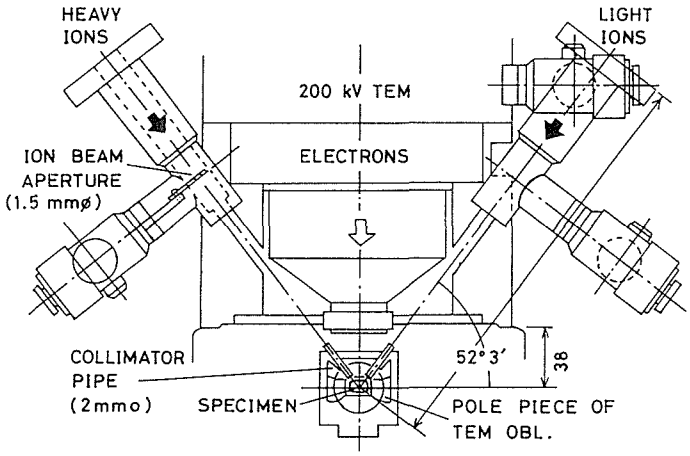

Figure 2. Details of the specimen chamber of 200 keV TEM with two inlet ports of ion beams and apertures.

The details of the inside of the TEM are shown in figure 2. The modified TEM condenser apertures with 1 mm diameter hole were located in the beam course for fixing the position and size of ion beams. Two collimator pipes of 2 mm diameter were inserted into the objective lens pole pieces of the TEM. It was confirmed that the ion fluxes of 10 keV H^+ and 50 keV He^+ from both systems reached about $6x10^{17}$ ions$\cdot m^{-2}\cdot s^{-1}$ at the specimen position in the dual-

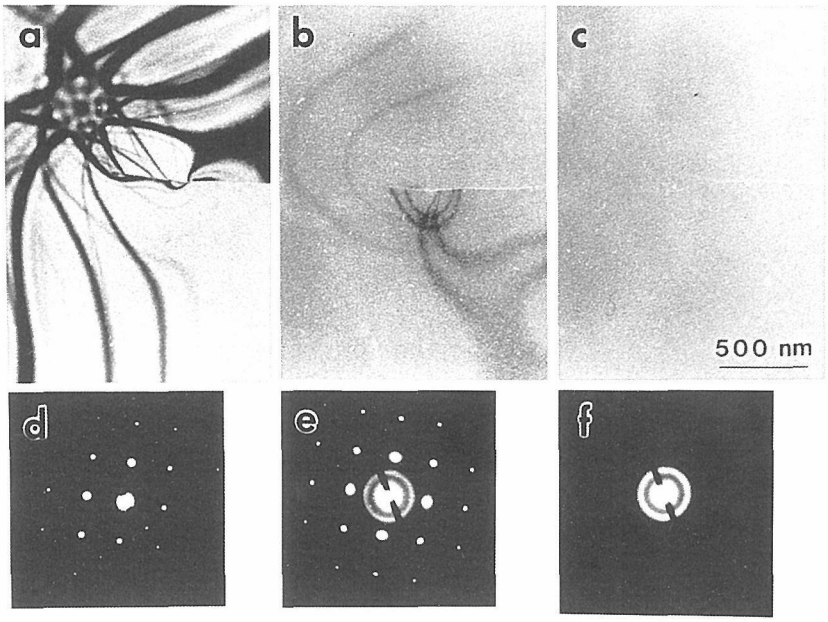

Figure 3. A set of TEM results for the continuous observation of Si(100) implanted with 70 keV Ar^+ as a function of irradiation time. a) no irradiation, b) 15 sec ($5x10^{18}$ ions·m^{-2}) and c) 30 sec ($1x10^{19}$ ions·m^{-2})

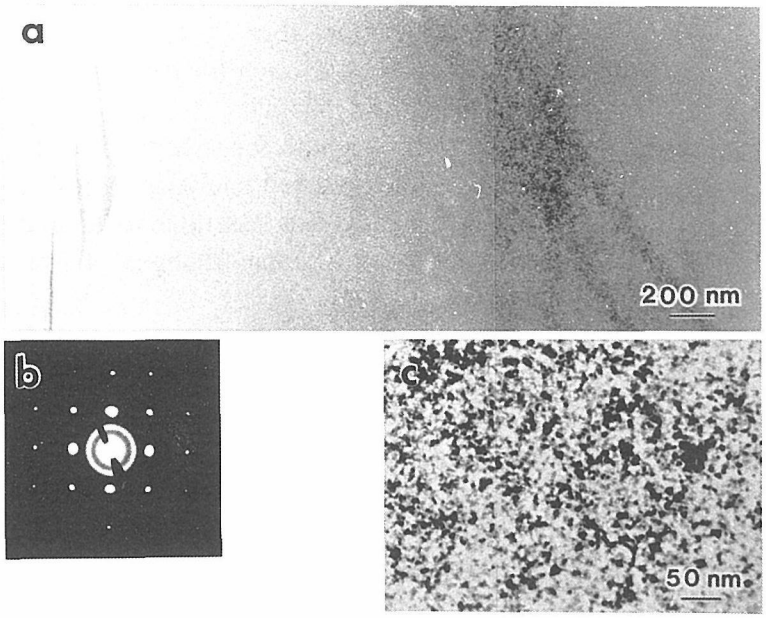

Figure 4. The details of the structure near bend contours of Si(100) implanted with 70 keV Ar^+ to a dose of $3x10^{18}$ ions·m^{-2}

beam irradiation.

The commercial grade N-type Si(100) TEM specimens were irradiated at room temperature with 70 keV $Ar^+$of $3.5x10^{17}$ ions·m^{-2}·s^{-1}. A set of typical results for the continuous observation of same area of Si(100) are shown in figure 3 as a function of irradiation time. Indicated is that the bend contours and bend center in the bright-field images (BFI) have disappeared rapidly as started Ar^+ irradiation. From the corresponding results in selected area diffraction (SAD) that the ring pattern instead of (100) pattern became to dominate with irradiation, it can be clearly pointed out that the structure of this area of Si(100) crystal has changed to polycrystalline and/or amorphous by Ar^+ implantation. It was reported [2] that heavy ion implantation to Si changed the surface to amorphous layers and that the critical dose for Ar^+ irradiation was about $4x10^{18}$ ions·m^{-2}. The fluence of Ar beam for figs. 3-c and 3-f was about $1x10^{19}$ ions·m^{-2} which is close to the reported value for amorphization. However, no one can discuss the physical meaning of this value without the consideration for the thin foil implantation. One interesting result of Ar^+-implanted Si is the detail of bend contours in BFI and SAD at the

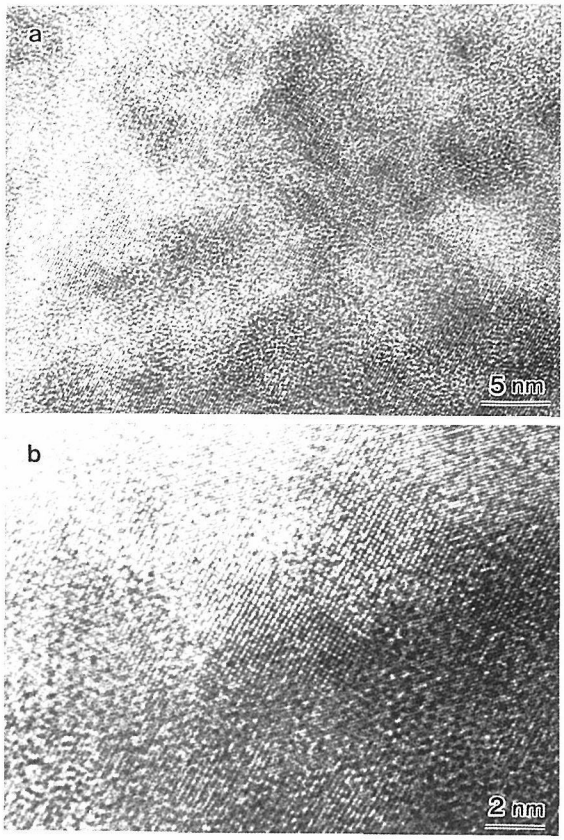

Figure 5. High resolution TEM photographs of Si (100) implanted by 70 keV Ar^+ to a dose of $3x10^{18}$ ions·m^{-2}

dose of $3x10^{18}$ ions·m^{-2} (shown in figure 4). SAD indicated both crystal and amorphous phase contained in this area and a high magnification picture showed the high density of small particles in amorphous matrix (fig. 4-c).

The specimen irradiated with DIBI/TEM were subsequently examined with JEM-4000EX high resolution TEM and the results were presented in figure 5. Looking along (110) zone axis, small particles with dark contrast in fig. 4-c turned out to be Si nano-crystals surrounded by amorphous substance. There is no secondary defects and clusters formed in the region and the boundary between crystal and amorphous is not clear, probably due to successive change in the structure form crystal to amorphous. The value of fluence for amorphization obtained above must be the fluence at which the crystals have completely converted to the amorphous. These data clearly implies the usefulness of high resolution TEM to investigate the structural changes occurring with ion irradiation. However, further development must be required for the "in-situ" observation of the structural changes in atomic scale, because of the high mobility of point defects and clusters which are introduced in the course of ion irradiation even at room temperature.

2.2. Development of ARUHV-TEM for ion irradiation studies.

Based on the results of the prototype DIBI using 200 keV TEM, a new 1000 keV ARUHV-TEM system with dual ion beam interface is now being developed at NRIM. The schematic drawing of the system is shown in figure 6. The voltage of 1 MeV for electron was chosen with following four reasons. 1) The efficient production of Frenkel defects in most of metals and alloys, 2) To secure the resolution better than 0.15 nm, 3) The penetration large enough for the observation of thick foils and 4) The space at specimen position large enough for stressing, heating and cooling. The attached analytical tools such as EDS and EELM are essential to characterize the micro compositional changes of irradiated materials.

The construction of the ARUHV-TEM is now in the final stage for installing ion beam interface. The DIBI consists of 200 keV and 30 keV ion implanters, which are transferred and modified after the prototype DIBI was decommissioned. Both high and low energy beams in this system are, however, deflected vertically with an angle of 44 degrees for introducing into the ARUHV-TEM. The beam lines were carefully controlled by electrostatic lens and evacuated by ion pumps and the magnetically suspended turbo pumps for keeping the resolution of the TEM. TEM images are collected and magnified directly in a CCD-TV camera through a real time image processor.

The preliminary experiments to clarify the "dynamic" resolution of ARUHV-TEM was carried out on aluminum TEM specimens at room temperature. The specimens were irradiated with the relatively strong 1000 keV

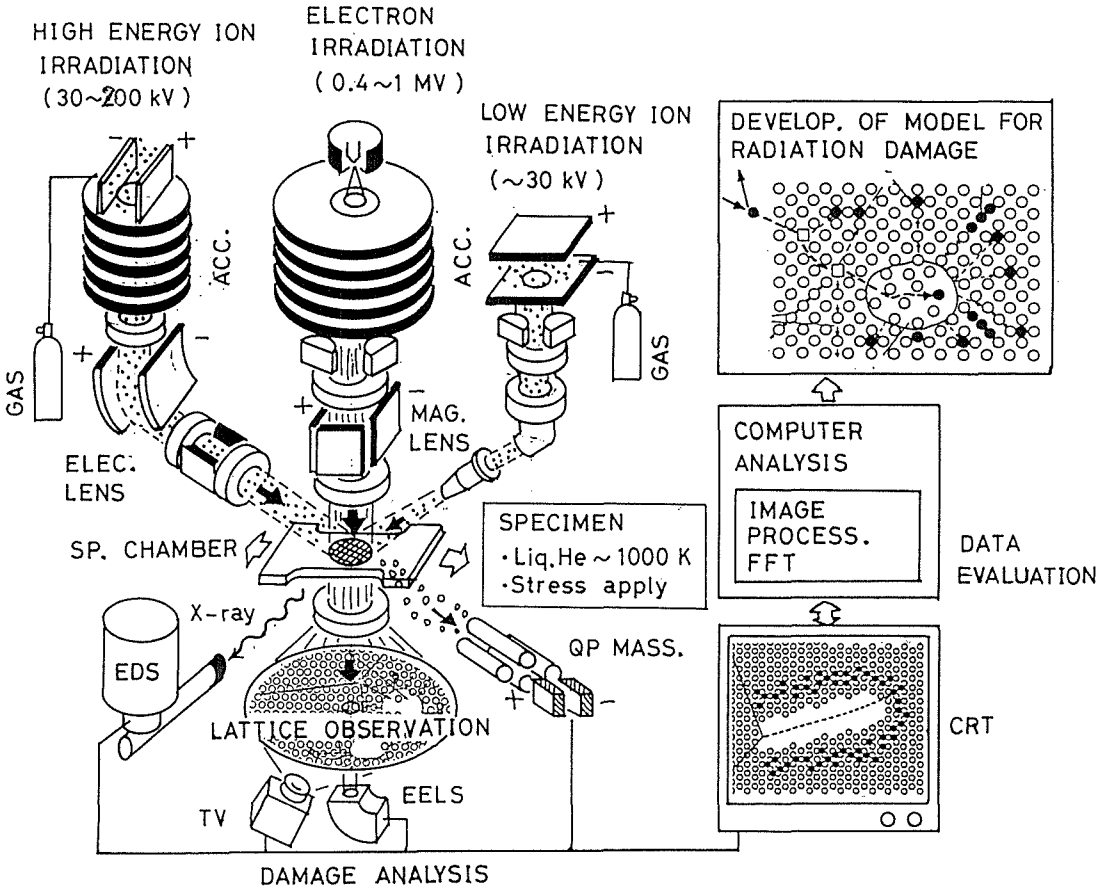

Figure 6. Schematic drawing of the atomic resolution ultra high voltage TEM (ARUHV-TEM) system with dual ion beam implanter and with several analytical tools, such as EDS and EELM.

electrons of 1.0×10^{23} electrons·m^{-2}·s^{-1} and, the atomic displacements and the dynamic changes in the morphology of secondary defects were recorded with VTR tapes. The results in figure 7 are a set of images grabbed from the tape at which the specimen was irradiated to 6.0×10^{25} electrons·m^{-2}. Since the specimen was aligned along (110) zone axis, one can observes aluminum atoms showing the interatomic distance of 0.2 nm. Especially pointed out is the line shape atomic displacement associated with large distortion of lattice fringes in one of two series of apparent (111) planes, while no alteration in the number of lattice planes happens on both sides of lattice distortion. Further noted is extraordinary contrast appearing below the line which implies the atomic disorder and strain on the preferential (111) plane. Successive illumination of electrons resulted in the shrinkage of the line defect which indicated the recovery and rearrangement of atoms by the thermally activated process and by the electron irradiation. Although the physical model of the line defect could not be proposed without any image simulation of the crystalline of aluminum containing defects and clusters, it should be reminded the fact that the faulted Frank loops are generally formed on (111) plane for FCC metals [13]. The present results surely demonstrate the usefulness of the "in-situ" irradiation of materials in TEM followed by or with HRTEM observation for disclosing the mechanism of radiation damage in sub-nanometer scales.

3. Focused Ion Beam Interface with Transmission Electron Microscope (FIB/TEM)

The above mentioned technique of introducing ion beams at the specimen position of TEM has been applied to the "in-situ" observation of ion beam micro lithography of semiconductors [11-12]. Focused Ion Beam (FIB) with less than

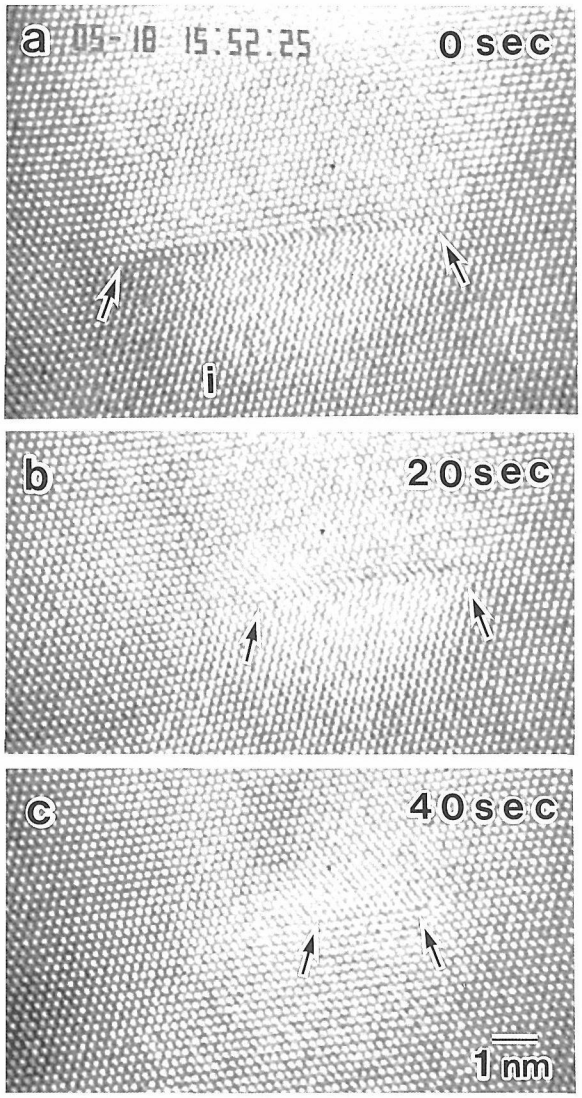

Figure 7. A set of high resolution TEM photographs of Al irradiated with electrons to a dose of 6.0×10^{25} electrons·m^{-2} at room temperature.

200 nm diameter of a beam spot can offer a potential to create submicron heterostructures on the TEM specimens and the structural changes by ion implantation and lithography can be examined immediately. The TEM used for this interface is JEM-200CX with the beam scanning capability for EDS analysis. A FIB system adapted was basically FEI-2LI which can generate a relatively low energy (5-25 keV) beam with the liquid metal ion source, mostly Ga.

Figure 8 exhibits the schematic drawing of FIB/TEM. FIB column has been attached at the upper front of the TEM, forming a 55

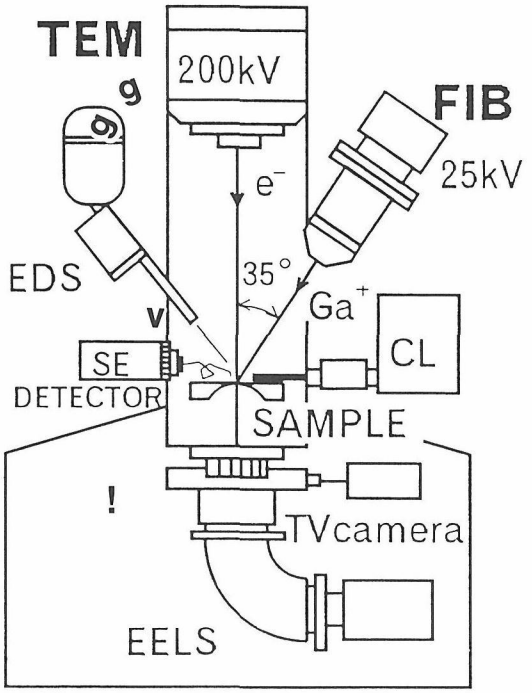

Figure 8. Schematic drawing of the focused ion beam (FIB) interface with a 200 keV TEM for "in-situ" micro lithography

degree and is differentially pumped by an ion pump maintaining 10^{-6} Pa. Ion beam was introduced along the upper yoke of the pole piece of the TEM. The working distance of FIB is about 100 mm where an obtained spot size reached 150 nm at the minimum value in the collimated mode of 25 keV Ga beam. The deflection of ion in the magnetic field of the objective lens has been adjusted by the quadrupolar lens of FIB, but this effect was negligible at the normal operation of TEM.

N-type of Si (100) was chosen to demonstrate the performance of FIB/TEM. Thin section of the specimen was checked by TEM prior to FIB lithography at the magnification of 10 k. Then, 25 keV Ga^+ with a beam spot of 150 nm and with the intensity of 75 pA was applied at room temperature in the area of 3x3 μm in both area and line scanning modes of 25 sec/frame and 2 sec/line, receptively.

Figure 9 presents the TEM photographs of whole views of micro fabricated Si (100) thin section by Ga^+ FIB. Ga ions sputtered out Si atoms uniformly, but the morphology change in

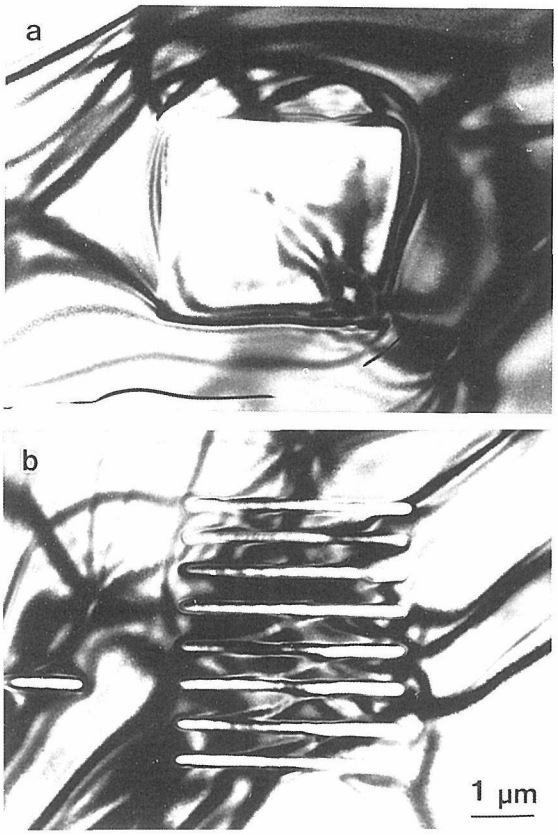

Figure 9. TEM photographs of the micro fabricated area of Si (100) by 25 keV Ga^+-FIB. a) area scann. and b) line scann. modes

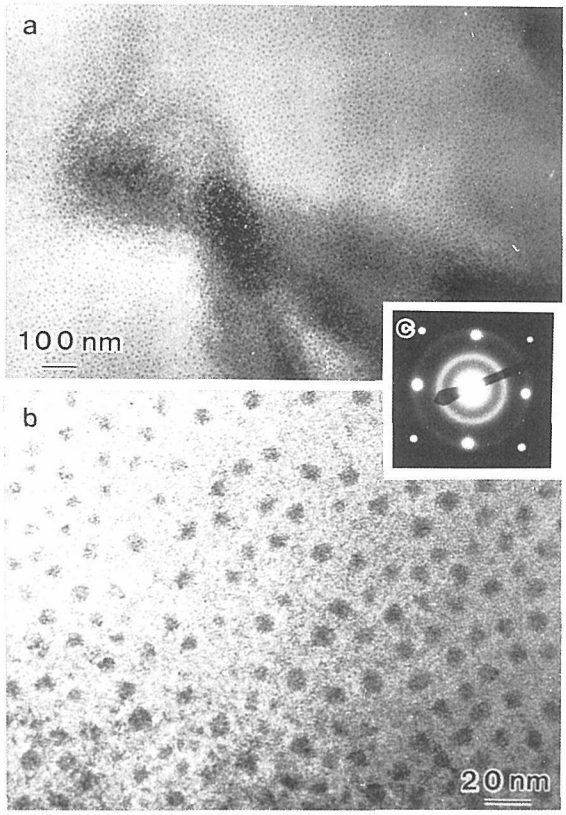

Figure 10. The detail of the structure in the micro fabricated area of Si (100) by 25 keV Ga^+-FIB.

bend contour implies its influence on the crystalline structure. High magnification photographs and SAD of fig. 9-a are shown in figure 10 and indicate that the FIB has partially amorphized and polycrystallized Si specimen and initiated many small patches which are considered to be Ga related precipitates. Clearly seen here is the complicated process of Ga^+ FIB exposure to Si in which the implantation of Ga occurred simultaneously with the sputtering of Si and these results show the potentiality of FIB/TEM for "in-situ" observation of micro lithography of semiconductors.

4. Summary

The technique of "in-situ" ion irradiation during the observation in the transmission electron microscope (TEM) has been applied to metals and semiconductors in this study. Two different ion beam interfaces have been developed by using 200 keV TEM with dual ion beam implanters (DIBI) and with focused ion beam (FIB) for the purpose of the irradiation and lithography studies of metals and semiconductors. The results of Ar^+ irradiation with DIBI/TEM and of Ga^+ ion beam micro fabrication with FIB/TEM on Si thin samples were presented for clarifying the performance of the systems. For "in-situ HRTEM", another dual-ion beam interface is now being developed with 1000 keV ARUHV-TEM and preliminary results demonstrated the possibility of the dynamic HRTEM observation under the irradiation. However, there remains a common problem which is generally inherent in the observation on thin films where most of point defects, especially high mobility interstitials, annihilate easily on the surface during irradiation, and then the nature of defects and subsequent structural changes by irradiation and lithography could be different form bulk materials. Further consideration has to be made on the simulation technique taking into account for the thin film conditions.

Acknowledgment

This work has been carried out as a part of the program in high resolution beams laboratory NRIM, promoted by the Science and Technology Agency of Japan. The author wish to thank Dr. Nobuhiro Ishikawa for his collaborations of the experimenatal work and Dr. Tetsuya Saito for his encouragement on this program.

References

[1] Morehead and Crowder: in 1st Int. Conf on Ion Implantaion, eds. F. Eisen and L. Chadderton (Gordon and Breach, New York, 1971) p25.
[2] M. Takai: in Ion Implantation Technology for Semiconductors, eds. K. Gamo (Sangyo Tosho, Tokyo, 1986) p41.
[3] P. A. Thackery, R. S. Nelson and H. C. Sensom: AERE-R-5817 (1968).
[4] S. Ishino, H. Kawanishi, K. Fukuya and T. Muroga: IEEE Trans. Nucl. Sci. NS-30 (1983) 1255.
[5] S. Furuno, K. Hojou, K. Izui and T. Kino: J. Nucl. Mater. 155-157 (1988) 1149.
[6] T. Takeyama, S. Ohnuki and H. Takahashi: J. Nucl. Mater. 133-134 (1985) 571.
[7] P. Sudraud, G. B. Assayag and M. bon: J. Vac. Sci. Technol. B6 (1988) 234-238.
[8] K. Furuya and N. Ishikawa: Proc. of 2nd Japan Intern. SAMPE Symp., (1990) p323.
[9] N. Ishikawa and K. Furuya: Proc. of ICEM-13., (1994) p95.
[10] N. Ishikawa and K. Furuya: Ultra-microscopy (to be published in 1994)
[11] K. Furuya, T. Saito, T. Hata and I. Yamada: Proc. of ICEM-13., (1994) p1139
[12] K. Furuya and N. Ishikawa: Rad. Effects and Defects in Solids, 124 (1992) 61-67
[13] W. Schilling: J. Nucl. Mater., 216 (1994) 45-48.

Energy-Filtering Transmission Electron Microscopy: Current State and Future Prospects

O.L. Krivanek
Gatan Research and Development, 6678 Owens Drive, Pleasanton, CA 94588, USA

Abstract

Imaging filters developed over the last few years are briefly described, and their performance illustrated on examples including convergent beam electron diffraction, high resolution imaging, elemental mapping and chemical imaging. The principal effect of the filters on transmission electron microscopy of inorganic materials is likely to be three-fold: they will make microscopy more quantitative by removing the hard-to-model inelastic component, they will popularize elemental and chemical mapping, and they will lead to the development of new imaging techniques.

I. Introduction

An electron traversing a thin sample can be scattered in angle (elastic scattering) and in energy (inelastic scattering). The information in the two scattering channels is of comparable complexity and richness. However, the majority of today's transmission electron microscopes (TEMs) cannot sort the electrons according to their energies. As a result, valuable information produced by inelastic scattering remains greatly underutilized in transmission electron microscopy.

Our team has developed, over the last several years, an efficient post-column imaging filter that attaches to the bottom flange of an electron microscope, and transforms it into a full-featured energy-filtering transmission electron microscope (EFTEM). The development started as a modest exploratory contribution to the 1986 International EM Congress held in Kyoto [1]. Encouraged by early interest from Professors H. Hashimoto and T. Kobayashi, the filter has since been greatly improved and adapted to microscopes operating at energies from 100 keV to 1.25 MeV. It promises to revolutionize electron microscopy by making the inelastic scattering information widely available.

II. EFTEM instrumentation

Energy-filtering transmission electron microscopes operate in 5 discrete stages:

1) an unfiltered image (or diffraction pattern) is formed,
2) the image (or d.p.) is transformed into a spectrum by an energy-dispersing element (such as a magnetic prism or an assembly of prisms),
3) a part of the spectrum is selected by an energy-selecting slit,
4) the selected part is transformed back into an energy-filtered image (or diffraction pattern) by a projection lens system, and
5) the image (or d.p.) is detected by a suitable detector.

The energy-filtering process is analogous to dark-field electron microscopy, in which an image is transformed into a diffraction pattern, a part of the diffraction pattern is selected by the objective aperture, the selected part is transformed back into an image, and the image is detected. The analogy can be carried further: zero loss imaging corresponds to bright-field imaging (both use unscattered electrons), the energy-selecting slit corresponds to the objective aperture, and forming a spectrum by refocusing the filter's projection lenses onto the spectrum plane corresponds to forming a diffraction pattern by refocusing the microscope's intermediate lenses onto the diffraction plane.

There are two main approaches to EFTEM instrumentation: in-column filters introduced by Castaing's group [2, 3] and improved by Zanchi and coworkers [4] and Rose and coworkers [5, 6], and post-column filters first unsuccessfully tried by Castaing's group [Colliex, private communication], re-introduced by Shuman [7] and recently substantially improved by us [1, 8-12]. The performance attained by the two approaches is comparable, but there are also important differences.

The key difference is that the projection lens system of current in-column filters uses round lenses that do no aberration correction, whereas the projection system of our post-column filters uses quadrupole and sextupole lenses that correct all the important image-level aberrations and

distortions, no matter how distorted is the image sent into the projection system by the energy-dispersing element. This means that the energy-dispersing element of in-column filters has to simultaneously correct all the important aberrations that arise with imaging filters in both the spectrum plane and the image plane, whereas the energy-dispersing element of post-column filters only needs to correct the aberrations arising in the spectrum plane. The result is that post-column filters achieve the same degree of correction with fewer components than in-column filters, and greatly exceed the performance of in-column filters using a similar number of components. As an example, existing post-column filters with a single magnetic prism, 4 strong quadrupoles and 5 strong sextupoles [12] give an optical performance similar to a proposed in-column filter using 4 separate prism passes, 9 sextupoles and 3 round lenses [6]. Further, because the optical path through their quadrupole-sextupole system is straight, post-column filters are much less prone to misalignment problems than in-column filters that typically have a complicated central trajectory.

The optical performance of imaging filters is best measured in terms of "filter transmissivity", defined as the product of the largest image area times the largest solid collection angle that a filter can accept simultaneously while operating at a specified energy-resolution level. (The image size and the collection angle can be changed individually by coupling lenses, but their product is fixed for a given electron-optical design.) Measured in these terms, current post-column filters exceed the performance of in-column filters using 4 prisms, one sextupole and 2 round lenses [5] by about 100x [9, 12]. The quadrupole-sextupole technology that makes this possible has more in common with particle accelerators and various proposed aberration correctors than with round lenses traditionally used in electron microscopes. It gives us hope that practical correction of spherical and chromatic aberration in TEM using similarly constructed multipole systems is not too far away.

There are now three members in the family of post-column filters that we have developed. The first one is the original "Gatan Imaging Filter" (GIF) [9, 10]. It uses 4 strong quadrupoles and 5 strong sextupoles after the slit, and 2 strong pre-slit quadrupoles that magnify the spectrum produced by its single prism of 10 cm bending radius. It is optimized for operation at 200-400 keV, and has a dispersion of 2.8 μm per eV at the slit at 400 keV. It detects images and spectra by a fiber-optically coupled slow-scan CCD camera [13] or a fiber-optically coupled TV-rate camera. The second member is a high voltage filter [11] which uses a scaled-up quadrupole-sextupole system that is otherwise similar to the original filter, a single prism of 25 cm bending radius, and a lens-optically coupled slow-scan CCD camera. It gives a dispersion of 3.2 μm per eV at 1 MeV, and is optimized for operation at 800 keV to 1.25 MeV. The most recent member is a filter optimized for biological electron microscopy [12]. It uses no spectrum-magnifying quadrupoles, and has a quadrupole-sextupole projection system and detectors similar to the original filter. It gives a dispersion of 1.8 μm per eV at 100 keV, and is optimized for operation at 80 to 200 keV.

All three filters readily achieve energy resolution better than 1 eV with entrance apertures ≥ 1 mm in diameter, image distortion of < 3%, and maximum deviations from isochromaticity smaller than $\pm$ 1 x 10^{-5} E_o. (An isochromatic filter selects the same energy interval at all image points. A non-isochromatic filter selects different energy intervals for different image points.) Their practical performance is illustrated in the examples in the next section.

III) EFTEM applications

Current applications of energy-filtered TEMs can be divided into three broad classes:

1) elastic-only imaging and diffraction, in which inelastically scattered electrons are excluded by the energy-selecting slit,
2) inelastic-only imaging and diffraction, in which inelastic scattering is used to form images and diffraction patterns with types of contrast not available with elastic scattering, and
3) spectroscopy, in which spectra of many channels are formed, detected in parallel, and analyzed to provide quantitative information about the sample.

1) Elastic-only imaging and diffraction are principally contrast-enhancement techniques. They are particularly useful in imaging of thick and unstained biological samples, in weak-beam imaging of crystalline defects, and in electron diffraction. The improvement in convergent beam electron diffraction (CBED) patterns is especially remarkable, as illustrated in Fig. 1. Removing the hard-to-model inelastic component also makes it easier to simulate experimental results by theory. This has found important applications in quantitative electron diffraction [14], and has lead to a promising start towards a full quantitative accounting for contrast levels in lattice-fringe and Fresnel-contrast

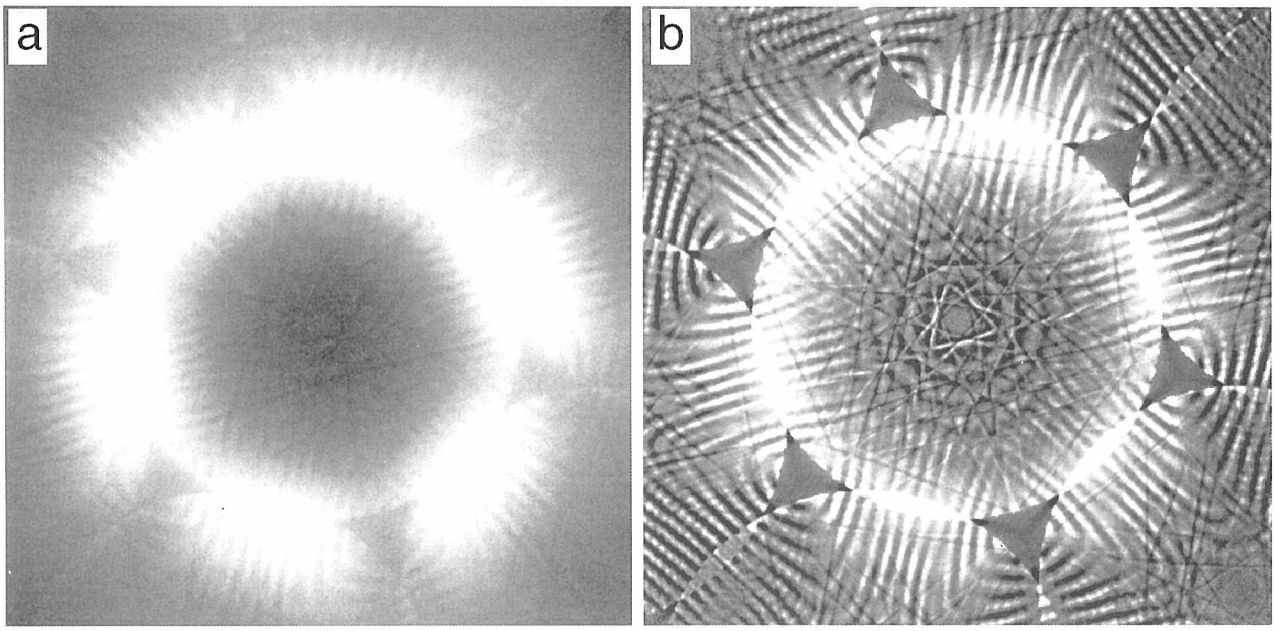

Figure 1. Unfiltered (a) and filtered (b) CBED patterns from (111) Si about 0.2 μm thick. Gatan Imaging Filter, 200 keV, 15 eV wide energy-selecting slit. Identical image processing has been applied to both patterns.

TEM images [Stobbs, private communication]. The filters are able to produce energy-filtered images at a resolution limited only by the microscope to which they are attached. For instance, a high voltage filter attached to a JEOL 1.25 MeV ARM has recorded images with point-to-point resolution approaching 1 Å (Fig. 2.)

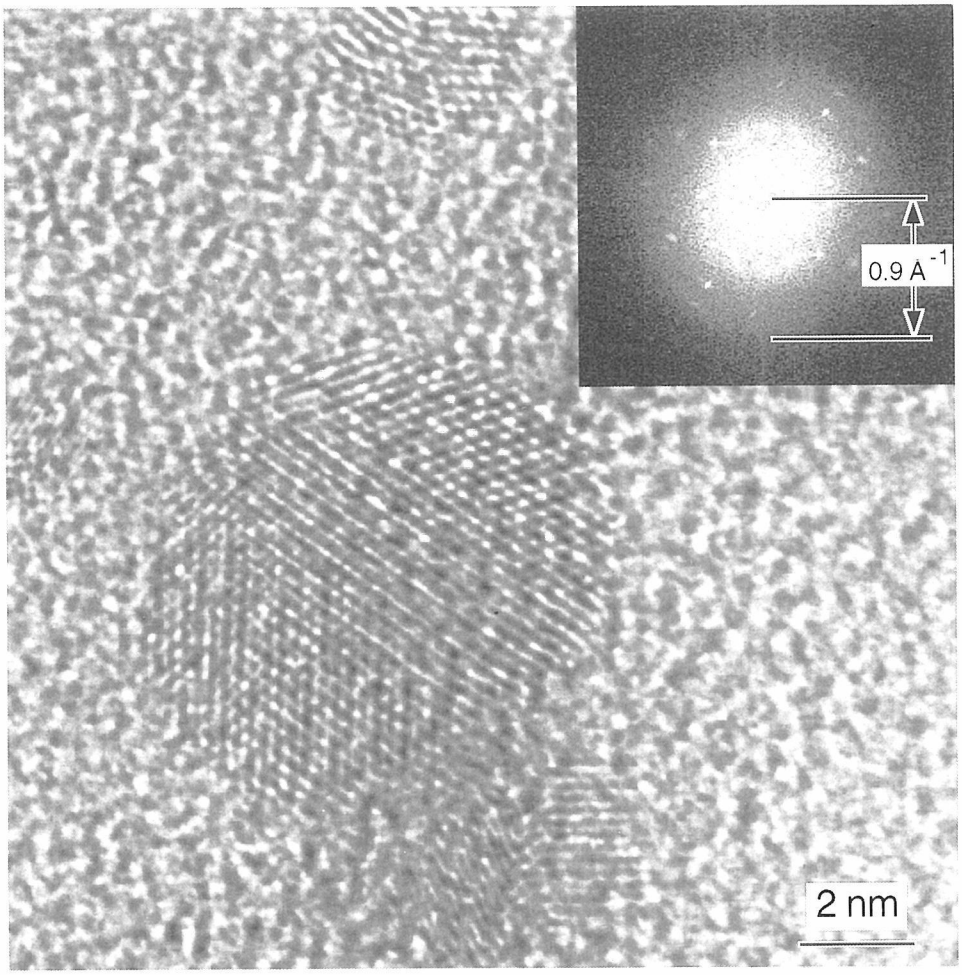

Figure 2. Zero-loss-only image of gold particles on an amorphous carbon substrate. JEOL ARM, high voltage GIF, 1.25 MeV, 10 eV wide slit. The diffractogram insert shows various Au reflections and a continuous intensity due to the amorphous carbon extending to $(1.1\ Å)^{-1}$. Courtesy A.J. Gubbens, B. Kraus, J. Mayer, F. Phillipp and M. Rühle.

2) Inelastic-only imaging is similar to dark-field microscopy. It is able to selectively image sample "phases" that give rise to specific types of scattering. The most general inelastic contrast mechanism is provided by inner-shell loss edges, which occur at element-specific energy losses. Selecting electrons that have lost an energy corresponding to a particular edge produces images in which regions rich in the element that gave rise to the edge become brighter. In order to form "elemental maps" rather than "element-enhanced images", one has to subtract the brightness contribution arising from the edge background, which is an inherent part of energy-loss spectra [15]. Different techniques are available for doing this, e.g. [16]. The one that is the most generally applicable involves recording two images with energies smaller than the threshold of the edge of interest, and using them to model and subtract the pre-edge background at every pixel in the image.

Fig. 3 shows a practical example of elemental mapping applied to a composite ceramic. The sample was a cross-sectioned SiC fiber coated by boron nitride and embedded in a glass matrix. The fiber, whose diameter is much bigger than the image, is at lower right in the maps, the glass matrix at top left. All maps were obtained by recording three energy-filtered images, and using AE^{-r}-type background subtraction [15] to extract the net edge signal. The profiles show the composition variation between the two arrows drawn on the boron map. They were prepared by drawing equivalent lines on all the maps, and integrating map intensity values over 50 pixels perpendicular to the lines. They also include profiles prepared from Mg and Si maps not shown in this figure.

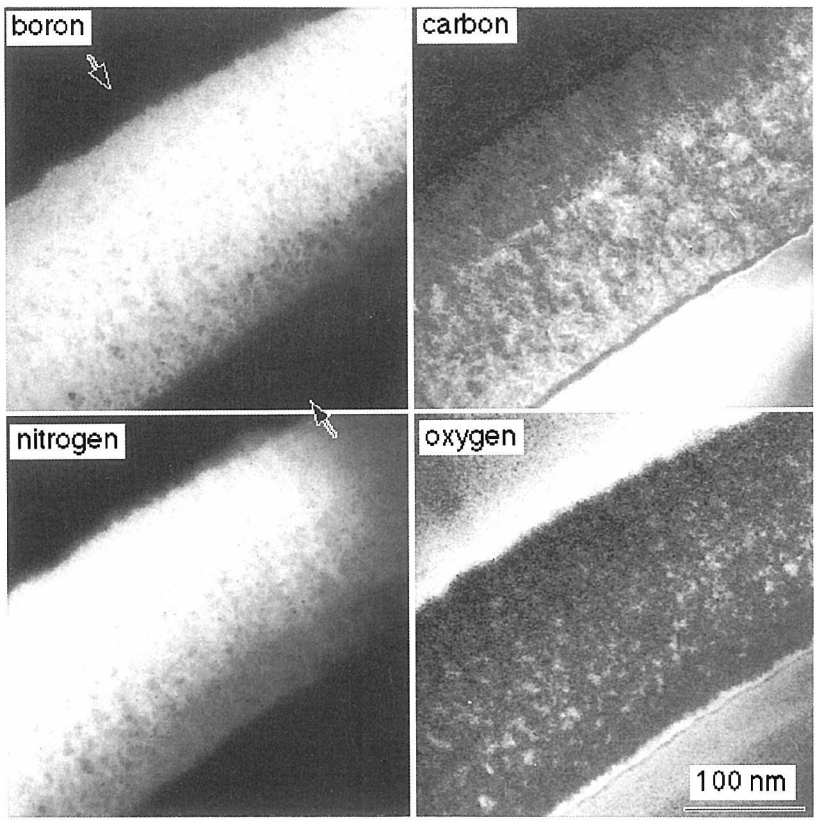

Figure 3a. 512 x 512 pixel elemental maps of a composite ceramic. 200 keV, exposure time per map 18 to 120 s, slit width 20-30 eV. Specimen courtesy Dr. X. Bourrat.

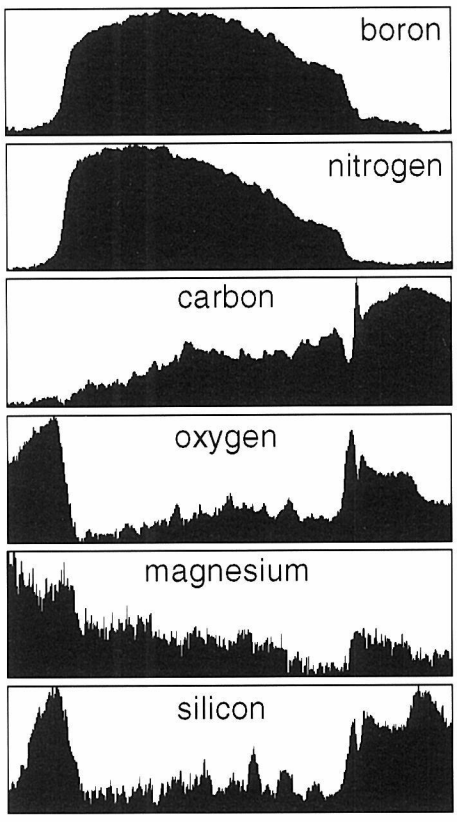

Figure 3b. Intensity profiles through the elemental maps.

The maps reveal a wealth of information about the sample [16], much of which was not known previously. For example, the maps show that the coating layer contains fibrous BN interleaved with carbon and small SiO_2 particles. The outer 50 nm of the SiC fiber is enriched in B, O and Mg and depleted in silicon. The outermost 3 nm of the fiber consists mainly of SiO_2, due to surface oxidation of the fiber. The carbon displaced by the oxidation has accumulated in a narrow layer just under the SiO_2 layer. The spatial resolution in the maps is 2-3 nm, as evidenced by the sharp peak in the carbon profile. There is simply no other way all the information contained in the maps could have been obtained by any other technique in a similarly short period of time.

Another useful contrast mechanism is associated with features in energy-loss spectra that are

specific to particular types of chemical bonding. The classic example is carbon, whose energy-loss spectra are different for its different chemical states, with especially pronounced features arising when there is aromatic bonding (the π^* peak at the carbon K-edge and also the π^* plasmon at 6-8 eV). Imaging with such features gives rise to "chemical" rather than "elemental" images. Reliable separation of the contrast due to chemistry changes from other contrast mechanisms requires image data to be recorded at many different energies. It is easier when a complete spectrum is available at every image point, as is done in STEM-based "spectrum-imaging" [17, 18]. Single-energy chemical imaging, however, can be performed just as easily with an imaging filter as with a STEM, and is likely to be much faster for any image whose size is greater than about 16 x 16 pixels.

Fig. 4 shows images of unstained polystyrene particles in a polyethylene matrix taken with our "biological" GIF at 120 keV, with the specimen at room temperature. The image on the left is a zero-loss image taken with a 4 eV wide slit. It shows no useful contrast, as expected because the two polymers have similar density and composition. The image on the right was recorded with energy losses from 5 to 9 eV. It shows polystyrene (which has aromatic rings that give rise to a π^* plasmon at 7 eV) as bright, and polyethylene (which has no aromatic bonding) as dark. Because of radiation damage destroying the aromatic rings, it was essential to keep the exposure level for the images (including set-up time) to less than about 10^2 e^- / nm^2. In this respect, STEM-PEELS spectrum-imaging applied to polymers [19] has a major advantage. It collects all the energy data with just one exposure of the sample to the beam, whereas an imaging filter needs to expose the sample for every new energy imaged. Nevertheless, because spectrum-imaging takes about 10 mins to record data for a 100 x 100 pixel chemical image, whereas imaging filters can record 1024 x 1024 pixel chemical images in about 10 sec, it is likely that the filters will prove highly useful for this type of work.

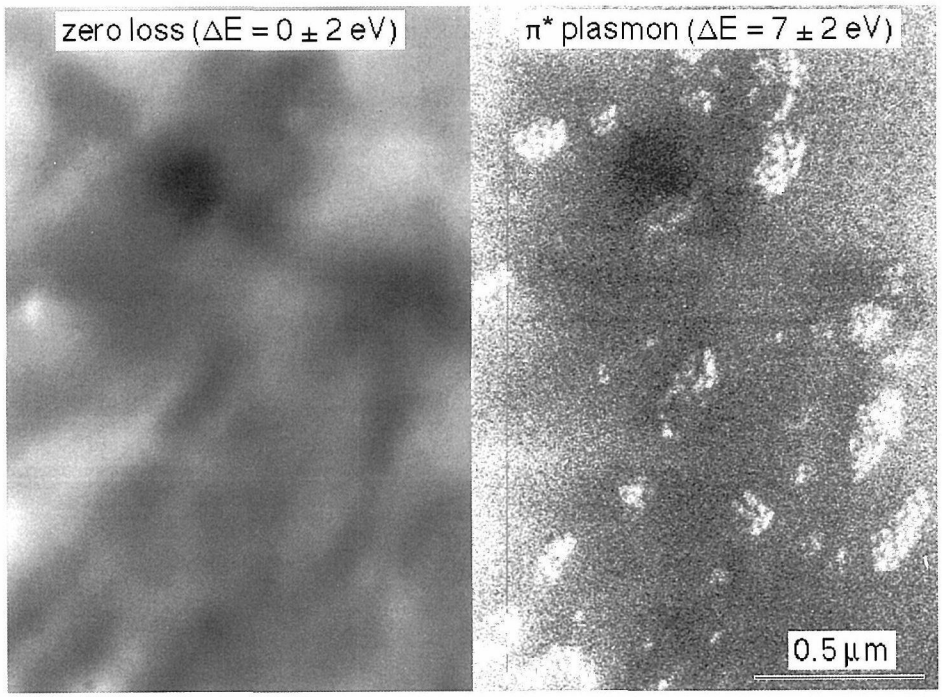

Figure 4. Energy-filtered images of unstained polystyrene particles in a polyethylene matrix. 120 keV, 4 eV wide slit, 1 s exposure for the zero loss image, 8 s exposure for the π^* plasmon image.

3) Our post-column filters match the spectroscopy performance of the Gatan PEELS in aspects such as attainable energy resolution and collection efficiency, and they improve on the PEELS with a more sensitive detector (2-dimensional scientific-grade CCD rather than a 1-dimensional photodiode array) and a more efficient beam trap [12]. The filters have achieved 0.6 eV energy resolution at 1.25 MeV on the zero loss peak [11] and 0.4 eV resolution at 100 keV with a 4 mm diameter entrance aperture. Because the gain response of a 2-dimensional detector can be accurately characterized and compensated by gain normalization, they have been able to record spectra with channel-to-channel gain variation as low as 0.05% [12] This level of performance promises to significantly improve EELS detection limits for elements present in low concentrations [21].

IV. EFTEM prospects

The examples presented above show only a small sub-section of possible EFTEM applications. A more complete coverage is provided in reference [22]. Compared to elastic imaging techniques that have been available since the very beginning of electron microscopy, there clearly remains much

exploration to be done in EFTEM. Nevertheless, some trends have already become clear:

1) Imaging and diffraction with elastically scattered electrons are greatly improved by energy filtering, particularly in thicker samples. The resolution in such images (and diffraction patterns) is the same or better than in unfiltered images (and diffraction patterns).

2) Imaging with inelastically-scattered electrons is limited by the nature of the available signals more than by presently available instrumentation. This is mainly because element-specific inner-shell losses are typically very weak. For inner shell energy losses of 50-500 eV, the intensity of the loss image is normally 10^2 to 10^4x weaker than the intensity of the bright-field image recorded with the same illumination intensity. For energy losses greater than 2 keV, the loss image can be more than 10^6x weaker than the bright-field image. For plasmon-loss imaging, the intensities are typically 10 to 100x weaker than the zero-loss image, but the plasmon signal is much harder to interpret than the inner-shell loss signal, and its spatial resolution is more severely limited by delocalization.

3) The best spatial resolution in elemental images and maps is obtained with radiation-resistant materials, because doses of 10^5 to 10^{10} electrons per $Å^2$ are needed if the image resolution is not to be unduly limited by poor signal-to-noise ratio. Such doses are most readily obtained at 200-300 keV with field emission guns and efficient condenser systems. Cold field emission guns (FEGs) with an energy spread of 0.3 eV and less are especially valuable, because they give good energy resolution that is useful in EELS fine-structure studies. An optimized instrument should be able to attain 1 nm resolution in elemental maps on a routine basis. Improving the resolution to 2-5 Å should be possible for elements that give strong edges in the 500 eV to 1000 eV loss range, such as first row transition metals, and rare earths. In order to reach this level of performance, operational parameters such as the slit width and the acceptance angle will need to be carefully adjusted so as to avoid image blurring due to the chromatic aberration of the microscope's lenses without needlessly reducing the total intensity. Elements with edges at lower energies are not likely to give sufficiently localized inner shell loss images. Elements with edges at higher energies will give images limited by low signal-to-noise ratios, and practical problems such as specimen drift during long exposures.

4) EFTEMs will permit rapid imaging and mapping, but will remain behind dedicated STEM-PEELS instruments in providing quantitative spectroscopic data at high spatial resolution. However, since an optimized post-column filter can also function as an improved-performance PEELS, any TEM with a FEG, good probe-forming capabilities and an optimized imaging filter will also be able to operate as an efficient STEM-PEELS instrument.

V. References

[1] O.L. Krivanek and C.C. Ahn, Proc. 11th Int. EM Congr. (Kyoto, 1986) vol. **1**, p. 519.
[2] R. Castaing and L. Henry, C.R. Acad. Sci. Paris B255 (1962), p. 76.
[3] S. Senoussi, L. Henry and R. Castaing, Journal de Microscopie 11 (1971), p. 19.
[4] G. Zanchi, J.P. Perez and J. Sevely, Optik 43 (1975), p. 495.
[5] S. Lanio, Optik 73 (1986), p. 99.
[6] H. Rose, Ultramicroscopy **56** (1994) 11.
[7] H. Shuman and A.P. Somlyo, Proc. Nat. Acad. Sci. USA 79 (1982), p. 106.
[8] US patent #4,851,670.
[9] O.L. Krivanek, A.J. Gubbens and N. Dellby, Microscopy, Microanal., Microsctr. **2** (1991) 315.
[10] O.L. Krivanek et al. Microscopy, Microanal., Microsctruct., **3** (1992) 187.
[11] A.J. Gubbens et al. Ultramicroscopy, to be published (1995).
[12] O.L. Krivanek et al., Ultramicroscopy, to be published (1995).
[13] O.L. Krivanek and P.E. Mooney, Ultramicroscopy **49** (1993) 95.
[14] P.A. Midgley et al., Ultramicroscopy, to be published (1995). Also J.W. Steeds, this symp.
[15] R.F. Egerton, "EELS in the Electron Microscope" (Plenum Press, New York, 1986).
[16] O.L. Krivanek, M.K. Kundmann and X. Bourrat, MRS Symp. Proceedings vol. **332** (1994) 341.
[17] C. Jeanguillaume and C. Colliex, Ultramicroscopy **28** (1989) 252.
[18] J.A. Hunt and D.B. Williams, Ultramicroscopy **38** (1991) 47.
[19] J.A. Hunt et al., Ultramicroscopy, to be published (1995).
[20] O.L. Krivanek et al. in: Proc. 13th Int. EM Congr. (Paris, 1994) vol. **1**, p. 167.
[21] Y.-Y. Wang, R. Ho, Z. Shao and A.P. Somlyo, Ultramicroscopy **41** (1992) 11.
[22] Proceedings 1994 Leukerbad workshop on EEL Spectroscopy and Imaging. Part 1: Techniques, Ultramicroscopy, to be published. Part 2: Applications, MMM, to be published.

Ultra-High Spatial Resolution Analysis by a 300 kV Field Emission Analytical Electron Microscope

Yoshio Bando
National Institute for Research in Inorganic Materials, 1-Namiki, Tsukuba, Ibaraki 305, Japan

Instrumental characteristic features of a new 300kV field emission analytical transmission electron microscope and some applications to ultra-high spatial resolution analysis of advanced materials are given. The present new microscope enables us to carry out the ultimate chemical analysis at subnanometer to nanometer level regions using an extremely fine electron probe of about 0.5 nm in size. A crystal structure of 33R-9AlN.Al_2O_3 and a modulated structure of $InFeO_3(ZnO)_{13}$ and also grain boundary phase analysis of Si_3N_4 are well performed in combination with high resolution lattice imaging.

1. Introduction

Analytical transmission electron microscope (ATEM) equipped with both an energy dispersive x-ray spectrometry (EDS) and an electron energy loss spectrometry (EELS) is becoming a most powerful tool in materials science. The relations between local structures and compositions can be successfully determined in thin specimens. Since the brightness of the field emission gun is approximately 100 times larger than that of the conventional thermal emission gun using LaB_6 emitter, the field emission gun is most powerful to produce the very fine electron probe with high current density for the use of the ultra-high spatial resolution analysis.

It is so far understood that the analytical observation capabilities can be significantly improved by increasing the accelerating voltages. The medium voltage ATEM having the voltages from 300 kV to 400 kV increases the observation capabilities in terms of the image resolution, the peak to the background ratio (P/B) in both EDS and EELS spectra, and the spatial resolution, as compared to those at 100 kV and 200 kV[1-2].

Based on the above view points, a new 300kV medium voltage ATEM with a field emission gun is recently developed[3-5]. In the present paper, some characteristic instrumental features of the new microscope and its application to subnanometer level analysis of materials are given. It is emphasized that the ultra-high spatial resolution chemical analysis using the fine probe of about 0.5 nm diameter are successfully carried out in combination with high resolution lattice imaging. Crystal structures of 33R-9AlN.Al_2O_3 and $InFeO_3(ZnO)_{13}$, and the grain boundary phases of Si_3N_4 are well determined.

2. Instrumental Features

2.1 Field Emission Gun

The thermal assisted-type field emission gun using a <100>-oriented tungsten chip is employed. A basic design of the present field emission gun working at 300kV is identical

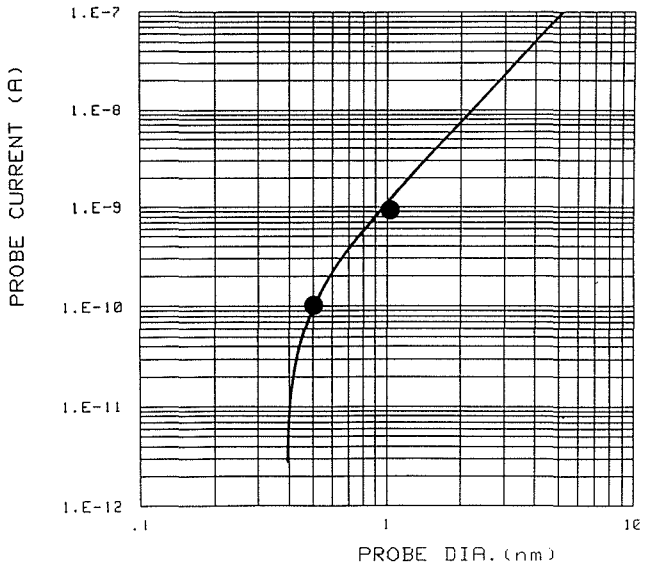

Fig.1 A result of calculation of a probe diameter as a function of probe current at 300kV. The observed values are indicated by dark circles.

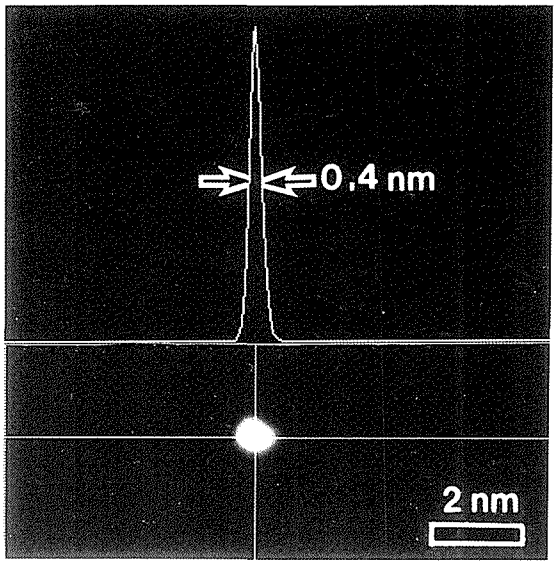

Fig.2 A minimum probe size and its corresponding photometric trace. The minimum probe size is assigned as about 0.4 nm

to that of 200kV[6]. The field emission gun consists of an emitter, an extraction electrode, an electrostatic lens and an accelerator having 10 accelerating stages. The probe current can be varied by changing the extracting electrode potential where the crossover point is unchanged. Therefore, the probe size can be maintained constant at different probe currents. The emission currents are about 10-30 uA with the extraction electrode potential of about 3 to 5 kV and the electrostatic lens potential of about 7.2 kV. A tip temperature is about 1600^{o}K.

The field emission gun is evacuated by a differential pumping: the emitter region is evacuated by a 15 litter/sec sputter ion pump (SIP) and the accelerator by a 150 l/s SIP. An intermediate chamber between the accelerator and the condenser lens is evacuated by 20 l/s SIP. The accelerator and the intermediate chamber can be baked at 300^{o}C with using an oven furnace when a new emitter is used. The vacuum at the emitter, the accelerator and the intermediate chamber is $3x10^{-8}$ Pa, $3x10^{-7}$ Pa and $1x10^{-6}$ Pa, respectively.

For the better operation of the present field emission gun, the emission pattern can be monitored through the pattern observation window where the fluorescent screen is placed at the top surface of the electro static lens. After the long time use of about 3 to 5 days, the emission currents drop. Then, the oxygen processing is applied. A small amount of oxygen gas is introduced into the accelerator using oxygen leak valve. The oxygen gas pressure near the emitter is set at about $2x10^{-7}$ Pa. During the introduction of the oxygen gas for about 10 minutes, the emission currents decrease gradually and finally drop to almost a zero value. In about a few minutes later, the emission currents start to increase up to 10 to 30 uA. This phenomena is closely related to a reconstruction of a well-defined W(100) surface.

2.2 Probe Size

The illumination lens system consists of a double condenser lens, a condenser mini lens

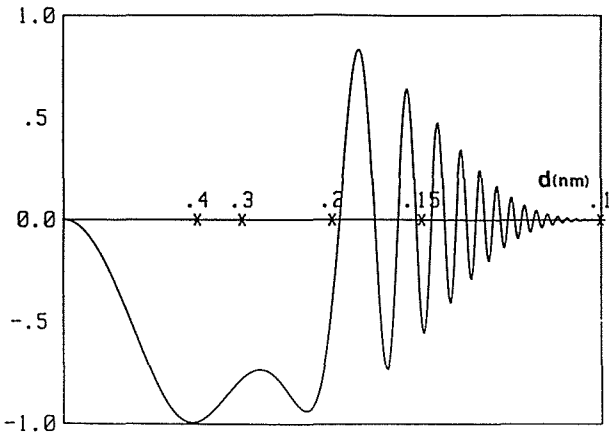

Fig.3 A contrast transfer function of the present new microscope (JEM-3000F) using an analytical objective polepiece.

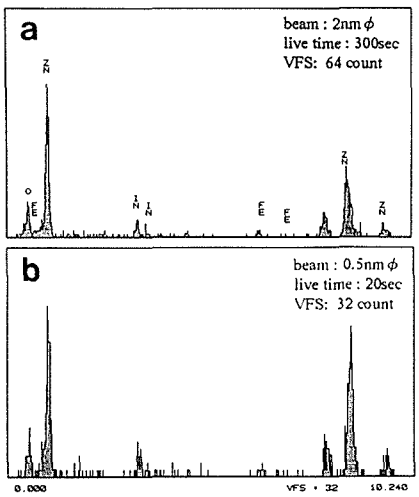

Fig.4 A comparison of detection sensitivity for EDS analysis between the conventional ATEM (JEM-3010) (a) and the present field emission ATEM (JEM-3000F) (b). The detection sensitivity is increased by about 100 times in the JEM-3000F.

and a prefield of the condenser-objective (C/O) lens. The probe diameter, D, at the specimen point can be calculated and the results are shown in Figure 1. The brightness of the W(100) emitter is considered as 7×10^8 A/cm^2·str at 300kV. The result of the calculation suggests that the minimum probe size at 300kV is about 0.4 nm.

Figure 2 shows a direct measurement of the minimum probe size which is recorded by an imaging plate. The exposure time is about 0.1 s. The half-width of the minimum probe size measured by photometer trace is about 0.4 nm, which agrees well with the calculation. The probe currents are also measured by a Faraday cup and they are about 0.1 nA and 1.0 nA for the probe sizes of 0.5 nm and 1.0 nm, respectively, which are indicated in Fig.1. For the routine analysis, the probe of the 0.5 nm size is usually used.

2.3 Resolution

An analytical polepiece is used for the objective lens, in which a scanning transmission electron microscope (STEM) attachment can be equipped. The spherical and chromatic aberration coefficients for the analytical objective lens are 1.1 mm and 1.8 mm, respectively. Figure 3 shows a phase contrast transfer function curve of the present microscope. In the calculation, the envelope function due to a partial coherency and a chromatic effect is included. The beam convergence half-angle and the energy spread of the field-emission source are considered to be 0.2 mrad and 0.8 eV, respectively. A theoretical resolution limit and an information limit are estimated to be 0.195 nm and about 0.13 nm, respectively, at an optimum Scherzer defocus of about 56 nm. The lattice image of the (0001) plane of the graphite is also well observed in the STEM image.

2.4 Analytical Capabilities

The analytical equipments such as an ultra-thin window (UTW) EDS detector and a parallel-recording electron energy loss spectrometer (Gatan PEELS 666) are attached to the microscope column. In order to carry out high sensitivity elemental analysis, a solid angle for X-ray detection is increased up to be 0.20 str, where the active area of Si(Li) UTW detector and the distance between the specimen and the detector are 40 mm^2 and 13.5

mm, respectively, with a take-off angle of 26 degrees. The peak to the background ratio (P/B) using Fiori method is about 3700 at 300kV.

Figure 4 shows a comparison of detection sensitivity for EDS analysis between the conventional ATEM using a LaB_6 emitter(JEM-3010) and the present FE-ATEM (JEM-3000F) at 300kV, where EDS spectra are obtained from the same specimen regions of $InFeO_3(ZnO)_{13}$. Based on the estimation of the beam size and acquisition time between the two microscopes, the detection sensitivity of the JEM-3000F is improved by about 100 times as compared to the conventional JEM-3010.

A PEELS is equipped with a TV camera. Figure 5 shows a zero loss peak of EELS spectrum at 300kV, where a tail of a zero loss peak due to the scintillator noise is removed by deconvolution. The full-width at half-maximum (FWHM) is then assigned to be 0.6 eV at an emission current of about 14 uA.

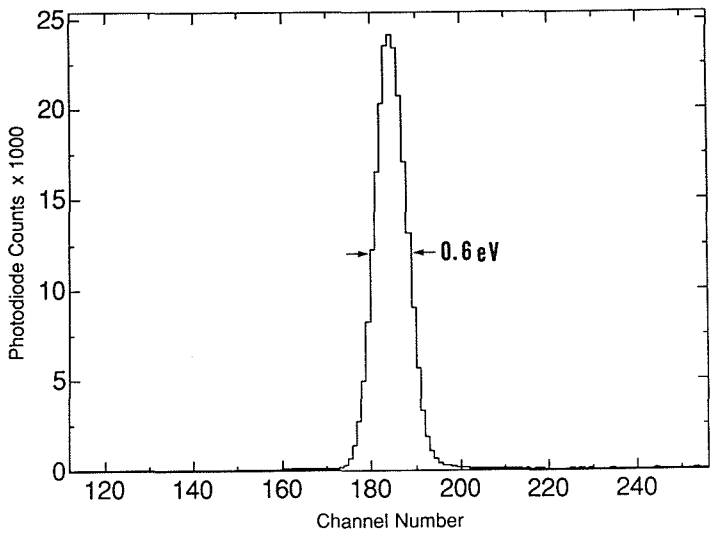

Fig.5 A zero loss peak at 300kV. A full-width of half-maxima (FWHM) of the zero loss peak is estimated to be 0.6 eV after the deconvolution.

3. Ultra-high Spatial Resolution Analysis of Advanced Materials

3.1 Structure Determination of Aluminum Nitride Polytypes

Aluminum nitride (AlN) reacts with Al_2O_3 and SiO_2 at high temperature to form compositional polytypes or polytypoids where the composition varies with a periodicity. In the AlN-Al_2O_3 system, the polytypes observed are 12H, 15R, 33R, 39R and 32H and their general compositions are considered as $mAlN.Al_2O_3$, where m is an integer[7]. Based on the x-ray powder diffraction study, the structure is speculated to be AlN_4 tetrahedral layers interleaved with AlO_6 octahedral layer. Since the identification between oxygen and nitrogen is difficult in the x-ray diffraction, the distribution of oxygen and nitrogen in each layer is not determined.

Figure 6 shows a crystal structure image of 33R polytype, observed at Scherzer defocus. The incident electron beam is normal to the (110) plane. The result of the electron diffraction indicates that the crystal is 33R with lattice parameters a=0.308 and c=8.69 nm. In the image, each of aluminum atoms site is well resolved as dark dots, while those of N and O

atoms are not imaged. The separation between the dark dots normal to the c axis is 0.26 nm.

To perform a chemical analysis of a single atomic layer level, EDS spectra are observed when the fine electron beam of about 0.5 nm size is placed on the each layer. Figure 7(a) and (b) shows EDS spectra, observed from the single atomic layer marked as Al-O and Al-N, respectively. The acquisition time is about 20 s. In (a), the oxygen and aluminum peaks are clearly observed with a very weak peak of nitrogen, while in (b) the nitrogen peak is identified as well as aluminum peak. No oxygen peak is observed. The present monolayer level elemental analysis confirms that oxygen and nitrogen atoms are not randomly distributed among the layers, but they are confined to form Al-N and Al-O layers.

Based on the above observations, the crystal structure of 33R is then derived. The 33R aluminum oxynitride polytype consists of 9 layers of AlN tetrahedral layers interleaved with 2 layers of AlO octahedral layers along the c axis. From the rhombohedral symmetry, the structure unit is repeated by three times to give a total of 33 layers. The chemical composition is then assigned as $9AlN.Al_2O_3$, which is consistent with the general chemical formula as m=9.

3.2 Modulated Structure Determination of $InFeO_3(ZnO)_{13}$

Recently, a new series of the homologous compounds $InFeO_3(ZnO)_m$ has been found in the In_2O_3-Fe_2ZnO_4-ZnO system[8]. Based on the powder x-ray diffraction study, the crystal structure is speculated to be isostructure with that of $LuFeO_3(ZnO)_m$, where the structure is built up of a succession of Lu-O layers interleaved with (Zn,Fe)-O layers. It is considered that metal atoms are randomly distributed within the layers of (Zn, Fe). However, the structure analysis has not been carried out in detail[9]. Figure 8 shows a high resolution lattice image of $InFeO_3(ZnO)_{13}$, observed at a relatively thick region. The separation between the white dots normal to the c axis is 0.16 nm. The modulated structures corresponding to the sinusoidal contrast are only formed within the layers of (Zn,Fe)-O. Their periodicities are not the same from area to area and they slightly vary from 51 lattice planes (8.2nm) to 54 lattice planes (8.7nm), which correspond to the observation of the non-integral super lattice diffraction spots with a periodicity of about 8.37 nm. The each phase of the sinusoid is in an order among the layers.

In order to study whether the modulated structure is caused by the successive displacement of Zn and Fe atoms or the compositional ordering of Fe or Zn atoms, the point analysis are performed. Figure 9 (a) and (b) are EDS spectra, when the fine electron beam are placed on the region of the modulated contrast and the region out of the contrast, respectively. The analysis points are marked in the figure. In (a) and (b), a strong peak of Zn and a weak peak of Fe are present with the absence of In peak. This confirms that these layers are consisting of Fe and Zn atoms. The intensities of Fe peaks between (a) and (b) are very different. The intensities of Fe peaks for the modulated region are significantly higher as compared to that of the non-modulated region. This suggests that Fe atoms are not randomly distributed in the (Zn,Fe)-O layers, but they are ordered within the layers. It therefore concluded that the modulated structure of $InFeO_3(ZnO)_{13}$ is caused by the compositional ordering of Fe atoms within the layers.

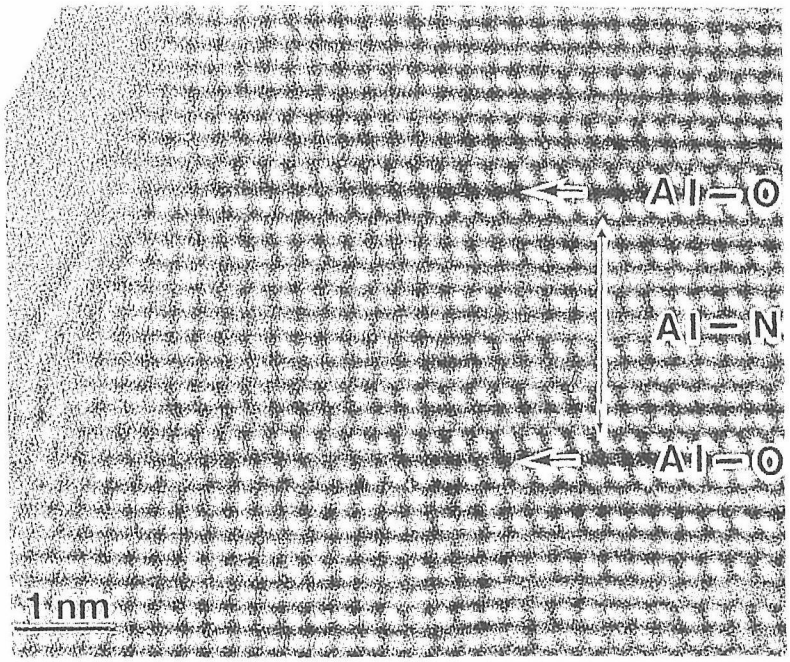

Fig.6 A crystal structure image of 33R-9AlN.Al_2O_3 , observed at Scherzer defocus. The incident electron beam is normal to the (110) plane. Each of Al atoms is well resolved.

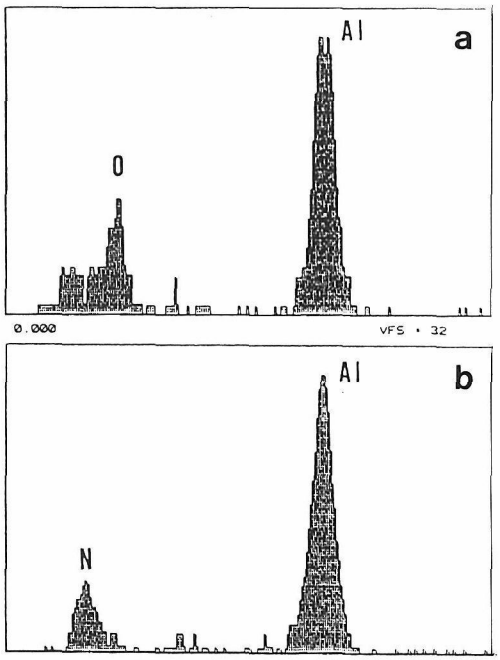

Fig. 7 EDS spectra obtained from one of the single atomic layers marked Al-O (a) and Al-N (b) in the Fig. 6. The probe size is 0.5 nm and the exposure time is 20 s.

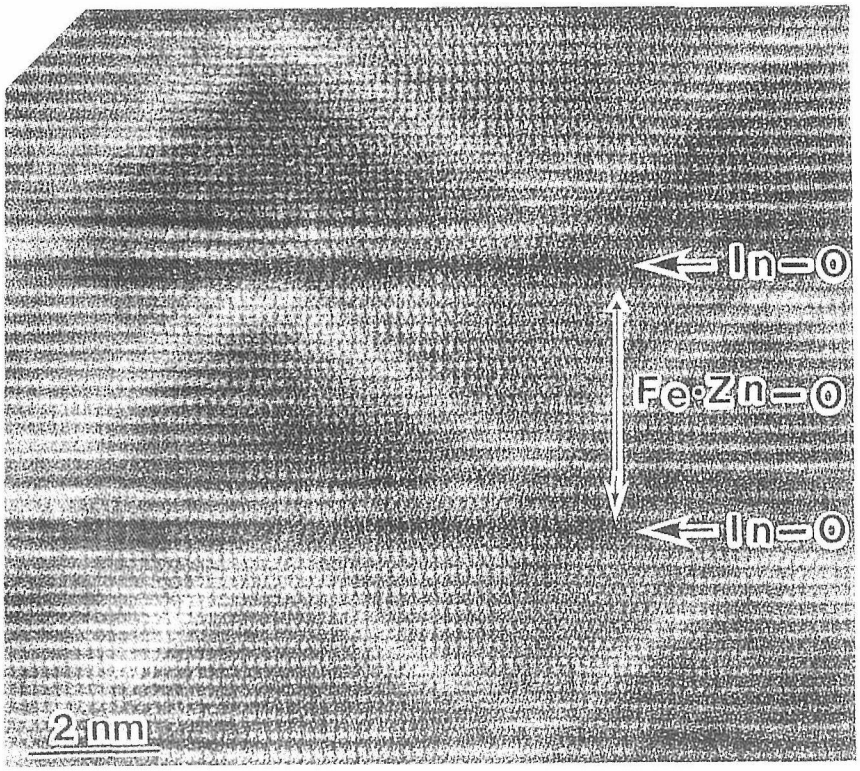

Fig.8 A high resolution lattice image of a modulated structure of $InFeO_3(ZnO)_{13}$, observed at a relatively thick region. The sinusoidal modulated image contrast with the periodicity of about 8.47 nm is only observed within the layers of (Zn, Fe)-O.

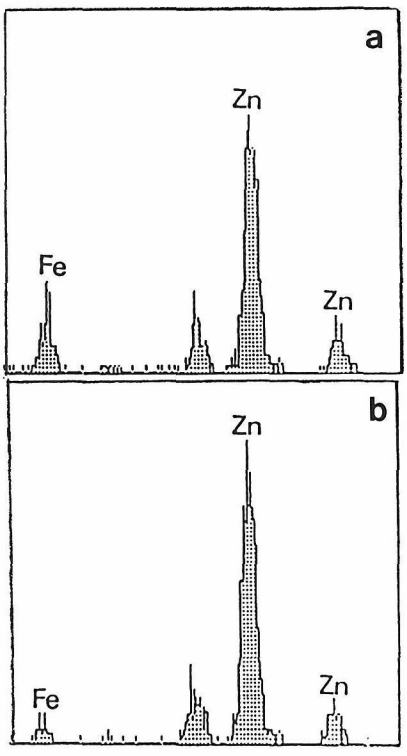

Fig.9 EDS spectra obtained from the region of the modulated contrast (a) and the region out of the contrast (b), in which the analysis points are shown by *. Note that the intensities of Fe peaks in (a) are higher than those in (b), indicating that the modulated structure is caused by the compositional ordering of the Fe atoms.

3.3 Grain Boundary Phase Analysis of Silicon Nitride

Silicon nitride is one of the best candidate for the use of high-temperature engineering ceramics. In order to improve the mechanical properties, the grain boundary characterization is most important. Since the intergranular thin films formed between the two matrix grains are extremely thin as about 1 nm, their compositions have not been well analyzed. Figure 10(a) shows a high resolution image of an intergranular thin grain boundary of silicon nitride containing additives of 1 mol% of Y_2O_3 and Nd_2O_3. The amorphous thin layer having about 1 nm thick is well identified between the two grains. The corresponding EDS spectra obtained from the intergranular thin films is shown in Fig.10(b), where the minor constitution of Y and Nd atoms are well detected.

The chemical compositions between the intergranular films and the triple points are also studied. For the quantitative analysis of the EDS spectra from the intergranular boundary, in which Si peak intensities are enriched due to the electron beam broading, the x-ray intensities of Si peaks caused by the matrix grains are subtracted based on the measurement of the x-ray intensity of N peaks. This procedure may contain an experimental error of about 10 to 20%. However, it can be concluded that the composition between them are not the same and the contents of (Y_2O_3-Nd_2O_3) are poor in the two-grain boundary, while they are rich in the triple points. Based on the above observations, the grain boundary composition profile of silicon nitride is illustrated in Figure 11. The chemical compositions of the grain boundary glassy phase are not uniform among the boundaries. The additive atoms are highly concentrated in the inner part of the triple points and their contents decrease gradually along the outer part of the triple points, which is shown as (Y-Nd)-poor(1). The

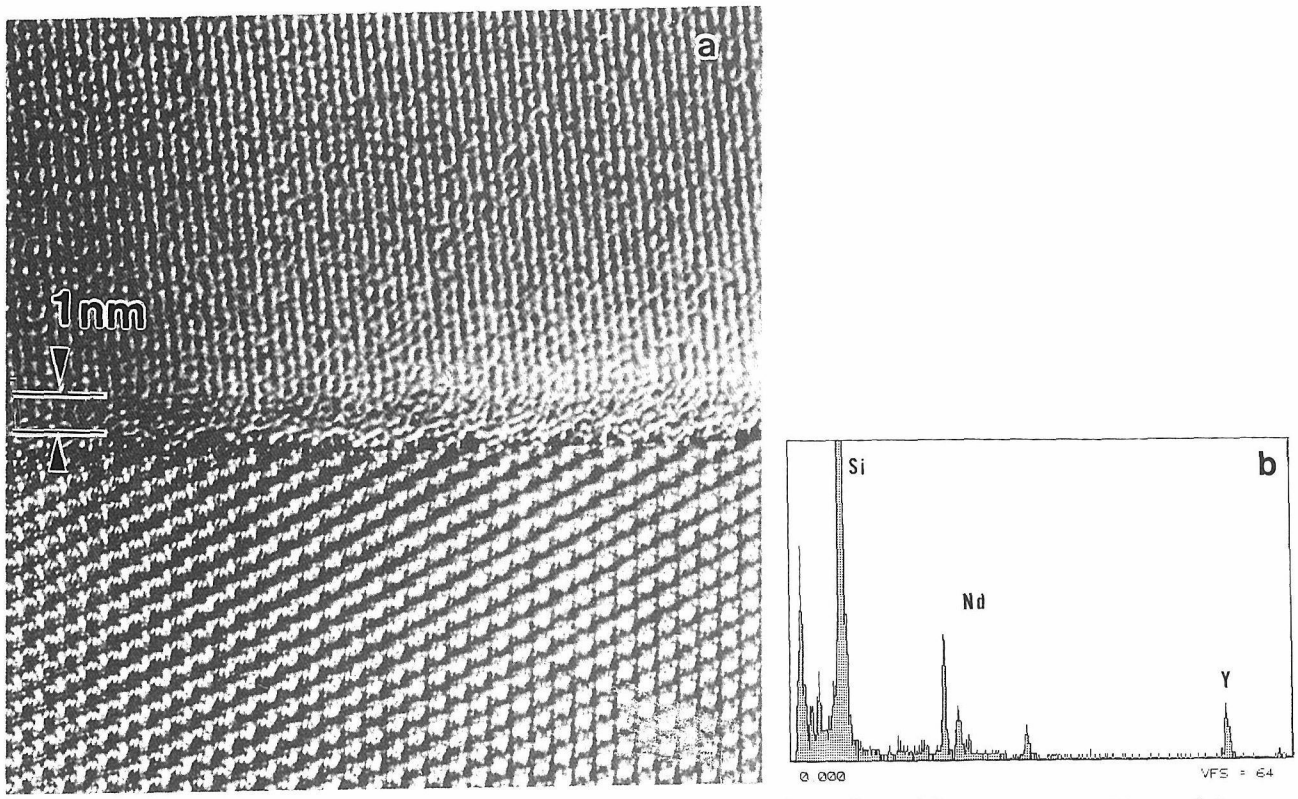

Fig. 10 A high resolution image of an intergranular thin grain boundary of Si_3N_4 with additives of 1 mol% of Y_2O_3 and Nd_2O_3 (a) and corresponding EDS spectra (b). The amorphous intergranular phase of about 1 nm thick is present in (a), in which minor constitutions of Y and Nd atoms are clearly detected in (b).

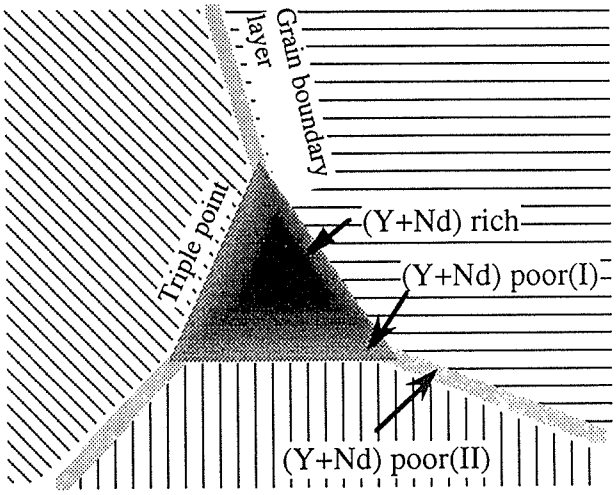

Fig. 11 A schematic illustration of the grain boundary structure. The compositions among the boundaries are not the same, in which the additives of Y_2O_3-Nd_2O_3 are highly concentrated in the inner part of the triple points as indicated (Y+Nd) rich, whereas those are less at the intergranular boundary as (Y+Nd) poor(II).

matrix grains are always covered with very thin films of SiO_2-rich glassy phase as indicated in (Y+Nd)-poor(II). The contents of SiO_2 in these thin films are higher than those of the outer region of the triple point.

Acknowledgements

The author would like to thank Drs.M.Mitomo, N.Kimizuka for supplying the specimens. He also thank Mrs.S.Uchida,Y.Kitami, K.Kurashima, T.Tomita, T.Honda, Y.Ishida and K.Ibe for their supports to the present work.

References

1) Bando Y., Matsui Y., Uemura Y., Oikawa T., Suzuki S., Honda T., Harada Y., Ultramicroscopy 18 (1985),117.
2) Bando Y., Mitomo M., Kitami Y., Izumi F., J. Microscopy 142, (1986), 235.
3) Bando Y., Kitami Y., Tomita T., Honda T., Ishida Y., Jpn. J. Appl. Phy., 32, (1993), L1704.
4) Bando Y., Proc. ICEM 13-Paris, p.591 (1994).
5) Bando Y., Kitami Y., Kurashima K., JEOL News, 31E, (1994) 17.
6) Bando Y., Kitami Y., Kurashima K., Tomita T., Honda T., Ishida Y., Microbeam Analysis (1995) in press.
7) Tomita T., Katoh S., Kitajima H., Kokubo Y., Ishida Y., Proc. XII Int. Congr. Electron Microsc., P.94 (1990).
8) Bartram S.F., Slack G.A., Acta Cryst., B35, (1979), 2281.
9) Kimizuka N., Isobe M., Nakamura M., Mori T., J. Solid State Chemistry 103, (1993), 394.
10) Uchida N., Bando Y., Nakamura M., Kimizuka N., J. Electron Microsc., 43 (1994) 146.
11) Bando Y., Suematsu H., Mitomo M., Mat. Res. Soc. Symp. Proc. vol.346, p.733 (1994).

Energy-Filtered RDF Analysis of Amorphous and Polycrystalline Materials

David Cockayne
Electron Microscopy Unit, The University of Sydney, Sydney NSW 2006 Australia

The structure of small volumes of amorphous or polycrystalline material can be obtained by an electron diffraction technique which parallels the neutron and X-ray scattering technique, and gives nearest neighbour distances accurate to 0.001 nm. As well, it can be used to obtain nearest neighbour distances and coordination numbers from the same region of specimen from which high resolution electron microscopy, X-ray and electron energy loss data is obtained.

The analysis of amorphous materials in terms of radial distribution functions (eg giving nearest neighbour distances and coordination numbers) can be carried out routinely on bulk material using neutron and X-ray scattering techniques. However there are many situations where the amount of available material (eg thin films, intergranular phases, multi-phased systems) is insufficient for such an analysis. In the case of amorphous materials, there has been a long history of obtaining radial distribution functions (RDF) from electron diffraction data (for a summary, see Bentley et al[1]), but compared with the major advances made with RDF analysis using neutrons and X-rays, development of structural refinement techniques using electrons has been slow. The use of scanning diffraction methods developed by Grigson[2] in 1962, and the introduction of energy filtering by Graczyk and Moss[3] in 1969, overcame some of the early difficulties, but there have been relatively few detailed electron microscope or electron diffraction structural studies of amorphous materials which compare in accuracy with the neutron or X-ray results . This can only be attributed to the fact that no suitable electron diffraction or microscopy techniques have been available.

The TEM diffraction pattern from a selected volume of material I(s) can be transformed into the reduced density function G(r) using the standard algorithm

$$G(r) = 4\pi r(\rho(r) - \rho_0) = 8\pi \int_{s_{min}}^{s_{max}} s.\frac{I(s) - Nf^2(s)}{Nf^2(s)}.\frac{\sin(-2\pi sr)}{2\pi sr}.ds \qquad (1)$$

where $\rho(r)$ is the local atomic density at distance r from a central atom, ρ_0 is the mean atomic density, $s = 2\sin\theta/\lambda$, s_{max} and s_{min} are the limits of collection of I(s), f(s) is the atomic scattering factor, and N is the number of atoms contributing to I(s).

In the case of single element materials, the derivation of equation (1) involves few approximations, the most important being that small-angle shape-dependent scattering be removed from I(s). In the case of multi-element materials (eg amorphous alloys) the approximations involved in deriving G(r) in the above form are severe (see below).

The most important requirements for obtaining accurate nearest neighbour distances from G(r) are that

1 I(s) should involve single electron scattering only
2 s should be collected to high scattering angles
3 I(s) should exclude inelastically scattered electrons

Early studies had difficulty with each of these requirements. In particular, ensuring single scattering of electrons was difficult, and, despite the work of Blackman[4], the limitations on the thickness of

amorphous material necessary to maintain single scattering were (and are) poorly understood; collection of I(s) onto photographic film was tedious because of the wide dynamic range of I(s) over the large scattering angles involved; maintaining linearity in s over large scattering angles (eg because of lens aberrations) was difficult. The pioneering work of Grigson[5] and of Graczyck and Moss[3] introduced energy filtering to the analysis, and the studies of Maher[6] and of Bentley et al[7] showed the benefits of electronically recording I(s), but there were few accurate structural studies reported because of the other difficulties referred to above.

Many of these problems have been overcome by the technique reported by Cockayne and McKenzie[8,9]. In this technique, single scattering is approached by using thin films and 300keV electrons; energy filtering of the diffraction pattern removes inelastically scattered electrons from I(s); and use of scanning coils immediately beneath the specimen ("post-specimen scan coils") allows collection to large s, and ensures that for all values of s, the electrons in the collected I(s) are on the microscope axis (thus avoiding lens aberrations). The system is shown in figure 1. Using a Philips EM430 TEM, data to s = 5 $Å^{-1}$ can be obtained. Either a parallel or a serial energy loss spectrometer can be used. The main advantage of this system is that it integrates the collection and data reduction into a package, using a GATAN spectrometer and custom function software, which collects I(s) and reduces it to G(r), on-line, in a few minutes - an enormous advantage over previous electron diffraction techniques and over the long times required for equivalent collection and analysis of neutron and X-ray data.

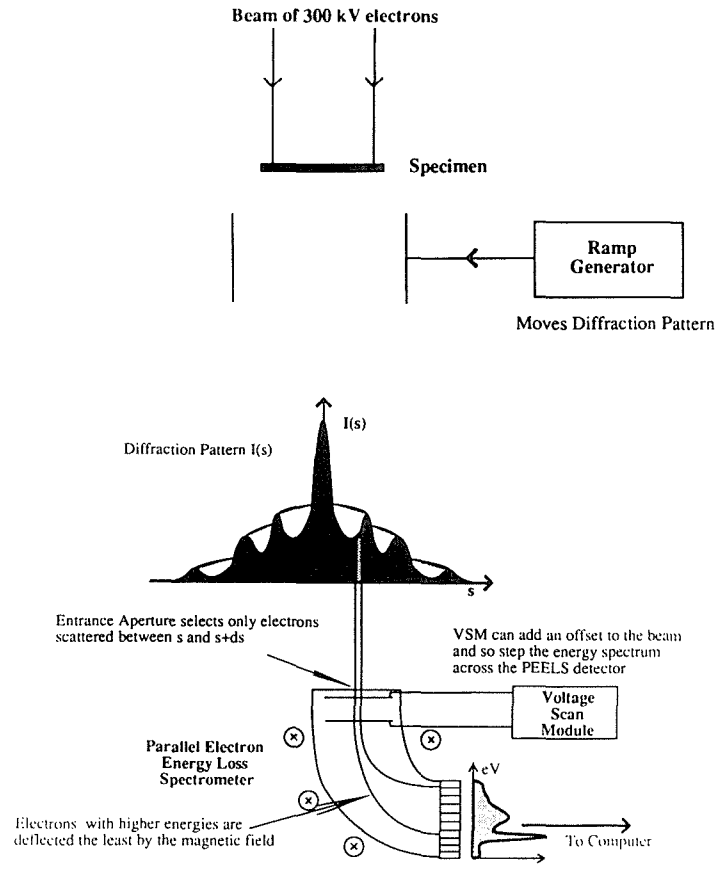

Figure 1 Block digram of energy filtered electron diffraction instrumentation using PEELS (Ref 9)

Studies of well-characterised single-element thin films (eg polycrystalline Pt, Au; graphitised carbon; tetrahedrally coordinated carbon) show that the technique can routinely give nearest neighbour distances accurate to ±0.02Å, and to ±0.01Å in favourable cases[8,9], which is comparable with the best that can be achieved in bulk materials with neutrons or X-rays.

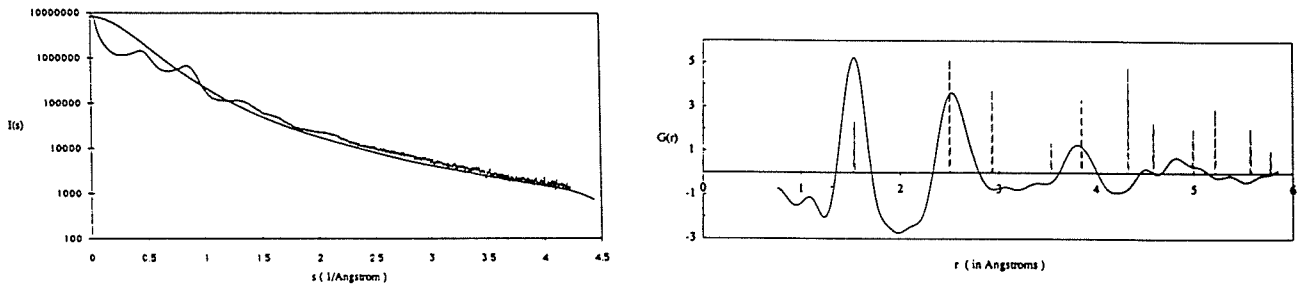

Figure 2 I(s) and G(r) from amorphous tetrahedrally-coordinated carbon. The vertical dotted lines mark nearest neighbour distances in crystalline diamond (Ref 10).

The technique has been applied to a wide range of single-element materials, including amorphous semiconductors and fullerenes. Figure 2 shows examples of I(s) and G(r) from amorphous carbon[10], collected with this system. The nearest neighbour distances of diamond are marked (vertical dashed lines), and it is seen that the first- and second-nearest neighbour distances of G(r) correspond with those of the crystalline phase, but that the third-nearest neighbour alters appreciably. This corresponds to the amorphous phase being tetrahedrally-coordinated carbon[10], consistent with the retention of tetrahedra in the amorphous phase. Further confirmation was obtained by determining the interbond angle from the ratio of the first- and second-nearest neighbour distances, which was measured to be 110°±0.5°, compared with 120° for graphite and 109.7° for diamond. Moreover the coordination number of the amorphous phase determined from G(r) was 4.1±0.1, compared with 3 for graphite and 4 for diamond. This analysis[10] was the first direct structural confirmation of the tetrahedral form of a-C (amorphous diamond).

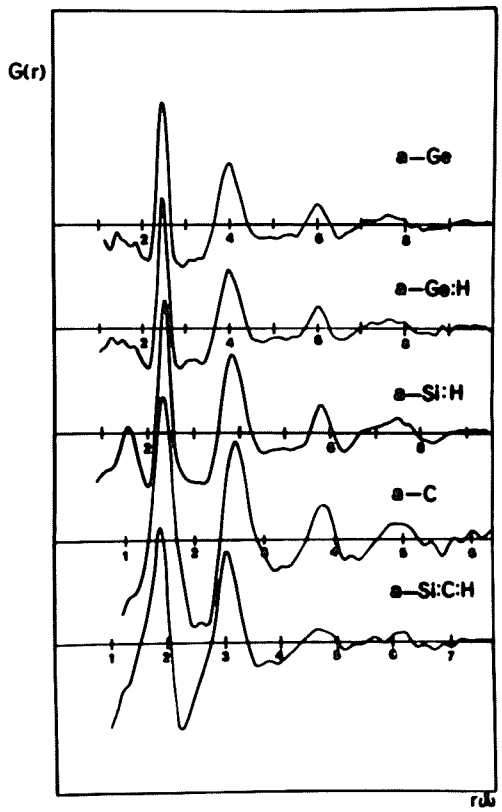

Figure 3 G(r) from diferent materials (shown), scaled to match lattice parameters.

Figure 3 shows a set of reduced density functions from amorphous Ge, amorphous tetrahedrally coordinated carbon, amorphous Si and amorphous SiC. The r axis is scaled in each case to make the crystalline lattice parameters equal. The close similarity between all G(r) reflects the fact that all materials have the same structural unit (the tetrahedron), and that the tetrahedra are similarly packed in each material. The fact that the G(r) from a-C is so similar to that from a-Si further confirms that it is the tetrahedral (diamond) form. A study of BN thin films prepared by reactive ion plating has shown them to have the same form of G(r), confirming them to be the cubic form of BN[11].

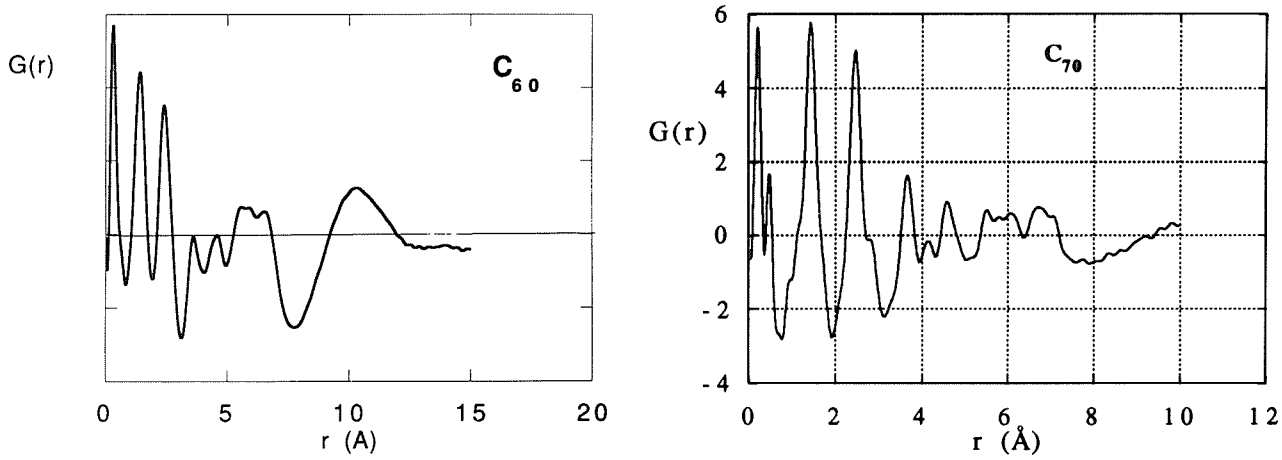

Figure 4 G(r) for C_{60} and C_{70} (Ref 12)

Figure 4 shows G(r) from C_{60} and C_{70}. Information beyond r ≈ 1.0 nm for C_{60} corresponds to spacings between molecules, while data below r ≈ 1.0 nm corresponds to carbon-carbon distances within the molecules. Refinement of the C_{60} and C_{70} models has been achieved[12] by allowing models of the molecules to relax under an interatomic potential V(r) = - G(r), which approximates to the "potential of mean force" of two atoms in an ensemble[13]. The final relaxed molecule shown in Figure 5 is derived from the experimentally measured G(r) and has only small deviations from the expected D_{5h} symmetry, even though symmetry was not imposed on atom positions during the refinement. An analysis of the bond lengths shows that they fall into four size ranges. A similar result is found for the C_{60} relaxed model, for which two bond lengths are obtained. In C_{70}, the bonds defining a pentagon (types 3,4,6,8 in the figure) are long (relative to the graphite value of 1.42Å), with a mean value of 1.46Å, which is equal to the value obtained for the equivalent bond in C_{60}. The bonds joining the apices of two pentagons (types 5 and 7) are short (mean value 1.37Å), and again are equivalent in length to the equivalent bond in C_{60}. The remaining bonds in C_{70} have no equivalent bonds in C_{60}. It is of particular interest that the relative bond lengths determined by this electron diffraction study all agree with the predictions of Johnson et al[14], who argue that an increase in the p character of the bonding within a pentagon results from the smaller pentagonal bond angle, causing an increase in the bond length. This effect in turn leads to an increase in the s character of bonds leading from a pentagon and hence to a decrease in their length.

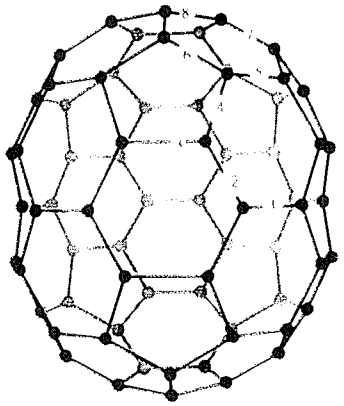

Figure 5
C_{70} from G(r) (Ref 12)

As in the case of neutron and X-ray diffraction studies, the diffraction data from multi-element systems is more difficult to analyse in terms of nearest neighbour distances and coordination numbers than for single-element materials. This is because the mathematical analysis which leads to equation (1) cannot correctly proceed unless, for all elements i,j in the system, $f_i(s) = K f_j(s)$ for all s, where K is a constant. (Many studies, especially those using electrons, have ignored this difficulty, casting doubt upon the integrity of the structural parameters obtained[15].) This problem is overcome with neutrons by combining data obtained from isotopically-related alloys, so that only the scattering factor, and not the structure, is changed. In this way isotopically-related sets of I(s) allow partial structure factors (and hence pair correlation functions) to be derived, from which the structure can be determined. A similar approach using anomalous X-ray absorption allows partial structure factors to be obtained with X-ray studies. Similar techniques are not yet available for electrons. But, just as neutron and X-ray data can be combined to form one data set (S. Lefebvre,

private communication), it seems possible that electron, neutron and/or X-ray data might be similarly combined.

Despite this problem, some progress has been achieved with alloys. Equation (1) can be employed, taking care what value of f(s) is used, and investigating the effect on G(r) of using different f(s)[15]. Alternatively, films of known structure can be used to give standard G(r), against which G(r) from unknown specimens can be compared. This approach has been successfully used to study Fe_xTb_{1-x} thin films used for magneto-optic storage (Cockayne and Song, unpublished). Tewes et al[16] have attempted to derive partial pair distribution functions using known FeTb alloys as standards.

One of the greatest difficulties in the analysis of the data, whether it be for X-rays, electrons or neutrons, lies in the determination of $Nf^2(s)$ in equation (1). In most studies, N is determined by using tabulated values of $f^2(s)$ and fitting $Nf^2(s)$ to I(s) at large s. In neutron and X-ray studies, corrections to I(s) involving removal of multiple and Compton scattering are often employed. Investigations are in progress to determine what, if any, corrections need to be made in the case of electrons. If an incorrect fit of $Nf^2(s)$ is used, it has a major effect upon the determination of coordination numbers, but little effect upon the nearest neighbour distances obtained. This is because differences between the correct and incorrect $Nf^2(s)$ are slowly varying with s, and hence, in the Fourier transform of equation (1), produce a "noise" peak near the origin of G(r) and a scaling of G(r) (which directly scales coordination number determinations).

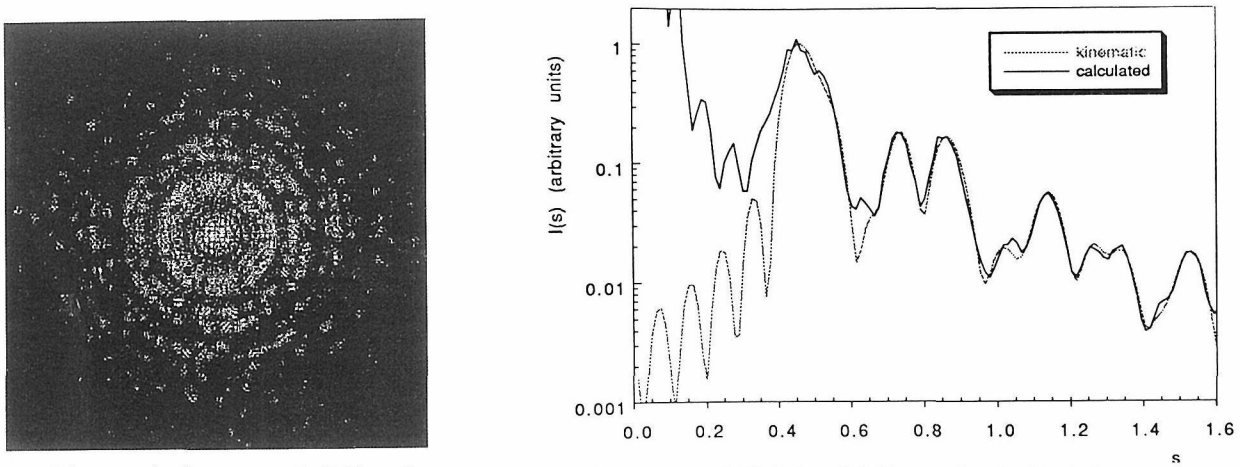

Figure 6 Computed diffraction pattern and computed I(s) (multislice calculation) from polycrystalline carbon, compared with calculated kinematical diffraction pattern from same specimen (Ref V Keast, honours thesis, University of Sydney)

In all of these investigations, the analysis of the data assumes single scattering. A study has been made of the degree to which multiple scattering occurs, and the extent to which it causes inaccuracies in the analysis (with V Keast and D McKenzie, in preparation). Computed diffraction patterns have been calculated from polycrystalline models containing 8000 atoms using multi-slice techniques. An example of a calculated diffraction pattern for carbon is shown in figure 6, for a polycrystalline specimen of thickness 6 nm, with a density of $\approx$22 atoms/nm^3. By averaging over several such calculated patterns, the calculated I(s) can be obtained, and compared with the kinematical (ie single scattering) I(s), suitably broadened with the shape function (figure 6). In this way, the effects of multiple scattering on I(s), and hence on G(r), are being investigated for model single-element and alloy systems. The results have been compared with the Blackman curve[1,17], which predicts the extent to which multiple scattering causes I(s) to deviate from the single scattering value (to be published).

Conclusion

Nearest neighbour distances and coordination numbers can be obtained from small volumes of material using electron diffraction techniques in an electron microscope. The technique is rapid, giving the information on-line in a few minutes. For single element materials the technique gives

nearest neighbour distances accurate to 0.001nm, and accurate coordination numbers. For alloys, results are sufficiently accurate to differentiate between alternative structural models; but for more accurate structural studies of alloys, methods similar to those developed for neutron and X-rays, involving partial structure factors, are yet to be developed.

Acknowledgments

Financial support from the Australian Research Council, from DITARD, and from the Universite de Paris-Sud is acknowledged. I appreciate the collaboration with Dr D McKenzie, D Muller, L Hall and V Keast in many of the studies referred to here.

References

1 Bentley, J., Angelini, P., Gove, A.P., Sklad, P.S. and Fisher, A.T., Inst. Phys. Conf. Ser 98(1990)107
2 Grigson, C.W.B., J. Electronics and Control, 12(1962)209
3 Graczyck, J.F. and Moss, S.C., Rev. Sci. Instrumen. 40(1969)424
4 Blackman, M., Proc. Roy. Soc. Lond., A173(1939)68
5 Grigson, C.W.B., Rev. Sci. Instrumen., 36(1965)1587
6 Maher, D.M., Scanning E.M. (Ed O Johari; IITRI; Chicago) (1974)215
7 Bentley, J., Lehman, G.L. and Fisher, A.T., Analytical EM - 1984 (eds D.B. Williams and D.C. Joy) (San Francisco Press; San Francisco) (1984)143
8 Cockayne, D.J.H. and McKenzie, D.R., Acta Cryst., A 44(1988)878
9 Cockayne, D.J.H ., McKenzie, D.R. and Muller, D., Microsc. Microanal. Microstruct., 2(1991)359
10 McKenzie, D.R., Muller, D.A., Kravtchinskaia, E., Segal, D., Cockayne, D.J.H., Amaratunga, G. and Silva, R., Thin Solid Films, 206(1991)198
11 McKenzie, D.R., Cockayne, D.J.H., Muller, D.M., Murakawa, M., Miyake, S., Watanabe, S. and Fallon, P., J. Appl. Phys., 70(1991)3007
12 McKenzie, D.R., Davis, C.A., Cockayne, D.J.H., Muller, D.A. and Vassallo, A.M., Nature, 355(1992)13Feb
13 McQuarrie, D.A., Statistical Mechanics, (Harper and Row, New York, 1976) 264
14 Johnson, R.D., Meijer, G., Salem, J.R. and Bethune, D.S., J. Am. Che. Soc., 113(1991)3619
15 Hall, L. and Cockayne, D.J.H., Micron 24(1993)357
16 Tewes, M., Zweck, J. and Hoffman, H., J. Phys. Condens. Matter, 6(1994)835
17 Cowley, J.M., Diffraction Physics (North Holland, Amsterdam) 1975

High Resolution Electron Microscopy of New Carbon

Y. Ishida, H. Ichinose, T. Kuzumaki, T. Hayashi and K. Ito
Dept. of Materials Science, University of Tokyo, 7 Hongo, Bunkyo-ku, Tokyo 113, Japan

Abstract

Atomic structures of grain boundaries in (1) vapor-grown diamond foil and (2) nanocrystalline carbon 60,and (3) defect structuers in heavily deformed carbon nanotube as well as (4) nanotube fibre reinforced nanocrystalline carbon 60 were examined by high resolution electron microscopy and their influence on the mechanical properties were investigated as part of our efforts to develop the new carbons as engineering materials.

1. Introduction

High resolution electron microscopy has opened new doors of research in a number of high technology materials. New carbon is one of them. The subject,however, should be appropriate with NIRIM, because the researches of new diamond is one of the well known high lights of the Institute.

In the present contribution, we include our recent examination of new diamond as well. The main focus,however,shall be on fullerenes and carbon nanotube,whose defect structures play important roles in defining the mechanical properties of the new carbons.

The examination shall demonstrate the usefulness of high resolution electron microscopy in the study of new carbons. The crucial need of other new techniques such as chemical bond analysis was revealed at the same time for the true understanding of the fine defect structure.

2. Structure of vapor grown diamond[1]

High resolution electron microscopy of vapor grown polycrystalline diamond film deposited on Si of thickness less than 10μm was ion thinned and observed by JEM 2000EX high resolution electron microscope and the electron energy loss spectrum was obtained by JEM 2010 field emission analytical microscope.

The main interest of our study centered on the nature of internal interfaces in the film because the mechanical,electrical and other

interconnection properties of engineering importance are to be infuluenced by them. They could be vital to the future use of the diamond film in electr onic devices and other applications.

The observation showed the film consisted mainly of (111) coherent twin just as was experienced in Si and Ge (Photo.1). Occasionally,however, incoherent and high order twin such as $\Sigma 9$ were observed. The latter high angle boundaries may be produced as the result of the encounter of two $\Sigma 3$ twin systems. It often appears bright, indicating the selective yield of the region to incoming ion during thinning. We concluded that the enhanced thinning of the high order twin region reflects the weakeness of bonding at the interface. High resolution electron energy loss spectroscopy (HREELS)[1] showed that the interface is with π^* component and suggested that the interface region contains dangling bonds of carbon. The combined study of atomic structure and bonding is considered particulaly useful in characterizing the nature of the internal interface in new carbon materials.

3. Sturcture of carbon 60 crystal[2]

Carbon 60 is a fullerene whose structure is most spherical(Fig.2). Higher fullerenes with 12 pentagonal carbon ring distributed widely apart result in structures with 12 pointing corners as deviatious from the sphere.

The spherical molecule crystalizes at room temperature in the form of face centered cubic structure with C60 molecules at the 8 corners and 6 centers of a dice. Photo.2 is a high resolution electron micrograph with elecron beam parallel to [110] of the single crystal. Each white dot is the site of carbon 60 molecules aligned parallel to [110].The molecule is,of course, not sphere but appear round in the photograph because it rotates rapidly at room temperature. The carbon 60 crystal is unique in the mechanical property due to this highly symmetrical crystal sturcture. Face centered cubic structure with many slip planes allow the crystal to deform by a large amount. In the later section the actual extent of the deformation shall be described.

At below 260K,however,where the rotation mode is frozen,the crystal is no more face centerd cubic but tetragonality shows up in the crystal structure and the crystal becomes less ductile.

4. Structure of Carbon Nanotube[3]

Carbon nanotube, discovered by Iijima[4] is a cylindrical high order fullerene which grows in the debris on the anode as a biproduct during

production of carbon 60.

The atomic structure of carbon nanotube is shown in Fig.3, where an atomic monolayer of hexagonal carbon network corresponding to the basal plane of graphite was bent in the form of a cylinder and the two ends were filled with two halves of a spherical fullerene. The hexagonal network is often sheared parallel to the axis so that two or more two-dimentional edge dislocations in the form of pentagon + heptagon carbon ring pairs stay on either end of the nanotube besides the usual number of pentagons(6) on each site of the nanotube. The lack of angularity in a large multilayered fullerene indicated that the spherical crust of the high-order fullerene and the hemi-spherical crust of multilayered carbon nanotube contains a large number of pentagons and heptagons nicely distributed to allow the overall spherical shape of the crust.

Photo.3 is an example of high resolution electron micrograph of a multi-layered carbon nanotube. Large nanotube in the debris of graphite anode are mostly multi-layered.

5. Mechanical properties of carbon 60[5,6].

Mechanical properties of carbon 60, especially the elastic moduli were measured by ultrasonic microscope equipped with burst wave reflection analyzer made by Olympus Optics Co[5].

The measured propagation rates of Rayleigh waves in the {100} and {111} surface layer are shown in the following table.

	m/sec.
(100) [010]	2860
(100) [011]	3380
(111) [011]	3660
(111) [211]	3510

Using these values, the elastic stiffness tensol components were calculated[5] assuming Cauthy relations: C_{11}=13.1GPa, $C_{12}=C_{44}$=8.8GPa, G=6.2GPa, E=15.4GPa and ν=0.25.

The above values agree with the value E=20GPa measured by the ultrasonic resonance method and indicated carbon 60 is rather weakly bonded. Micro-Vickers hardness values were {100} 14.8Hv and {111} 18.8Hv[6], which is below those of pure Au. The compression tests of single crystals by micro-tensile tests (Fig.4)indicated the presence of yield and work hardening. Slip line marks on the surface of the deformed single crystal is shown in

Photo.4[6]. A stereographic analysis of the slip traces showed that the active slip system at room temperature is {111} 〈110〉.

The high resolution electron microscopy of the deformed carbon 60 crystal showed dislocation extended into partials on {111}.

In order to increase the ductility of carbon 60, the nanocrystalline aggregate was produced by vapor condensation on substrate cooled by liquid nitrogen in the inert gas atmosphere. Photo.5 shows an example of such nanocrystalline aggregate produced by vaporization in Helium at 10 Torr[7]. The average diameter of the nanocrystal changes not only by the gas pressure but also by the shape and size of the apparatus indicating the gas flow during the vaporization influences the diameter. The nanocrystalline powder was compacted by uni-axis compression of 13.5MPa in vacuum at room temperature. Thin sheet specimen of thickness 1mm was produced. The X-ray spectrum may be compared with those of coarse grained polycrystalline specimen(grain diameter $\sim 5\mu m$)in Fig.5. Lack of 〈110〉 component nomal to the specimen sheet in nanocrystalline specimen in contrast to that of polycrystalline specimen indicated that the nanocrystalline specimen compacted without crystalline slip deformation. The room temperature hardness of the nanocrystalline specimen was lower than that of polycrystalline specimen. The tensile stress-strain curve of the thin sheet specimen at room temperature is compared with those of single crystalline and polycrystalline C60 specimens[7] in Fig.6. The nanocrystalline specimen was most ductile and the work hardening rate comparable or below that of single crystalline C60. The Fig.6 suggested that superplastic behavior of fine crystalline aggregate operates even at room temperature in carbon 60. In metals and ceramics, superplastic behavior has been observed only at elevated temperatures at about $0.5T_m$ where T_m is the melting temperature.

6. Mechanical properties of carbon nanotube[8]

Carbon nanotube is a kind of whisker,so that an extremely high tensile strength and zero plasticity is generally anticipated. A multi-layered nanotube could exhibit a macroscopic plasticity where after the fracture of the surface utmost layer,pull out of inner tube layers may occuer requiring a certain low stress equivalent to the shear stress parallel to the graphite basal plane. Motion of a pentagon-heptagon carbon ring pair,which is virtually a two-dimensional edge dislocation is generally not expected to operate because it requires the break of a C-C bond of energy $\sim 4eV$.
In fact,carbon nanotubes observed in the anode debris are mostly straight. Spiral carbon nanotubes,however,have been reported occasionally with the

nanotube prepared by catalytic decomposition of organic vapors at above 600℃[9]. All the non-cylindrical shape require pentagonal or heptagonal carbon rings in the networks. Possible movement of the pentagon-heptagon pairs mentioned above couldn't be excluded with such nanotubes.

Our present experiment proved the movement is the crucial issue[8]; Photo.6 is electron micrograph deformed nanotubes found in the anodic debris crushed heavily in the agate mortar. Curved nanotubes were observed, while no example of fracture was obtained. The brittle fracture of nanotube utmost surface layer at room temperature has been disproved by the experiment. The deformation observed instead was bending of the nanotubes. High resolution electron microscopy (Photo.7) showed that the deformation is buckling of inner compressive side of the nanotube. Whether the buckling is the process involving the nucleation of pentagon-heptagon pair in the hexagonal carbon network of the cylindrical nanotube wall or just the bending of the hexagonal network is an important issue to predict if the buckling process is reversible or irreversible.

A bar and ball model of the atomic structure shown in figure 7 seems to support bending model over the pentagon-heptagon pair type disclination model. If the bending model is correct, the reversing process could show an ideal tensile stress-strain curve as a fibre, because the buckling is a shrinkage of the region[10] (Fig.8). The snake shaped nanotube predeformed by alternative buckling can elongate by consuming individual bucklings one by one starting from weak ones,which statistically produces quasi-continuons increase of the stress with strain similar to work hardening of the annealed metals. At the end ,however,unlike metals the work hardening does not saturate but steep increase of strength results when all the buckling units were consumed so that the nanotube returns to it original straight shape. Whether or not this ideal mechanisum is correct awaits experimental verification,but it surely lead us to ponder what would be the ideal stress-strain curve in materials.

7. Mechanical properties of carbon nanotube fibre-reinforced carbon 60[11]

The issue of the nanotube deformation mechanisum awaits a more detailed study. The engineering of the carbon nanotube,however, can proceed because the material has been proved ductile. The use of nanotube as the fibre to strengthen carbon 60 or soft metals has been suggested. In the past,carbon fibre/Al composite has met an unfortunate fate. Aluminium carbide Al_4C_3 needles were found to grow on the surface of the carbon fibre and a drastic decrease of the strength resulted.

High resolution electron microscopy proved that Al_4C_3 needles grow into carbon fibre forming a sharp notch in the case of less graphitized high strength fibre[12]. The invasive growth,however,is rather limited and only epitaxial on the outer surface of the highly graphitized high elasticity fibre where no notch effect is suspected. The high resolution electron microscopy revealed that the interface between the fibre and the carbide needle was often found fractured by the thermal stress unrelieved during cooling of the composite because both the fibre and the carbide needle are brittle. In contrast the thermal stresses in the metal/fibre and metal/carbide interfaces must have been relieved by the ductility of metal.

The carbon fibre/carbon 60 system is free from such a chemical reaction induced problem but the manufacturing without damage to the carbon fibre is still difficult. The carbon nanotube/carbon 60 system can be produced simply by extrusion instead. Photo.8 is an example of such composite,where the alignment of nanotube is achieved by the extrusion of the composite in a silver sheath[11]. High resolution electron micrograph showed that the carbon nanotubes are defect free in the as extruded composite. The matrix carbon 60,however,was nanocrystalline suggesting a good ductility at room temperature.

8.Concluding remark

High resolution electron microscopy has proved powerful in understanding the mechanical properties of new carbons and the composites. Since carbon can assume almost infinite structures and by no means limited to diamond film,carbon 60 and nanotubes ,the challenge of high resolution electron microscope continues. The challenge tends to become tougher as a more detailed advanced design of carbon materials is developed in order to meet increasing demands in industry for higher performances.

Acknowledgment

The authors thank Dr.Y.Bando at NIRIM for the use of the analytical electron microscope,Mr.T.Endo at Olympus Optics Co.Ltd. for the use of the supersonic acoustic microscope,Mr.H.Kobayashi at Showa Electric Wire & Cable to extrude the composite and other members of the laboratory in cooperating the production of carbon 60 and nanotube. The first author thank sponsorship of a Grant-in-Aid for Scientific Research,the Ministry of Education,Science and Culture,Japan for the researches.

【References】

1. H.Ichinose,Y.Zhang,K.Ito,Y.Ishida and O.Nakanose: JIM. Annual Lecture Meeting,1077(1994,10)(in Japanese)
2. T.Kato,K.Suenaga,T.Takayama,K.Ito and Y.Ishida:Trans.JIM.57(9)1101(1993) (in Japanese)
3. T.Kuzumaki,T.Hayashi,H.Ichinose,K.Ito and Y.Ishida:Proc.JIM. Annual Lecture Meeting,131 (1994,10)(in Japanese)
4. S.Iijima:Phys.Rev.Lett.,56,616(1986)
5. T.Kato,S.Tanaka,K.Ito and Y.Ishida:Trans JIM.(to be published)
6. K.Suenaga(Ph.D. thesis 1994)
7. K.Suenaga,M.Tanaka,T.Kato,Y.Takayama,K.Ito and Y.Ishida:Trans. JIM 57(9)1103(1993)(in Japanese)
8. Y.Ishida,T.Hayashi,H.Ichinose,T.Kuzumaki and K.Ito:Proc.ICEM13-Paris, 3,9(1994)
9. S.Amelincks,X.B.Zhang,D.Bermaerts,X.F.Zhang,V.Ivanov and J.B.Nagy:Science 257,635(1994)
10. Y.Ishida(to be published)
11. T.Kuzumaki,K.Ito and Y.Ishida:Proc.JIM,Annual Lecture Meeting(1995.4) (in Japanese)
12. Y.Ishida,H.Ichinose,J.Wang and T.Suga:Proc.46th,EMSA,728(1988)

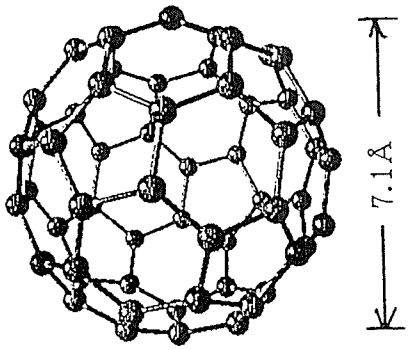

Fig.2 C60 cluster

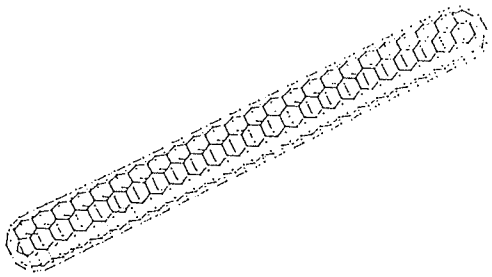

Fig.3 The atomic structure of carbon nanotube

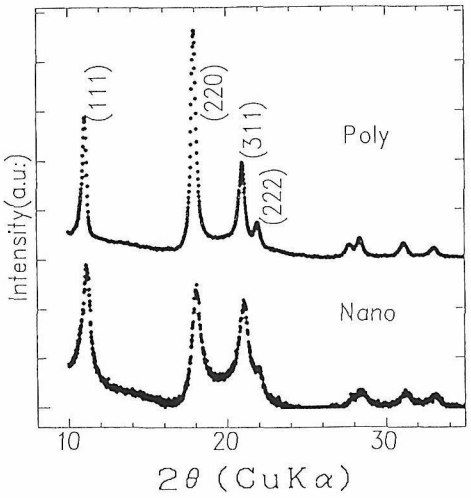

Fig.5 X-ray spectrum of the specimen

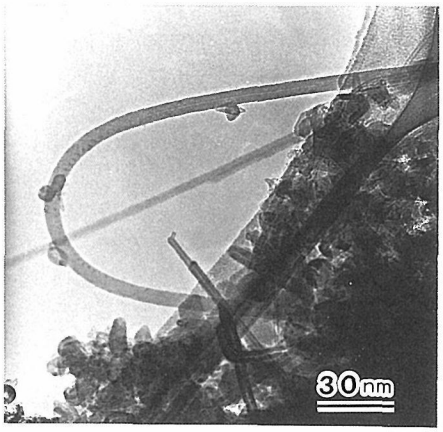

Photo.6 Electron micrograph of deformed nanotube

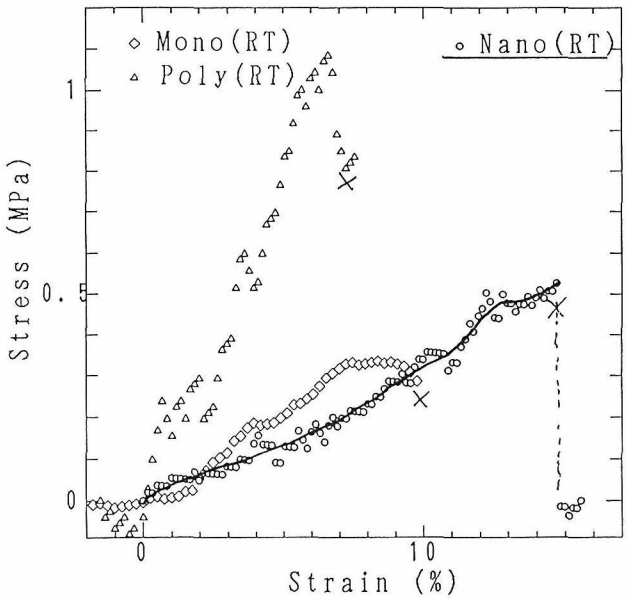

Fig.6 Tensile stress-strain curve of the specimen

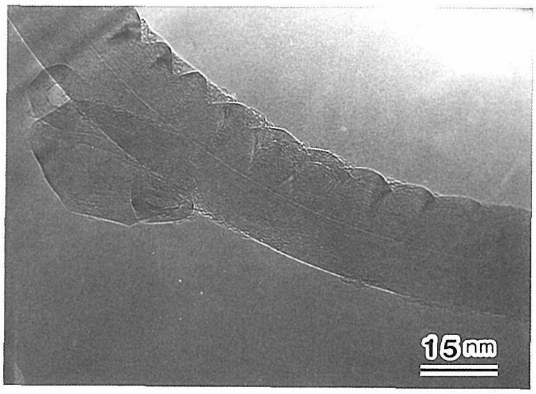

Photo.7 High resolution elecron micrograph of deformed nanotube

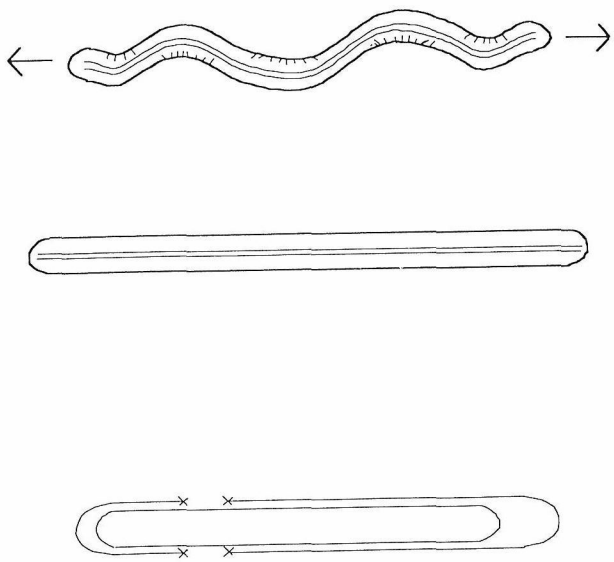

Fig.8 A possible mechanism of ductility for a multi-layered nanotube

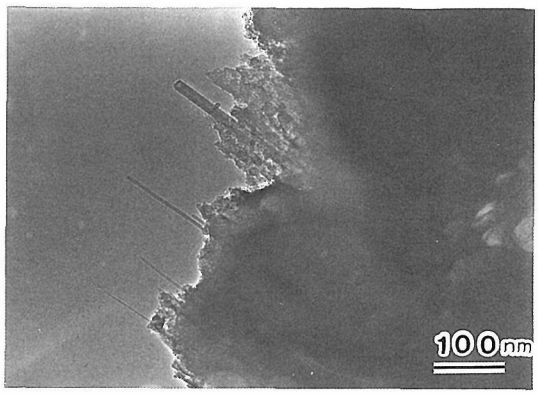

Photo.8 Electron micrograph of the composite

Structure Investigation of High Pressure Phases in W-O System by High Voltage HRTEM

N.D. Zakharov

Max-Planck-Institut für Mikrostrukturphysik, Weinberg 2, D-06120 Halle, Germany

Permanent Address: Institute of Crystallography, Russian Academy of Sciences, Leninsky, pr.59, 117333 Moscow, Russia

Abstract

The abilities of high voltage high resolution electron microscopy for unknown crystal structure analysis were demonstrated. Three new structures of tungsten oxide synthesized under high pressure (T=1773 K, P=$50 \cdot 10^5$ kPa) were revealed. Two new phases I and II with unit cell dimensions a=0.6386(9) nm, b=1.043(5) nm c=0.38(1) nm (V=0.2531 nm^3, space group *C222*, Z=2) and a=1.035(5)nm, b=1.399(5)nm, c=0.378(1) nm (V=0.5473 nm^3, space group *Pbam*, Z=4) have the composition W_3O_8. The structure of the third phase belongs to space group *Pbam* or $P2_12i2$ having the following unit cell parameters: a=2.1431(9), b=1.7766(7), c=0.3783(2) nm, V=1.44 nm^3, Z=32. The new phases revealed show that the structure of tungsten oxides is rather sensitive to external high pressure. The phase transition $W_3O_8(I) \leftrightarrow W_3O_8(II)$ is accompaned with the transformation of pentagonal bipyramids into the groups of edge-sharing octahedra without changing of stoichiometry, giving rise to the free energy variation $\Delta F = P \cdot \Delta V = 0.027$ eV/at. Thus, the application of high pressure can facilitate the new phase formation and additional reduction of the sample.

Introduction

The electrons are scattered by matter approximately 10^4 times severely than X-rays are. This advantage (and disadvantage at the same time) is effectively used for chemical and structural microanalysis. In X-ray and electron diffraction experiments the intensities of diffracted beams can be measured while their phases remain unknown. Thus the main problem in X-ray crystallography is to find out these phases. Fortunately, electrons can be focused by magnetic and electrostatic lenses, providing a possibility for diffracted electron beams to interfere at each point in the image plane in consistent with their amplitudes and phases. It makes it possible to solve, at least partially, the phase problem appeared in diffraction experiments. For the structure determination thin enough ($t<t_{max}$) specimen regions should be used where the image contrast can be interpreted in terms of structure projection. The thickness t_{max} depends on the accelerating voltage $\mathbf{t_{max} \sim V^{1/2}}$ and atomic number $\mathbf{Z}$ ($\mathbf{t_{max} \sim Z^{-4/3}}$) [1]. It gives very approximately $\mathbf{t_{max} \sim V^{1/2} Z^{-4/3}}$. Hence, for structure determination an accelerating voltage as high as possible should be preferred, especially for the materials with high **Z**. However, there are limitations imposed by radiation damages. If the energy of electrons is high enough, they may kick out atoms from their positions in the crystal lattice. Besides, the electron dose needed to get the high resolution image of the structure severely depends on resolution level d_r and image contrast p. Indeed, the atomic scattering amplitude can be approximated at $f(u_r)=f_0A/u_r=f_0Ad_r$ where A is a constant. Hence the number of electrons scattered at u_r and hitting the image element $d_r \cdot d_r$ during the exposure time t_e should be proportional to $N \sim 2\pi f_0^2 A^2 d_r^3 t_e = 2\pi I_0 A^2 d_r^3 t_e$, with I_0 being primary electron beam intensity. On the other hand, the number of electrons per image element required to detect contrast p must be larger than k^2/p^2 [2], where k=5. As a result, the intensity of primary electron beam I_0 should be higher than $k^2/(2\pi A^2 d_r^3 t_e p^2)$. Thus the I_0 has to be increased drastically as the resolution d_r is improving and/or image contrast p is decreasing. This means that each particular object can be characterized by the highest resolution limit, determined mainly by the strength of the chemical bonds, the atomic number, thermoconductivity, and specimen preparation. From this point of view crystal structures of ionic, covalent and metallic types of bonding are characterized by the highest resolution limit. This limitation is a price we should pay to obtain information about the structure of a material at atomic resolution.

One of the most characteristic features of the oxides is the presence of the cation sublattice with distances between cations varying in the range 0.3-0.4 nm. These distances are large enough to resolve the cation sublattice in electron microscope. Besides, there is a grate variety of oxides stable enough under the electron beam to be investigated in high voltage electron microscope. All these features make oxides rather convenient objects for HRTEM investigations. Plenty of transition metal oxide structures were determined by HRTEM even when the resolving power of microscopes was insufficient to reveal individual cation positions [3,4]. The situation improved drastically when the high-voltage high resolution microscopes were developed and heavy atom positions could be reliably resolved [5,6]. The point-to-point resolution of modern electron microscopes is close to 0.1 nm which very often is high enough to determine the atomic structure of very small crystalline fragments several nanometers in diameter. This level of resolution enables us to obtain images of structure projections not only in the direction of highest symmetry, which is extremely important when we are dealing with three dimensional unknown structures with a≈b≈c. As an example of HRTEM application to structure analysis the phase transformations in binary W-O system under high pressure conditions will be described.

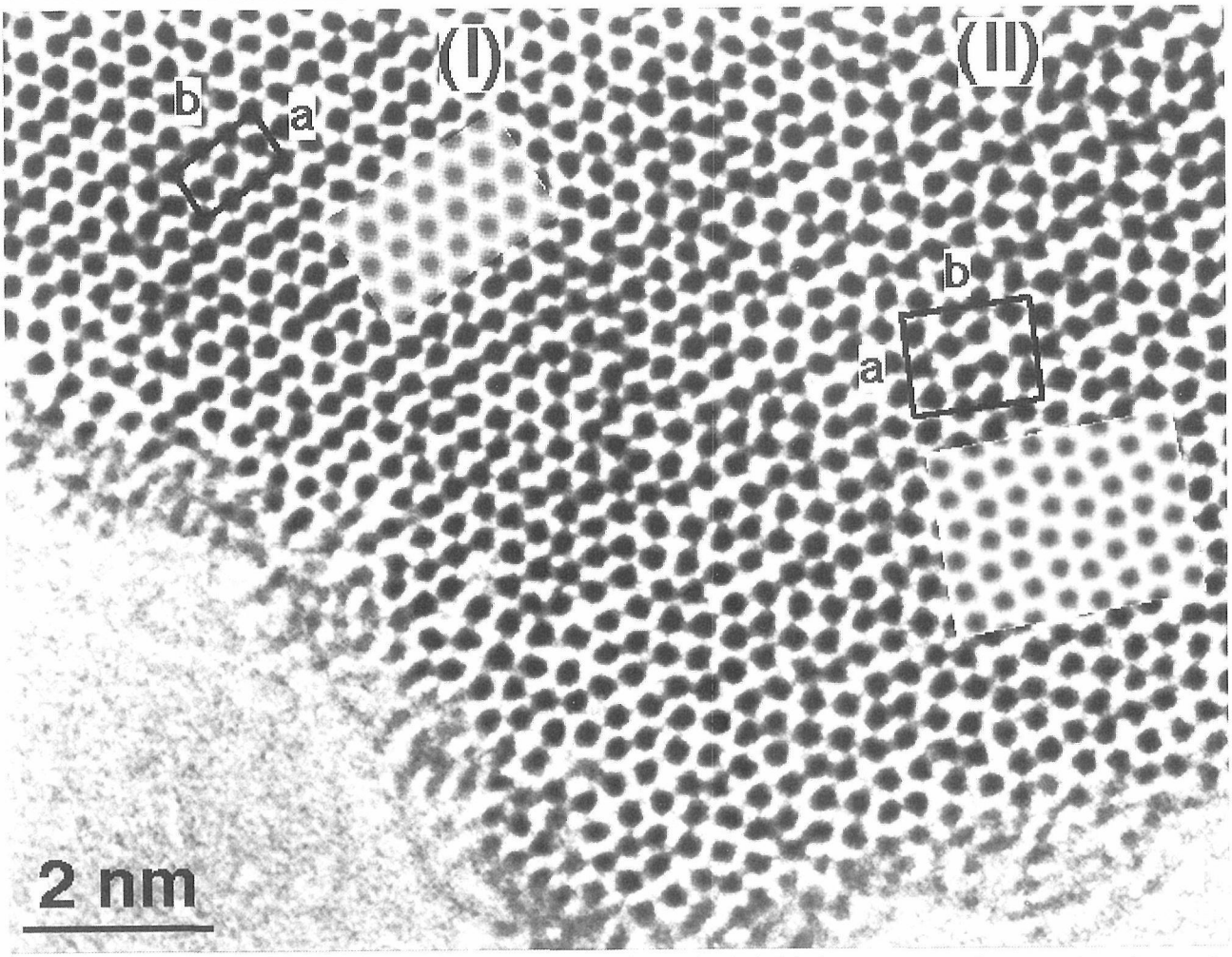

Fig.1. [001] HRTEM image of W_3O_8(I) and W_3O_8(II) high pressure phases. Accelerated voltage 400 kV. Computer simulated images are inserted.

Products obtained by the reduction of tungsten trioxide at ambient pressure have been extensively investigated both by X-ray diffraction and electron microscopy techniques. Four structure types have been reported for WO_x within a $3 \geq x \geq 2.6$ region [7-14]. Two of them consist of slabs of corner-sharing WO_6 octahedra running in two dimensions and separated by crystallographic shear (CS) structures in the third one. In the CS structures the WO_6 octahedra form a groups of four ({102} CS structure) or six ({103} CS structure) edge-sharing octahedra. Two other structures, i.e. $W_{12}O_{34}$ and $W_{18}O_{49}$, are built up of WO_6 octahedra and WO_7 pentagonal bipyramids. Approximately four years ago an investigation of high pressure influence on the

structure of transition metal oxides was started at the Institute of High -Pressure Physics of the Russian Academy of Sciences. It was shown that even at relatively low pressure (about $P=50\cdot10^5$ kPa) new reduced WO_x phases were formed [15,20].

Experimental

The samples were prepared by partial reduction of WO_3 with carbon at high temperature in combination with high pressure. The reaction occurred between the graphite container and a pressed tablet of WO_3 in closed system ($T=1773$ K, $P=50\cdot10^5$ kPa). X-ray analysis was carried out with an powder diffractometer HZG-4, using Ni-filtered Cu $K\alpha$ radiation. A thermogravimetry unit (Q-1500D) was used for analysis of the reaction products.
The electron microscopy specimens were prepared by crashing of a small amount of the sample in an agate mortar, dispersing the resulting fine powder in acetone and putting the received suspension on a holey carbon film. JEOL ARM operated at 800kV, C_s=2 mm (NCEM Berkeley) and JEM-4000EX operated at 400 kV (Halle, Germany) were used. ARM was equipped by top entry goniometer stage making it possible to tilt the object at the maximum angle ±45° what is extremely important for structure investigation.
Positions of tungsten were obtained from the processed images, while the oxygen atoms were introduced into the structure models by consideration of cation coordination and interatomic (W-W, W-O and O-O) distances.
The DigitalMicrograph 2.0 software was used for image filtration and processing. Images were scanned by CCD TV camera from the negatives. Theoretical images of crystal structure were simulated with the help of MacTempas program [21].

Structure of W_3O_8

X-ray powder diffraction and electron microscopy reveal the presence of two unknown WOx phases I and II with unit cell dimensions a=0.6386(9) nm, b=1.043(5) nm c=0.38(1) nm (V=0.2531 nm^3), space group *C222*, Z=2 and a=1.035(5)nm, b=1.399(5)nm, c=0.378(1) nm (V=0.5473 nm^3), space group *Pbam*, Z=4 respectively [15]. Fig.1 shows the intergrowth of these two phases. In the image of phase I a pseudo hexagonal arrangement of black spots corresponding to cation positions can be seen. Analysing observed contrast the model of structure was deduced (Fig.2a). The O-atom positions were located in the proposed model by consideration of interatomic (W-O) and (O-O) distances. The shortest W-W distance is 0.34 nm and W-O distances are in the range 0.185-0.26 nm. The framework of polyhedra corresponds to stoichiometry W_3O_8 and space group *C222*. The computer simulated image of this structure is in a rather good agreement with experimental one (Fig.1, insert). The W_3O_8(I) structure (Fig.2a) is built up of WO_6 octahedra and WO_7 pentagonal bipyramids sharing corners and edges in the (001) plane. Along a axis the WO_7 pentagonal bipyramids are linked by edges forming zig-zag chains. In b direction these chains are mutually connected by corner-sharing and additional WO_6 octahedra. The structure is isotypic with that of U_3O_8 [16] and the high-pressure modification of Nb_3O_7F [17].

The structure model of phase II is shown in Fig.2b. There is a good agreement between the experimental image and the simulated one (Fig.1, insert). This structure is built up of groups of four edge-sharing WO_6 octahedra (shown by black color in Fig.2b) and has the same as phase I composition W_3O_8. Similar but more regular groups of four edge-sharing WO_6 octahedra have been previously observed in the {102} CS structure of WO_{3-x}, $0<x<0.07$ (Fig.2c) [18,19].

Analysis of derived structure models shows that one structure can be easily transform to another by small metal and oxygen atoms displacements without stoichiometry changing. The model of interface boundary is shown in Fig.2 d. The two phases do not appear in the binary W-O system at ambient pressure. The structure W_3O_8(I) (density γ = 86.65 at/nm^3) is about 7,6% denser than W_3O_8(II) one (γ =80.32 at/nm^3). Annealing of this specimen at ambient pressure and T>573 K gives rise to phase transformation W_3O_8(I) =>W_3O_8(II). At higher annealing temperatures T>1073K in turn the phase W_3O_8(II) decompose into the $W_{18}O_{49}$ and WO_2. Thus, the intermediate stage of phase transition W_3O_8(I) =>W_3O_8(II) is observed in Fig.1. It occurred by movement of interface between these two phases due to small displacements of atoms.

Structure of $WO_{2.65}$

At the higher extent of reduction under high pressure condition another type of structure containing pentagonal columns was observed [20]. It belongs to space group *Pbam* or $P2_12_12$ and has the following unit cell parameters: a=2.1431(9), b=1.7766(7), c=0.3783(2) nm, V=1.44 nm^3, Z=32, D x=8.33g cm^{-3}. The image of this structure is shown in Fig.3 a. The

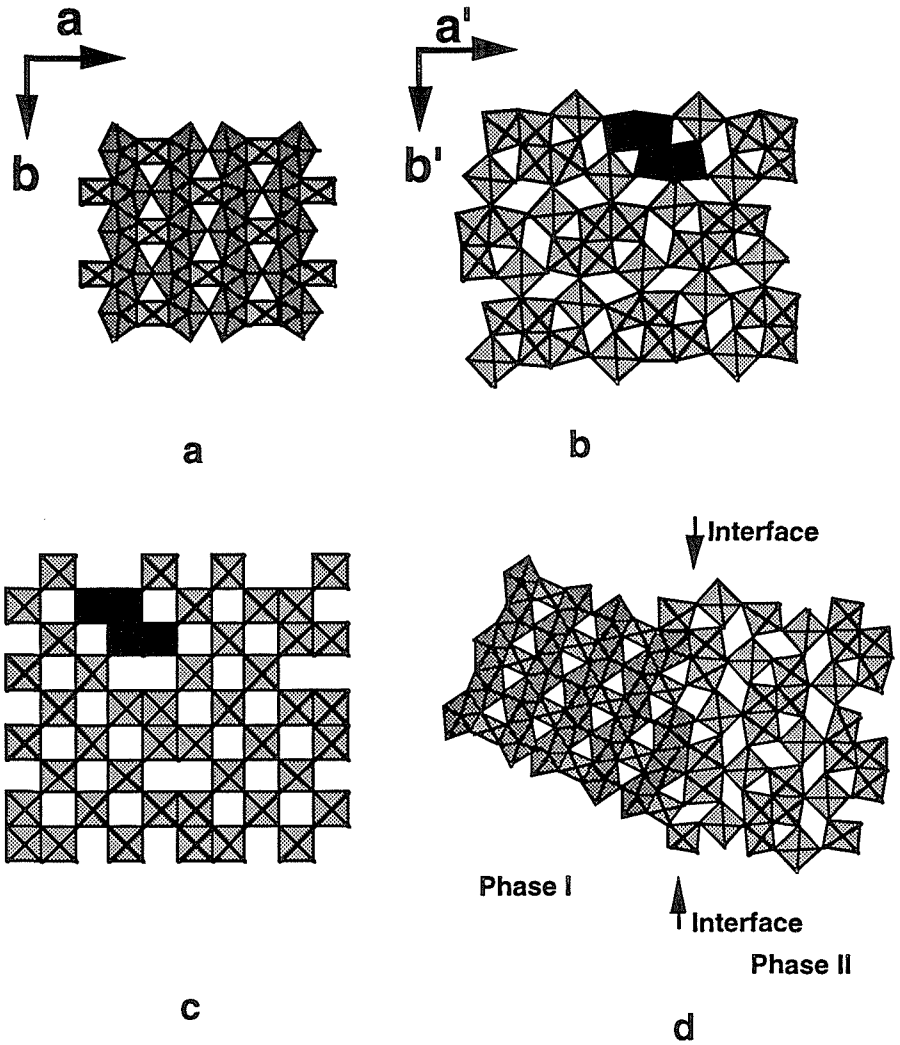

Fig.2. (a,b) Models of crystal structures W_3O_8(I) and W_3O_8(II). (c) Model of {102} CS structure in W_8O_{23}. Groups of four edge-sharing octahedra in b,c are marked by black. (d) Structure of the interface between two phases W_3O_8(I) and W_3O_8(2).

calculated image (Fig.3 b) is in a rather good agreement with experimental one supporting proposed model of structure (Fig.5 a). The framework of the polyhedra corresponds to the stoichiometry W_8O_{21} ($WO_{2.625}$) and density γ = 80.38 at/nm^3. It formed by the blocks of 2x4 corner-sharing WO_6 octahedra, edge-sharing octahedra and WO_7 pentagonal bipyramids. The composition of this phase is rather close to $W_{18}O_{49}$ one ($WO_{2.72}$, γ = 76.16 at/nm^3) (Fig.4, 5b) [11]. It is obvious that the $WO_{2.625}$ structure can be easily deduced from the $W_{18}O_{49}$ one (Fig.5a,b) by removal only four octahedra (shown by black color in Fig.5 b) and subsequent shifting of two remaining parts of unit cell by 0.53 nm in c direction. This procedure will entail some reduction of the oxide, increasing both the number of pentagonal bipyramids and density of the structure. The presence of both these structures at the same time was observed in the sample slightly doped by Nb (10 at. % Nb). The EDX spectra of these crystals did not reveal any peaks of Nb. There was also no effects of ordering found in the diffraction pattern. But the ratio of unit cell parameters a/b=1.303 differed from that quoted in the literature (a/b=1.261,[11]). It means that only small amount of Nb was incorporated in this structure statistically.

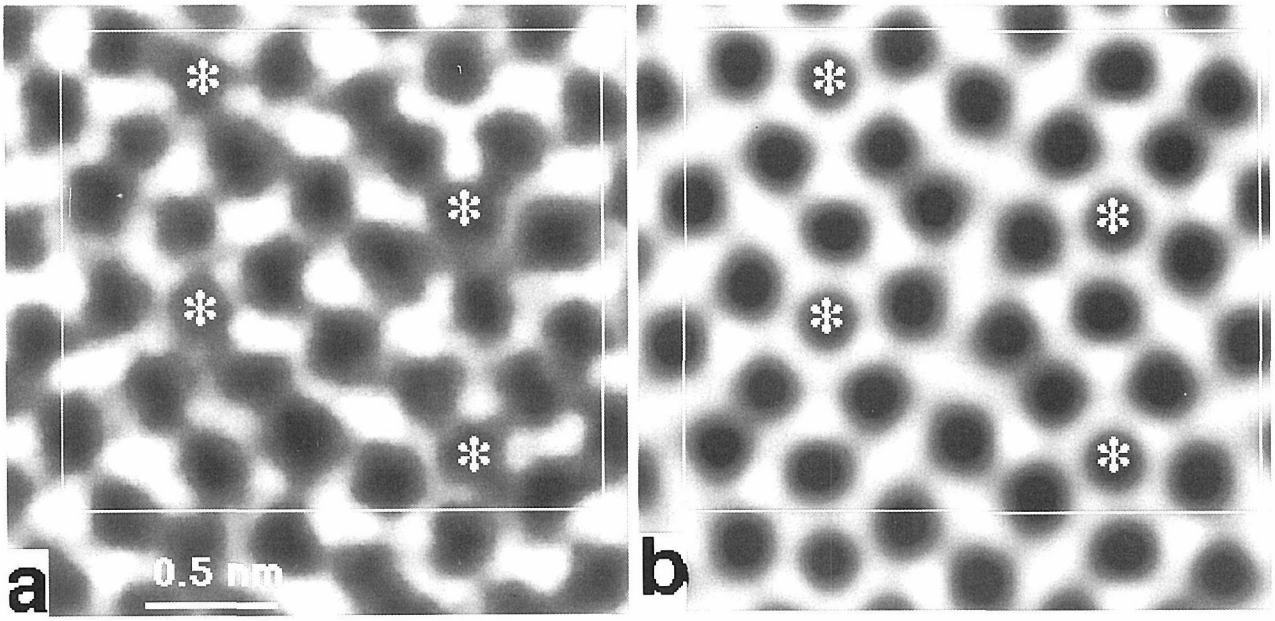

Fig.3. [001] experimental (a) and theoretical (b) images of the $WO_{2.625}$ high pressure phase. Pentagonal columns are marked with asterisks. Accelerated voltage: 800 kV.

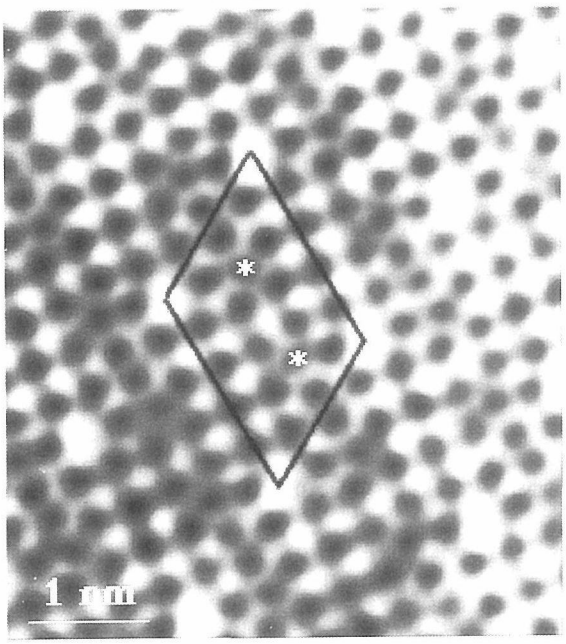

Fig.4. [001] HRTEM image of $(W_{1-x}Nb_x)_{18}O_{49}$ phase ($x<0.1$). Pentagonal columns are marked with asterisks. Accelerated voltage 800 kV.

Conclusions

It was shown that high voltage HRTEM is a very useful tool for investigation of phase transformations between different metastable structures taking place in binary W-O system under high pressure conditions. We could not succeed to receive the structure images of these phases at accelerated voltage 100 kV, because even at the thinnest place of the wedge-shaped crystal the weak phase object approximation was violated so that the image could not be interpreted in terms of structure projection.

The new phases revealed show that the structure of tungsten oxides is rather sensitive to external high pressure applied. The phase transition $W_3O_8(I) \leftrightarrow W_3O_8(II)$ is accompanied with the transformation of pentagonal bipyramids into the groups of edge-sharing octahedra, and vice versa without changing of stoichiometry. It gives rise to the free energy variation $\Delta F = P \cdot \Delta V = 0.027$ eV/at. In the samples grown at ambient pressure these pentagonal columns were observed in an ordered manner at higher extent of reduction than that of CS planes.

The phase transition $W_{18}O_{49} \leftrightarrow WO_{2.625}$ is accompanied by variation of stoichiometry and atom volume at the same time. The variation of the free energy function due to transition:

$WO_{2.72}=WO_{2.625} + 0.095/2\ O_2\uparrow$.

obeys the equation

$F(WO_{2.72})-F(WO_{2.625})=P\Delta V$, or

$$\frac{dF(x)}{dx} = P\frac{dV}{dx} \approx P\frac{\Delta V}{\Delta x} \approx \mu,$$

where Δx, μ are the variations of concentration of oxygen atoms and free energy per oxygen atom respectively. As a result μ= 0.24 eV/at (P= $50\cdot10^5$ kPa=30 eV/nm^3 , ΔV=$0.69\cdot10^3$ nm^3) is obtained. This value is quite close to the enthalpy of {103} shear planes formation in $WO_{2.9}$ (0.28 eV/at) estimated by R.J.D.Tilley [22], who showed that changes in the bonding energy are dominant in this reaction. Thus, the application of high pressure may facilitate the formation of new phases and the additional reduction of the sample.

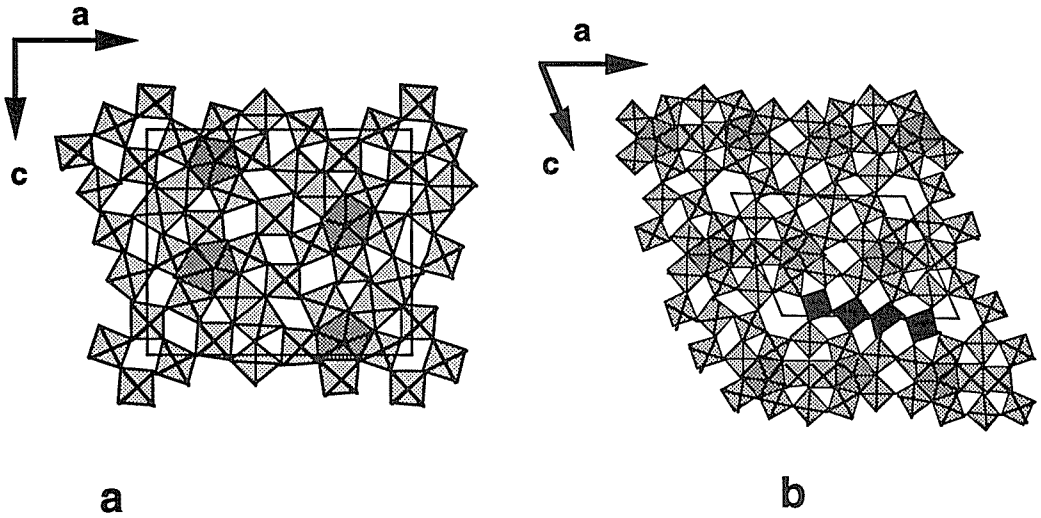

Fig.5. (a,b) Models of crystal structures $WO_{2.625}$ and $W_{18}O_{49}$, respectively.

This study has partly been performed within a Swedish-Russian joint research project. The results of high pressure phase investigations included here were received by Yu.A.Barabanenkov[1], N.D.Zakharov[1], I.P.Zibrov[1], V.P.Filonenko[2], P.Werner[3], M.Sundberg[4].

[1] Institute of Crystallography Russian Academy of Sciences,
[2] Institute of High Pressure Physics of the Russian Academy of Sciences,
[3] Max-Planck-Institut für Mikrostrukturphysik, Halle, Germany;
[4] Department of Inorganic Chemistry, Arrhenius Laboratory, Stockholm University, Stockholm, Sweden.

The use of the facilities at the National Centre for Electron Microscopy at the Lawrence Berkeley Laboratory is gratefully appreciated.

References

1. F.Lenz, Z.Naturforsch (1954) **9A**, 185
2. A.Rose, (1973), Vision Human and Electronic, New York-London, Plenum Press
3. M.Sundberg, Chemica Scripta (1978-1979) **14**, 161
4. W.Sahle and M.Sundberg, Chemica Scripta (1980) **16**, 163
5. N.D.Zakharov, M.A.Gribeluck, B.K.Vainshtein, L.M.Kovba, S.Horiuchi, Acta Cryst. (1988) **A44**, 821
6. N.D.Zakharov, M.A.Gribeluck, B.K.Vainshtein, N.O.Rozanova, K.Uchida, C.Horiuchi, Acta Cryst. (1983) **B39**, 575

7. R.J.D.Tilley, Mater.Res.Bull. (1970) **5**,813
8. M.Sundberg, R.J.D.Tilley, J.Solid State Chem. (1974) **11**, 150
9. R.J.D.Tilley,Chem.Scr. (1978-1979) **14**, 147
10. A.Magnéli, Ark.Kemi (1950) **1**,513
11. A.Magnéli (1949) Ark.Kemi,**1**, 223
12. M.Sundberg,Chem.Commun. Univ. Stockholm (1981) **5**, 1
13. W.Sahle,Chem.Commun. Univ. Stockholm (1983) **4**, 1
14. M.Sundberg,Chem.Scr. (1978-1979) **14**, 161
15. M.Sundberg, N.D.Zakharov, I.P.Zibrov, Yu.A.Barabanenkov, V.P.Filonenko, P.Werner, Acta Cryst. (1993) **B49**, 951
16. A.F. Andersen,Acta Crysta. (1958) **11**,612
17. L.Jahnberg,Chem. Commun. Univ. Stockholm (1971) **13**, 1
18. R.J.D.Tilley, Mater.Res.Bull. (1970) **5**,813
19. M.Sundberg, R.J.D.Tilley, J.Solid State Chem. (1974) **11**, 150
20. Yu.A.Barabanenkov, N.D.Zakharov, I.P.Zibrov, V.P.Filonenko, P.Werner, A.I.Popov, M.D.Valkovskii, Acta Cryst. (1993) **B49**,169
21. R.Kilaas, Proc. EMSA (1987) **45**, 66
22. R.J.D.Tilley, Journal of Solid State Chemistry (1976) **19**, 53

High-Resolution Transmission Electron Microscopy of New Superconductors

Yoshio Matsui[1], Tetsuya Kawashima[1], Eiji Takayama-Muromachi[1], Fujio Izumi[1] and Julio Ramirez-Castellanos[1, 2]

[1)]National Institute for Research in Inorganic Materials, 1-1 Namiki, Tsukuba, Ibaraki 305, Japan
[2)]Institute of Applied Physics, University of Tsukuba, Tennodai, Tsukuba, Ibaraki 305, Japan

ABSTRACT

Crystal structures, superstructures and intergrowth defects of new series of oxycarbonate superconductors, obtained in a Ba-Ca-Cu-C-O system under high-pressure condition, are examined by high-voltage, high-resolution transmission electron microscopy. Superstructures due to ordered arrangements of Cu and CO_3 in the planes sandwiched by BaO layers, are commonly observed. New types of crystal structures, having blocks with three BaO and two (Cu,C)O layers, are also discovered in this system. Planar defects due to local invasions of CO_3 groups into the HgO layers are observed in Hg-Ba-Ca-Cu-O superconductors. "Infinite-layer" types of superconductors also contain CO_3 defects which replace parts of the CuO_2 conduction planes. New series of oxyborate and oxysulfate superconductors are also obtained, and arrangements of BO_3, as well as SO_3, groups are examined by HRTEM.

INTRODUCTION

After the discovery of high-T_c superconductivity in $(La,Ba)_2CuO_4$ system by Bednorz and Muller[1)], various new series of superconductors have been discovered, and high-resolution transmission electron microscopy (HRTEM) often played major roles to elucidate basic structures, defect structures, micro-structures, modulation structures and surface/interface structures of these new superconductors[2-5)]. One of the recent topics in high-T_c superconductivity research is the discovery of oxycarbonate and related "anion-doped" superconductors, which are prepared mainly under high-pressure condition of several GPa. Structures of these new types of superconductors were investigated successfully by HRTEM, and characteristic features on the ordered or disordered arrangements of anion groups have been clarified. For instance, superstructure with $a=2a_t$, $b=a_t$ *and* $c=2c_t$ was found in the so-called (Cu,C)-1212 compound, $(C_{0.5}Cu_{0.5})Sr_2(Y,Ca)Cu_2O_y$[6)], where a_t, b_t and c_t stand for the lattice parameters of the YBCO/123-like substructure, due to ordered repetition of C and Cu along the *a*-direction in each basal plane. More complicated superstructure was found in $TlBa_2Sr_2Cu_2(CO_3)O_y$[7)], in which the central CuO_2 plane of the basic Tl-1223 sub-structure are replaced with CO_3 groups and, crystallographic-shear with shear-planes parallel to (100) planes are introduced with every three (or four) unit cells along the *a*-direction. Similar superstructure was also found in Hg-1223 based

oxycarbonate $HgBa_2Sr_2Cu_2(CO_3)O_y$[8], although the crystallographic-shear planes are found parallel to the (110) planes of the tetragonal substructure. In the Bi-based systems, parts of CuO_2 layers of the conduction blocks can be replaced with CO_3 groups[9]. Partial doping of borate groups, BO_3, was found to be effective to obtain superconductivity in some non-superconducting oxycarbonates[10].

Recently, Kawashima et al.[11-13] discovered a new homologous series of oxycarbonate superconductors in a Ba-Ca-Cu-C-O system and obtained superconductivity at 117K. Basic- and super-structures of the series of compounds are examined by HRTEM[14]. Another anion-based superconductors containing borate (BO_3), sulfate (SO_3) and phosphate (PO_3) groups are also produced by high-pressure technique[15,16]. In this paper, we represent some of the recent HRTEM data on such anion-based new superconductors.

EXPERIMENTAL

Most of the specimens are prepared by high-pressure conditions under 5 GPa, at about 1200 °C for several hours. Sometimes, the oxidizer such as Ag_2O is added in the starting materials, in order to stimulate formations of superconducting phases. It is confirmed, by both EDX and EPMA analysis of the obtained materials, that no Ag_2O remains in the finally obtained superconducting phases. High-resolution electron microscope observations are made by high-voltage electron microscope[17] operated at 800 - 1000kV. Specimen for HRTEM observations are prepared by the crushing method.

RESULTS AND DISCUSSIONS

1 New Homologous Series of Oxycarbonate Superconductors in a Ba-Ca-Cu-C-O System

The compositions of a series of compounds newly found in a Ba-Ca-Cu-C-O system are described by general formula $(C_{0.5}Cu_{0.5})_mBa_{m+1}Ca_{n-1}Cu_nO_y$, where m=1 & 2; n=3, 4 (and 5 for m=2). They are conveniently described as (Cu,C)-m(m+1)(n-1)n. The first m=1 series of materials, $(C_{0.5}Cu_{0.5})Ba_2Ca_{n-1}Cu_nO_y$, show superconductivity at T_c=67K (n=3) and 117K (n=4). They have structures closely related to that of the (Cu,C)-1212 type of oxycarbonate, $(C_{0.5}Cu_{0.5})Sr_2(Y,Ca)Cu_2O_y$[3], while the conduction blocks contain one or two additional Ca and CO_2 layers. The *h0l* electron diffraction pattern of the (Cu,C)-1234 in Fig.1(a) shows weak satellite reflection spots due to double periodicity along both *a*- and *c*-directions. The corresponding [010] HRTEM image in Fig.1(b) shows alternative sequences of white and dark dots in the basal layers and this indicates that ordered arrangements of Cu and C are formed. Almost the similar features of electron diffraction and HRTEM images are observed in (Cu,C)-1223 phase. Structure models of both (Cu,C)-1223 and 1234 superconductors, based on these HRTEM observations, are shown in Fig.2(a) and (b), respectively. It is worth mentioning that Cu and C positions in the neighboring BaO-(Cu,C)O-BaO blocks have "anti-phase" relations to each other. Formations of domains with *a-c* and *b-c* orientations, where domain boundary is (001), are widely

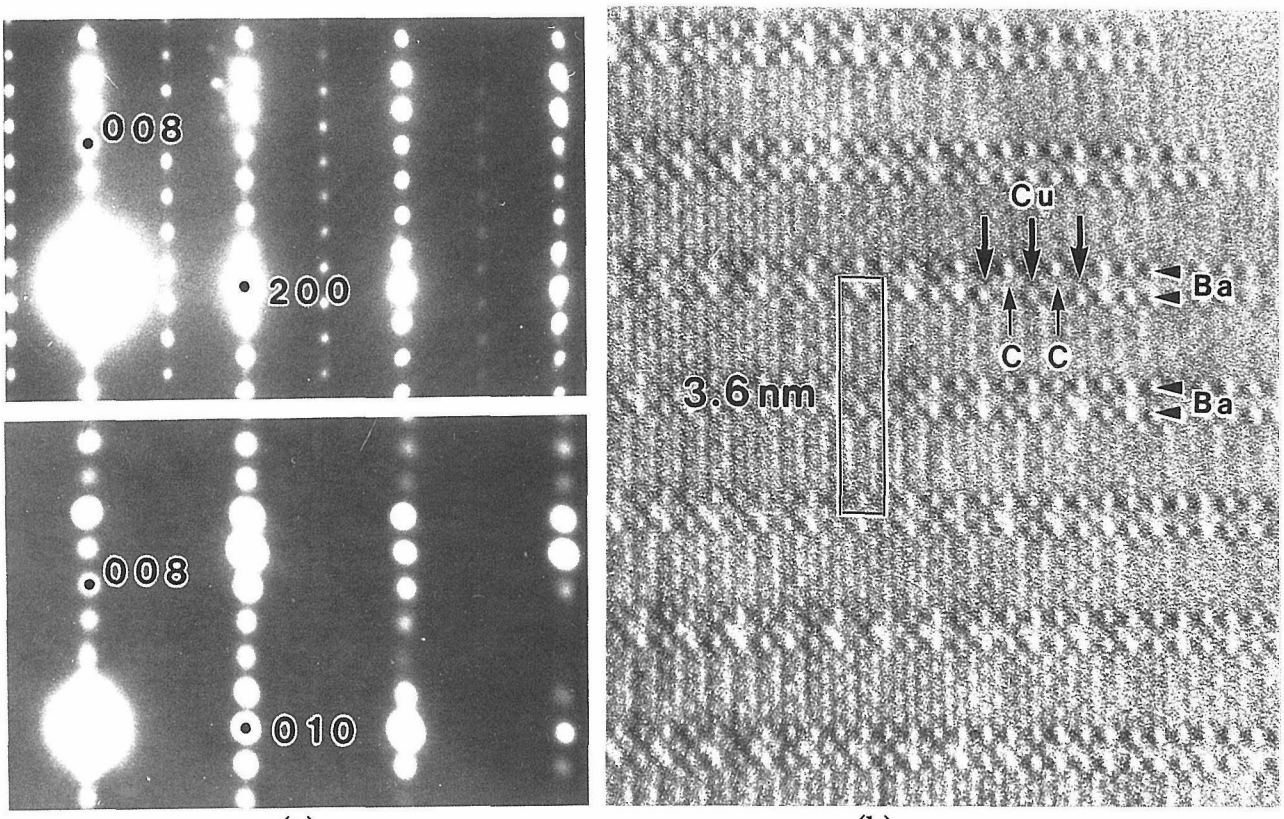

(a) (b)

Fig.1 (a): The *h0l* (upper) and *0kl* (lower) electron diffraction patterns of (Cu,C)-1234 superconductor. (b): The HRTEM image of (Cu,C)-1234 phase, projected in the b-direction.

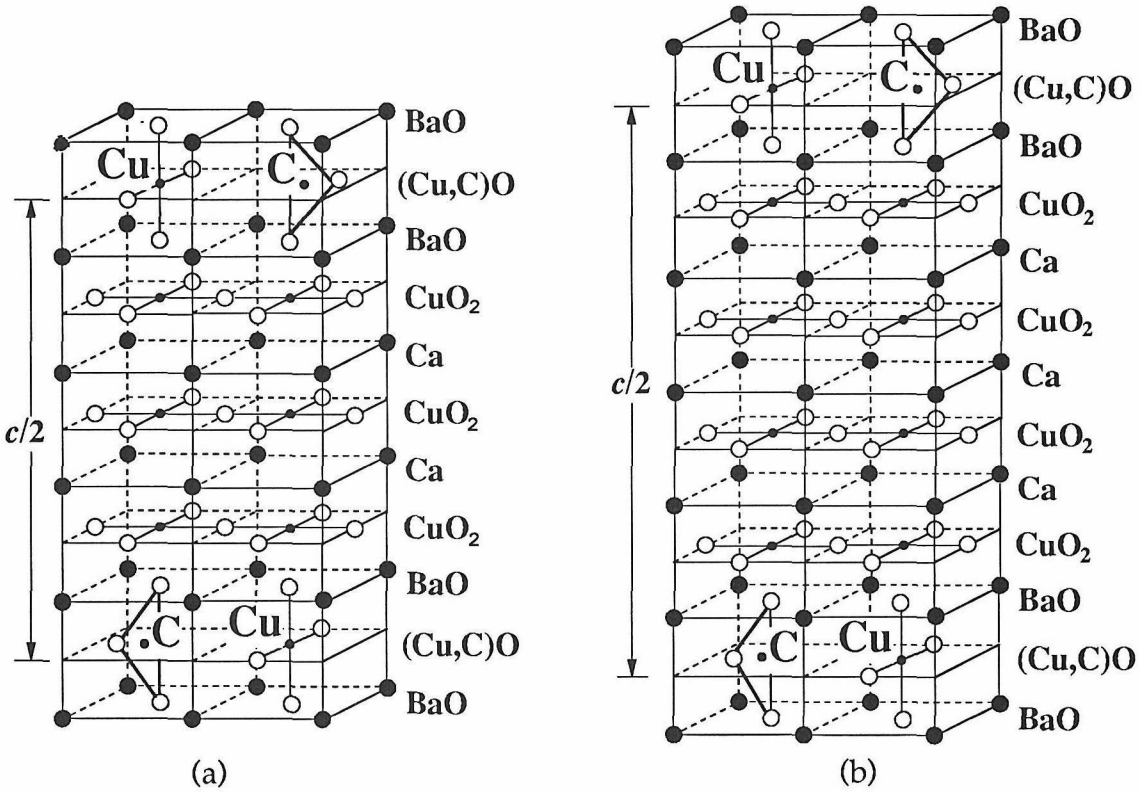

Fig.2 Crystal structure models of (a): (Cu,C)-1223 and (b): (Cu,C)-1234 types of superconductors.

observed. Phases with higher *n*-values, such as (Cu,C)-1245, are not yet obtained as bulk materials.

The second m=2 series of materials, $(C_{0.5}Cu_{0.5})_2Ba_3Ca_{n-1}Cu_nO_y$, also show superconductivity at 91K (n=3), 113K (n=4) and 110K (n=5). They have rather new type of crystal structures with blocks of three BaO and two (Cu,C) O layers. Ordering of Cu and C is also observed in these compounds. The structure models of the three phases are shown in Fig. 3(a) to (c). Besides the three phases with n=3 to 5, the mixed layer compound (Cu,C)-2679 with alternate repetitions of 2334 (n=4) and 2345 (n=5) units was also observed as shown by the *h0l* electron diffraction and HRTEM image in Fig. 4 (a) & (b).

The compounds with m>3 are not yet found as bulk materials in the present stage, but local formations of blocks with 8 and 10 BaO layers are observed in HRTEM image as shown in Fig. 5(a). It may be interesting to note that such structure corresponds to that of the C-1201 phase with c-axis oriented horizontally. HRTEM image of the actual C-1201 superconducting phase[18], which is the first oxycarbonate superconductor discovered by Kinoshita & Yamada[19], is shown in Fig.5(b).

2 Planar Defects in Hg-Based and Infinite-Layer-Based Superconductors Due to Carbonate Invasion

The structures of (Cu,C)-series mentioned above sometimes appear unexpectedly as planar defects in other "oxide" superconductor systems, due to local invasions of carbonate from starting materials such as $BaCO_3$. One typical example of such accidental carbonate defects formed in Hg-based superconductor is shown in Figure 6(a), where the defects due to local formation of (Cu,C)-23(n-1)n structure, mentioned previously, are observed. Defects due to (Cu,C)-12(n-1)n structure was also found locally in Hg-based superconductors, as shown in Fig.6(b).

Another example of planar defects due to carbonate is found in the so-called "Infinite-Layer" type of compound, obtained in Sr-Ca-Cu-O system under high-pressure conditions. Formations of planar defects in this compound were already reported[20] and the models of Cu-deficiency, as well as triple SrO layers with vacancy, are proposed. Recently, we observed HRTEM image of the corresponding planar defects in such IL-compound, as shown in Fig.7(a). Quite weak contrast in the planar defect layer strongly suggest that the defects are produced by replacing some of the CuO_2 layers by CO_3 groups. It is also considered that the CO3 layers are sandwiched mainly by SrO layers. Structure model of the carbonate layer is schematically represented in Fig.7(b).

3 New Oxyborate and Oxysulfate Superconductors

It is found recently that other element such as boron (B), sulfur (S) , phospher (P) can also replace some of Cu sites of the superconductors. For instance, the B-1234 compound, $BSr_2Ca_3Cu_4Oy$ with T_c=100K, was successfully obtained and the structure was examined by HRTEM, as shown in Fig.8(a). No superstructure, as seen in (Cu,C)-series, was observed and therefore it is concluded that the basal-layers are fully replaced with borate groups. Formations of B-1223 structure is also observed in some HRTEM images, but this phase is not yet obtained as bulk materials.

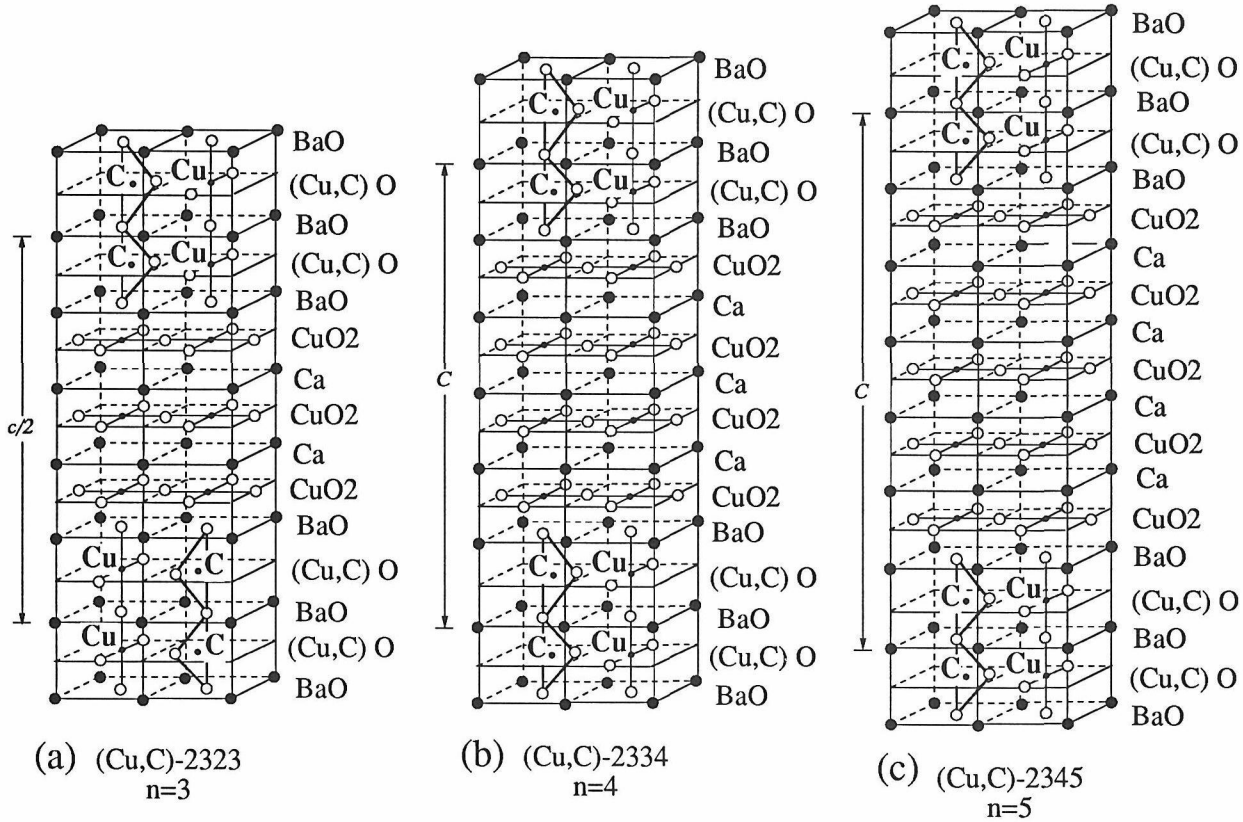

Fig. 3 Crystal Structures of $(Cu,C)_2Ba_3Ca_{n-1}Cu_nO_y$

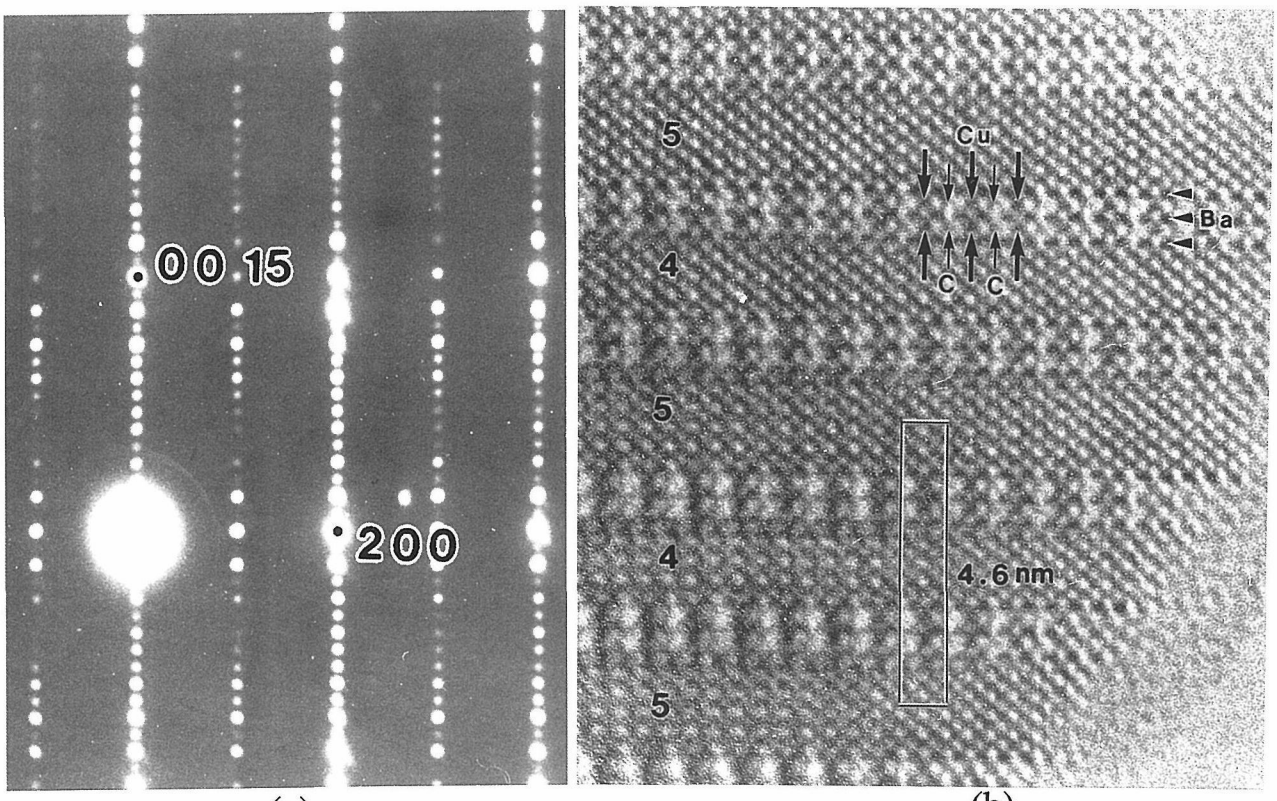

Fig.4. The *h0l* electron diffraction pattern (a), and HRTEM image (b) of (Cu,C)-4679 phase, which consists of alternate blocks of (Cu,C)-2334 and 2345 structures along the *c*-direction.

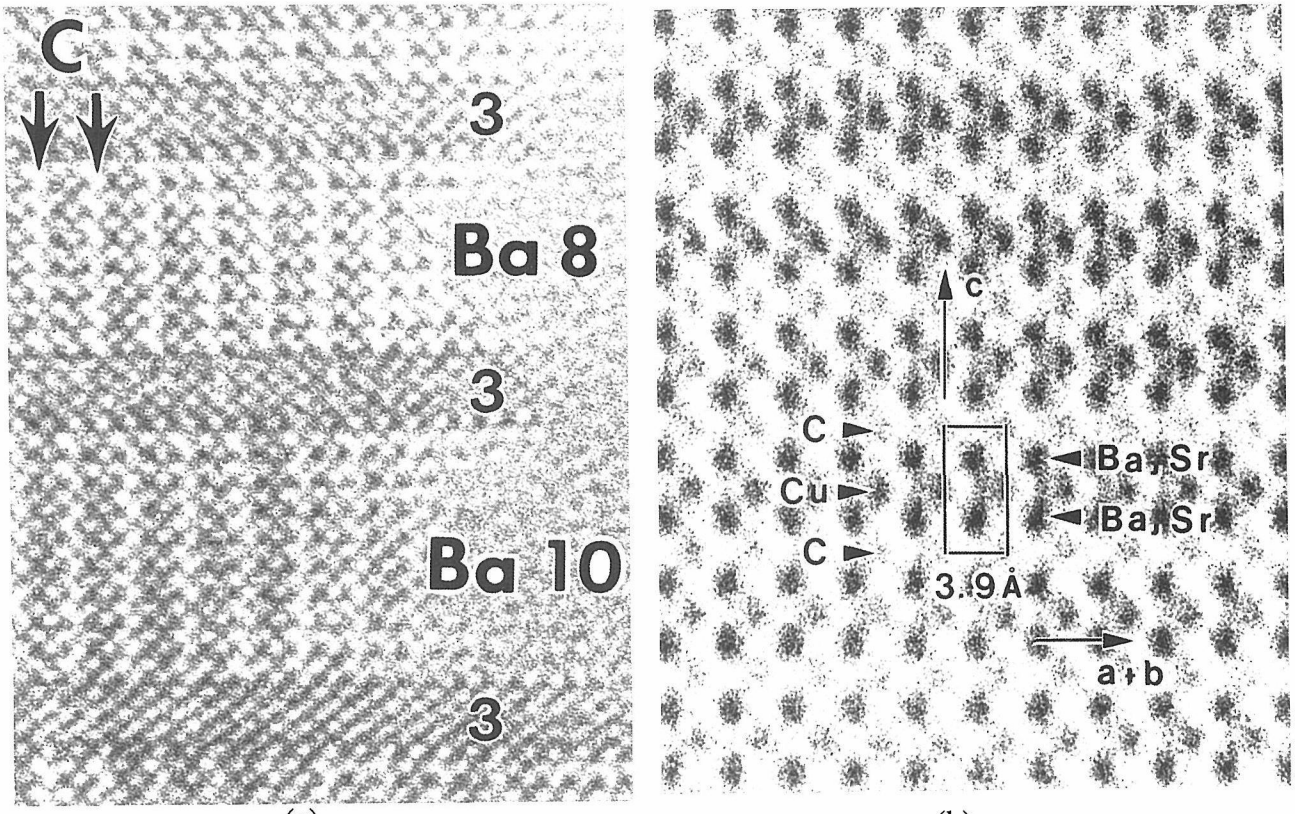

(a) (b)

Fig. 5 (a): HRTEM image of intergrowth of large block with eight and ten BaO layers, observed in (Cu,C)-2323 phase. (b): HRTEM image of C-1201 super-conductor previously discovered by Kinoshita & Yamada[19].

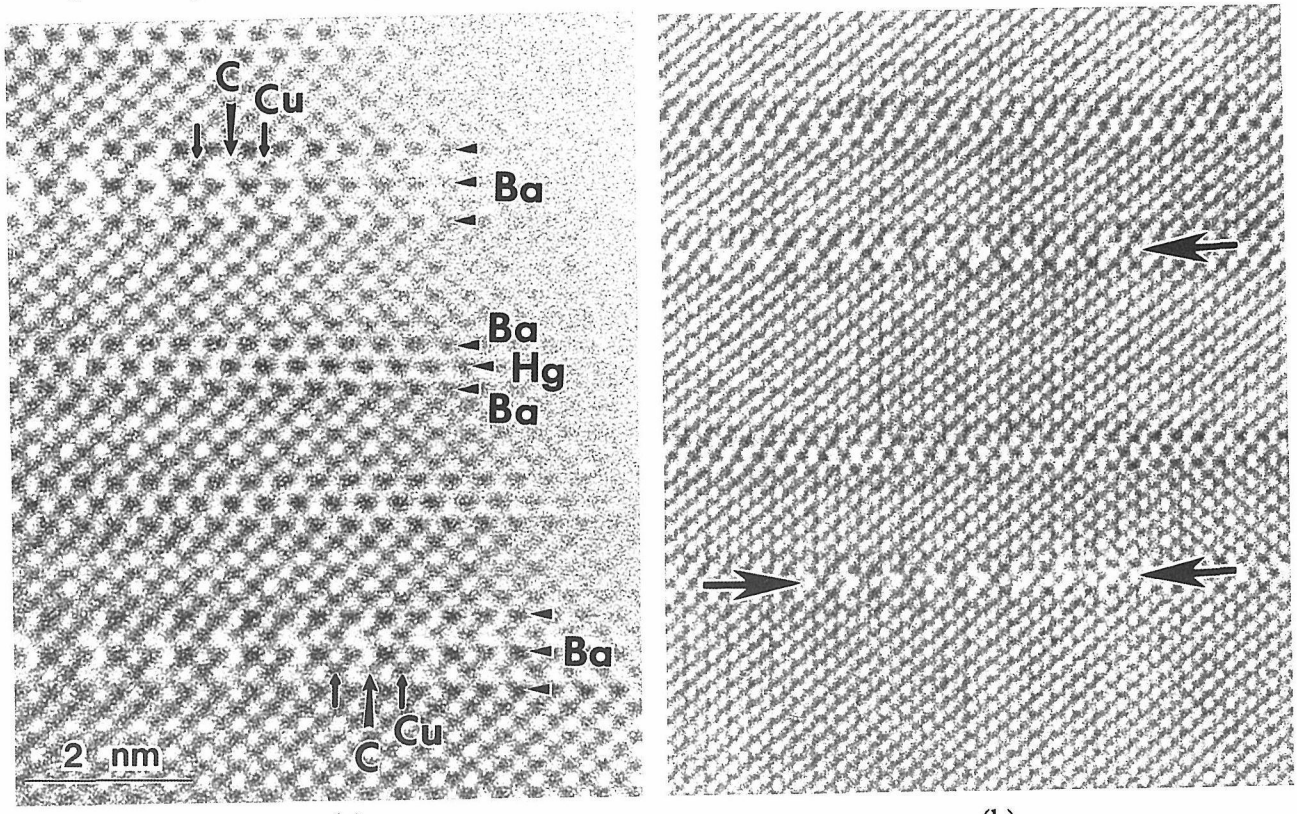

(a) (b)

Fig. 6 Planar defects due to carbonate invasions found in Hg-Ba-Ca-Cu-O superconductor. Defect similar to (Cu,C)-23(n-1)n structures is shown in (a), while that similar to (Cu,C)-12 (n-1)n structure is shown in (b), respectively.

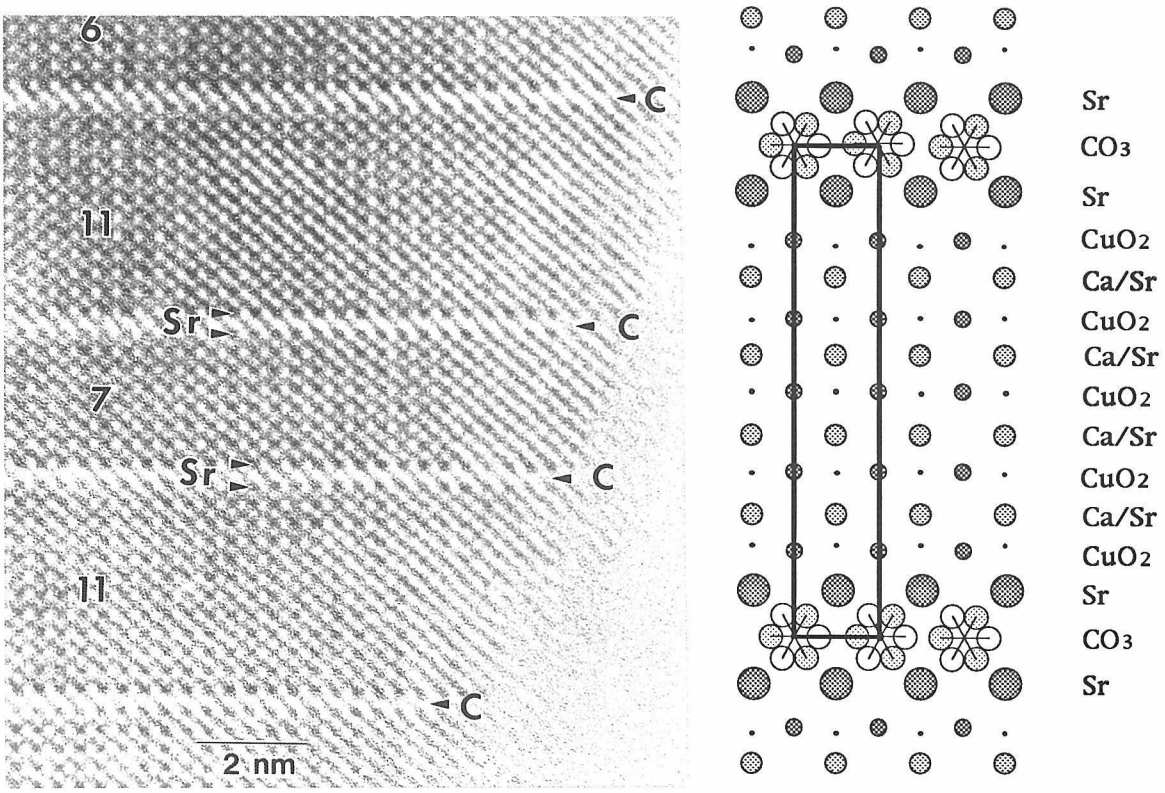

(a) (b)

Fig. 7 (a): HRTEM image of planar defects in "infinite-layer" type of superconductor, and (b): model of carbonate defects.

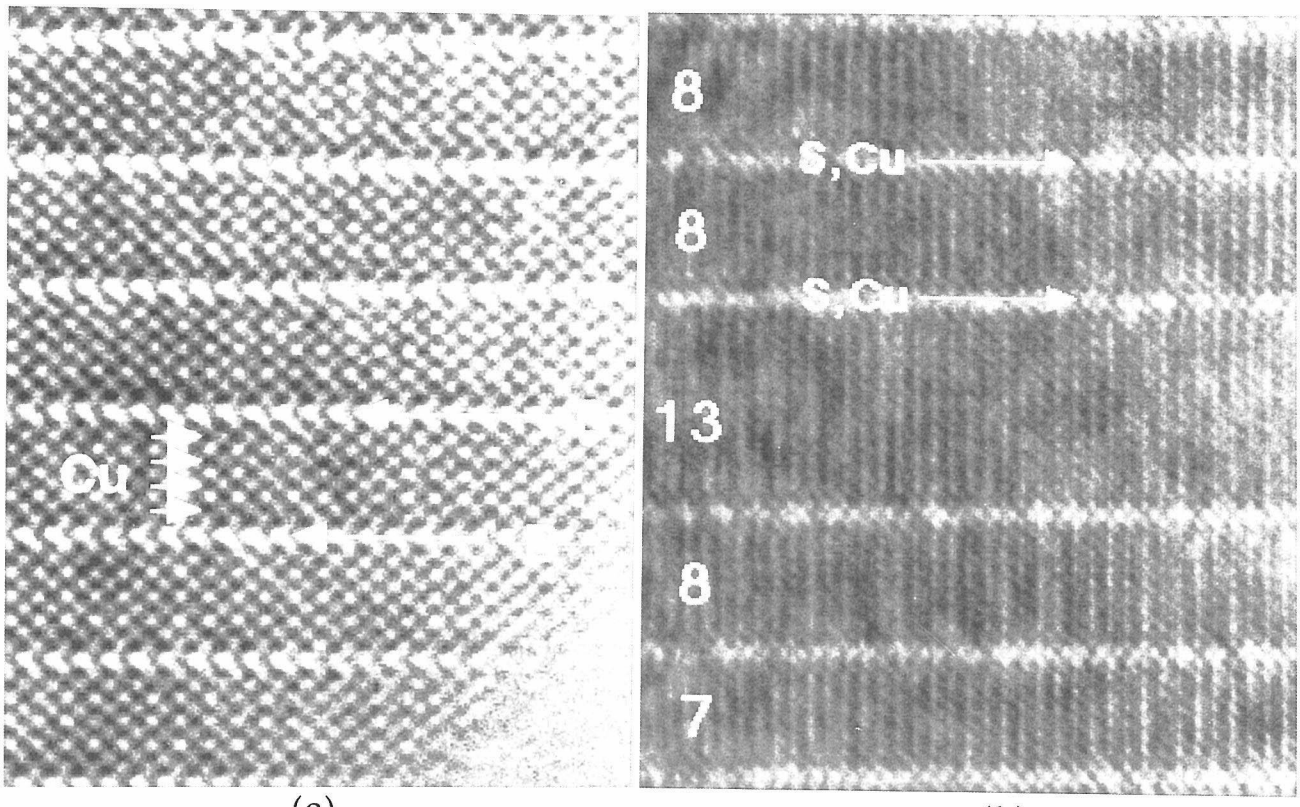

(a) (b)

Fig. 8 HRTEM images of (a) B-1234 and (b) (Cu,S)-12(n-1)n types of superconductors.

Finally, examples of oxysulfate superconductors, containing SO_3 groups, are also shown in Fig.8 (b). Weak contrast due to ordered arrangement of -Cu-S-Cu-S-Cu- are observed in the series of compounds. This indicates that the present oxysulfate superconductors have superstructures quite similar to those observed in the (Cu,C)-series of oxycarbonates. Unfortunately, the oxysulfate superconductors so far obtained contain plenty of planar defects, as is actually the case for Fig.8(b).

ACKNOWLEDGMENT

The authors deeply thank Dr. M. Hirabayashi & H. Ihara (ETL) for providing Hg-Ba-Ca-Cu-O specimen, Dr. K. Kinoshita (NTT) for providing C-1201 specimen, and Prof. J. Akimitsu & co-workers (AGU) for helpful discussions. This work is supported by Multi-Core Superconductors Research Program run by Science and Technology Agency of Japan.

REFERENCES

1. J.G. Bednorz & K.A. Müller, Z. Phys. B 64 (1986) 189.
2. Y. Matsui, E. Takayama-Muromachi, A. Ono, S. Horiuchi & K. Kato, Jpn. J. Appl. Phys. 26 (1987) L777.
3. Y. Matsui, H. Maeda, Y. Tanaka & S. Horiuchi, Jpn. J. Appl. Phys. 27 (1988) L372.
4. Y. Matsui, S. Takekawa, K. Kishio, A. Umezono, S. Nakamura, C. Tsuruta & K. Ibe, Mat. Trans. JIM, 31 (1990) 595.
5. Y. Matsui, S. Takekawa, S. Horiuchi, K. Shoda, A. Umezono, S. Nakamura & C. Tsuruta, J. Electron Microsc., 39 (1990) 223.
6. J. Akimitsu, M. Uehara, M. Ogawa, H. Nakata, K. Tomimoto, Y. Miyazaki, H. Yamane, T. Hirai & Y. Matsui, Physica C 211 (1992) 320.
7. Y. Matsui, M. Ogawa, M. Uehara, H. Nakata & J. Akimitsu, Physica C 217 (1993) 287.
8. M. Uehara, S. Sahoda, H. Nakata, J. Akimitsu & Y. Matsui, Physica C 222 (1994) 27.
9. M. Uehara, H. Nakata, J. Akimitsu, T. Den, T. Kobayashi & Y. Matsui, Physica C 213 (1993) 51.
10. M. Uehara, M. Uoshima, S. Ishiyama, H. Nakata, J. Akimitsu, Y. Matsui, T. Arima, Y. Tokura & N. Mori, Physica C 229 (1994) 310.
11. T. Kawashima, Y. Matsui & E. Takayama-Muromachi, Physica C 224 (1994) 69.
12. T. Kawashima, Y. Matsui & E. Takayama-Muromachi, Physica C 227 (1994) 95.
13. T. Kawashima, Y. Matsui & E. Takayama-Muromachi, Physica C 233 (1994) 143.
14. Y. Matsui, T. Kawashima & E. Takayama-Muromachi, Physica C 235-240 (1994) 166
15. E. Takayama-Muromachi, Y. Matsui & K. Kosuda, Physica C, in the press.
16. E. Takayama-Muromachi, Y. Matsui & J. Ramirez-Castellanos, submitted.
17. Y. Matsui, S. Horiuchi, Y. Bando, Y. Kitami, M. Yokoyama, S. Suehara, I. Matsui & T. Katsuta, Ultramicroscopy 39 (1991) 8.
18. F. Izumi, K. Kinoshita, Y. Matsui, K. Yanagisawa, T. Ishigaki, T. Kamiyama, T. Yamada & H. Asano, Physica C196 (1992) 227.
19. K. Kinoshita & T. Yamada, Nature 357 (1992) 313.
20. M. Azuma, Z. Hiroi, M. Takano & Y. Bando, Nature 356 (1992) 775.

EELS Profiling and Mapping at Nanometre Spatial Resolution

C. Colliex, M. Achèche, N. Brun, P. Redlich, O. Stephan, M. Tencé and P. Williams*
Laboratoire de Physique des Solides associé au CNRS
Bâtiment 510, Université Paris Sud 91405, Orsay, France

Abstract

The combination of an efficient parallel electron energy loss spectrometer (PEELS) with an electron microscope equipped with a field emission source provides the access to a sub-1 eV spectroscopy of unoccupied electron states with a sub-nanometre spatial resolution. It is therefore particularly suited to the investigation of local electron properties within heterogeneous materials or nanostructures. This paper describes recent progress in theory and instrumentation realized within the general concept of spectrum-imaging, which aims at recording profiles or maps of EELS fine structures and at associating the identified information (bonding state, site symmetry) to the detailed topography and structure of the specimen.

Introduction

Electron energy loss spectrometry (EELS) measures the rate of energy transfer from an incident monochromatic high energy electron beam into a specimen prepared as a thin foil. These spectral data cover a wide range of energies, typically from 1 eV to 1000 or 2000 eV, reflecting complementary aspects of the electron excitation spectra of the target under investigation. In the low-energy loss range, the population of valence electrons is concerned and the EELS spectrum displays a mixture of individual (inter- or intraband transitions) and collective (plasmons) processes involving these electrons. A joint density of states information convolving all possible occupied states in the valence band and all unoccupied states in the conduction band, coupled via allowed transitions, can be deduced from these spectra, with the help of numerical transformations relying on the causality principle (Kramers-Kronig transform). In the high-energy loss range, the involved transitions imply atomic core electrons which are promoted to empty levels lying above the Fermi level, giving access to a density of unoccupied states explored on a given site, i.e. with an atomic point of view. Of great interest is the fact that several such edges associated with the different atoms present in the solid can thus be easily investigated offering complementary information, on the cation as well as on the anion site in an insulator, on the A-type atom as well as on the B-one in an AB intermetallic compound. Furthermore the fine structures visible on different edges offer characteristic signatures, not only of the elemental specificity of the component atoms, but also of their insertion within their nearest and eventually more distant neighbours. They are sensitive to charge transfers, site symmetries and more generally speaking, to bonding nature.

When performed within the general context of an electron microscope column, this technique can benefit from the associated electron optics capabilities, i.e. focus, with the illumination system, the incident beam into a small electron probe, of a fraction of nanometre in diameter when the high energy electrons are delivered from a field emission source. The analysed volume is roughly made of a cylinder whose section is defined by the diameter of the incident probe and length by the local specimen thickness. This elementary volume can then consist of a small number of atoms and the present technique

constitutes therefore one of the most sensitive analytical tools in terms of the number of identifiable atoms. Furthermore the primary beam can be scanned at will on the specimen surface and spectra recorded for any probe position. By combining the spectroscopic analysis with the scanning process, one can build a very interactive tool between spectroscopy and microscopy, defined as the spectrum-image in the 2D (or spectrum-line in 1D) approach. One collects sequences of spectra as a function of the probe displacement. Specific software has been developed for processing these extended sets of data in order to extract the spectral changes as a function of probe position, and will be discussed in the present paper. Finally these changes in fine structures have to be associated with modifications of given physical parameters. Consequently it is necessary to summarize how our present level of theory can be used for this purpose.

Interpretation of core-loss fine structures (a summary)

A major step in order to benefit from the complete information contained in EELS spectra lies in a satisfactory interpretation of these fine structures. As a matter of fact their similarity, in the small angle scattering limit, with those observed in X ray absorption spectra, has been recognized for a long time. Progress in understanding these structures relies on the same theoretical tools, basically on computations of accessible states in molecular or solid state physics descriptions[1-2]. If in the present situation no *ab initio* theoretical frame is available for interpreting all the edges, there exists a diversity of approaches which are of great value at least for a comparison of edges in different compounds, now extending beyond a simple fingerprint use.

As an example, let us consider the oxygen K edge and the iron L_{23} edge in a specimen of α-Fe_2O_3 (fig. 1). The first one corresponds to the excitation of the 1s electrons on the oxygen ions and the second one to the excitation of the 2p electrons on the iron ions. As a consequence of the dipole transition rule, they probe respectively the local density of unoccupied states of p symmetry on the O site and of d symmetry on the Fe site. These signals carry different levels of information:

i) The integrated characteristic signal over a given energy window Δ after subtraction of an extrapolated background, is a measurement of the number of relevant atoms N_O or N_{Fe} in the analysed volume, after scaling with a reference cross-section $\sigma_{O\text{-}K}$ or $\sigma_{Fe\text{-}L23}$ per atom corresponding to the experimental parameters employed. This is the most common use of core-losses for quantitative elemental analysis[3]. The cross-sections have either been calculated in different types of atomic models, or measured from reference specimens.

ii) The oxygen K edge fine structures are made of a succession of peaks labeled a to f in the moderate energy resolution spectrum (fig. 1a) or a_1, a_2 and b_1, b_2 and b_3 in the improved energy resolution curve (fig. 1c). The weak oscillations b, d, e and f correspond to the first of the extended fine structures quite similar in essence to the EXAFS type structures. They can be analysed with the same algorithms used in X ray absorption spectroscopy, i.e. in terms of single scattering of the outgoing excited wave within shells of neighbouring atoms of increased size. This constitutes a first route to the structural determination of the neighbourhood of the excited atom, in terms of distances and coordination numbers. However, signal to noise criteria and overlapping edges in this spectral range constitute severe constraints for an extensive use of these structures. Consequently the features a to d visible over the first thirty eV above the threshold, have been more extensively investigated over the past few years. They are known as ELNES data and can be described with methods such as band structure, multiple scattering and molecular orbital calculations. These are suitable for weakly correlated systems where the interaction of the excited electron with the core hole created in the process remains weak. Summarizing these theoretical developments:

Peak (a) can be assigned to transitions to unoccupied 2p states hybridized with iron 3d character states, the strength of which being due to the number of d holes available and to the degree of covalency[4-5]. Furthermore the doublet of peaks a_1 and a_2 separated by 1.1 eV corresponds to the ligand field splitting into t_{2g} and e_g terms on the distorted octahedral iron site. This is a kind of paradox: the excitation of 1s electrons probing delocalized vacant states on the oxygen sites provides, through the hybridization mechanism, a rather reliable picture of the available 3d electron states on the transition metal sites as these are weakly perturbed by the presence of the hole.

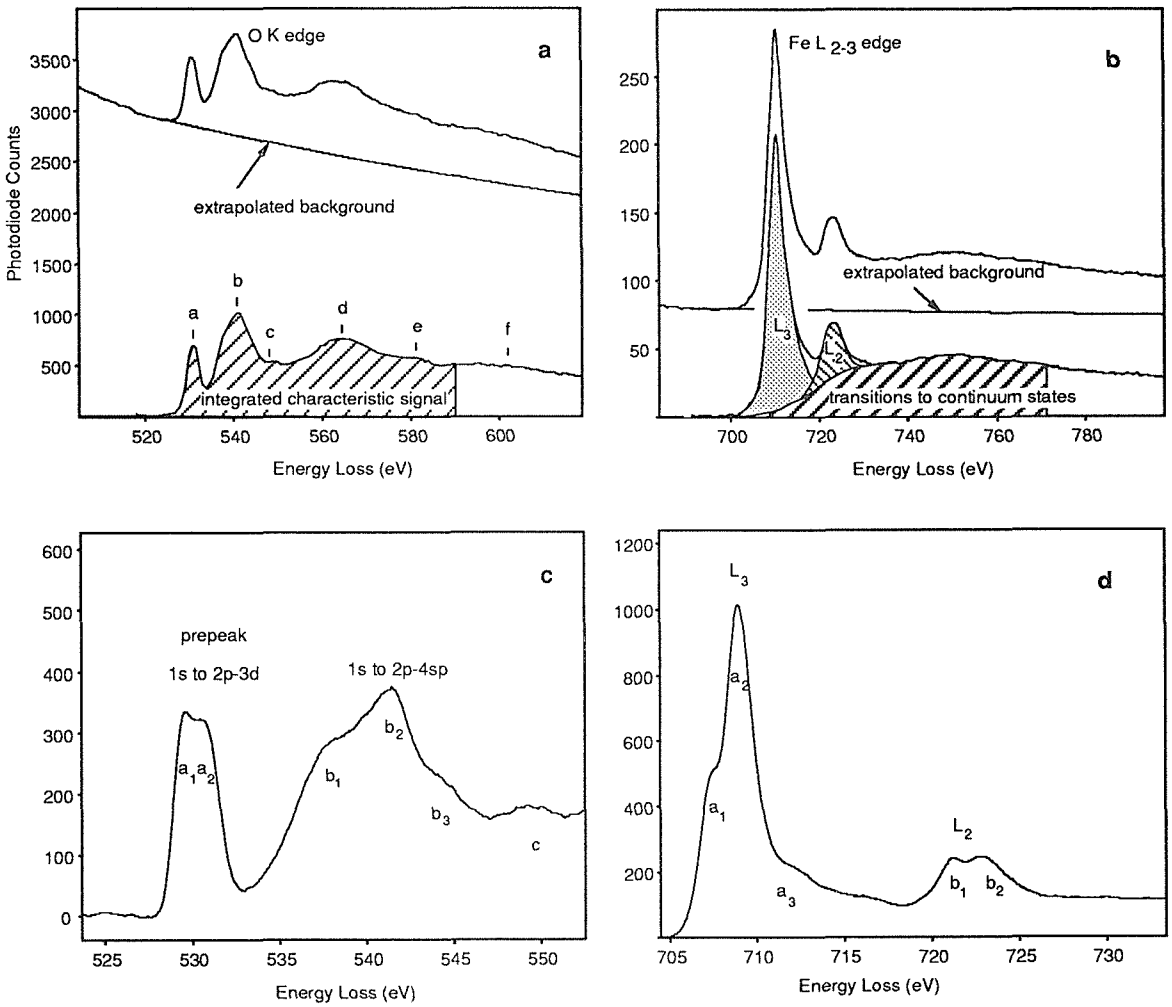

Figure 1: Analysis of the information carried by typical core-loss edges (O-K and Fe-L_{23} in a peanut-type hematite (α-Fe_2O_3) specimen). In figs. a and b, recorded at medium energy resolution, the methods for extracting partially integrated information for elemental analysis or white line quantification are shown. In figs. c and d recorded with improved sub-1 eV resolution, the detailed fine structures are demonstrated giving rise to splittings which can be more straightforwardly associated to the break in degeneracy for the unoccupied 3d electron states in the O case than in the Fe one.

Peaks (b) to (d) can be successfully reproduced by multiple scattering (MS) calculations in clusters of increased sizes. Peak (b) arises due to intra-shell multiple scattering within the first oxygen coordination shell and reflects transitions to unoccupied oxygen 2p states hybridized with metal 4s and 4p states typically 5 to 10 eV above theshold. Peak (d) is mostly due to single scattering within the first shell of neighbouring oxygen ions which are rather strong backscatterers for the outgoing electron wave and create a kind of potential cage or barrier for electron scattering. The position of the resonance peak (d) has been shown to constitute an

accurate measurement of the nearest neighbour distance in the case of a simple crystal symmetry. Finally the interpretation of the existence and position of peak (c) requires the introduction of several oxygen coordination shells around the excited site, providing structural information beyond the nearest neighbour.

iii) On the other hand, the iron 2p electron excitation should provide, as a consequence of the dipole selection rule, a direct fingerprint of the unoccupied d band. This is only partially true. There are obviously high densities of unoccupied d states at the threshold, as revealed by the two intense lines (called white lines L_3 and L_2) and attributed to the excitation from the spin-orbit splitted initial levels $2p_{3/2}$ and $2p_{1/2}$. But their relative weight and detailed fine structures displayed as contributions a_1, a_2 and a_3 on the L_3 line and b_1 and b_2 on the L_2 line cannot be interpreted in this simple scheme. As a consequence of the strong localization of the excited wave function, their modelling requires theories taking explicitly into account the electron-electron and electron-core hole interactions in strongly correlated systems, such as the atomic multiplet description incorporating the crystal field effect[6]. With the support of such tools, one can then extract several types of information, such as the weight of the unoccupied d-holes as compared to that of transitions to continuum states ($(I_{L3}+ I_{L2}) / I_{cont}$), the branching ratio ($I_{L3} / (I_{L3} + I_{L2})$) which may be correlated to the local magnetic moment[7-8]. But there is no evident relation between the experimental spectra and the valence state, because the position and intensity of the fine structures in the L_3 and L_2 white lines are due to a superposition of electron charge and site symmetry effects in an excited state highly perturbed by the presence of the core hole, and require therefore a descriptive frame beyond the one-electron model[9].

Recording and processing schemes for sequences of spatially resolved EELS spectra

The acquisition of a sequence of spectra for all probe positions along a line scan or over a predetermined rectangular array of pixels results from the practical implementation of the spectrum-line and spectrum-image modes introduced by Jeanguillaume and Colliex[10]. One major product of this technique is to store an assembly of data which can be processed *a posteriori* in order to correlate as accurately as possible the spatial coordinate and the spectral features. In our laboratory, the combination of a field emission source, a digital scanning unit and a parallel EELS spectrometer on a dedicated STEM instrument, makes profiling and mapping of EELS spectra achievable with typical (sub)nanometre spatial resolution[11]. Experimental parameters employed are summarized in the table below.

Any imaging software handling data in the appropriate format can be used to visualize the results as images with one axis corresponding to the energy loss scale and the other one to the pixel position on the specimen. A "3D plot" provides an isometric view of the series of spectra aligned parallel one to another and is very useful for a quick survey of the location of the different edges appearing during the line-scan.

A more elaborate goal is to obtain a quantitative measurement of the changes appearing in these sequences. The first approach consists in applying successively to all spectra gathered in one series the quantification techniques available for single spectrum processing, i.e. standard background modelling and extrapolation routines, MLS fitting techniques with a collection of reference edges. In both cases the results are displayed as atomic concentration profiles or maps for the different elements detected. Examples relative to multilayer systems have already been described in reference[12].

Spectrum-line	Probe size	Typical extent of the used signal	Number of pixels involved	Pixel step on the specimen	Average recording time per spectrum
Low losses (plasmons, dielectric coefficients)	1-2 nm	> 1-2 nm	64 to 256	0.5-1 nm	25-250 ms
Elemental mapping from core-losses	0.5 nm	<0.5 nm	32 to128	0.3-0.5 nm	1 s
Fine structures on core-losses	0.5 nm	<0.5 nm	32 to128	0.3-0.5 nm	1-5 s
Spectrum image					
Elemental mapping from core-losses	1-2 nm	<0.5 nm	32x32 or 64x64	0.5-1 nm	0.1-1 s

In order to extend the information gained from recording spectrum-lines beyond elemental profiling, one needs to take into account the full spectral distribution over all relevant energy loss channels. As a matter of fact, the interesting changes concern only a reduced number of these channels and a small number of pixels. It is the reason why specific procedures are presently being adapted to identify and measure the relevant changes The first of these attempts is to calculate spatial-difference spectra defined as the difference between spectra recorded at selected positions on the specimen, for instance on the bulk on each side of an interface and on the boundary by itself[13] This approach has been used to determine the fine structures of the atoms in an interface but as it has to be done manually, spectrum per spectrum, it is rather tedious and subjective.

Our present aim is to apply developments in spectral processing techniques to profile or map any type of fine structure and consequently any associated information such as bonding type, d hole occupancy, site symmetry... It employes MLS fitting techniques, the preliminary step being to define or select templates of the fine structures which are to be searched for along the line scan. This can be done *a priori* relying on our knowledge of the problem. It can also be achieved with more sophisticated pattern recognition and classification techniques which distribute all the spectra of a sequence into families possessing a certain degree of similarity. One of these approaches, the use of artificial neural networks (ANN) has recently been introduced for the analysis of near-edge structure components at interfaces[14]. The basic idea is to consider any spectrum as a vector in a multidimensional composition space, the number of dimensions being equal to the number of energy loss channels in the range of interest. Several criteria (scalar product, cross correlation) can be used for the search of the basis vectors of this space, on which the projection of all spectra in the sequence provides a measure of their composition in terms of the reference spectra. Other methods such as the factorial analysis of correspondence would provide other routes to classify in a hierarchical order the variance of components within a large data set[15]. In all cases the full impact of these classification and analysis tools relies on a satisfactory physical understanding of the basis vectors or principal components

Examples are now shown in order to demonstrate how these approaches can open quite new fields of applications. Because of its dominant role in silicon technology, the Si-

SiO_2 interface has been investigated by a number of authors, using EELS[16] as well as XPS[17], in order to determine the changes in structure, chemistry and bonding states in the near-interface region. Several signals in the EELS spectra (interband transitions, plasmons, core-level signals on the Si and O ions) can be used. Fig. 2 demonstrates how a spectrum-line focusing on the changes of the Si 2p electron excitation can be processed to provide a profile of the variation of a given fine structure. Here the interest lies in the changes of the edge shape over an energy-loss range between 98 and 110 eV, from the pure Si case with its tetrahedral coordination of a Si atom to four Si neighbours, to the SiO_2 case with its coordination to four O neighbours. The reference spectra have been defined either arbitrarily as a selection of individual spectra at pixels lying far from the interface in the sequence, or have been provided by ANN analysis, using a software kindly transferred to us by G. Duscher (Stuttgart). The difference between the two sets of references is vanishingly small, indicating that with the spatial resolution and signal to noise achieved in this sequence, it is not possible to identify a third independent edge structure pattern corresponding for instance to an intermediate oxidation state.

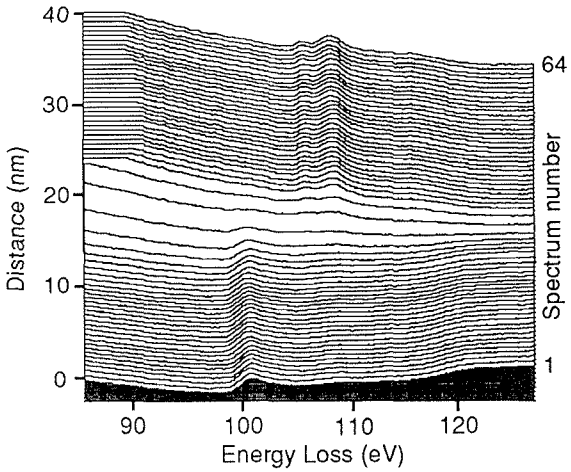

Figure 2a. Evolution of the Si L23 edge during an EELS linescan across a Si-SiO2 planar interface.

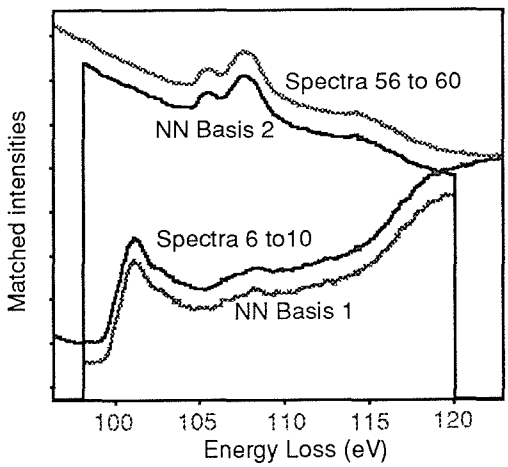

Figure 2b. Comparison of models calculated from the average of selected spectra with those generated by the neural network.

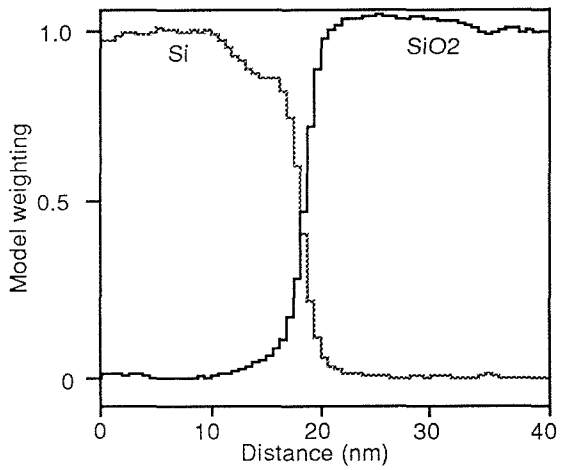

Figure 2c. MLS weighting profiles of the models calculated from the average of selected spectra.

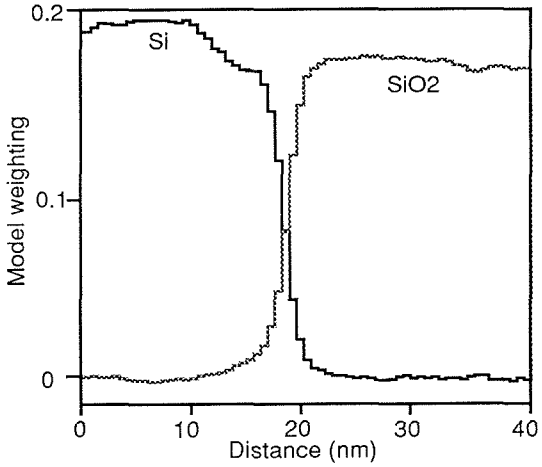

Figure 2d. Projection weighting profiles of the models generated by the neural network.

The spatial distribution of the reference spectra for the two bonding states, is very similar when using the MLS fit of the reference spectra or the projection on the ANN basis vectors. The width of the present interface, measured as a change of the characteristic

bonding state fine structure, is of the order of 2 nm and it is accompanied by an extended tail of the SiO_2 signal over a typical thickness of 3 nm in the Si area. This is only one example of the capabilities of these data processing schemes which are presently being applied to many sets of EELS signals and different types of interfaces.

The final example has been obtained during the characterization of nanocomposites made of carbon nanotubes and manganese compounds[18]. An EELS elemental analysis using the standard background extrapolation routine for quantitative analysis has revealed that some of the tubes have their hollow cores filled with Mn metal while others are covered by a manganese oxide. One sequence across such a nano-object with both types of Mn signal is displayed in fig. 3. It can be used to identify the position of the pixels with a strong Mn L_{23} signal, from which it is thus possible to extract reference profiles of the L_{23} white lines for the core and peripheral Mn. In preliminary studies, it has been shown that the white line ratio (I_{L3}/I_{L2}) varies from about 3 to 6 when comparing Mn^0 and Mn^{3+} edges[8]. The MLS profile clearly discriminates areas with different white line ratios.

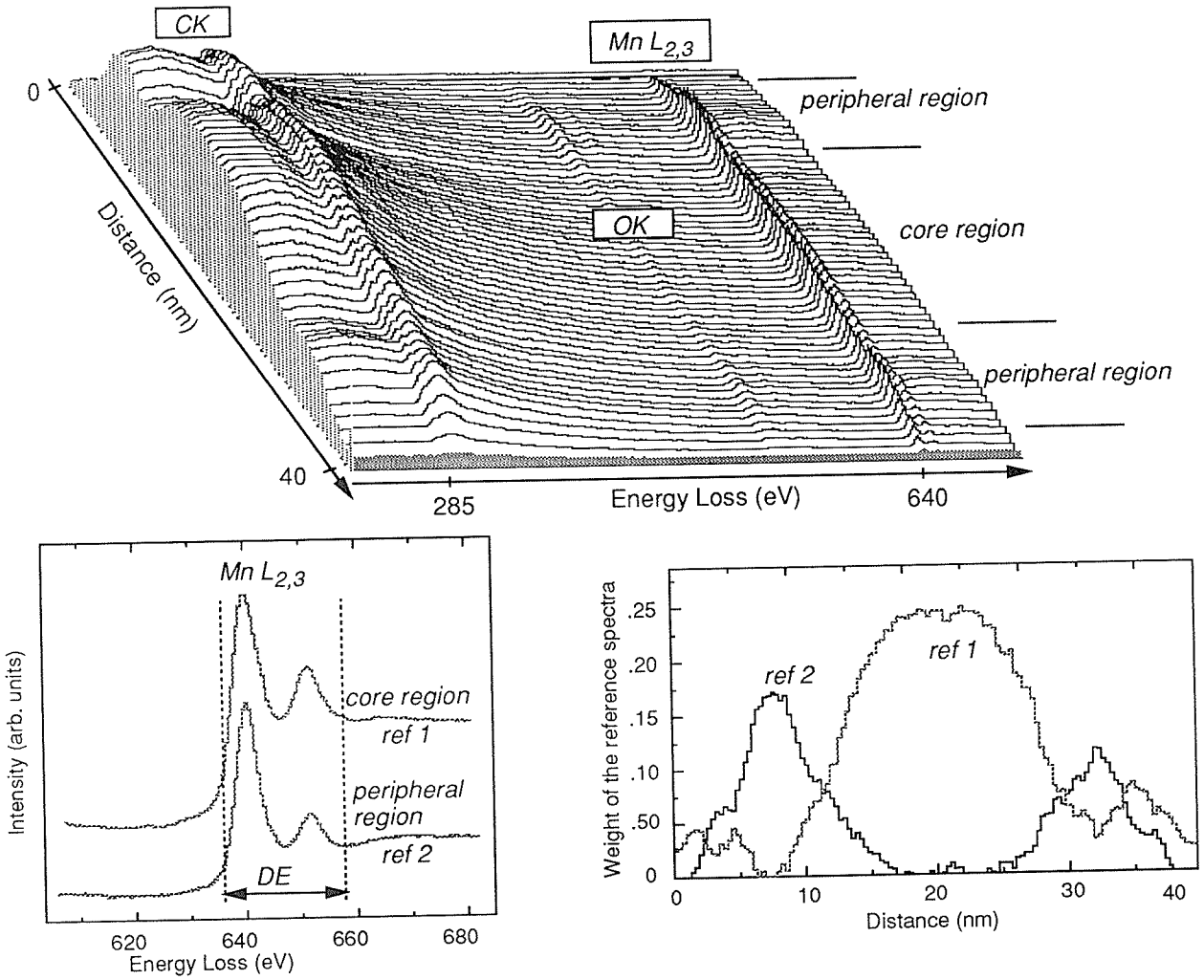

Figure 3: Line-spectrum across a carbon nanotubular object with manganese metal or compounds filling the core or covering the outer surface. The edges associated with C, O and Mn are visible. For profiling the Mn L_3 and L_2 white line intensities, two reference spectra have been defined from the core and peripheral regions, exhibiting clear differences in white line ratio. The weight of these two references is plotted across the line-spectrum, discriminating clearly a metal Mn core from a peripheral oxide (likely Mn_2O_3) Mn compound.

Obviously these are only preliminary examples. They have already required some improvements in the available software. As an example a routine has been introduced in order to realign all spectra after a line scan, with respect to a reference one. This has been necessary to avoid confusion between an instrumental shift and a real chemical shift due to a change in electronic properties. Other improvements are also now being introduced in the neural network analysis by G. Duscher[19] who has demonstrated that the analysis of the normal spectra as performed in the above example, is less sensitive than on background stripped edges or spectral sequences acquired in the first difference mode. For the low-loss domain, the pattern recognition and analysis techniques could also be fruitfully applied to processed spectra, eventually to more reliable profiles or maps of dielectric constants[20-21]. Nevertheless the essential message of this contribution is that the presently available instruments and processing tools can be used for mapping any type of refined EELS fine structure information at a near-atomic spatial resolution, which should be of foremost importance for the detailed characterization of advanced materials.

Acknowledgements : For the present study, thanks are due to all our colleagues and external collaborators who have stimulated and helped us at various stages : O. Krivanek (Gatan) for the instrumentation, R. Brydson (Surrey) for the interpretation of fine structures, G. Duscher (Stuttgart) for the transfer of software, D. Shindo (Sendai) for the peanut-type hematite specimen, F. Varnière and C. Agius (Orsay) for the Si-SiO_2 specimen, P. Bernier, J.M. Lambert (Montpellier) and P. Ajayan (Orsay) for the Mn composite carbon nanotube.

* Permanent address : Ecole Nationale d'Ingénieurs, Nabeul, Tunisie.

References :

1) P. Rez, in "Transmission Electron Energy Loss Spectrometry in Materials Science", p.107, M.M. Disko, C.C. Ahn and B. Fultz eds. , TMS, Warrendale, Pa 15086 (1992).
2) R. Brydson, H. Sauer, W. Engel, ibidem, p. 131 (1992).
3) R.D. Leapman, ibidem, p. 47 (1992).
4) F.M.F. de Groot,, M. Grioni, J.C. Fuggle, J. Ghijsen, G.A. Sawatzky, H. Petersen, Phys. Rev. B 40, 5715 (1989).
5) H. Kurata, E. Lefèvre, C. Colliex, R. Brydson, Phys. Rev. B 47, 13763 (1993).
6) F.M.F. de Groot, J.C. Fuggle, B.T. Thole, G.A. Sawatzky, Phys. Rev. B 42, 5459 (1990).
7) B.T. Thole, G. van der Laan, Phys. Rev. B 38, 3158 (1988).
8) H. Kurata, C. Colliex, Phys. Rev. B 48, 2102 (1993).
9) L.A.J. Garvie, A.J. Craven, R. Brydson, Am. Mineralogist 79, 411 (1994).
10) C. Jeanguillaume, C. Colliex, Ultramicroscopy 28, 252 (1989).
11) C. Colliex, M. Tencé, E. Lefèvre, C. Mory, H. Gu, D. Bouchet, C. Jeanguillaume, Mikrochim. Acta 114-115, 71 (1994).
12) M. Tencé, M. Quartuccio, C. Colliex, to be published in Ultramicroscopy (1995).
13) H. Müllejans, J. Bruley, Ultramicroscopy 53, 351 (1994).
14) C. Gatts, H. Müllejans, J. Bruley, M. Rühle, Proc. ICEM 13, Paris 1, 745 (1994).
15) P. Trebbia, N. Bonnet, Ultramicroscopy 34, 165 (1990).
16) P.E. Batson, Nature 366, 727 (1993).
17) F.J. Himpsel, F.R. McFeely, A. Taleb-Ibrahimi, J.A. Yarmoff, G. Hollinger, Phys. Rev. B 38, 6084 (1988).
18) P. Ajayan, C. Colliex, J.M. Lambert, P. Bernier, L. Barbedette, M. Tencé, O. Stephan, Phys. Rev. Lett. 72, 1722 (1994).
19) G. Duscher, private communication (1994).
20) M.A. Turowski, T.F. Kelly, Ultramicroscopy 41, 41 (1992).
21) P. Redlich, C. Colliex, Proc. EELSI meeting, Leukerbad, in preparation (1995).

EELS and Energy-Selecting Image on High-Voltage Electron Microscope

Hiroki Kurata, Seiji Isoda and Takashi Kobayashi
Institute for Chemical Research, Kyoto University, Uji, Kyoto 611, Japan

Abstract

Energy-selecting transmission electron microscopy was applied to carbon nanotubes in order to investigate quantitative property of elemental maps obtained by inelastically scattered electrons corresponding to the carbon K-edge. An 1MeV high-resolution electron microscope (JEOL, ARM-1000) equipped with a GATAN imaging filter was employed. Because of a cylindrical structure of nanotubes it is expected that the number of carbon atoms projected on the image changes across the tube axis. We detected the contrast difference due to 20 carbon atoms in the carbon distribution image of 6 layers tube. Furthermore, we examined the carbon mapping from a conical tip region with progressive closure of carbon layers, which showed an intensity profile clearly distinguishing the difference of 6 and 12 graphene sheets.

INTRODUCTION

Energy-filtering technique in conventional transmission electron microscopy [1] provides energy-filtered high-resolution imaging and diffraction, and also elemental mapping which promise quantitative analyses of specimens. In particular the elemental mapping makes it possible not only to visualize a 2D-distribution of a particular element, but also to count the number of atom existing in a specific region by analyzing the intensity of image quantitatively. In order to investigate the quantitative property of an elemental map, a specimen with a thin thickness is needed because multiple scattering effects disturb the intensity distribution.

Carbon nanotubes have a variety of structure characterized by the diameter of a tube, the inner diameter and the number of graphene sheet [2]. Typical size of a tube is the order of nanometer which is thin enough to analyze the intensity of the elemental distribution image without taking account of multiple scattering effects. Since the structural parameters of each nanotube can be identified by high-resolution electron microscopy, the carbon distribution image observed from a well-defined nanotube is very suitable for studying the quantitative property of the elemental map.

In the present work, we investigate the carbon distribution images observed from a various size of nanotubes and the conical tip region of a tube. The intensity profile of the image is compared with the distribution of the number of carbon atoms estimated by a

cylindrical structure model of the nanotube. The image quality is evaluated using the signal to noise ratio calculated from the intensity of the carbon distribution image and the background image, and the detection limit is discussed.

EXPERIMENTAL

The investigations were performed using the JEOL ARM-1000 (operated at 1MeV) [3] equipped with the Gatan imaging filter (GIF) [4]. High resolution lattice images and carbon distribution images of self-supported nanotubes were observed with a magnification of the microscope of 20,000x which corresponds to an effective magnification of 340,000x on the slow-scan CCD camera with the pixel size of 24 x 24μm^2 of the GIF. This means the pixel size referred back to the objective plane is 0.07nm, allowing certainly the elastic imaging of the (002) lattice planes (d=0.34nm) of graphite. In the carbon distribution images, however, 4x4 pixels were integrated into one effective pixel (binning mode) because of the small inelastic scattering cross-section of the carbon K-edge compared to that of elastic scattering, so that the effective pixel size was 0.28nm. The inelastic scattering images were

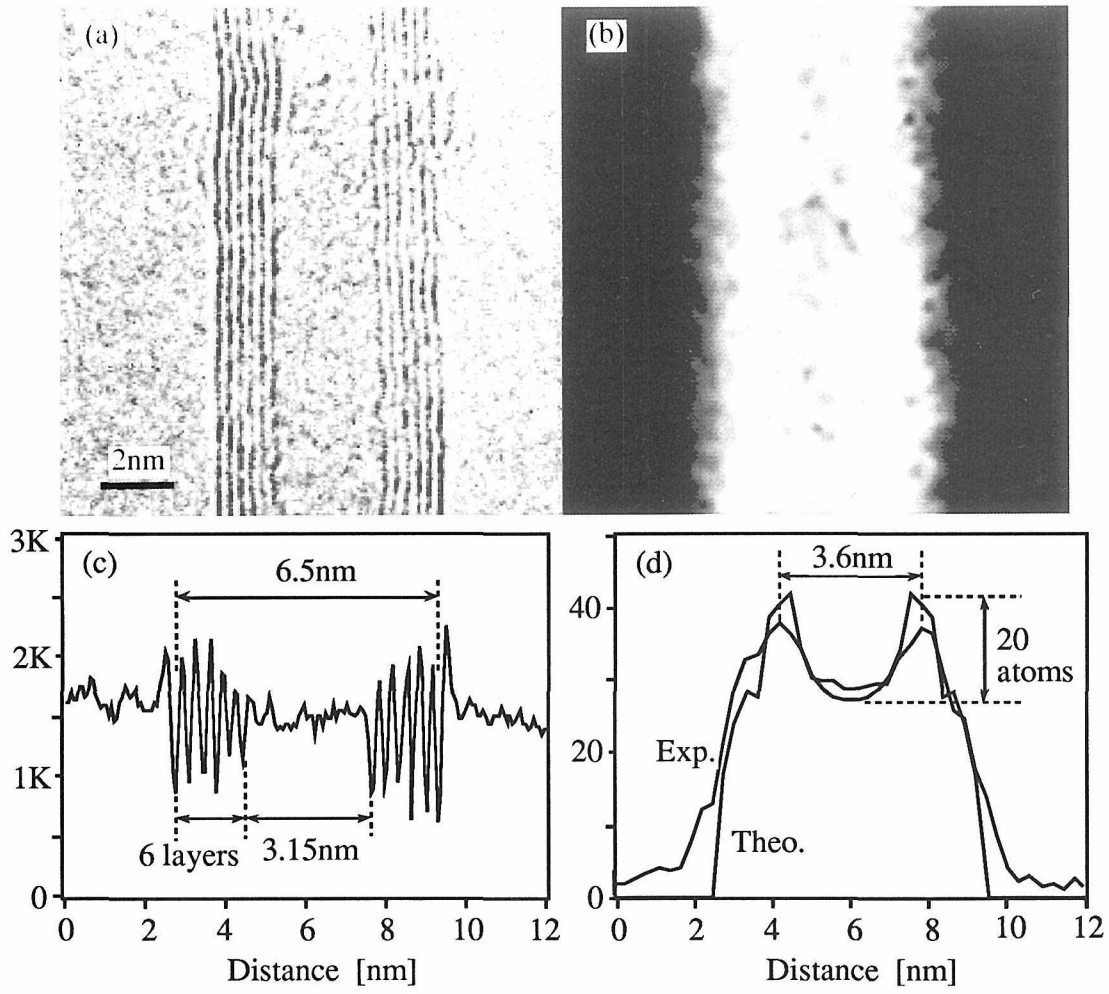

Fig. 1 Lattice image (a) and carbon distribution image (b) of carbon nanotube. Intensity profile of lattice image (c) and of carbon image (d) across the tube axis.

observed with an electron dosage of 200 to 400C/cm^2. Under such strong irradiation some kinds of lattice distortion might occur but the shape transformations in nanotubes recently reported by Ajayan et al. [5] was not observed. The objective aperture angle and the width of an energy selecting slit of GIF were set to be 10mrad and 30eV, respectively. Under these conditions the chromatic broadening [6] by objective lens (C_c=3.6mm) is almost the same as the pixel size. The carbon distribution images were obtained by subtracting the background image from the post carbon K-edge image using the three windows technique [7]: Two pre-edge images were taken at 239 and 269eV for the background subtraction procedure. The post-carbon K-edge images were observed at 304eV, and the exposure time of each image was 10sec.

RESULTS AND DISCUSSION

A high-resolution lattice image and the corresponding carbon distribution image of a nanotube are shown in figs. 1a and 1b. The intensity profile of the lattice image across a tube axis (fig. 1c) indicates clearly the 6 layers cylindrical structure as the lattice fringe oscillations at both sides of the tube. The size of the tube is 6.5nm in diameter and the inner diameter is 3.15nm. The carbon distribution image shows the change of intensity reflecting the number of carbon atom. The intensity profile of the carbon distribution image is shown in fig. 1d, in which the intensity was averaged over about 10 pixels (40 pixels on CCD) intensity along the tube axis to increase the signal to noise ratio. The intensity maxima separated with a distance of 3.6nm are observed in the line profile. This profile was compared with the theoretical profile determined by the following procedure.

In order to calculate the intensity I_i at pixel i of the detector, we used the following equation [7],

$$I_i(\beta,\delta E) = D \cdot \sigma(\beta,\delta E) \cdot N_i \cdot \eta. \qquad (1)$$

Here D is the electron dosage irradiated (=200C/cm^2), $\sigma(\beta, \delta E)$ is the partial inelastic scattering cross-section of the carbon K-edge calculated using the SIGMAK software [7] with the collection angle β of 10mrad and the energy window δE of 30eV. η is the conversion efficiency of the detection system of the GIF, which is assumed to be 0.3 in the present analysis. N_i is the number of carbon atom projected to the pixel i of the detector, which is estimated using the structure model of fig. 2. The cross section of the nanotube across the tube axis consists of six concentric graphene circles. The N_i can be represented by the equation,

$$N_i = t_i \cdot \Delta \cdot \rho. \qquad (2)$$

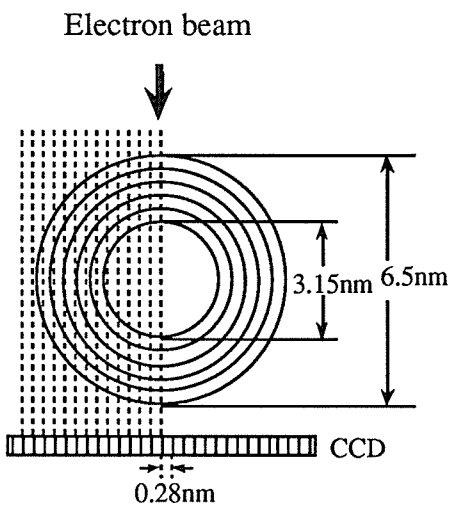

Fig. 2
Structure model of the nanotube

Here t_i is the total length of graphene arcs cut by the size of each pixel, Δ the pixel size (=0.28nm) and ρ the carbon density in one graphite layer.

The experimental and theoretical intensity profiles are compared in fig. 1d. The agreement of both profiles is quite satisfactory, which means the elemental distribution image is very quantitative as long as thin specimens are examined. The intensity maxima and minimum at the central region of the nanotube correspond to about 50 and 30 carbon atoms per pixel, respectively. Therefore, we conclude that the difference of 20 carbon atoms can be detected at nanometer scale with a good signal to noise ratio.

Next example of carbon distribution image is the observation of the conical tip region of nanotube as shown in fig. 3. The lattice image (fig. 3a) shows that the tip is made by progressive multilayer of curved graphene sheets. In this case the number of multilayer are 5, 3 and 6 layers from the tip to inside of the tube. Because the tip changes its shape linearly along the cone axis, the number of carbon atoms, which is projected on the specimen surface along the direction of electron beam, is constant even in the respective multilayer tip region as well as in the straight nanotube. Such the distribution of the carbon atoms can be visualized by the elemental mapping. The carbon distribution image taken from the same region (fig.

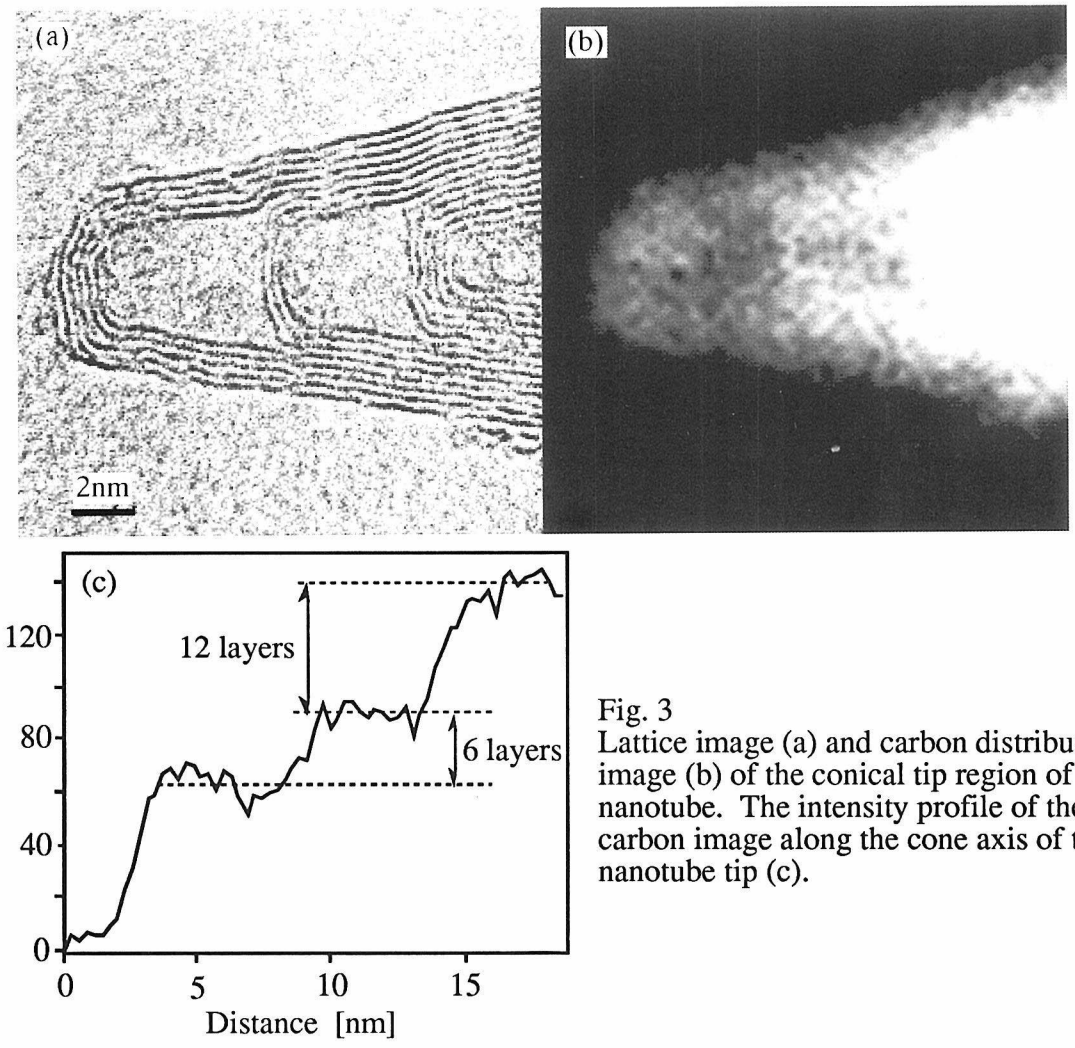

Fig. 3
Lattice image (a) and carbon distribution image (b) of the conical tip region of nanotube. The intensity profile of the carbon image along the cone axis of the nanotube tip (c).

3b) shows the gradual intensity change from the tip to inside of the tube as expected from the increase of graphene layers. The line profile of the image along the cone axis is shown in fig.3c. The step like change in the intensity profile indicates the progressive increase of graphene multilayers. The differences of the step height correspond to 6 and 12 graphene layers, respectively, because the electron beam travels through the upper and lower multilayers of the nanotube. Such differences of the graphene layers are equivalent to 18 and 36 carbon atoms per pixel, respectively. In this example, therefore, we can also detect the difference of about 20 carbon atoms.

Finally, we discuss the statistical properties of the carbon distribution image of fig. 1b by means of the signal to noise ratio (SNR). The SNR is deduced from the images using the following equation [8],

$$SNR = N_i^s \cdot \sqrt{\frac{DQE}{N_i^s + h \cdot N_i^b}} \qquad (3)$$

Here N_i^s is the intensity at pixel i of the carbon distribution image, N_i^b is the background intensity of the pixel i which is extrapolated using the three windows technique assuming the power-law energy dependence of background intensity. h is the parameter to specify the quality of the background subtraction procedure and depends on the positions of the three windows to take the pre- and post-carbon K-edge images [9]. In the present experiment h was 7. The DQE is the detection quantum efficiency of the detector system, which was assumed to be 0.7. In general cases the noise component coming from the background extrapolation procedure determines the SNR dominantly. In the present case, however, the background intensity arising from the tail of valence electron excitations is small compared to the signal one ($N_i^b << N_i^s$), because the nanotubes are supported by themselves on a hole and consisted of a small number of carbon atoms. So the SNR of the carbon distribution image of fig. 1b was proportional to the square root of the signal intensity approximately.

Fig. 4 shows the SNR calculated for each pixel across the tube axis of fig. 1b. In the specimen region the SNR for non-averaged 1-line

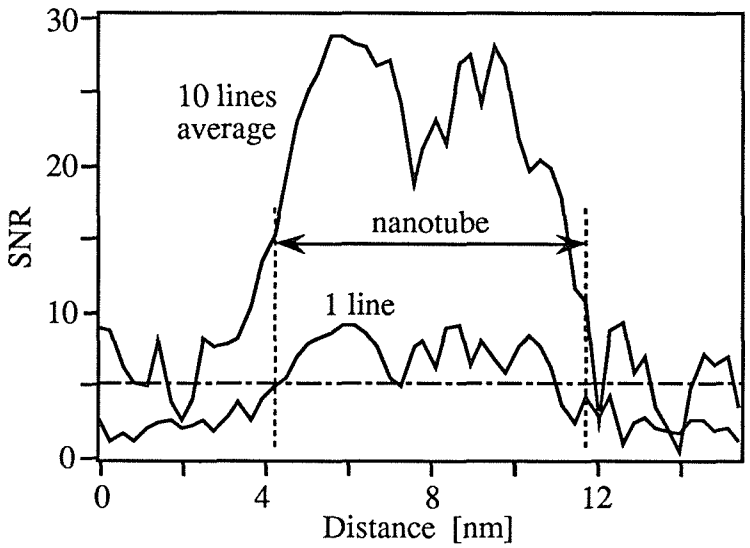

Fig. 4 Signal to noise ratio of the carbon distribution image of fig. 1b

case is a little larger than about 5 which corresponds to the Rose's criterion for the detection limit [10]. So the carbon distribution image of fig. 1b seems to be the almost critical observation to detect about 20 carbon atoms by one pixel (0.28x0.28 nm^2) of the detector. The upper line in fig. 4 represents the SNR calculated from the integrated signal of 10 pixels along the tube axis, which indicates the increase of the SNR about factor of 3. This is the reason why the difference of 20 carbon atoms can be detected with a good SNR as shown in the intensity profile of fig. 1d.

CONCLUSION

From the application of energy-selecting electron microscopy to the carbon nanotube the quantitative elemental imaging has been demonstrated. The experimental intensity profile of the carbon image was in good agreement with the distribution of carbon atoms theoretically calculated from the structure of the nanotube. The difference of about 20 carbon atoms was clearly detected in the intensity profile at nanometer scale. From the SNR of the carbon distribution image the detection limit was estimated to be about 20 carbon atoms in one pixel (0.28x0.28 nm^2) under the present experimental conditions.

Acknowledgment

We would like to thank Mr. Y. Ohtuka of TORAY corporation for providing the carbon nanotubes.

References

[1] L. Reimer ; Adv. Electron. Phys. **81**, 155 (1991).
[2] S. Iijima ; Nature **354**, 56 (1991).
[3] S. Isoda, S. Moriguchi, H. Kurata and T. Kobayashi ; Ultramicro. **39**, 247 (1991).
[4] A. J. Gubbens and O. L. Krivanek ; Ultramicro. **51**, 146 (1993).
[5] P. M. Ajayan, C. Colliex, P. Bernier and J. M. Lambert ; Microsc. Microanal. Microstruct. **4**, 501 (1993).
[6] H. Shuman, C. F. Chang and A. P. Somlyo ; Ultramicro. **19**, 121 (1986).
[7] R. F. Egerton ; "Electron Energy Loss Spectroscopy in the Electron Microscope" Prenum Press, New York (1986).
[8] A. Berger, J. Mayer and H. Kohl ; Ultramicro. **55**, 101 (1994).
[9] A. Berger and H. Kohl ; Optik **92**, 175 (1993).
[10] A. Rose ; Image Technol. **12**, 13 (1970).

Applications of Advanced Techniques of Electron Diffraction in Materials Science

J.W. Steeds, P.A. Midgley, M.A. Saunders and R. Vincent
H.H. Wills Physics Laboratory, University of Bristol, Tyndall Avenue, Bristol BS8 1TL, U.K.

Abstract

There is a great variety of different techniques for obtaining accurate quantitative information from electron diffraction data. These include large angle techniques for lattice parameter or quantum-well thickness determination, HOLZ diffraction for atom location, coherent diffraction for phase determination and spectrum diffraction for site-selection of atomic sub-species. In particular, the process of automated analysis of CBED to determine bonding charge distributions is progressing very rapidly at present and some recent results are given.

Introduction

The great wealth of information available in electron diffraction patterns is now more widely appreciated. However, the availability of instruments that generate energy-filtered electron diffraction patterns and of computer programs that facilitate the extraction of accurate quantitative data from them will undoubtedly cause a major step forward in the quantity and quality of the results that can be achieved. From a theoretical point of view electron diffraction is well-understood and accurate calculations may be performed rapidly and routinely. However, it is likely that with the level of quantitative comparison now possible between theory and experiment discrepancies will be discovered that will challenge some of the basic assumptions that are commonly made in formulating the diffraction problem.

In convergent beam electron diffraction (CBED) each order of reflection is studied over a range of incident angles that may be varied considerably from a few milliradians to greater than 0.1 radians. For the larger convergence angles special techniques (LACBED) are required to prevent the overlap of the different orders of diffraction. By careful choice of aperture sizes LACBED may be used to reduce the diffuse background dramatically giving accurately quantitative data [1]. The resulting patterns may be used, for example, in accurate lattice parameter determinations or for detecting monolayer changes in quantum-well structures [2].

For CBED patterns where the convergence angle is chosen to eliminate overlap between different orders completely different information can be obtained by concentrating on reflections near the centre of the pattern or on reflections in the higher order Laue zones (HOLZ). We shall consider each in turn.

As has long been appreciated, reflections close to the centre of a diffraction pattern are strongly affected by the charge redistribution that occurs on bonding between atoms in a solid. However, very high quality data and efficient computing procedures are required to extract the details of bonding charge distributions. We have found that

strongly dynamical zone axis CBED patterns are particularly effective for this purpose. The patterns have to be energy filtered and formed by elastically scattered electrons using a very small probe size to eliminate thickness averaging. A quasi-Newton method of steepest descent to a global minimum of parameter space has been used in the investigation to be described in this contribution [3].

The intensities of reflections in the HOLZ rings is strongly dependent on the atom locations ($\underline{r}_i$) within the unit cell. For large $\underline{g}$, the product $\underline{g}.\underline{r}_i$ that appears as a phase factor in the expression for the structure factor is sensitively dependent on $\underline{r}_i$. Small deviations $\underline{\Delta r}_i$ are readily detected. In order to overcome some of the limitations of zone axis CBED for data collection a new technique has been devised that is related to the precession camera of X-ray crystallography. By conical-scan of a convergent beam around a zone axis a much wider range of HOLZ reflections is generated than for zone axis incidence and the orientational averaging serves to reduce dynamical effects that can otherwise complicate the interpretation of the data obtained from HOLZ reflections [4]. In this way excellent data sets may be determined from which Patterson functions may be generated. These Patterson function maps give accurate measurements of heavy atom spacings. By subtracting the heavy atom positions deduced in this way, the lighter atom positions may be determined [5].

In the case of a microscope equipped with a cold field emission gun, coherent electron diffraction experiments may be performed. Using a slightly over-or under-focused probe, interference fringes in the overlap region between adjoining orders of Bragg reflections may be used to deduce their relative phases [6], [7]. In the case of thin crystals, the relative phases are those of the associated structure factors so that ab initio structure determination may be carried out. Even when the crystal thickness is too great for the kinematical approximation to apply, the relative phases of the reflections can be very useful in solving an unknown structure by the HOLZ-reflection precession method.

Until now we have concentrated on elastic diffraction. However, it is also possible to form diffraction patterns in energy-loss electrons. This technique, at present in its infancy, offers the prospect of an alternative method of determining atom locations. HOLZ reflections have fine structure that is related to Bloch states or clusters of Bloch states that are concentrated on particular atomic rows ('strings') along the zone axis direction. By choosing energy-loss diffraction patterns, corresponding to different elements in the structure under examination, and studying the relative changes of the intensity of HOLZ fine-structure lines, it should be possible to deduce the association of particular atomic species with particular Bloch states. We have direct evidence that this is the case in some preliminary experiments on $LaAlO_3$ [8]. An alternative approach to this problem is to perform the electron diffraction experiments in a different way that we will call spectrum diffraction. This has been implemented on a Hitachi HF2000 with a Gatan imaging filter (GIF) by placing a rectangular slit of controlled width in a plane almost coincident with the entrance aperture of the electron spectrometer. By using this slit to select a particular line of interest in the diffraction pattern, an image is produced with energy dispersion as one axis and the chosen diffraction pattern line as the other axis. This spectrum diffraction technique may be used to investigate how the fine structure lines of a particular HOLZ reflection vary in intensity with increase of energy loss. It has been used in electron diffraction experiments on $SrTiO_3$ to investigate the atomic species associated with particular Bloch states [8].

Bonding charge distribution of group 4 elements

This is an aspect of the various developments in electron diffraction that is at a particularly interesting state at present. Different groups use different approaches, both experimental and computational [9], [10]. We shall concentrate on experimental results obtained with the Hitachi HF2000/GIF combination.

The samples were held at liquid nitrogen temperatures and the microscope operating voltage was determined as 198.8 ± 0.1 kV at the <110> zone axes of silicon, diamond and germanium. The results were obtained with a probe size of approximately 3 nm and recorded with a CCD camera. The distortions introduced into the patterns by the GIF were minimized by adjusting the image of a circular aperture to be circular (to an accuracy of 1%). The intensities were stored for the central beam and the six surrounding diffracted beams in the form of a 21 x 21 pixel array for each reflection. The data had to be deconvoluted for the point spread function, $S(\underline{R})$, of the CCD detector; the method chosen was that of de Ruiter and Weiss. Suppose $I^m(\underline{R})$ is the measured two-dimensional intensity distribution and $I^r(\underline{R})$ is the required (true) intensity distribution. Then

$$I^m(\underline{R}) = I^r(\underline{R}) * S(\underline{R})$$

i.e.

$$I^m(\underline{q}) = I^r(\underline{q}) \times S(\underline{q})$$

or

$$I^r(\underline{q}) = \frac{I^m(\underline{q})}{S(\underline{q})}$$

where $\underline{q}$ is a two-dimensional Fourier space vector conjugate to the pixel vector $\underline{R}$.

$S(\underline{q})$ may be obtained by Fourier transformation of the (noisy) intensity recorded on the CCD array by uniform illumination and hence $I^r(\underline{q})$ recovered.

The next step in the analysis of the data is to calculate a set of diffracted intensities by starting with neutral atom data using an appropriate number of diffracted beams in a matrix diagonalisation and including additional beams using Bethe potentials. the actual numbers used for each material studied are given in Table 1.

Table 1

	Beams in diagonalisation	Bethe potentials
Si	121	270
Ge	173	270
Diamond	121	270

A computer algorithm was then used, based on the quasi-Newton method, to match the calculated intensities with the experimental data varying seventeen adjustable parameters as listed in Table 2.

Table 2

Real and imaginary parts of six lowest order structure factors	12
Thickness	1
Background constant	3
Scaling constant	1
Total	17

The quality of the global minimum arrived at was judged by the value of X^2 obtained, where

$$X^2 = \frac{1}{N_d} \sum_{i=1}^{N_d} \frac{\left(I_i^{exp} - I_i^{th}\right)^2}{\sigma_i^2}$$

with N_d = number of data points

σ_i^2 = variance of the experimental data

By measurements on the random noise images the variance for our detector was found to obey the relation

$$\sigma_i^2 = \left(I_i^{exp}\right)^{1.18}$$

The lowest value of X^2 obtained so far is around 3; perfect agreement would give X^2=1. The values obtained for the low-order structure factors of silicon germanium and diamond are given in Table 3. The results for silicon have been confirmed for a number of thickness at the <110> zone axis and also for off-axis orientations. In order to arrive at the Debye Waller factor the minimization was carried out at a series of choices near the accepted (isotropic) value for X-ray data and the selected value was that giving the smallest value of X^2. Unfortunately this parameter cannot be included in the normal minimization routine. The resulting change density distributions that we have obtained are shown in the figure.

One future development of this work would be to investigate the nature of bonding in intermetallic compounds. However, investigations of this nature highlight difficult problems associated with stoichiometry, point defects, the state of order and the Debye Waller factors. We are therefore at present investigating carefully the temperature and doping dependence of the results for silicon. It has been claimed previously that the effects of doping on the silicon potential can be investigated successfully by CBED measurements [11] and we intend to explore this interesting possibility thoroughly. It is important to know whether the dopant enters only into substitutional sites or if

(a)

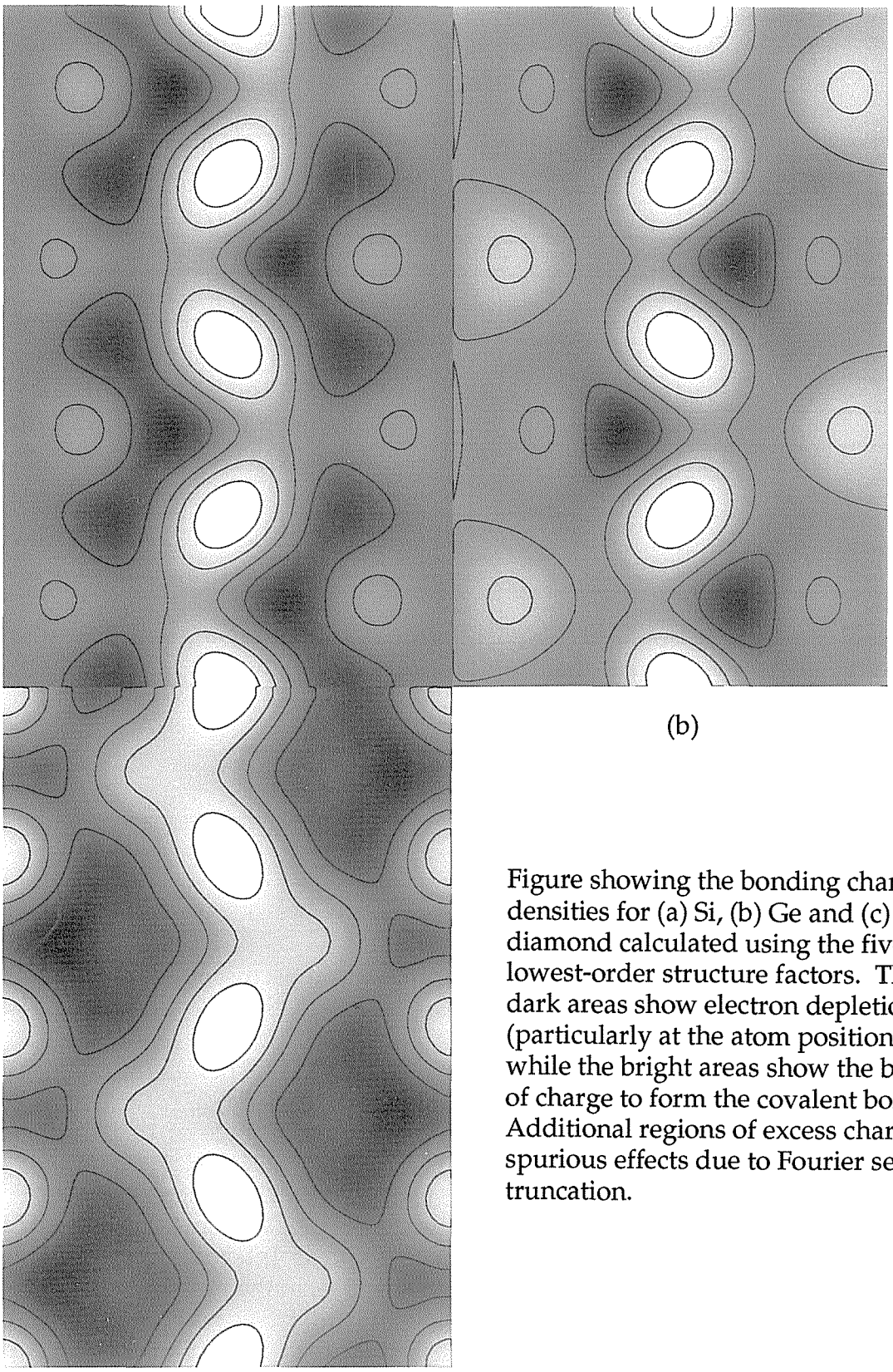

(b)

(c)

Figure showing the bonding charge densities for (a) Si, (b) Ge and (c) diamond calculated using the five lowest-order structure factors. The dark areas show electron depletion (particularly at the atom positions) while the bright areas show the build-up of charge to form the covalent bond. Additional regions of excess charge are spurious effects due to Fourier series truncation.

Structure Factor	Silicon			Germanium		
	Theory	X-ray	CBED	Theory	X-ray	CBED
111	10.600	10.603(3)	10.600(1)	27.156	27.29(6)	27.170(8)
220	8.397	8.388(2)	8.389 (7)	22.861	22.69(5)	22.94(6)
113	7.694	7.681(2)	7.686(5)	21.121	20.92(6)	21.0(1)
222	0.161	0.182(1)	0.18(1)	0.114	0.13(1)	0.30(3)
004	6.998	6.996(2)	7.07(5)	18.932	18.67(5)	19.0(2)
331	6.706	6.726(2)	6.86(9)	17.868	17.82(7)	17.6(1)
χ^2	------	---------	2.97	--------	----------	2.65
	Diamond					
	Theory	X-ray	CBED			
111	3.256	3.25(1)	3.260(2)			
220	1.934	1.920(5)	1.965(8)			
113	1.650	1.648(4)	1.74(1)			
222	0.108	0.14(1)	0.194(1)			
004	1.498	1.491(6)	1.42(3)			
331	1.480	1.483(7)	1.26(4)			
χ^2	------	---------	3.22			

Table 3: Fitted structure factors are Si(Debye Waller factor 0.25Å^2), Ge (0.24Å^2) and diamond (0.13Å^2) compared to the best X-ray and theory values. Note: A 'perfect' fit would correspond to a χ^2 value of 1.

interstitial sites may also be occupied. Fortunately there is a good deal of existing knowledge about the doping of silicon to use as a basis for this development of our work.

Acknowledgements

The authors wish to thank the Engineering and Physical Science Research Council of the United Kingdom for support of this research.

References

[1] I. K. Jordan, C. J. Rossouw and R. Vincent. Ultramiscroscopy 35 (1991) 237.
[2] N. Grigorieff, D. Cherns, M. G. Yates, M. Hockly, S. D. Perrin and M. R. Aylett. Phil.Mag. A68 (1993) 121.
[3] D. M. Bird and M. Saunders. Ultramicroscopy 45 (1992) 241.
[4] R. Vincent and P. A. Midgley. Ultramicroscopy 53 (1994) 271.
[5] P. A. Midgley, M. E. Sleight & R. Vincent Proceedings of the Thirteenth Int. Congress on Electron Microscopy (ICEM 13) Paris 1994, Vol. 1, p.919.
[6] W. J. Vine, R. Vincent, P. Spellward & J. W. Steeds. Ultramicroscopy 41 (1992) 42.
[7] J. W. Steeds, P. A. Midgley, P. Spellward and R. Vincent "Coherent Electron Diffraction and Holography", Proceedings of International Workshop on Electron Holography, Knoxville, Tennessee 1994, in the press.
[8] P. A. Midgley, M. Saunders, R. Vincent and J. W. Steeds "Energy-filtered Convergent Beam Diffraction: Examples and Future Prospects". Ultramicroscopy, in the press.
[9] J. M. Zuo and J. C. H. Spence Ultramicroscopy 41 (1992) 211.
[10] C. Deininger, G. Necker and J. Mayer. Ultramicroscopy 54 (1994) 15.
[11] R. Voss, G. Lehmpfuhl and P. J. Smith, Zeit Naturf. 35a (1980) 973.

Structure Analysis by Convergent-Beam Electron Diffraction

Michiyoshi Tanaka and Kenji Tsuda
Research Institute for Scientific Measurements, Tohoku Univ., Japan

Abstract

A method to refine crystal structural parameters (atom positions and Debye-Waller factors) using convergent-beam electron diffraction (CBED) is described, which is applicable to crystal structure analysis of a small specimen area down to a few nm in diameter.

CBED is entering a stage of quantitative studies, among which crystal structure analysis is the most important one. The CBED method has the following advantages compared with the X-ray and neutron diffraction methods with respect to crystal structure analysis.

Firstly, the CBED method enables us to obtain diffraction patterns from a small specimen area about one nanometer in diameter. The area illuminated with the incident electron beam is small enough to expect that a crystal is perfect and has a constant thickness and no bending. Consequently, CBED patterns can be directly compared with calculated ones based on the dynamical theory of electron diffraction. The method can be applied not only to the determination of perfect crystal structures but also to that of local crystal structures which change with the specimen position. This is contrasted with the fact that X-ray and neutron diffraction analyses determine the structural parameters averaged over a large specimen volume which consists of mosaic crystals and includes many domains and lattice defects.

Secondly, CBED intensities possess information on the phases of crystal structure factors because of strong dynamical diffraction effects. This fact shows a great difference from X-ray and neutron diffraction analyses, in which the intensities can be explained by the kinematical diffraction theory and information on the phases of crystal structure factors is lost. Therefore, CBED can determine atom positions without encountering the phase problem with which X-ray structure analysis is confronted.

In X-ray analysis, corrections of intensity data especially for extinction and absorption are important while such corrections are not necessary in the case of CBED. Hence, raw intensity data on CBED patterns are of good quality to compare directly with theoretical intensities when the patterns are taken from thin specimens. However, one important thing to be done for accurate structure determination is the subtraction of inelastically scattered electrons. A comparison between structure analysis by X-rays and that by CBED is given in Table 1.

	Electron diffraction	X-ray diffraction
Scattering length	Large ($\sim 10^4$) (dynamical)	Small (1) (kinematical)
Lenses	Usable	Not usable
Specimens	Small specimens (local structure)	Large crystals (average structure)
Influence of twins and defects	No (perfect crystal, single-domain)	Yes (mosaic crystal, multi-domains)
Important corrections of intnesity data	Background due to inelastic scattering	Absorption and extinction
Phase information on structure factors	Obtainable (dynamical)	Not obtainable (kinematical)

Table 1: Comparsion between structure analysis by X-rays and that by CBED.

We should not forget to emphasize that recent technical developments have enabled the structure analysis by the CBED method. The first is new recording tools for electrons – an imaging plate (IP) and a slow scan CCD camera, which have taken the place of negative films. They have high sensitivity, a wide dynamic range and a linear response for electron doses. The second is energy filtering techniques to eliminate inelastically scattered electrons, using energy filters of the sector-type and the omega-type. Those filters are indispensable for the structure analysis with high precision. The third is high-speed computers for laboratory use or work stations. Many-beam dynamical calculations using more than one hundred beams are necessary for obtaining accurate CBED intensities. The calculations are carried out for a large number of points with different excitation errors, and further repeated

by changing structural parameters to obtain their final values, using the nonlinear least square method. Without use of a recent work station, the structure analysis by CBED is impossible.

Vincent *et al.* [1] first applied the CBED method to the determination of the atom positions of AuGeAs. They estimated the experimental intensities of the HOLZ reflections recorded on negative films, using their eyes. They determined the positional parameters by fitting the experimental intensities with the theoretical ones calculated under a quasi-kinematical approximation. Vincent & Exelby [2] applied the same method to the structure determination of a metastable Al-Ge phase. Tanaka & Tsuda [3], [4] refined the structural parameters (the rotation angle of the oxygen octahedron and the Debye-Waller factor) of the low-temperature phase of $SrTiO_3$, which is known to undergo a typical second-order phase transformation, on the basis of the dynamical theory of electron diffraction.

Recently, the automatic matching of experimental and theoretical CBED patterns has been challenged by minimizing the R factor by the steepest-descent method (Marthinsen, Høier & Bakken [5]), the simplex method (Zuo & Spence [6]), the quasi-Newton method (Bird & Saunders [7]) and by the Marquadt method (Tsuda & Tanaka [8]). Bird & Saunders [9], [10] studied the sensitivity and accuracy of CBED pattern matching and tested an *ab-initio* determination method for the structure factors on the [110] axis of GaP, using simulated patterns as ideal experimental data.

We think that a method to refine crystal structural parameters is important for materials science. The procedure of our method for structure refinement is briefly described. A refinement of the structural parameters of $SrTiO_3$ is demonstrated. Another example of CdS will be reported at the conference.

Use of HOLZ reflections

HOLZ reflections are used for structure analysis by CBED. Generally, the intensities of HOLZ reflections with large reciprocal lattice vectors $\boldsymbol{g}$ are more sensitive to the displacements of atoms than those of ZOLZ reflections. This can be understood from the fact that the crystal structure factor F_g includes the phase factor $\exp(-2\pi i \boldsymbol{g}\cdot\boldsymbol{r})$ (Fig. 1). For a reflection with a large $\boldsymbol{g}$, the phase factor varies greatly with small changes of atomic coordinate $\boldsymbol{r}$. Thus, small displacements of atoms can be sensitively detected using HOLZ reflection intensities.

HOLZ reflection intensities change not only in the radial direction but also in the azimuthal direction, which are explained in terms of dispersion surfaces of Bloch waves. The best way for structure analysis is to use all the two-dimensional data. We, however, we use them as one-dimensional line profiles along the radial direction to reduce the computing time of dynamical intensities, since the intensities of HOLZ reflections are almost uniform to a limited extent in the azimuthal direction when a CBED pattern is taken from a thin specimen area. It is possible to use integrated intensities as fitting data instead of line profiles.

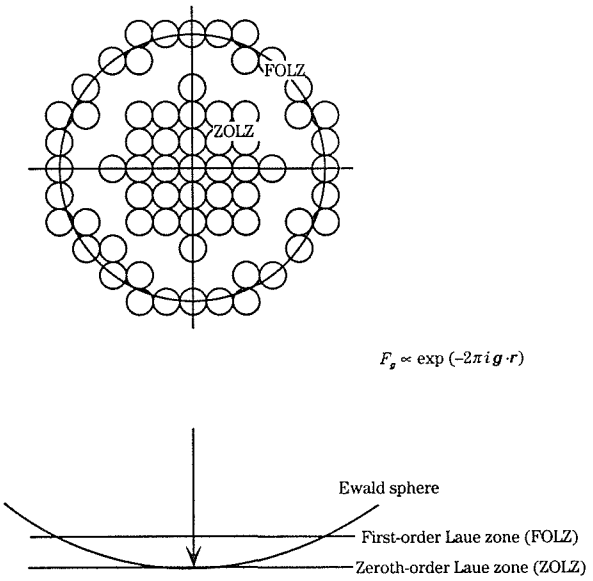

Fig.1: FOLZ reflections having larger g are more sensitive to the atoms positions than ZOLZ reflections.

Analysis Procedure

In advance of analysis, the space group, the lattice parameters and the tentative positional parameters of atoms of a crystal are assumed to be known, and the accelerating voltage of the incident electrons is separately determined using a HOLZ line pattern of a standard specimen like Si. The analysis procedure is as follows :

(i) CBED patterns are taken from the crystal, using IPs in an electron microscope. A thin area of the specimen has to be chosen to reduce inelastically scattered intensities. We do not use an energy filter at present. If the expected atomic displacements are known in advance, an electron incidence that makes CBED patterns sensitive to the displacements should be selected.

(ii) The intensities of the CBED patterns are read out from the IPs in an IP-reader and are transferred to a work station as a digital images.

(iii) The distortion of the patterns due to the lens aberrations of the electron microscope is numerically corrected on the work station. The line profiles of HOLZ reflections along the radial directions through the centers of the disks are

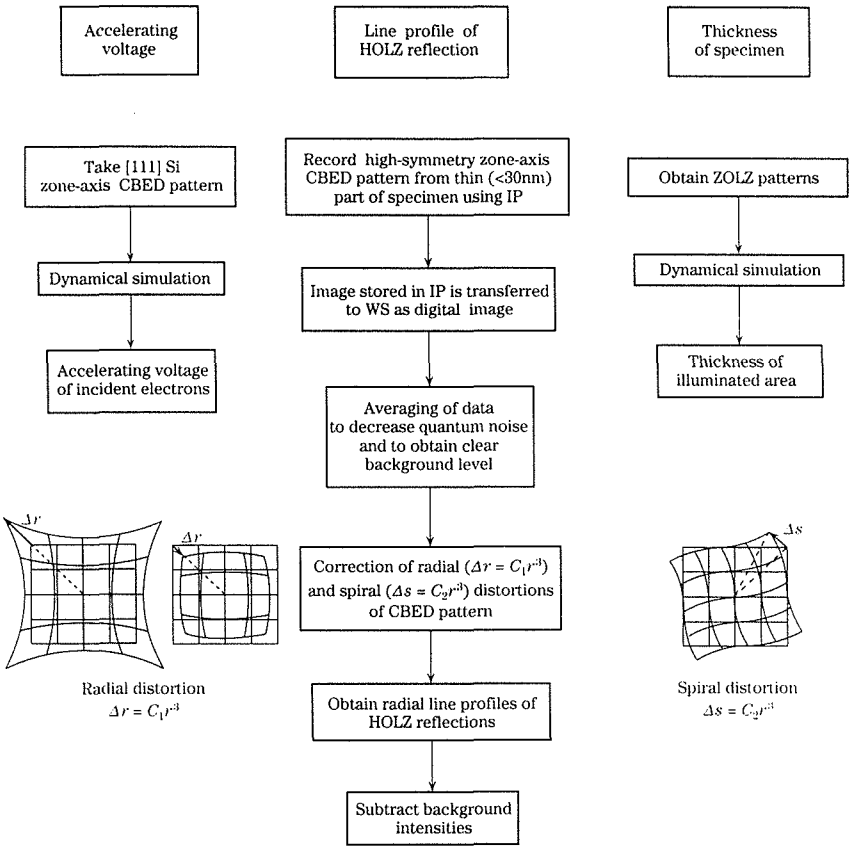

Table 2: Procedure of the crystal structure analysis (experiments).

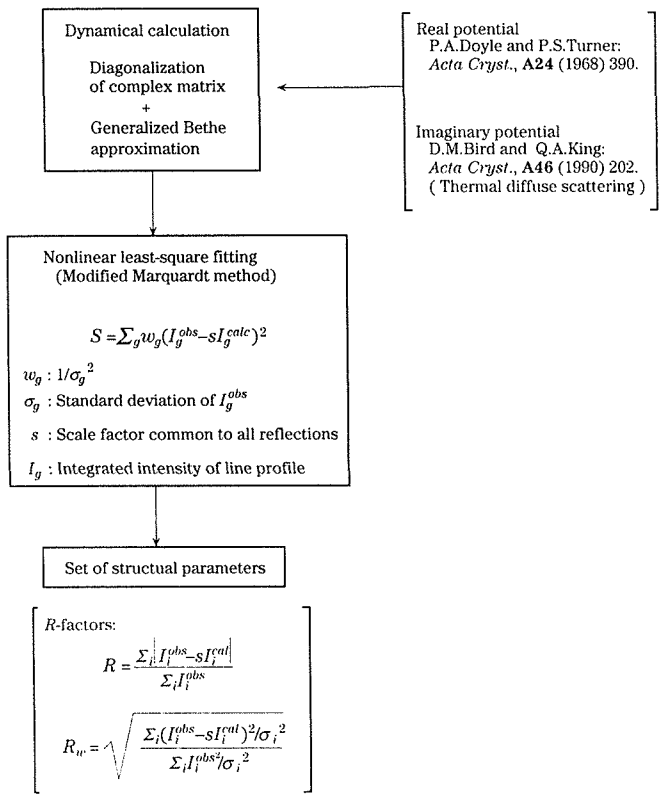

Table 3: Procedure of the crystal structure analysis (calculations).

taken from the CBED patterns. Background intensities are subtracted from the line profiles in a certain approximation.

(iv) The thickness of the specimen is determined by comparing a ZOLZ pattern with those simulated at different thicknesses. Since the patterns are not so sensitive to the structural details, the dynamical simulations are carried out using the structural parameters initially assumed.

(v) The structural parameters are refined by a nonlinear least square method [11] so as to minimize the residual sum of squares S between the experimental HOLZ line profiles and calculated ones. Intensity calculations are carried out by the Bloch wave dynamical theory of electron diffraction with the aid of a generalized Bethe approximation [12]. The analysis procedure is summarized in Tables 2 and 3.

To attain better accuracy for the present method, 1) two-dimensional fittings of the intensity distributions of HOLZ reflections are necessary instead of one-dimensional fitting of the line profiles, 2) energy filtering to remove plasmon-loss electrons is required, 3) the installation of image-forming lenses with small distortion is necessary, and 4) the number of fitting parameters, which is limited to a small number at present to reduce the calculation time, should be increased. It is noted that an increase of the calculation time with the number of the parameters should be compensated, for example, by a perturbation method [13], [14] to calculate Jacobian matrices.

The maximum entropy method (MEM) is worth applying to obtaining crystal-potential distribution from CBED patterns without determining Debye-Waller factors — ambiguous parameters due to anisotropy, anharmonicity, etc —.

$SrTiO_3$

We have applied the present method to the low-temperature phase of $SrTiO_3$. $SrTiO_3$ undergoes a second-order phase transformation at 105K from the high-temperature phase of the space-group $Pm3m$ to the low-temperature phase of the space-group $I4/mcm$. The high-temperature phase has a cubic Perovskite structure, in which Sr atoms occupy the lattice corners, oxygen atoms the face centered positions and a Ti atom occupies the body center (Fig. 2(a)). In the low-temperature phase, an oxygen octahedron slightly rotates clockwise with respect to the z-axis and the neighbouring oxygen octahedra rotate anticlockwise. This type of atom displacements is described by the condensation of the R_{25}-phonon mode of the high-temperature phase. The positions of Sr and Ti atoms are unchanged. The rotation manner of the octahedra in the successive unit cells is shown in Fig. 2(b). The lattice

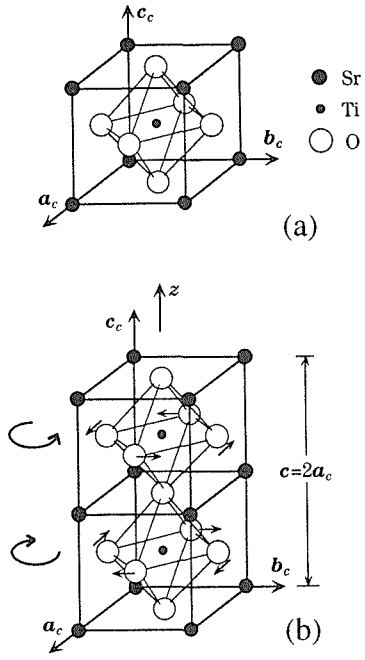

Fig.2: Crystal structures of $SrTiO_3$ (a) high-temperature phase, (b) low-temperature phase.

parameters a and c of the low-temperature phase are given by $a \sim \sqrt{2}a_c$ and $c \sim 2a_c$, where a_c is the lattice parameter of the high-temperature phase.

Table 4 shows the atomic coordinates of the low-temperature phase. The rotation angle ϕ of the oxygen octahedron is related to the parameter x for the O(2) atoms by the equation $x = (1 - \tan\phi) / 4$. Therefore, the structure analysis of the low-temperature phase implies to determine only one positional parameter, the rotation angle ϕ of the octahedron and the Debye-Waller factor B of the oxygen ions, where B is assumed to be isotropic. $SrTiO_3$ is the most suitable substance for the first application of the present method.

Figure 3(a) shows a CBED pattern of the low-temperature phase of $SrTiO_3$ taken with the [001] incidence at 87K from a 3-nm-diameter area in one domain. The electron microscope used was a JEM-100CX equipped with a field emission gun (FEG). The first-order Laue zone (FOLZ) reflections are superlattice reflections

Atom	Wyckoff position	x	y	z
Sr	4*b*	0	1/2	1/4
Ti	4*c*	0	0	0
O(1)	4*a*	0	0	1/4
O(2)	8*h*	x	1/2+x	0

Table 4: Atomic coodinates of the low temperature phase of $SrTiO_3$.

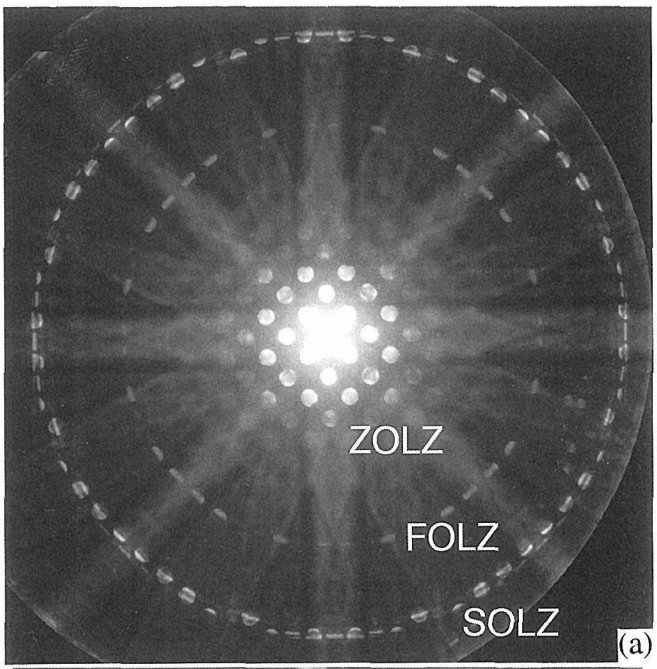

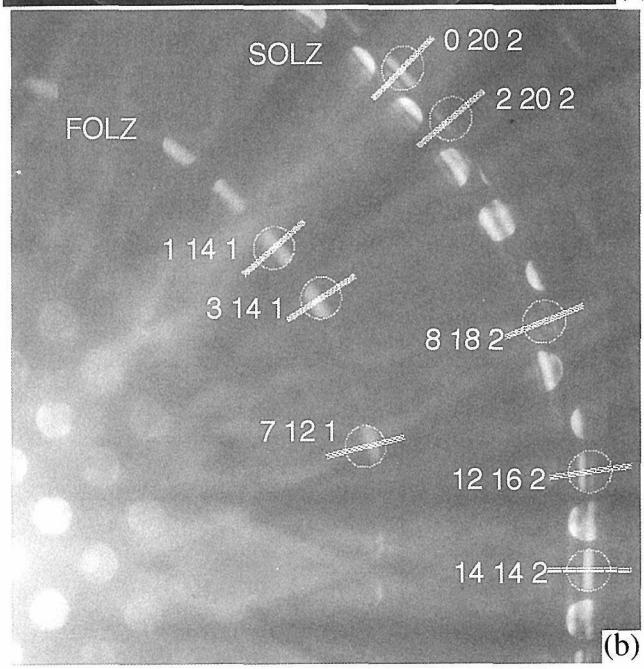

Fig.3: CBED patterns of the low-temperature phase of $SrTiO_3$.

appearing only in the low-temperature phase, where the lattice parameter c is twice that in the high-temperature phase. The intensities of the reflections are governed by the value of the rotation angle of the oxygen octahedron. The second-order Laue zone (SOLZ) reflections were the FOLZ reflections in the high-temperature phase. Only O(2) oxygens contribute to the h k 2 (h, k = even) reflections, but all the atoms to the h k 2 (h, k = odd) reflections. The CBED pattern exhibited a fourfold rotation and two types of mirror symmetries, the total symmetry being $4mm$. Hence, the reflections within one eighth sector are symmetry independent. Figure 3(b) shows a quarter sector of Fig.3(a). After performing distortion correction and averaging of the CBED pattern, three FOLZ reflections and five SOLZ reflections with even values of h and k indicated in Fig. 3(b) were used for the analysis, all of these reflections being unaffected by Sr, Ti and O(1) atoms but only by O(2) atoms.

Background subtraction

Background intensities are subtracted from the original line profiles. Figure 4(a) shows a line profile of the 1 14 1 reflection. The subtraction of a linear form background, using the intensities at both ends of the line profile, resulted in the profile of Fig. 4(b). Positional parameters of $SrTiO_3$ are determined by fitting the intensities of line profiles and the integrated intensities of HOLZ reflections with theoretical ones calculated by full dynamical treatment.

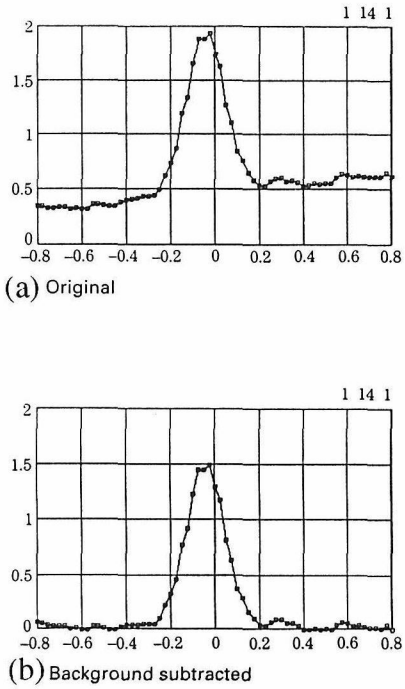

Fig.4: Experimental line profiles of 1 14 1 HOLZ reflection. (a)original profile, (b)profile whose background was subtracted.

Sensitivity of HOLZ reflections to ϕ and B

Figure 5(a) and (b) show sensitivity-test simulations of the 7 12 1 reflection to the rotation angle ϕ of the oxygen octahedron and the Debye-Waller factor B of the oxygen, respectively. Considerable intensity changes are seen to occur with small changes in ϕ and B, ensuring accurate determination of these parameters. It should be noted that the profiles do not change in peak positions but in intensities. This indicates that

the parameters can be determined by using the integrated intensities as well as the line profiles.

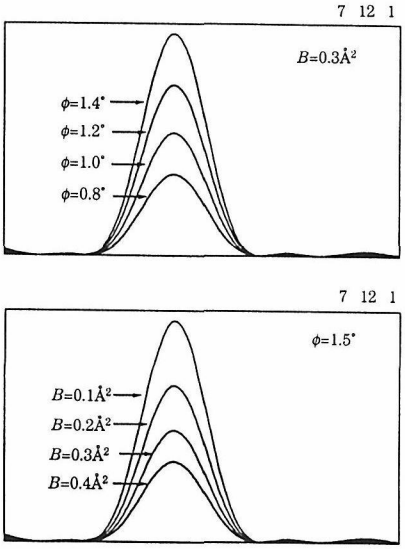

Fig.5: Simulated line profiles of 7 12 1 HOLZ reflection for different j (a) and for different B(b).

Determination of specimen thickness

The specimen thickness was determined by comparing an experimental ZOLZ pattern with calculated ones. Figure 6(a) shows the central part of Fig. 3(a). Figure 6(b) shows a dynamically simulated pattern for a specimen thickness of 20nm at an accelerating voltage of 86kV separately determined. Close comparison between the experimental and simulated patterns revealed that the specimen thickness was 20± 1nm.

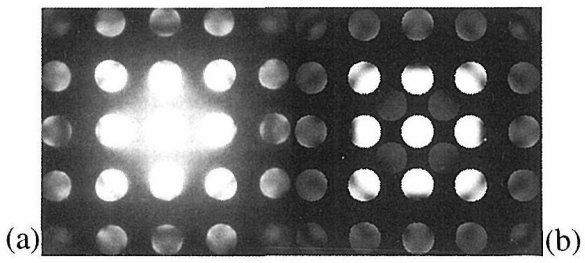

Fig.6: ZOLZ CBED patterns : (a)experimental pattern (the central part of Fig. 3) ; (b) dynamically simulated patterns with a specimen thickness of 20nm.

Results— Case I : integrated intensities

Using the integrated intensities of the HOLZ line profiles, the rotation angle of the oxygen octahedron ϕ and the Debye-Waller factor B(O(2)) were determined to minimize the residual sum of squares $S = \sum_g w_g (I_g^{obs} - sI_g^{calc})^2$ between experimental intensities and calculated ones. The values obtained were $\phi = 1.12 \pm 0.04°$ and B(O(2)) $= 0.35 \pm 0.06$Å^2 with R-factor values of $R = 8.2\%$ and $R_w = 5.3\%$. Table 5 gives the final results of the fitting between the experimental and calculated intensities, which show good agreement. Figure 7 shows the contour map of the residual sum of squares $S = \sum_g w_g (I_g^{obs} - sI_g^{calc})^2$ with respect to the parameters ϕ and B. Since no local minimum is seen, it is ascertained that the values of the parameters obtained are the true solution corresponding to the global minimum of S.

In the present analysis, the fitting parameters used were limited to ϕ, B(O(2)) and scale factor s to reduce the calculation time. The method will be extended to add lattice parameters, Debye-Waller factors of the other atoms (Sr, Ti and O(1)), the specimen thickness and low-order structure factors as fitting parameters.

h k l	obs.	cal.	res.
7 12 1	3.675	2.489	1.186
1 14 1	4.627	4.563	0.063
3 14 1	5.494	5.734	−0.240
14 14 2	8.518	8.501	0.017
8 18 2	1.675	2.405	−0.731
12 16 2	2.964	3.018	−0.054
0 20 2	4.458	4.429	0.029
2 20 2	1.000	1.353	−0.353

Observed intensities, calculated intensities and their residuals.

Table 5: Final results of the fitting (integrated intensity).

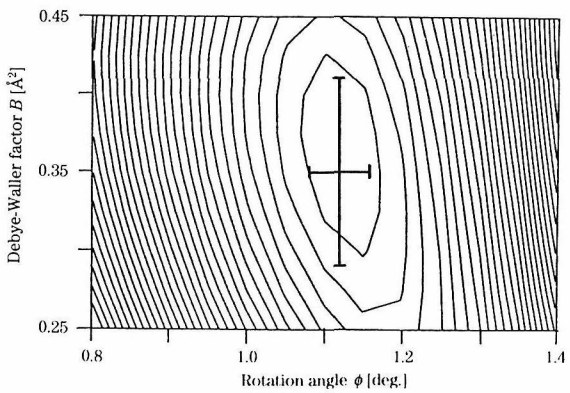

Fig.7: Contour map of the residual sum of squares S.

Case II : line profiles

Using the HOLZ line profiles, ϕ and B(O(2)) were determined so as to minimize S. The values refined were ϕ = 1.14 ± 0.01° and B(O(2)) = 0.37 ± 0.01Å^2. This result agrees with that obtained for the integrated intensities, within error.

Calculated intensities are seen to agree well with experimental ones in Fig. 8. However, the remaining small discrepancies give not good R-factors, R = 31.6% and R_w = 41.6%. One of the reasons for the large R and R_w factors compared with those for the integrated intensity (case I) is a uniform shift of the line profiles with respect to the calculated ones because of a distortion of the CBED pattern due to the aberration of the image forming lenses.

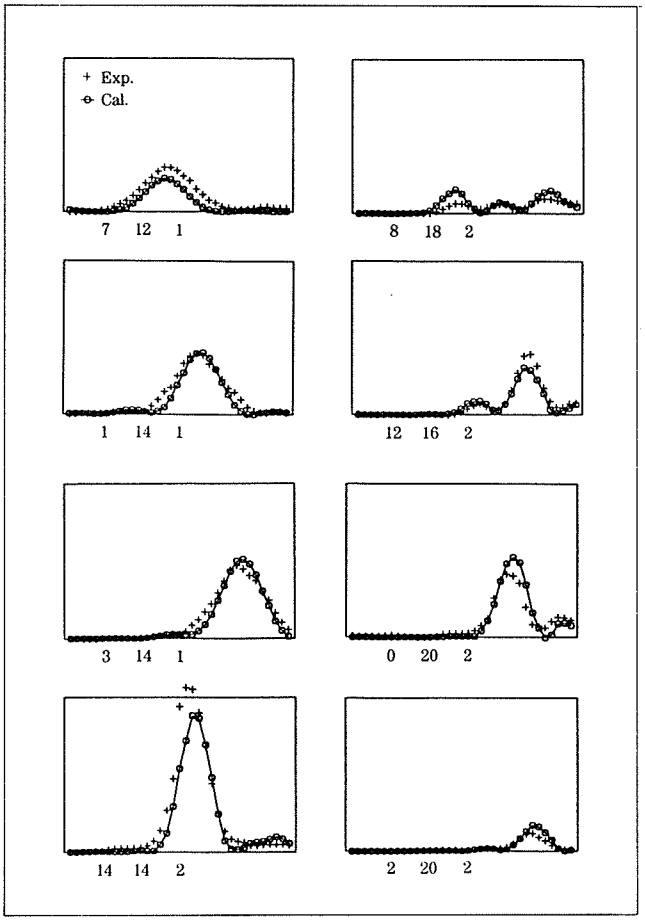

Fig.8: Experimental and calculated line profiles.

Comparison

By electron spin resonance experiments, Unoki and Sakudo [15] and Müller *et al.* [16] measured the rotation angle ϕ of the oxygen octahedron as a function of temperature over the temperature range from 4 to 105K. The former obtained 1.4 ± 0.1° as the value of ϕ and the latter 1.25°, both at 78K. Shirane and Yamada [17] determined ϕ to be a similar value of 1.37 ± 0.35° with a little low precision at 78K by neutron diffraction. Fujishita *et al.* [18] determined ϕ to be 1.6 ± 0.1° at 77K by X-ray diffraction.

Figure 9 shows the above results together with the present one. The present result, shown by a black circle, is in good agreement with those of Unoki and Sakudo (ϕ = 1.3° at 87K) and Müller *et al.* (ϕ = 1.1° at 87K). The present result also agrees with that of Shirane and Yamada when the temperature dependence obtained by Unoki and Sakudo and Müller *et al.* is assumed. The value by Fujishita *et al.* is a little larger than the other results reported and may be a little different from ours even if the temperature difference is taken into account.

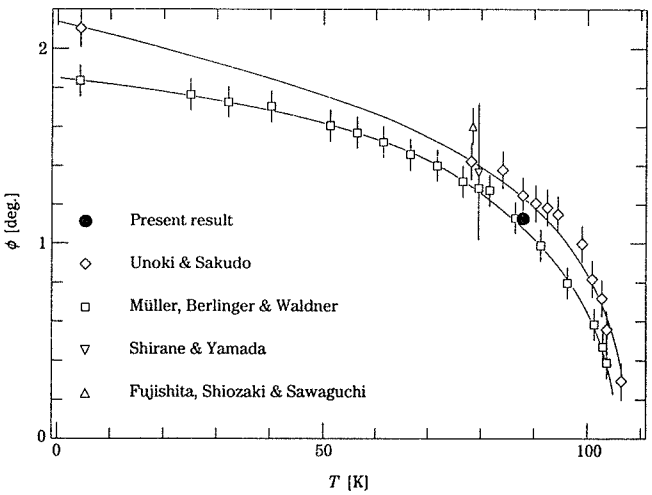

Fig.9: Present result agrees well with other results already reported.

References

[1] R. Vincent, D. M. Bird and J. W. Steeds : *Philos. Mag.*, **A50** (1984) 745 and *ibid* 765.

[2] R. Vincent and D. R. Exelby : Proc. XIIth International Congress on Electron Microscopy, Seattle, eds. L. D. Peachy and D. B. Williams, San Francisco press, Vol. 2, 1990, p.524.

[3] M. Tanaka and K. Tsuda : Proc. XIIth International Congress on Electron Microscopy, Seattle, eds. L. D. Peachy and D. B. Williams, San Francisco press, Vol. 2, 1990, p. 518.

[4] M. Tanaka and K. Tsuda : Proc. 26th Meeting of Micro-beam Analysis Soc., San Jose, ed. D. G. Howitt, San Francisco press, 1991, p. 145.

[5] K. Marthinsen, R. Høier and L. N. Bakken : Proc. XIIth International Congress on Electron Microscopy, Seattle, eds. L. D. Peachy and D. B. Williams, San Francisco press, Vol. 2, 1990, p. 492.

[6] J. M. Zuo and J. C. H. Spence : *Ultramicroscopy*, **35**, (1991) 185.

[7] D. M. Bird and M. Saunders : Proc. 26th Meeting of Micro-beam Analysis Soc., San Jose, ed. D. G. Howitt, San Francisco press, 1991, p. 153.

[8] K. Tsuda and M. Tanaka : *Acta Cryst.*, **A51** (1995) 7.

[9] D. M. Bird and M. Saunders : *Ultramicroscopy*, **45**, (1992) 241.

[10] D. M. Bird and M. Saunders : *Acta Cryst.* **A48**, (1992) 555.

[11] R. Fletcher : A modified Marquardt Subroutine for Nonlinear Least Squares, *Harwell Report*, AERE-R (1971) 6799.

[12] M. Ichikawa and K. Hayakawa : *J. Phys. Soc. Jpn.*, **42** (1977) 1957.

[13] D. M. Bird : *Acta Cryst.*, **A46** (1990) 208.

[14] J. M. Zuo : *Acta Cryst.*, **A47** (1991) 87.

[15] H. Unoki and T. Sakudo : *J. Phys. Soc. Jpn.*, **23** (1967) 546.

[16] K. A.Müller, W. Berlinger and F. Waldner : *Phys. Rev. Lett.*, **21** (1968) 814

[17] Y. Shirane and Y. Yamada : *Phys. Rev.*, **177** (1969) 858

[18] H. Fujishita, Y. Shiozaki and E. Sawaguchi : *J. Phys. Soc. Jpn.*, **46** (1979) 581

Detection of Cherenkov and Transition Radiation from Thin Films and Small Particles in TEM

N. Yamamoto and A. Toda
Department of Physics, Tokyo Institute of Technology
Oh-okayama, Meguro-ku, Tokyo 152, Japan

1.Introduction

It is known that a charged particle can emit light when it moves in transparent medium with a velocity larger than the phase velocity of light, which is called Cherenkov radiation. There is another type of radiation which is generated when a charged particle passes through a boundary between two media with different dielectric constants, called transition radiation. Recently these radiations were detected in TEM by a light detection system originally used for cathodoluminescence[1].

Specimen thickness used for TEM observation is usually less than 1 μm which is comparable with wavelength of visible light. Then some characteristic features are seen in the emission spectra of these radiations due to interference effect; for example, intensity oscillation against wavelength appears in the spectra from dielectric and semiconductor thin films, which depends on specimen thickness and accelerating voltage[2]. In the case of metal thin film, transition radiation is predominant. In addition, radiative mode of surface plasmon, called Ferrell mode ,gives rise to a sharp peak in an emission spectrum as a part of transition radiation. Such peak was observed for a silver thin film at the wavelength corresponding to the plasma frequency, and was found to be sensitive to imperfections such as grain boundary.

Recently we have developed an imaging system using the collected light signal, which visualizes 2-dimensional intensity distribution of the radiation. In this paper we show characteristic feature in the emission spectra from thin films of mica and silicon, and monochromatic images of the specimens using emission signal of particular wavelength. Particles of MgO and $BaTiO_3$ were also studied by this technique.

2. Results

Figure 1(a) shows a TEM image of a mica thin film. Several surface steps are seen as parallel lines, and broad dark line contrasts across the steps are bend contours. Figure 1(b) and (c) are emission spectra taken with an electron beam probe located at points marked A and B in (a). The accelerating voltage is 200 kV and the ellipsoidal mirror for light collection is set above the specimen, i.e., the spectra are for backward emission integrated over the solid angle of hemisphere. The intensity decreases in the wavelength region below 300 nm due to the deficiency of the detection system. A set of peaks are seen in the spectra, and their positions change from (b) to (c), since the specimen thickness at B is larger than at A. The peak wavelength λ_m of the m-th order is approximately given by the following relation,

$$\frac{d}{\beta}(1+\beta n\cos\theta')=(m+1/2)\lambda_m ,$$

where d is thickness of a specimen, β =v/c, v the velocity of electron, n the refractive index, and θ' the emission angle inside the specimen. By comparing with calculated spectra the thicknesses at A and B are found to be nm and nm, respectively. At the wavelength of 340 nm, the spectrum has a minimum in (b) and has a maximum in (c). While at 350 nm the situation is reversed. Figures 1(d) to (f) show monochromatic images of the same area in (a), taken at the wavelength of 340 nm, 350 nm and 550 nm, respectively. The terraces are seen to be contrasted with different brightnesses; the terrace of A is dark in (d) and bright in (e), while the terrace of B is bright in (d) and dark in (e). It is found from a calculation that the emission intensity at any wavelength change sinusoidally with increasing thickness, and the period is proportional to the wavelength as expected from the above equation.

Figure 2(a) shows a (220) dark field TEM image of a silicon thin film in the (111) orientation taken at 200 kV, where equal thickness contours are seen. An emission spectrum shown in Fig.2(b) is for backward emission taken from a flat region of constant thickness. Silicon absorbs light in the visible region, and then the refractive index is complex, n=n + ik; the absorption coefficient k is large in the short wavelength region and is small for wavelength longer than 500 nm. A set of peaks appear in the longer wavelength region, which are generated by interference between transition radiations generated at top and bottom surfaces. Then the spectral shape in this region changes with specimen thickness and accelerating voltage. On the other hand the spectral shape in the short wavelength region does not depend on those parameters; it corresponds to the spectrum from a single boundary between vacuum and a bulk silicon crystal. Cherenkov radiation is not observed at normal incidence, since it is totally reflected by surfaces because of the large refractive index. Figures 2(c) and (d) are monochromatic images of the same area as in (a) taken at the wavelengths of 300 nm and 550 nm, respectively. In (c) it is seen that a bright contrast appears near the edge and almost uniform contrast arises inside the crystal although the specimen thickness increases there. This feature is in good agreement with the calculation. However, a dark and bright bands appear in the thicker region as indicated by arrows. These contrasts are not expected from the calculation based on the plate shape specimen at normal incidence. The origin of these contrasts are not clear yet. In (d) fringe contrasts parallel to the edge are seen corresponding to the equal thickness contour in (a). The period of the fringes depends on the wavelength of the emission; it increases linearly with the wavelength.

As for radiations from metal thin films, silver films with thickness less than 100 nm were studied. In the backward emission spectra from a film of 50 nm in thick, a sharp peak are seen to appear at the wavelength of 330 nm, which corresponds to the radiative mode of surface plasmon. The peak disappears in the spectrum from a polycrystalline film. This means the radiative surface plasmon is sensitive to crystal imperfections. There is another broad peak around 400 nm in the spectrum, which is considered to be due to non-radiative mode of surface plasmon which can emits light through surface roughness. Monochromatic images using these radiations were observed, which indicates characteristic contrasts at hole edges of the film and grain boundaries. The lateral resolution changes in the images taken with different wavelengths.

Emission spectra from particles of $BaTiO_3$ and MgO were studied. A $BaTiO_3$ plate show a broad peak near 400 nm and rapid decrease below 400 nm due to absorption. A particle of $BaTiO_3$ with spherical shape shows a similar spectrum with a rather sharp peak, and the peak position moves to short wavelength as a particle size becomes small from 3 μm to 60 nm. A set of peaks due to interference were observed for a particle of diameter around 1 μm.

Figure 3(a) shows a TEM image of a MgO smoke crystal of cube shape, and (b) is a forward emission spectrum taken at 200 V. The electron beam with a probe size of 0.1 μm was located on the specimen as marked by a white circle. The spectrum has a shape similar to that of mica in Fig.1, and peaks are also seen in (b). The peak position changes with particle size, then their appearance is due to interference effect. A backward emission spectrum was also observed in which those peaks are less intense. Theoretical work for the radiation from particles has not been well developed yet. The radiation generated by electrons passing near the side surface of the cube should contain Smith-Purcell radiation, and so the interpretation may become more complicated.

References

[1]N.Yamamoto and H.Sugiyama;Radiation Effects and Defects in Solids,117(1991)5.
[2]H.Sugiyama, A.Toda and N.Yamamoto; Proc.13th Int.Conf.Electron Microscopy, (1994,Paris) vol.1,p.833.

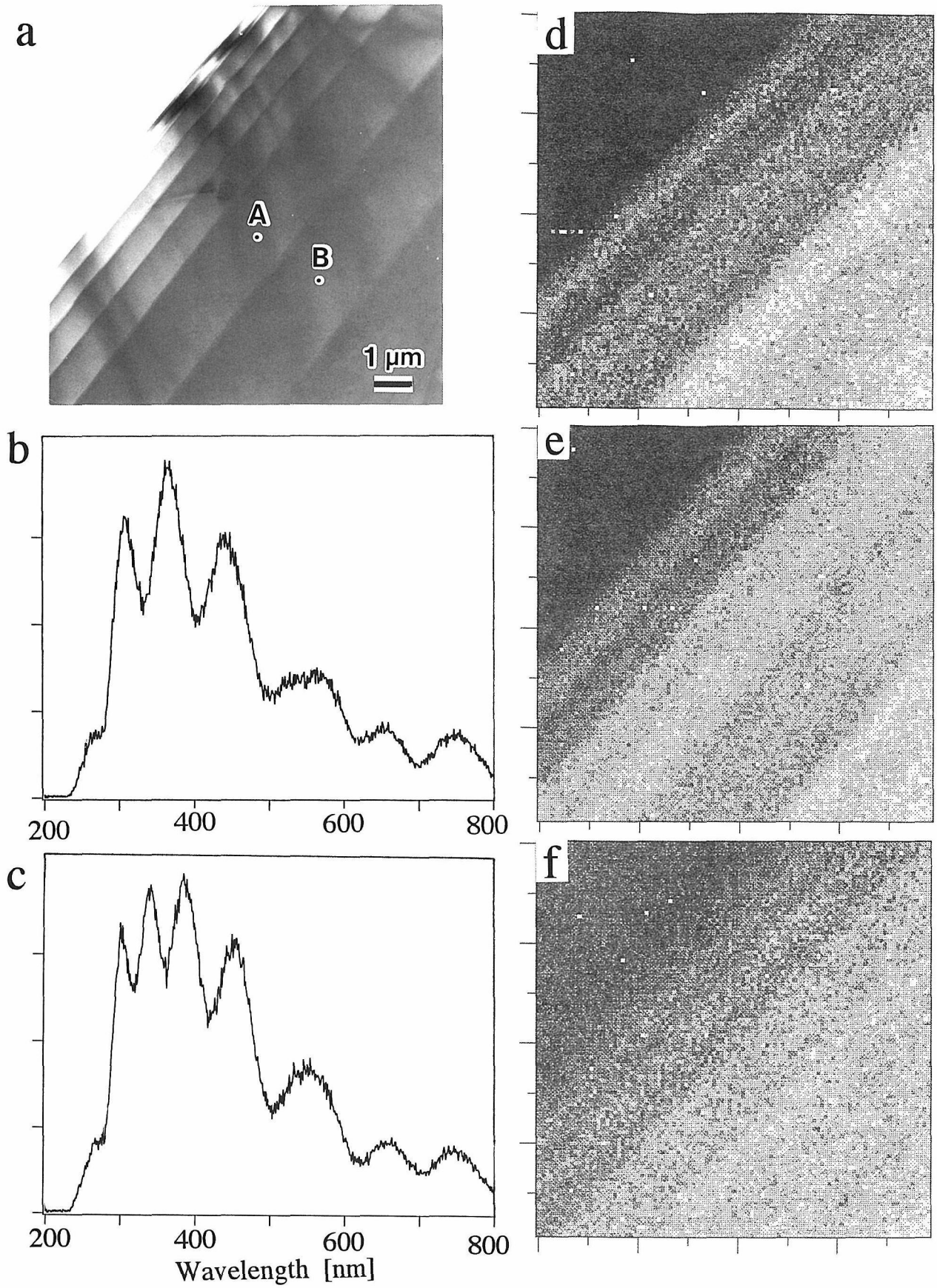

Fig.1 (a) a TEM image of thin mica film, (b) and (c) backward emission spectra from the position marked A and B in (a). Monochromatic images of (d) to (f) were taken at the wavelengths of 340, 350 and 550 nm.

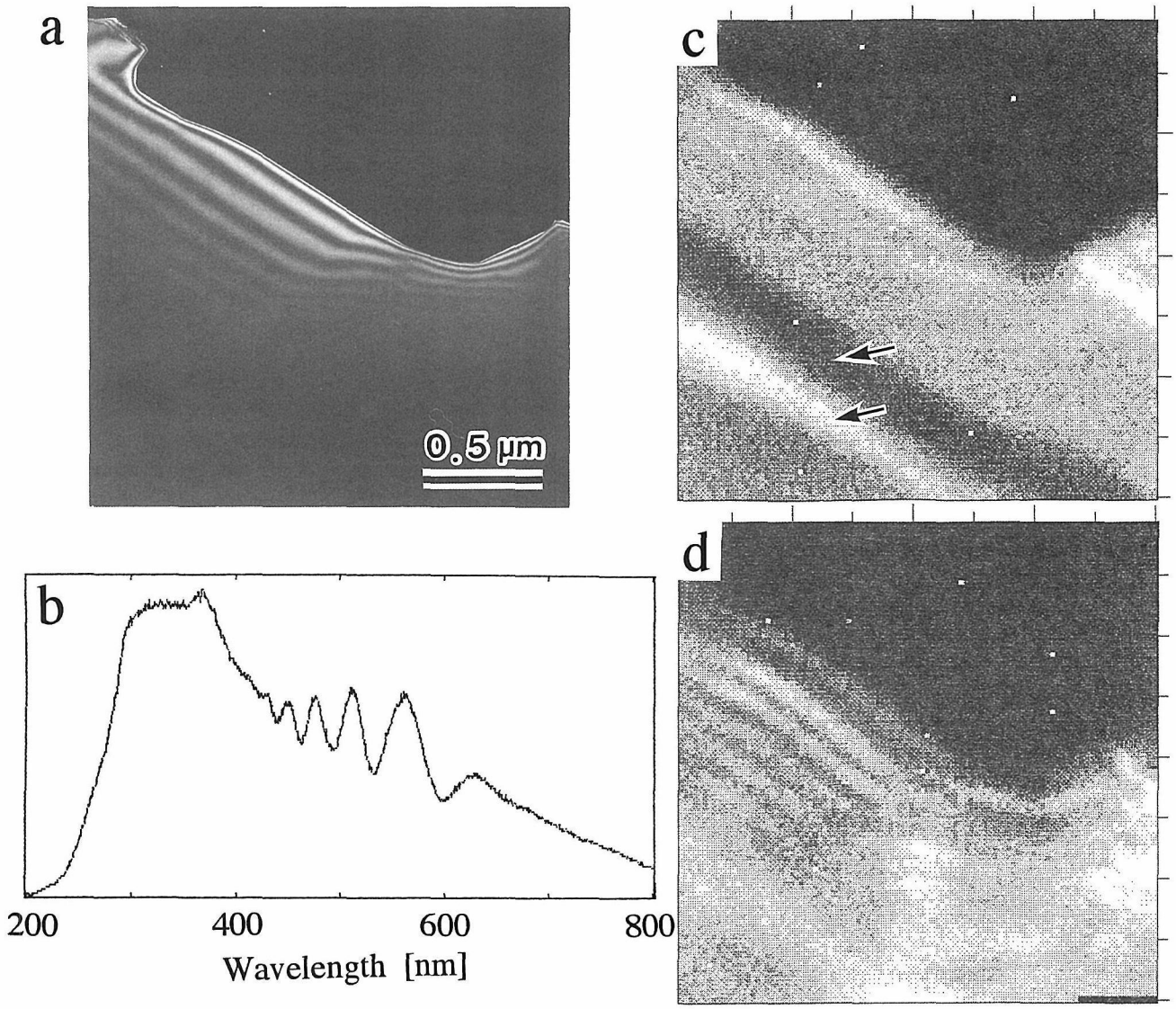

Fig.2 (a) a dark field TEM image of Si thin film, (b) a backward emission spectrum from a flat region, and (c) and (d) monochromatic images taken at 300 nm and 550 nm.

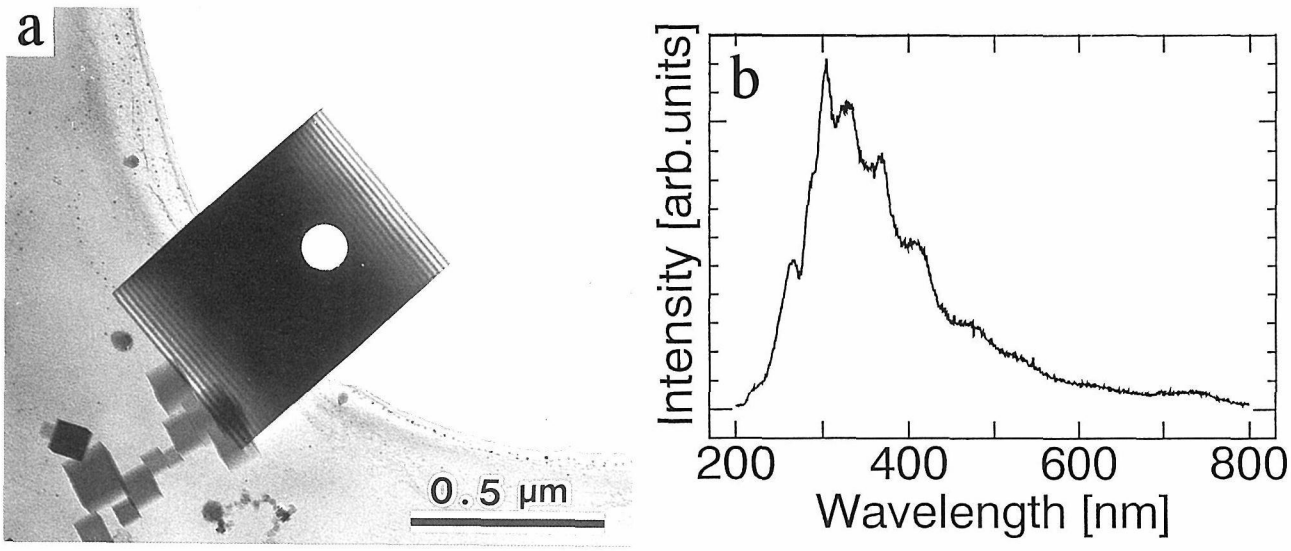

Fig.3 (a) a TEM image of a MgO smoke crystal, and (b) a forward emission spectrum taken with an electron beam located at the position marked a white circle in (a).

Multidetector Methods for Super-Resolution in STEM

J.M. Rodenburg and P.D. Nellist
Cavendish Laboratory, Madingley Road, Cambridge CB3 0HE, U.K.

Abstract

The advantages of processing data collected from an array of detector elements in the far-field of a scanning transmission electron microscope (STEM) are described. It is shown that such multidetector methods can allow atomic structure to be imaged at much increased resolution, without knowledge of the lens function. Data from a 100keV STEM is capable of matching the performance of state-of-the-art high-voltage TEMs.

Introduction

There are a number of difficulties encountered when studying material structure at the atomic scale using transmission high-resolution electron microscopy (HREM). Once the electron beam has traversed the specimen, it is necessary to re-interfere it into an image using a magnetic lens which always has a high degree of spherical and higher-order aberrations. A thin specimen only introduces a small phase change into the beam, which is proportional to the projected atomic potential, and so obtaining any image contrast whatsoever requires a lens transfer function which dephases the scattered amplitude, so that the intensity of the final image contrast can be made proportional to the phase of the exit wave. This can be achieved by balancing the spherical aberration of the lens with an appropriate amount of defocus, resulting in the so-called Scherzer condition [1]. However, this sort of conventional imaging is limited in resolution to about, say, one hundred times the electron wavelength, and the measured image contrast is a highly sensitive function of the lens excitation and beam alignment. Furthermore, relating contrast to the actual atomic structure is further complicated by the wave propagation within the specimen and the very rapid breakdown of the weak-phase approximation (upon which all Scherzer-type conventional imaging theory is based).

Conventional transmission electron microscopes (TEMs) can achieve a point-to-point resolution of between 0.1 and 0.2 nm, depending on accelerating voltage. Since typical atomic bond lengths are of this order of magnitude, it could be argued that further gains in resolution would not be particularly fruitful, especially since the scattering mechanism of electrons is via the atomic potential which is somewhat featureless at the sub-0.1nm scale. However, increased resolution is desirable for a number of reasons. Firstly, inferring structure at the very limit of the conventional resolution can be hazardous - large phase changes may be unwittingly introduced to the scattered beams by beam tilt and, perhaps more seriously, third-order astigmatism: in general, an imaging system should have a band-pass which is significantly wider than the spatial frequency under observation. Secondly, when seen in projection, as in the TEM, many structures have spacings which are much smaller than the atomic bond lengths. Thirdly, it should be possible to explore high-angle scattering information, for this contains three-dimensional information: ironically, the fact that scattering angles are so small in the TEM, so that all specimens are seen in projection, is often cited as a strength of the technique. If we could imagine an electron equivalent of a scanning optical microscope (SOM), which has wavelength-limited lateral and depth resolution, then we would have a truly powerful machine, capable of imaging each atom in a three-dimensional specimen directly.

Conceptually, the easiest route to increased resolution (though one which is not technologically trivial) is to raise the accelerating voltage, though in many specimens this

can cause unacceptable levels of knock-on damage. Here, we are concerned with indirect, multidetector methods in scanning transmission electron microscopy (STEM) for reconstructing the exit wave function at 'super-resolution' - that is to say, at several times the resolution dictated by the intrinsic useful aperture of the electron lens. This method differs from holography [2,3] and through-focal series reconstruction [4] in that the effective increase in the aperture size is achieved by the self-interference of diffracted beams, and not interference with a reference wave. This means that the requirements for stability in the microscope are much less severe, which in turn suggests that such methods could be considerably extended to much higher resolutions. Furthermore, the method employs much larger scattering angles than normal, suggesting that it may be possible to extract three-dimensional information.

Dedicated STEM

Although many TEMs have STEM facilities for performing micro-analytical work, the dedicated STEM is designed specifically to form a high-brightness focussed probe using a field-emission gun (FEG). The main differences are that UHV (10^{-9}-10^{-11}Torr) is held throughout column to avoid problems with contamination at the specimen and FEG tip degradation, the objective lens is mounted between the source and the specimen, and that great care is taken in ensuring the scan coils are extremely stable, even at minute excitations (in most TEM-STEMs, probe size is greatly compromised by electrical interference).

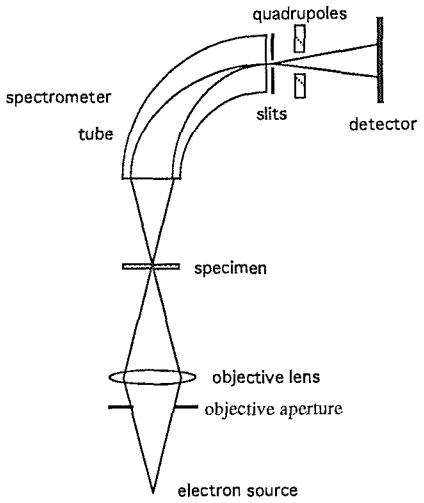

Figure 1: Schemetic diagram of the dedicated HB501 STEM used in these experiments. For simplicity, the condenser lenses have been omitted. The detector is described in the text. The quadrupoles are used to magnify or demagnify the electron diffraction pattern. The cross-over at the spectrometer slits means that all such diffraction patterns are energy-filtered (to about 1eV).

In the dedicated STEM (Figure 1), the probe cross-over, which is focussed in the specimen plane, is limited in size only by aberrations in the lens and the diffraction limit prescribed by the objective aperture. Bright-field imaging in STEM, in which a small collector aperture (1-5 mrad at 100keV) is used to collect the transmitted intensity as a function of probe position, gives contrast features which are identical to those in a TEM with equivalent lens/aperture parameters: Fresnel fringes, through-focal contrast reversal, lattice fringes and diffraction contrast are all visible. This is most eloquently explained in terms of reciprocity (ref). The STEM is essentially a time-reversed TEM. We can think of the FEG source lying in the image (detector) plane of the conventional TEM (the STEM condenser lenses are equivalent to the TEM projector lenses), while the collector aperture in STEM lies in the plane of the source in TEM (i.e. it is equivalent to the TEM condenser aperture).

When STEM first became a practical experimental technique, there was much work concerning the optical advantages of the configuration. It may be noted that by introducing a large defocus into the beam, Gabor's original proposal for holography is

realised [5]. Others suggested the introduction of filters in far-field plane or methods for employing the scattered wavefield lying outside the unscattered disc [6]. The essential basis of all of these techniques is that very large scattering angles are available in STEM which have not been significantly corrupted by spherical aberration in the lens (although all beams are affected to some degree by aberration, leading, for example, to a consistent breakdown of Friedel's law in the far-field microdiffraction plane [7]). In what follows, we attempt to illustrate in a consistent way that by using multidetectors in STEM, we can in principle overcome all the problems in electron microscopy: the phase problem, the deconvolution of the lens function, the limitations of the coherence envelope or 'information limit,' and hence the resolution problem.

The experiments have been performed on a VG Microscopes HB501 STEM which has, by the standards of high-voltage TEM, rather poor imaging characteristics. Working at 100keV with an objective lens with a spherical aberration constant of 3.1mm , its intrinsic bright-field point-to-point resolution is 0.42nm. However, we show that by processing the far-field microdiffraction intensity which can be recorded at the top of the column, this resolution can be improved by a factor of three or more. Microdiffraction patterns are energy-filtered via an electron-loss spectrometer (Figure 1), and incident upon a YAG scintillator which is optically bonded to a fibre-optic feedthrough. This signal enters an image-intensified CCD camera and is recorded by a real-time frame-grabber as the electron probe is scanned across the specimen.

Super-resolution imaging of crystals

Let us first illustrate super-resolution in STEM using a specimen which widely used as a test of conventional resolution, even at high accelerating voltages - crystalline silicon orientated along the <110> direction. It should be emphasised that the HB501 STEM cannot conventionally image any of the periodicities in this lattice. If we record the whole diffraction plane in the far-field (beyond the spectrometer - Figure 1), we see a series of diffracted discs similar to a convergent beam electron diffraction (CBED) pattern. The crucial difference, however, is that because the FEG source is so coherent, areas of disc overlap can interfere with one another. The straight fringes visible in Figure 2 arise from defocus in the beam. Each diffracted spot has been convolved with an aperture function - when parabolic (defocus) phase changes interfere, the result is a linear phase ramp, leading to the fringes.

The principles of super-resolution are now straightforward to understand. The relative position of all the interference fringes can give the phase difference between each of the pairs of beams. Even very high-angle diffracted beams can be phased with respect to the next lower order beam, and so on and so forth. The necessary width of the aperture or coherence function need only be as wide as the first-order diffracted disc, because the strength of the interference phenomenon depends only on the vector between diffracted discs, and not on their absolute distance from the optic axis. All other phase retrieval methods such holography and through-focal series reconstruction, rely on very wide coherence envelopes which can embrace all diffracted amplitude simultaneously. STEM is not subject to these constraints.

In order to extend the beam-phasing method to general non-crystalline specimens, the best way to determine the relative phase of beams is to scan the electron probe over the specimen. Each pixel in the microdiffraction plane now collects a separate image, thus accumulating a four-dimensional intensity data set. For a crystal, intensity in the detector pixels in the disc overlaps vary sinusoidally as a function of probe position (such pixels correspond to two-beam image interference fringes). Now if a Fourier transform is taken with respect to the probe-position coordinate, it is possible to extract directly the relative phase differences of all beams simultaneously [8]. This scheme is a variation on a method first proposed by Hoppe [9] and later referred to as 'ptychography' [10], although it can be thought of in much more general imaging terms. We have applied it to position-resolved data similar to Figure 2 (but without defocus) to obtain the real-space

image shown in Figure 3. This shows the characteristic silicon dumb-bell features, at an effective resolution of 0.136nm (compared to the point-to-point resolution of this microscope of 0.42nm).

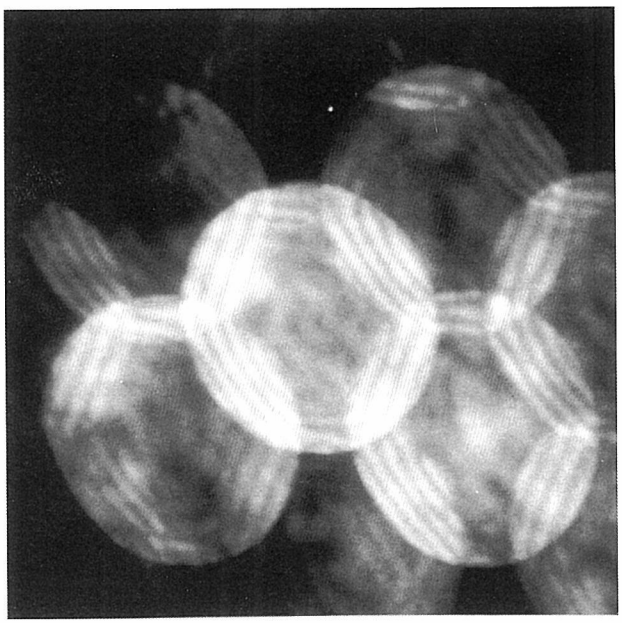

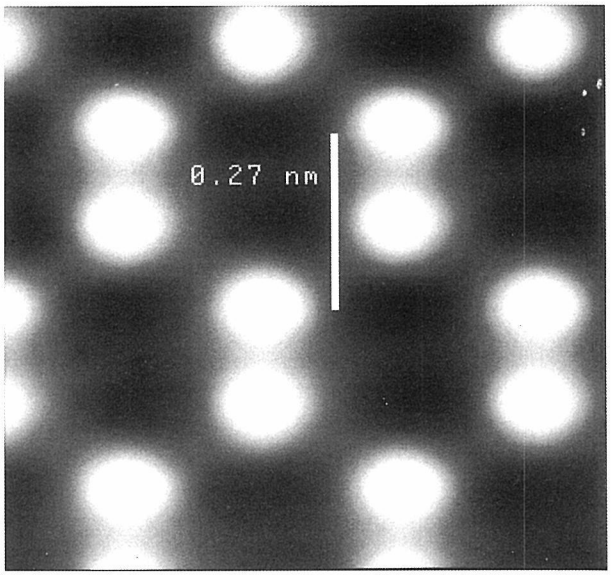

Figure 2 (left) shows defocus interference fringes occuring in the disc overlaps of the coherent electron microdiffraction plane from the <110> orientation in silicon. The aperture is 16mrad in diameter.
Figure 3 (right) shows the phase of the exit wavefield from silicon on the <110> pole, as calculated from a real-space scan of the probe (see text). Note the familiar dumb-bells could never be conventionally imaged in this microscope. We have tested extensively for effects such as defocus, specimen thickness, misorientation and phase error, and conclude that all the detail in this image is real.

The full 2D solution

A full formal mathematical solution for obtaining a super-resolution image of a non-crystalline material exists provided we can approximate the specimen as two-dimensional and assume that the probe interacts with it multiplicatively. Except for thin specimens (less than about 5nm thick), these conditions are not generally satisfied in electron scattering. However, the four-dimensional data set we employ is highly redundant, and it can be shown that, once Fourier transformed with respect to the probe position coordinate, there are privileged planes within the data set which correspond to slices through three-dimensional reciprocal space [11], thus suggesting that the method could be extended to infer three-dimensional structure.

Let the detector coordinate vector in a multidetector STEM be denoted $\mathbf{r}'$, and the probe-position coordinate vector be ρ. (Dashes will refer to reciprocal space coordinates.) Let $a(\mathbf{r})$ be the complex probe function in real space, and $\psi(\mathbf{r})$ be the complex specimen transmission function (which may be weak or strong phase, or attenuating), then, ignoring magnification and camera-length factors, the intensity recorded in the far-field as a function of both $\mathbf{r}'$ and ρ is

$$|M(\mathbf{r}',\rho)|^2 = \iint a(\mathbf{b}-\rho)a^*(\mathbf{c}-\rho)\,\psi(\mathbf{b})\psi^*(\mathbf{c})\,\exp[i2\pi\mathbf{r}'.(\mathbf{b}-\mathbf{c})]\,d\mathbf{b}\,d\mathbf{c} \qquad (1)$$

$$= \iint A(\mathbf{b}')A^*(\mathbf{c}')\,\Psi(\mathbf{r}'-\mathbf{b}')\Psi^*(\mathbf{r}'-\mathbf{c}')\exp[i2\pi\rho.(\mathbf{b}'-\mathbf{c}')]\,d\mathbf{b}'\,d\mathbf{c}' \qquad (2)$$

where A(**r**') is the aperture function of the lens (the inverse Fourier transform of a(**r**)), $\Psi(\mathbf{r}')$ is the Fourier transform of $\psi(\mathbf{r})$, and **b**,**b**',**c** and **c**' are dummy variables of the integrations, all of which are over two-dimensional vectors. If we ignore for a moment the exponential terms, then the first equation is simply a description of conventional imaging and the second is just the conventional CBED pattern: the aperture function of the lens convolved with the reciprocal space of the specimen. Neither of these conventional formulations can solve the phase and resolution problems. But taken together with the exponential terms - the first is equivalent to recording all beam-tilted images in TEM, the second is the inclusion of probe movement in coherent CBED - then the total four-dimensional data set offers a full solution. Via a Wigner distribution deconvolution, which is too lengthy to derive here (see [12]), we can form

$$D(\mathbf{r}', \rho') = \Psi^*(\mathbf{r}'-\rho')\Psi(\mathbf{r}'). \qquad (7)$$

This data set implicitly contains all the phase information of the Fourier transform of the specimen function (just as in the example above with the silicon specimen), but in a way which has removed all the influences of the lens transfer function, and which is not subject to the limitations of the coherence width. The method has been successfully applied to the optical bench to achieve large gains in resolution [13,14]. It is interesting to note that the data set can also be used for an iterative blind deconvolution of both the specimen function and the lens transfer function[15].

Approximations for weak scattering

The four-dimensional data set described above is highly redundant. In fact, large gains in resolution can be achieved using much simpler detector geometries if we assume the specimen is only weakly scattering. (Here, 'weak' implies the unscattered amplitude is strong relative to scattered beams - a much less severe constraint than 'weak phase' in conventional TEM.) In this case, the specimen is given by

$$\psi(\mathbf{r}) = 1 - if(\mathbf{r}), \qquad f(\mathbf{r})<<1 \qquad (8)$$

or, equivalently, in reciprocal space by

$$\Psi(\mathbf{r}') = \delta(\mathbf{r}') + \Psi_S(\mathbf{r}'), \qquad (9)$$

where $\delta(\mathbf{r}')$ is a Dirac delta function representing the unscattered beam and $\Psi_S(\mathbf{r}')$ is the scattered part of the wave-function. Now let us consider the Fourier transform of the original data set with respect to the probe position coordinate ρ. That is to say,

$$G(\mathbf{r}',\rho') = \int |M(\mathbf{r}',\rho)|^2 \exp(i2\pi\rho.\rho')\, d\rho \qquad (10)$$

from equ 2 and 9, this may be expanded, ignoring (small) cross-terms of Ψ_S, to give

$$G(\mathbf{r}',\rho') = |A(\mathbf{r}')|^2 \delta(\rho') + A(\mathbf{r}')A^*(\mathbf{r}'+\rho')\Psi_S^*(-\rho') + A^*(\mathbf{r}')A(\mathbf{r}'-\rho')\Psi_S(\rho') \qquad (11)$$

This equation defines where appreciable power arrives in the microdiffraction plane as a function of the Fourier component of the probe position, ρ'. It is illustrated experimentally in Figure 4, where a circular objective aperture (A(**r**')) has been used to collect a four-dimensional data set from amorphous carbon which has a broad spectrum of spatial frequencies. We show slices of $G(\mathbf{r}',\rho')$ as a function of **r**' (the detector plane coordinate) at various constant values of ρ'. As the value of ρ' increases, two shapes

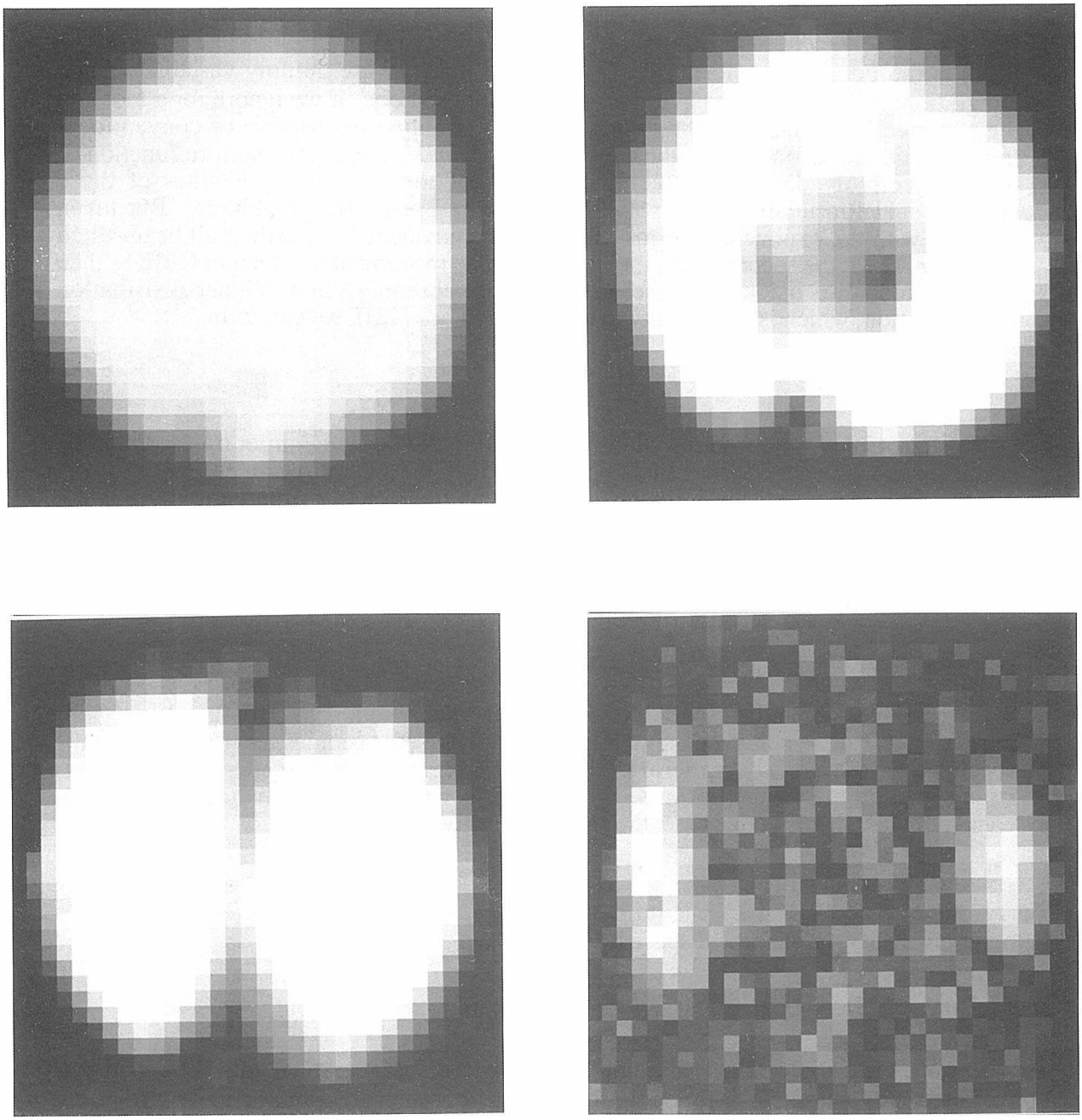

Figure 4: Slices through an experimental $G(\mathbf{r}',\rho')$ data set collected from amorphous carbon. What we see plotted in each picture is a slice of the data corresponding to the detector coordinates, $\mathbf{r}'$. These are plotted for different constant values of ρ', the Fourier transform of the probe position coordinate. If the aperture radius is α (corresponding in this case to 4mrad), then the top left shows $\rho'=0$, top right is $\rho'=0.6\alpha$, bottom left is $\rho'=\alpha$, bottom right is at $\rho'= 1.5\alpha$. As ρ' increases, two aperture shapes, which at first are overlapping (top two images), are seen to move apart, separate, and finally move beyond the edge of the central disc. These regions contain double-resolution information which does not depend strongly on the lens transfer function.

corresponding to occluded apertures are seen to separate and move apart to higher values of **r'**. This phenomenon can be understood by consideration the latter two terms of equation 11, each of which consists of an aperture shifted with respect to itself.

More importantly, these areas of amplitude represent transmittance of double-resolution information through the microscope. Consider the plane of data $\mathbf{r}'=\rho'/2$ in $G(\rho'/2,\rho')$, then if the aperture function is symmetric (which it usually is), all the phase parts of the aperture terms cancel and, because either only the second or third term is present at spatial frequencies higher than a third of the maximum available, we can write that approximately

$$\Psi(\rho') = G(\rho'/2,\rho'). \qquad (12)$$

This is a rather astonishing result, suggesting that we can obtain a full spectrum of the specimen function at twice the conventional resolution without any knowledge of the lens function. Indeed, if the real aperture is removed from the objective, the method still works because now the virtual aperture of the coherence envelope can separate the terms in equation 12 [16] and, for certain levels of defocus, the effective transfer of the lens can be more than doubled. A demonstration of this reconstruction method, which we call "the half-ρ' scheme", is shown in Figure 5. The specimen is amorphous carbon, and is the same data set as that used for Figure 4. The increase in resolution is a factor of two: this is not particularly informative for an amorphous film, but it has been shown that these results are reproducible [17].

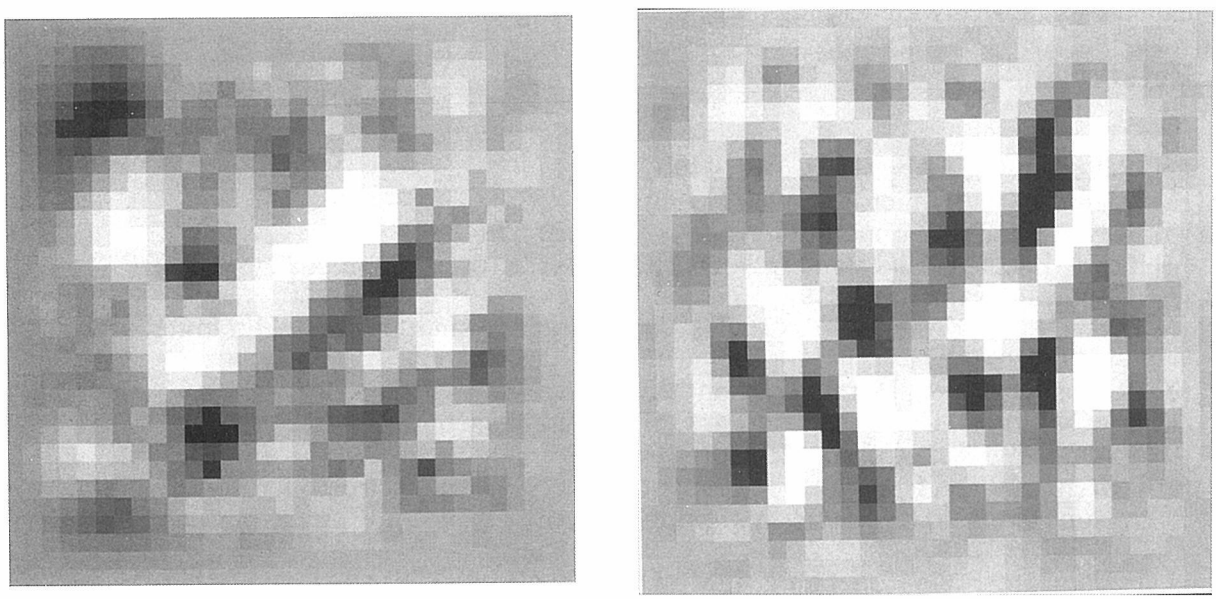

Figure 5: On the left is shown a small region of the conventional bright-field image of amorphous carbon (from the same data set as shown in Figure 4). On the right is the phase of a reconstruction at double resolution. The pixel size corresponds to 0.19nm. Such experiments can be shown to be reproducible.

The half-ρ' scheme requires a high-resolution detector pixels if it is to be entirely immune from the effects of lens aberrations. This poses certain data-handling difficulties: each pixel of every image (probe-position) has a two-dimensional diffraction pattern associated with it. In the preliminary experiments shown in Figures 4 and 5, only 32x32 detector pixels were used for an image of 32x32 probe positions - i.e. a data set of 1Mbyte, which converts into 16Mbyte of complex double-precision numbers suitable for Fourier transformation. A significant field of view could consume Gigabytes

of data. However, if we are prepared to assume that the lens function is reasonably well behaved (and the specimen is weakish), only a few detector elements are required, the minimum number possible being three in the form of sectors of a circle centred on the optic axis. Such imaging depends on the fact that for each periodicity in the image, ρ', a single detector can pick out all or part of the signal lying in the occluded aperture functions described in equation 11. If we have a small number of detectors filling up the unscattered central beam, the collected signals can be Fourier transformed, weighted by filtering functions that boost poorly transferred frequencies in each detector, and then added, and finally transformed back to create a double resolution image.

Conclusions

By putting multidetectors in the far-field microdiffraction plane of a STEM, it is possible to calculate the electron exit wave in complex amplitude at many times better than the conventional resolution limit. For non-crystalline strongly-scattering specimens there is a solution to the phase and resolution problems involving a four-dimensional deconvolution. However, for crystalline specimens, only a fraction of this data is needed to solve for the structure at super-resolution. Similarly with weak specimens, solution methods can be much simplified, but then we are limited to only double resolution (or slightly more than double if the outer regions of the virtual aperture is used). Both these latter simplifications have been demonstrated above. With further developments of these techniques, the results imply that in future material science need not be hampered by the failings of the conventional high-resolution electron microscope. Computational, multidetector techniques in the STEM mode may eventually provide reliable, sub-atomic resolution images of the solid state without the difficulties and expense associated with very high accelerating voltages.

References

[1] Scherzer, O., J Appl Phys **20** (1949) 20
[2] Lichte, H, Ultramicroscopy **20** (1986) 293
[3] Kawasaki, T and Tonomura, A, Phys Rev Lett **69** (1992) 293
[4] Op de Beeck, M and Van Dyck, D, Micron & Microscopica Acta **22** (1992) 279
[5] Gabor, D, Nature **161** (1948) 777
[6] Konnert, J, D'Antonio, P, Cowley, J, M, Higgs, A and Ou, H,J, Ultramicroscopy **30** (1989) 371
[7] Rodenburg, J, M, Ultramicroscopy **25** (1988) 329
[8] McCallum, B, C and Rodenburg, J, M, Ultramicroscopy **52** (1993) 85
[9] Hoppe, W, Acta Cryst **A 25** (1969) 495
[10] Hoppe, W and Hegerl, R, in 'Computer processing of electron microscope images,' Ed Hawkes, P, W, Springer: Berlin (Topics in Current Physics) **13** (1980) 127
[11] Plamann, T and Rodenburg, J, M, Optik **96** (1994) 31
[12] Rodenburg, J, M and Bates, R, H, T, Phil Trans R Soc London A **339** (1992) 521
[13] Friedman, S, L and Rodenburg, J, M, J Phys D: Appl Phys **25** (1992) 147
[14] McCallum, B, C and Rodenburg, J, M, Ultramicroscopy **45** (1992) 371
[15] McCallum, B, C and Rodenburg, J, M, J Opt Soc Am A **10** (1993) 231
[16] Nellist, P, D, and Rodenburg, J, M, Ultramicroscopy **54** (1994) 61
[17] Rodenburg, J, M, McCallum, B, C and Nellist, P, D, Ultramicroscopy **48** (1993) 304

Dynamic Observation of Flux Lines by Field Emission Lorentz Microscopy

Ken Harada, Hiroto Kasai, Tsuyoshi Matsuda, Masami Yamasaki, John E. Bonevich and Akira Tonomura*

Advanced Research Laboratory, Hitachi, Ltd., Hatoyama, Saitama 350-03, Japan

ABSTRACT

Interaction between magnetic flux-lines penetrating a superconducting film and material defects were directly observed in real-time and recorded on video tape with a time resolution of 1/30 s by field emission Lorentz microscopy. By hopping from one pinning center to another, flux lines kept moving until calming down at an equilibrium state. Frame-by-frame observation of video tape revealed how individual flux lines behaved when they came across and interacted with the subgrain boundaries.

INTRODUCTION

The dynamic behavior of magnetic flux lines is considered as a key element for the fundamental understanding and practical applications of superconductivity. In particular, flux-line interaction with pinning centers, which determines the critical current of a superconductor, is of great concern from practical viewpoints. However, there have been no direct techniques for observing individual flux lines in real time, even less for observing interaction between flux lines and pinning centers, until our 300-kV field emission electron microscope [1] succeeded in observing them by Lorentz microscopy [2,3] and by electron holography. [4,5] This paper presents field emission Lorentz microscopy for observing individual flux lines and their interactions with material defects. [6]

EXPERIMENTAL METHODS

(1) Specimen preparation

A single-crystalline thin film of Niobium (Nb) was prepared by chemical etching. The purity of the original Nb foil was 99% and the grain sizes were 10~20 μm in diameter. The Nb foil, which had a [110] surface, was annealed at 2200 °C for a few minutes in a vacuum of 1×10^{-6} Pa to increase the grain sizes to 200~300 μm. An average thickness of about 100 nm were investigated in our observation.

Scanning electron microscopy (SEM) and atomic force microscopy (AFM) revealed plate-shaped fine structures inside a single grain as shown in Fig. 1. Such fine structures were hard to observe after the annealing, while they became more apparent after chemical etching. However, high-resolution transmission electron microscopy (TEM) and micro-area electron diffraction could hardly reveal difference in crystallographic structures and orientations between the two sides of boundaries. We detected in some cases slight displacements of bend contour lines and concluded that even if there was any crystallographic misfit angle at boundaries, it was less than 10^{-2} rad. We considered that the fine structures were corresponded to the subgrains in the film. The average thickness variation measured by AFM was about 50 nm at the subgrain boundaries.

* *present address: Lawrence Berkeley Lab., MSD 72, Berkeley, CA 94720 USA*

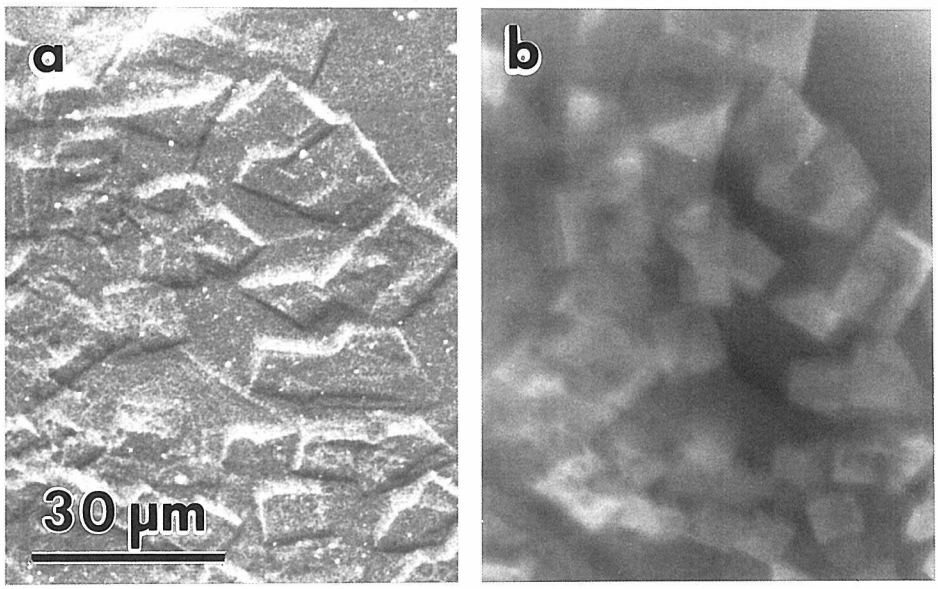

Fig. 1. Surface morphology of a Nb foil after chemical etching.
(a) Scanning electron micrograph, (b) Atomic force micrograph.

(2) Experimental arrangements for observation

A Nb film of 100~300 nm thick was mounted on the low-temperature specimen stage in the 300-kV field emission electron microscope. The film was tilted so that the film normal had an angle of 45° both to the incident electron beam and to the applied magnetic field as shown in Fig. 2. The defocused image was obtained as Lorentz micrograph by adjusting the focal length of the intermediate lens. The defocusing distance was 10~30 mm in case of Nb film.

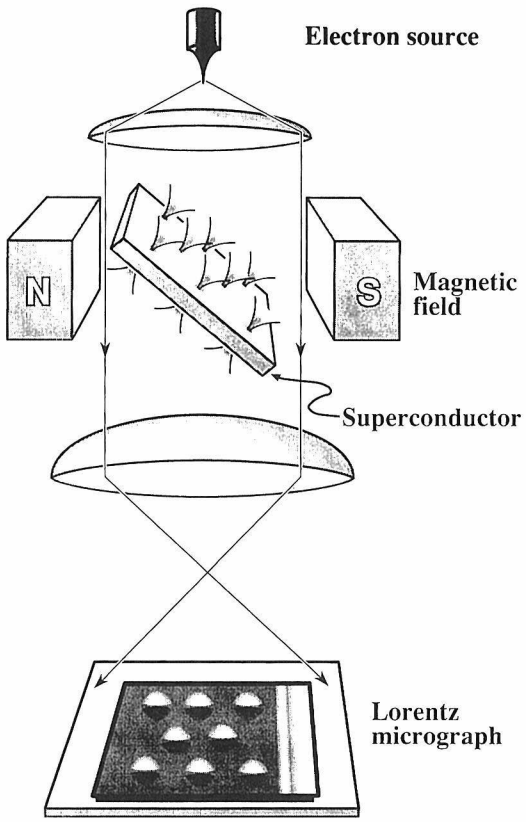

Fig. 2. Schematic diagram of the experimental arrangement.

RESULTS AND DISCUSSIONS

(1) Static observation of flux lines

An electron micrograph and a Lorentz micrograph of a Nb thin film at 4.5 K are shown in Fig. 3. A subgrain boundary can be seen with low contrast running horizontally in the middle of electron micrograph (a). Many black bend contours can be seen with high contrast in the vertical direction in the micrograph. Since these contours are not displaced at the subgrain boundary, the crystallographic orientation is almost the same on both sides of the boundary. The contrast in the micrograph implies that the region above the boundary is thinner than that below it.

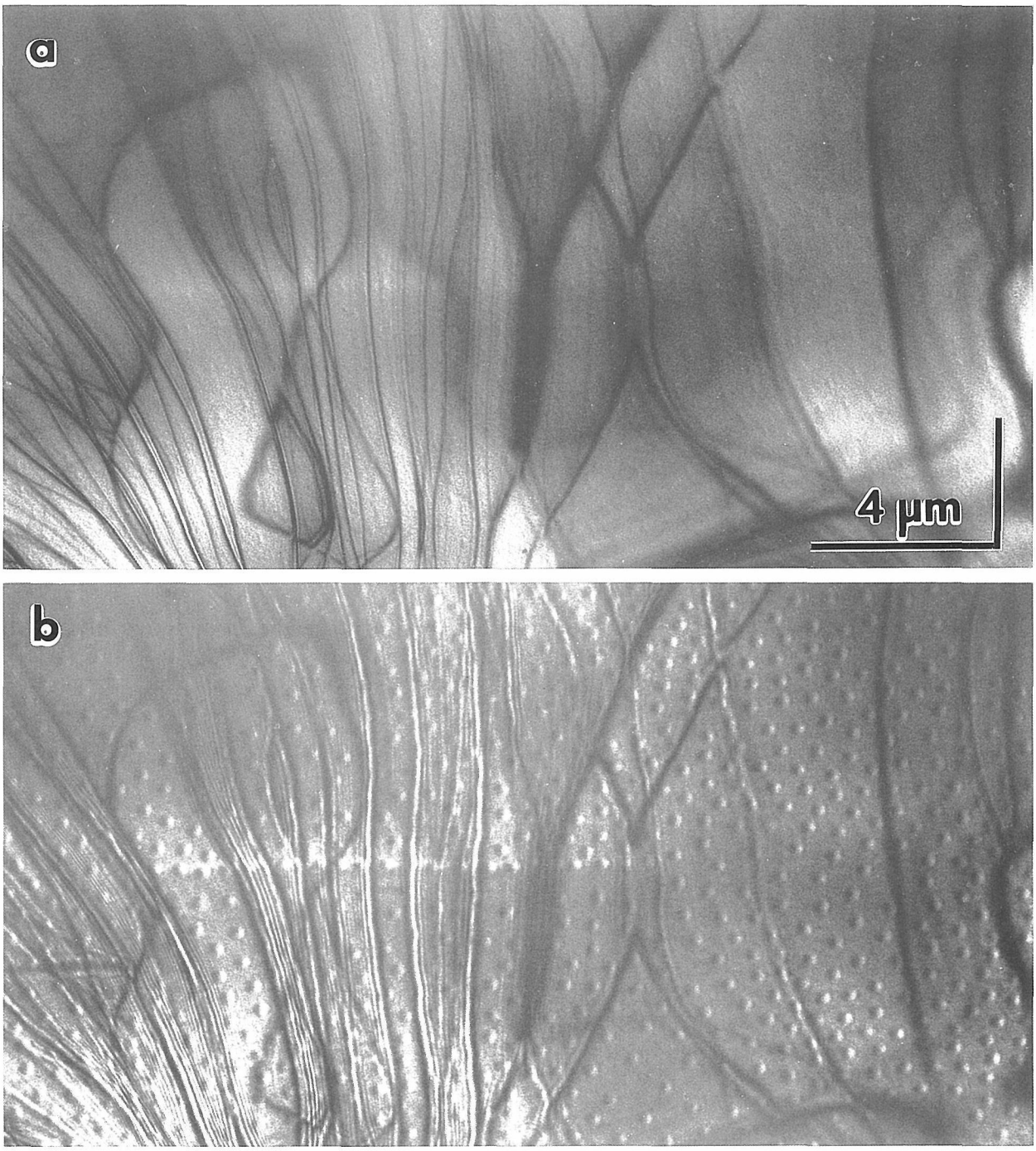

Fig. 3. Static observation of flux-lines and subgrain boundary in a Nb thin film at 4.5 K and in a 20 *G* magnetic field. (a) Electron micrograph (in focus), (b) Lorentz micrograph (Δf = 20 mm).

In Lorentz micrograph (b), which was obtained by defocusing the image by 20 mm, flux lines are seen as spots consisting of light and dark contrast. The boundary can be seen more clearly in the defocused image. Flux lines appear to be distributed at random but line up along the subgrain boundary.

Another example of specimen that has a large thickness change at a boundary is shown in Fig. 4. The lower, black, region in the micrograph corresponds to the thicker part of the film. Flux lines near the subgrain boundary make a row along the boundary and tend to be located on the thinner side of the boundary. The density of flux lines at the boundary is much higher than other regions. This is because the free energy of such a distribution due to the large difference in film thickness is lower than that of the uniform flux-line distribution.

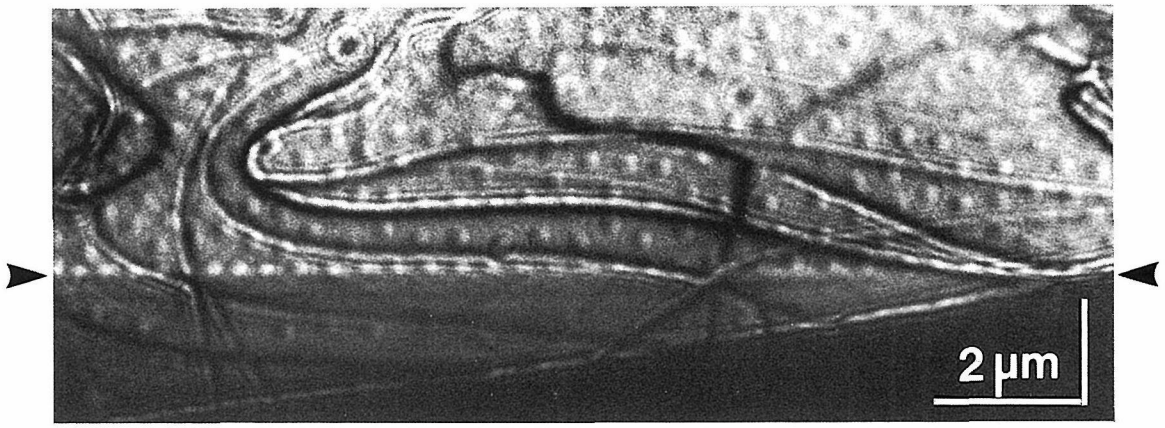

Fig. 4. Lorentz micrograph of flux lines near a subgrain boundary that has a large thickness change.

The static observation of the flux-line distribution near the boundaries allows us to understand flux pinning at defects due to film thickness changes. The actual situations of flux pinning, however, cannot be known without the dynamic observation.

(2) Dynamic observation of flux lines

The dynamic interaction between flux lines and subgrain boundaries was observed and recorded on video tape. When the magnetic field applied on a Nb thin film at 4.5 K was changed, flux lines moved quickly by hopping among weak pinning sites at first. When they came upon a subgrain boundary, they were trapped by it and began to move along it even if the direction of the boundary was not the same as that of the initial flux-line movement.

Some video frames demonstrating such a complicated flux-line movement are shown in Fig. 5. The movement of each flux line could be traced and marked with different colors. The three boundaries are identified by numbers respectively, and the direction of flux-line hopping is indicated by arrow in (a). When these flux lines arrived at the subgrain boundary 1, they could not cross it and began to move along it. For example, the dark blue, green, and red flux lines in the frame (a) are first above the boundary 1 and then move in the direction along the boundary. The dark blue flux line, when it arrives at the corner of the boundary, turns to the right and moves along boundary 2 in (b), while the succeeding red flux line also turns to the right but along another boundary 3. The blue and red flux lines trace the same path along the boundary 1 until reaching the corner, where they proceed separately along two different boundaries: 2 and 3, respectively--perhaps because of the repulsive interaction between them.

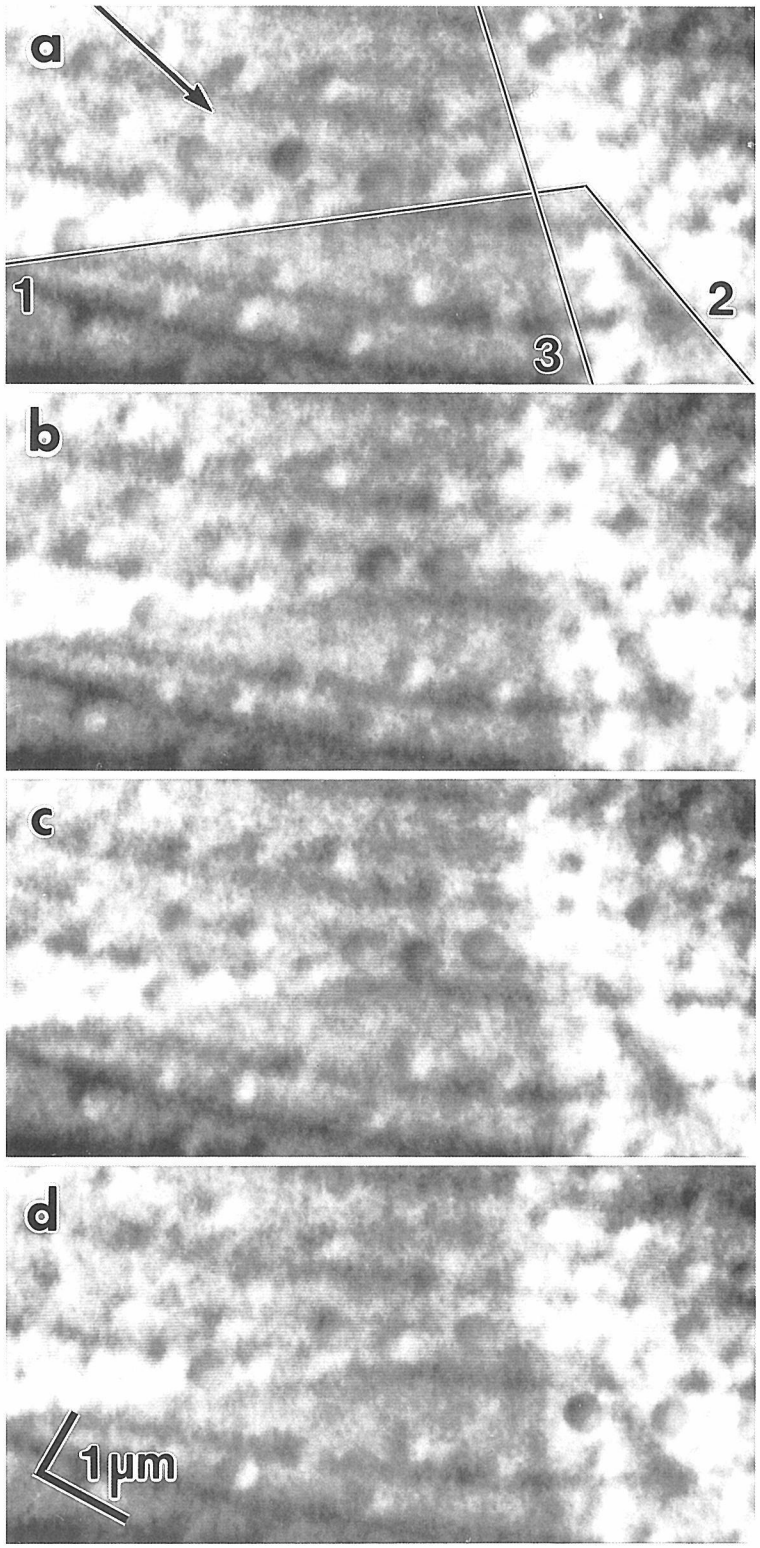

Fig. 5. Dynamics of individual flux lines when a magnetic field of 15 *G* is applied: (a) t=0.00 s, (b) t=6.00 s, (c) t=7.00 s, (e) t=13.03 s.

Flux lines below boundary 1 did not move during this time period. This is because the flux-line distribution was balanced so that their density below it was much lower than that above it and consequently no force was exerted on flux lines below the boundary.

In this way the flux-line dynamics near subgrain boundaries, which could not be observed with the static observation, have been clarified directly. These movements of individual flux lines can be considered to be correlated each other.

CONCLUSION

We have established a technique for observing both individual flux lines and defects. This technique can be applied to the investigation of interaction between flux line and crystallographic defects, such as some types of dislocations and/or stacking faults. The technique will provide detailed information for practical use of high-T_c superconductors and will be useful for elucidating the fundamental issues in superconductivity.

REFERENCES

[1] T. Kawasaki et al., Jpn. J. Appl. Phys. **29** (1990) L508.
[2] K. Harada et al., Nature **360** (1992) 51.
[3] K. Harada et al., Phys. Rev. Lett. **71** (1993) 3371.
[4] J. Bonevich et al., Phys. Rev. Lett. **70** (1993) 2952.
[5] J. Bonevich et al., Phys. Rev. B **50** (1994) 567.
[6] K. Harada et al., Jpn. J. Appl. Phys. **33** (1994) 2534.